

IEEE

microwave

for the Microwave & Wireless Engineer



MAGAZINE

Volume 22 • Number 7 • July 2021

Low-Noise Techniques





IEEE Radio and Wireless Symposium

16-19 January 2022, Caesars Palace Hotel, Las Vegas, NV USA

Paper Deadline
25 July 2021



IEEE



Part of Radio and Wireless Week

<https://www.radiowirelessweek.org/>

Steering Committee

General Chair

Kevin Chuang, *MaxLinear*

General Co-Chair

Alexander Koelpin, *Hamburg University of Technology*

Technical Program Chair

Changzhi Li, *Texas Tech. University*

Finance Chair

Holger Maune, *Technical University of Darmstadt*

PAWR Co-Chairs

Václav Valenta, *European Space Agency*
Roberto Quaglia, *Cardiff University*

WiSNet Co-Chairs

Rahul Khanna, *Intel*
Paolo Mezzanotte, *University of Perugia*

SiRF General Chair

Saeed Zeinolabedinzadeh, *Arizona State University*

SHaRC Co-Chairs

Markus Gardill, *Julius-Maximilians-University Würzburg*
Maximilian C. Scardelletti, *NASA Glenn Research Center*

Executive Committee Chair

Rashaunda Henderson, *University of Texas Dallas*

Conference Management

Elsie Vega, *IEEE*
Deidre Artis, *IEEE*

Call For Papers

The 2022 IEEE Radio and Wireless Symposium (RWS 2022) will be held during the week of 16 January 2022 in Las Vegas, NV, USA.

RWS 2022 and the 22nd IEEE Topical Meeting on Silicon Monolithic Integrated Circuits (SiRF 2022) are co-located and will continue to hold joint sessions. Topical conferences held in parallel provide more focused sessions in the areas of RF Power Amplifiers (PAWR), Wireless Sensors and Sensor Networks (WiSNet), and the IEEE Space Hardware and Radio Conference (SHaRC). The RWS Demonstration Track provides an interactive forum for hands-on demonstration of latest wireless experiments and innovations. There are also Special Sessions, Short Courses, and Design Competition. RWS Papers featuring innovative work are solicited in (but not limited to) the following areas:

1. High-speed and Broadband Wireless Technologies

- 3G/4G/5G Wireless Communication Services
- Broadband Fixed Wireless and Last-Mile Access
- Optical Networks Systems and Microwave Photonics
- Ultra-High Data Rate Communications Links - Powerline Communication Technologies
- Ultra-Wideband (UWB) Systems

2. Emerging Wireless Technologies and Applications

- Femtocell and Heterogeneous Networks
- Green, Sustainable Wireless Tech. & Networks
- M2M & V2V Technologies & Applications
- Resource Management, Security
- Wireless Security and RFID Technologies
- Wireless Power Transfer
- Quantum Technologies with Microwaves

3. Wireless System Architecture and Propagation Channel Modeling

- Ad Hoc Network Techniques for Internetworking
- Distributed Network Architectures and Systems
- Frequency and Channel Allocation Algorithms
- Propagation Considerations and Fading Countermeasures
- Wireless Channel Characterization & Modeling
- Wireless Mesh and Local/Personal/Body Area Networks

4. Wireless Digital Signal Processing and Artificial Intelligence

- Digital/Analog Adaptive/Collaborative Signal Processing
- Dynamic Spectrum Sharing, Coexistence, Interoperability
- Interference Mitigation and Cancellation Techniques
- MAC, Networking protocols, Policies, Standardization
- Methods for Signal Integrity and Signal Conditioning
- Artificial Intelligence & Machine Learning in Radio and Wireless
- Spectrum Sensing Technologies

5. Applications to Bio-Medical, Environmental, and Internet of Things

- Miniaturization and Integration of Wireless Technologies
- Biological Material Characterization
- Personal Area Networks and Body area Sensor Networks
- Wireless Positioning Technologies & Remote Sensing

6. MIMO and Multi-Antenna Communications

- Cooperative/Collaborative Technology
- MIMO, MU-MIMO, Space-Time Processing - Relaying Technologies
- Multi-Beam Smart Antennas

7. Antenna Technologies

- Miniaturized, Multi-frequency and Broadband Antennas
- Passive and Active Antennas from RF to THz Frequencies
- Wireless Platform Integrated Antennas

8. Transceiver and SDR Technologies

- Digital Transmitters for Sub-6 GHz Wireless
- Low-Power Cost-Effective IoT Solutions
- Multi-Mode Multi-Band Radios
- RF Imperfection Compensation Techniques
- Satellite Communication Systems

9. Passive Components & Packaging

- 3D-Packaging, Interconnects, and Applications
- Discrete and Highly Integrated Packaging
- Discrete, Embedded and Distributed Passive Components, Filters Couplers and Signal Separation Devices

- Packaging of MEMS, Biosensors and Organic ICs

10. MM-Wave to THz Technology & Applications

- Active and Passive Devices Demonstration
- Architectures for Next-Generation Large-Scale Systems
- High-Capacity Sensing and Imaging Arrays
- Phased Arrays for 5G Communication

11. 3D & Novel Engineered Materials

- Additive 3D manufacturing for wireless applications
- Novel Engineered Materials for Antenna, Packaging, Passive Devices and Flexible Electronic Integration

RWS 2022 General Chair

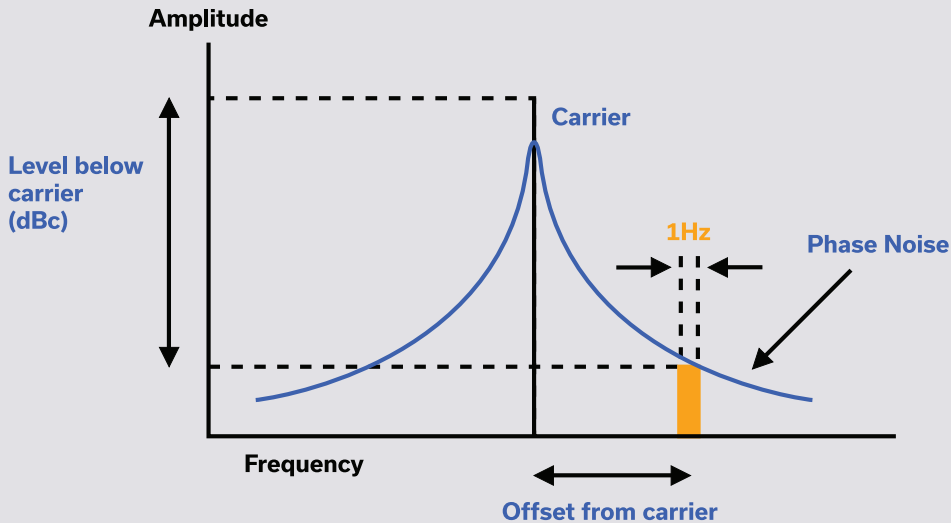
Kevin Chuang, *MaxLinear*

RWS 2022 General Co-Chair

Alexander Koelpin, *Hamburg University of Technology*

Authors of papers presented at RWW 2022 will be invited to submit an expanded version to the **IEEE T-MTT Mini-Special Issue**.

Paper submission instructions can be found at <http://www.radiowirelessweek.org/>. Submissions should be formatted according to the submission review template available on the RWW website. Authors should indicate preference for oral or poster presentation. All submissions must be received by **25 July 2021**. All accepted papers will be published in a digest and included in the IEEE Xplore® Digital Library. Submissions will be evaluated based on novelty, significance of the work, technical content, interest to the audience, and quality of writing.



INDUSTRY-LEADING PERFORMANCE

Low Phase Noise Amplifiers

For Sensitive Transceiver Systems

- Additive phase noise as low as -173 dBc/Hz @ 10 kHz Offset
- Ideal for radar, test instrumentation and more
- Wide selection in stock for the most demanding requirements
- State-of-the-art measurement capability in house



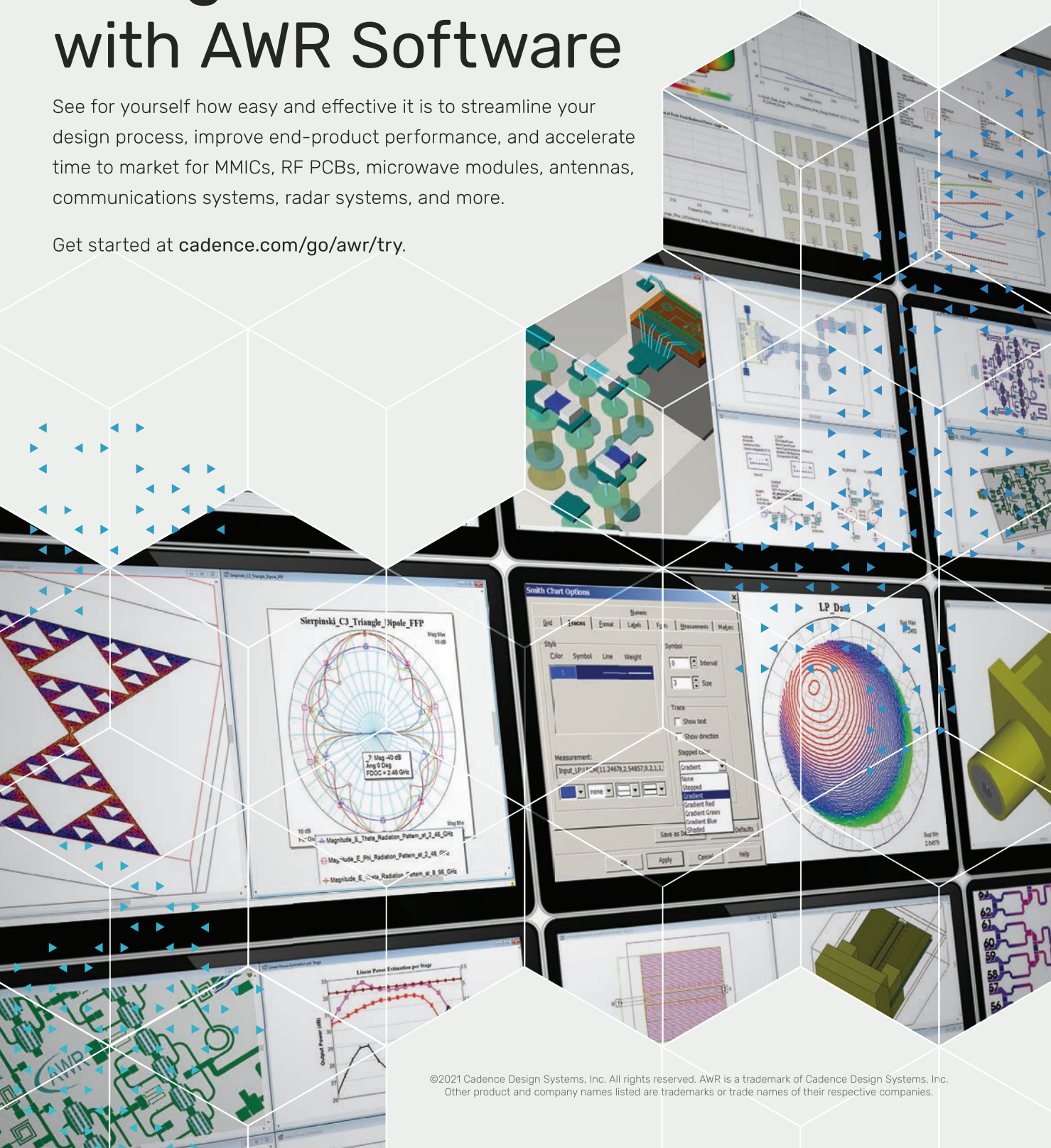
[View phase noise specs](#)

cadence®

Design Smarter with AWR Software

See for yourself how easy and effective it is to streamline your design process, improve end-product performance, and accelerate time to market for MMICs, RF PCBs, microwave modules, antennas, communications systems, radar systems, and more.

Get started at [cadence.com/go/awr/try](https://www.cadence.com/go/awr/try).



Editor

Robert H. Caverly, Villanova University,
Pennsylvania, USA, microwave.editor@ieee.org

Assistant Editor

Sharri Shaw, JWM Consulting LLC, USA,
microedt@outlook.com

Associate Editors

Nuno Borges Carvalho, University of Aveiro,
Portugal, nbcarvalho@ua.pt

Simone Bastioli, RS Microwave, New Jersey,
USA, sbastioli@rsmicro.com

Chia-Chan Chang, National Chung-Cheng
University, Taiwan, ccchang@ee.ccu.edu.tw

Ali Darwish, American University in Cairo,
Egypt, ali@darwish.org

Christian Fager, Chalmers University of Technology,
Sweden, christian.fager@chalmers.se

Jianguo Ma, Guangdong University of
Technology, China, mjg@gdut.edu.cn

Alfy Riddle, Quanergy Systems, Inc., Sunnyvale,
California, USA, alfred.riddle@quanergy.com

Luca Roselli, University of Perugia, Italy,
urlofi@tin.it; luca.roselli@unipg.it

Kamal Samanta, Sony Europe, U.K.,
kmlsamanta@googlemail.com

Almudena Suarez, University of Cantabria,
Spain, almudena.suarez@unican.es

Anding Zhu, University College Dublin,
Ireland, anding.zhu@ucd.ie

Columns and Departments

MicroBusiness

Fred Schindler, Newtonville, Massachusetts,
USA, m.schindler@ieee.org

Health Matters

James C. Lin, University of Illinois-Chicago,
Chicago, Illinois, USA, lin@uic.edu

Microwave Surfing

Rajeev Bansal, University of Connecticut,
Storrs, Connecticut, USA, rajeev@engr
.uconn.edu

Book Reviews

James Chu, Kennesaw State University, Marietta,
Georgia, USA, jameschu@bellsouth.net

Education Corner

Wenquan Che, Nanjing University of Science
and Technology, China, yeeren_che@163.com

Women in Microwaves

Sherry Hess, Cadence Design Systems, Inc.,
sherry.hess.us@ieee.org

Membership News

Bela Szendrenyi, Advantest, San Jose, California,
USA, bela.szendrenyi@advantest.com

New Products

Ken Mays, The Boeing Company, Washington,
USA, microwave.newproducts@ieee.org

In Memoriam Contributions

Jerry Hausner, USA, j.hausner@ieee.org

Ombuds Officer

Edward C. Niehenke, Niehenke Consulting,
USA, e.niehenke@ieee.org

IEEE Periodicals Magazines Department

Mark Gallaher, Managing Editor

Geraldine Krolin-Taylor, Senior Managing Editor

Janet Dudar, Senior Art Director

Gail A. Schnitzer, Associate Art Director

Theresa L. Smith, Production Coordinator

Felicia Spagnoli, Advertising Production Manager

Peter M. Tuohy, Production Director

Kevin Lisankie, Editorial Services Director

Dawn Melley, Senior Director, Publishing Operations

Advertising Sales

Mark David, Director, Business Development—
Media & Advertising

+1 732 465 6473, fax +1 732 981 1855

Digital Object Identifier 10.1109/MMM.2021.3069533



IEEE prohibits discrimination, harassment, and
bullying. For more information, visit <http://www.ieee.org/web/aboutus/whatis/policies/p9-26.html>.



Volume 22 • Number 7 • July 2021 • ISSN 1527-3342

focus features

24 The Complex World of Oscillator Noise

Modern Approaches to Oscillator (Phase and Amplitude) Noise Analysis

Fabio L. Traversa, Michele Bonnin, and Fabrizio Bonani

33 A Brief Walk Through Noise

From Basic Concepts to Advanced Measurement Techniques

Luciano Bogleione

47 Nonlinear Noise Modeling

Using Nonlinear Circuit Simulators to Simulate Noise in the Nonlinear Domain

Matthias Rudolph and Anisha M. Apte



on the cover:

@SHUTTERSTOCK.COM/DESIGNAB

IEEE Microwave Theory and Techniques Society

The IEEE Microwave Theory and Techniques Society (MTT-S) is an organization, within the framework of the IEEE, of members with principal professional interests in the field of microwave theory and techniques. All Members of the IEEE are eligible for membership in the Society. Information about joining the IEEE or the Society is available on the web, <http://www.ieee.org/membership>.

MTT-S AdCom

The Society is managed by an Administrative Committee (AdCom) consisting of 21 elected members of the Society plus additional ex-officio members as provided in the MTT-S Constitution and Bylaws, which is available on the web, <http://www.mtt.org>.

Officers

President: Gregory Lyons
 President-Elect: Rashaunda Henderson
 Secretary: Joseph Bardin
 Treasurer: Maurizio Bozzi

Elected Members

Scott Barker	Sherry Hess
Maurizio Bozzi	Sridhar Kanamaluru
Nuno Borges Carvalho	Dietmar Kissinger
Robert H. Caverly	Gregory Lyons
Goutam Chattopadhyay	Raafat Mansour
Wenquan Che	Daniel Pasquet
Terry Cisco	Ajay Poddar
Kamran Ghorbani	Jose Rayas-Sanchez
Xun Gong	Peter Siegel
Ramesh Gupta	Anding Zhu
Rashaunda Henderson	

Ex-Officio Members

Immediate Past Presidents:

Alaa Abunjaileh* (2020)
Dominique Schreurs* (2018–2019)
Dylan Williams* (2017)

Honorary Life Members*
 (max. three votes):

Józef Modelski
John T. Barr IV
Tatsuo Itoh
Richard Sparks
Peter Staecker

MTT-S Publications

IEEE Trans. Microwave Theory & Techniques Editor:	Jianguo Ma*
IEEE Microwave & Wireless Components Letters Editor:	Thomas Zwick*
IEEE Microwave Magazine Editor:	Robert H. Caverly
IEEE Trans. Terahertz Science & Technology Editor:	Imran Mehdi*
IEEE Journal of Electromagnetics, RF, and Microwaves in Medicine and Biology Editor:	Yongxin Guo
IEEE Journal on Multiscale and Multiphysics Computational Techniques Editor:	Costas Sarris
IEEE Journal of Microwaves Editor:	Peter Siegel

*Indicates voting AdCom ex-officio member

IEEE Microwave Magazine (ISSN 1527-3342) (IEMMFF) is published 12 times a year by the Institute of Electrical and Electronics Engineers, Inc. Headquarters: 3 Park Avenue, 17th Floor, New York, NY 10016-5997 USA. Responsibility for the contents rests upon the authors and not upon the IEEE, the Society, or its members. IEEE Service Center (for orders, subscriptions, address changes): 445 Hoes Lane, Piscataway, NJ 08854. Telephone: +1 732 981 0060, +1 800 678 4333. Individual copies: IEEE members US\$20.00 (first copy only), nonmembers US\$37.00 per copy. Subscription rates: Subscriptions for Society members are included with membership dues. Nonmember subscription rates available upon request. Copyright and reprint permissions: Abstracting is permitted with credit to the source. Libraries are permitted to photocopy beyond the limits of U.S. Copyright law for the private use of patrons those articles that carry a code at the bottom of the first page, provided the per-copy fee is paid through the Copyright Clearance Center, 222 Rosewood Drive, Danvers, MA 01923 USA. For other copying, reprint, or republication permission, write Copyrights and Permissions Department, IEEE Service Center, 445 Hoes Lane, Piscataway, NJ 08854 USA. Copyright © 2021 by the Institute of Electrical and Electronics Engineers, Inc. All rights reserved. Periodicals postage paid at New York, N.Y., and at additional mailing offices. Ride along enclosed. Postmaster: Send address changes to IEEE Microwave Magazine, IEEE Operations Center, 445 Hoes Lane, Piscataway, NJ 08854 USA. Canadian GST #125634188
 PRINTED IN THE USA

Digital Object Identifier 10.1109/MMM.2021.3069534

columns & departments

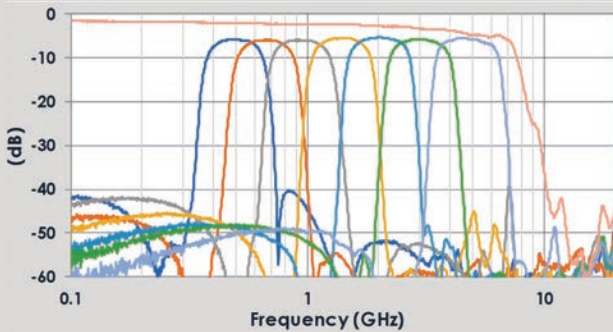
- 6 From the Editor's Desk**
 - Robert H. Caverly*Welcome to the July Issue!*
- 10 President's Column**
 - Gregory Lyons*MTT-S Virtual Successes*
- 14 MicroBusiness**
 - Fred Schindler*Weddings, Funerals, and Lives on Hold*
- 15 Microwave Surfing**
 - Rajeev Bansal*The Annual Quiz*
- 17 Microwave Bytes**
 - Steve C. Cripps*Iconic Circles*
- 23 From the Guest Editors' Desk**
 - Fabrizio Bonani and Alfred E. Riddle*Low-Noise Techniques*
- 66 Application Notes**
 - Benedikt Schweizer, Alexander Grathwohl, Gilberto Rossi, Philipp Hinz, Christina Knill, Simon Stephany, Herman Jalli Ng, and Christian Waldschmidt*The Fairy Tale of Simple All-Digital Radars: How to Deal With 100 Gbit/s of a Digital Millimeter-Wave MIMO Radar on an FPGA*
- 78 Women in Microwaves**
 - Malgorzata Celuch*Women in Microwaves at MIKON: (Not) for the First Time*
- 84 New Products**
 - Ken Mays, Editor
- 90 Enigmas, etc.**
 - Takashi Ohira*DC Power Consumption*
- 93 Conference Calendar**



RF MMICs Simplifying Receiver Design

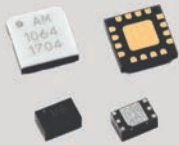
Chip-scale Filters, Tunable Filters and Filter Banks

Miniature analog and digitally tunable filters and filter banks up to 26 GHz in QFN packages.



AM3025A - 7 Band Filter Bank in a 9mm QFN

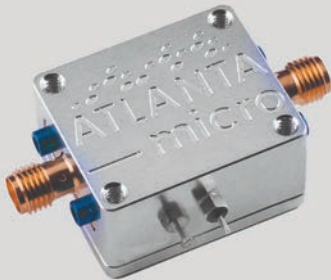
Now Also Available in Connectorized Modules



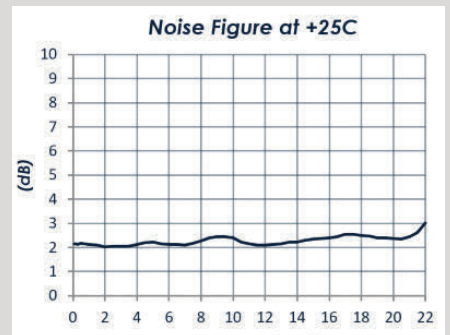
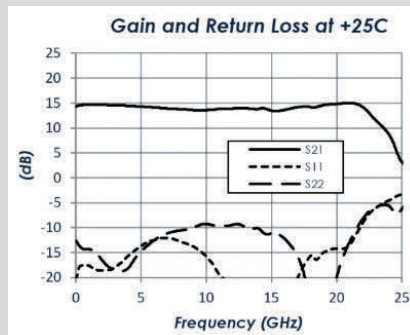
Low Noise Amplifiers and Bypassable Gain Blocks

Wide bandwidths with uniform gain, high IP3, and low noise figure. Package options include 3 mm QFN and 1.3 x 2.0 mm DFN. Also bypassable and bidirectional gain blocks in 4 mm QFN packages.

AM1102 – New Low Noise Gain Block



Now Also Available in Connectorized Modules



Miniature Tuner Modules and Chipsets

Completely integrated high performance superheterodyne tuner solutions for both receive and transmit applications up to 26 GHz with instantaneous bandwidths up to 1 GHz.



AM9017
0.1 to 18 GHz
 35.1 x 68.2 x 6.7 mm

Visit us at IMS in Atlanta, Booth # 1931

www.atlantamicro.com
 sales@atlantamicro.com
 470-253-7640



From the Editor's Desk

Welcome to the July Issue!

■ Robert H. Caverly

Understanding the linear properties of the various circuits and systems used in microwave engineering, as well as in general electrical engineering, is difficult enough without further increasing the level of difficulty by having to consider the fundamental impacts of noise. When noise is mentioned in the classroom, for example, concepts such as signal-to-noise-ratio are most often discussed in statistical terms without exploring the fundamental origins of the various sources of noise and how noise differs from other undesired signals such as distortion brought on by nonlinear processes. No matter the difficulty of the topic, noise is a major requirement for circuits and systems that must be considered; noise modeling represents our best



©SHUTTERSTOCK.COM/YAALAN

attempts to describe real-world behavior and improve performance based on this behavior.

Several times a year, we provide you with various focus issues that delve into a specific topic. This month's issue was organized by the IEEE Microwave Theory and Techniques Society's (MTT-S) MTT-11 Microwave Low-Noise Techniques Technical Committee and provides an in-depth look at the complex topic of noise and noise analysis and modeling, presented by experts in the field. I would like to thank the organizers of this focus issue, Fabrizio Bonani and Alfred Riddle, for

collecting three excellent articles describing noise phenomena and how to model system performance in the presence of noise. They have provided an in-depth "From the Guest Editors' Desk" column that I urge you to read first to learn a little bit about MTT-11 and the three focus issue features on noise.

In addition to these three technical features, we have two other technically oriented articles.

This month's "Application Notes" column, provided by Schweizer et al., offers a look at all-digital radars and how to use field programmable gate arrays (FPGAs) for their implementation. Using reconfigurable processors such as FPGAs allows changes in the digital signal processing algorithms as radar protocols change, while also providing the high data rates needed in these applications. This month's "Microwave Bytes" column looks at analog/graphical solutions to microwave problems, where Steve Cripps talks about the microwave and RF engineer's friend, the Smith chart, and

Robert H. Caverly (rcaverly@villanova.edu) is with Villanova University, Villanova, Pennsylvania, 19085, USA.

Digital Object Identifier 10.1109/MMM.2021.3072438
Date of current version: 1 June 2021



Radar Testing Over-the-Air? We just call it DARTS.

Over-the-air simulation of radar echoes has never been as easy, quick, and thorough as with the new dSPACE Automotive Radar Test Systems (DARTS). They reliably meet even the strictest requirements of safety-critical applications. DARTS get the job done in chip testing, R&D, end-of-line testing, type approval, you name it. [dspace.com](https://www.dspace.com)

the various ways that the chart can be used to gain insight into a circuit's operation.

Other articles in this issue include columns that appear monthly as well as those that appear less frequently. MTT-S President Gregory Lyons talks about how the MTT-S has handled the pandemic's travel and gathering restrictions with a wide variety of virtual activities presented over the last year. Although, at the time of this writing in early April, we are just over a year into these pandemic restrictions and have improved the planning of virtual activities, during 2020 MTT-S volunteers and IEEE staff were operating at the start of the pandemic in an uncertain and fluid environment and making decisions about how to best

proceed, often on a daily basis. Lyons highlights these achievements and provides well-deserved thanks to all involved in the planning of these events. Continuing with the theme of pandemic restrictions, our "Micro-Business" column focuses on the impact of these restrictions on family and cultural traditions. The "Microwave Surfing" column provides the annual quiz to test our knowledge of microwave engineering's history. Keeping in line with mental challenges, we have our next "Enigmas, etc." column, along with the solution to last month's problem. This month's "Women in Microwaves" column takes a look at microwaves in Poland, with a report on the annual MIKON conference, held last October (and in person),

and the part played by Women in Microwaves in the success of the conference. Finally, we have our "New Products" column, with six interesting new products that could be of interest to you, as well as our "Conference Calendar." You will also notice a large number of conference calls for papers in this issue. While many conferences are still virtual only, with the current vaccination rollouts increasing globally, there is hope that some conferences in late 2021 and early 2022 may be in person or at least hybrid. Now, there is a word—*hope*—that hasn't been used much lately but I'm glad to be able to use it now.

We invite you to explore this issue of *IEEE Microwave Magazine*.



TAP. CONNECT. NETWORK. SHARE.



Connect to IEEE—no matter where you are—with the IEEE App.



Stay up-to-date with the latest news



Schedule, manage, or join meetups virtually



Get geo and interest-based recommendations



Read and download your IEEE magazines



Create a personalized experience



Locate IEEE members by location, interests, and affiliations

Download Today!



Share Your Preprint Research with the World!

TechRxiv is a free preprint server for unpublished research in electrical engineering, computer science, and related technology. Powered by IEEE, TechRxiv provides researchers across a broad range of fields the opportunity to share early results of their work ahead of formal peer review and publication.

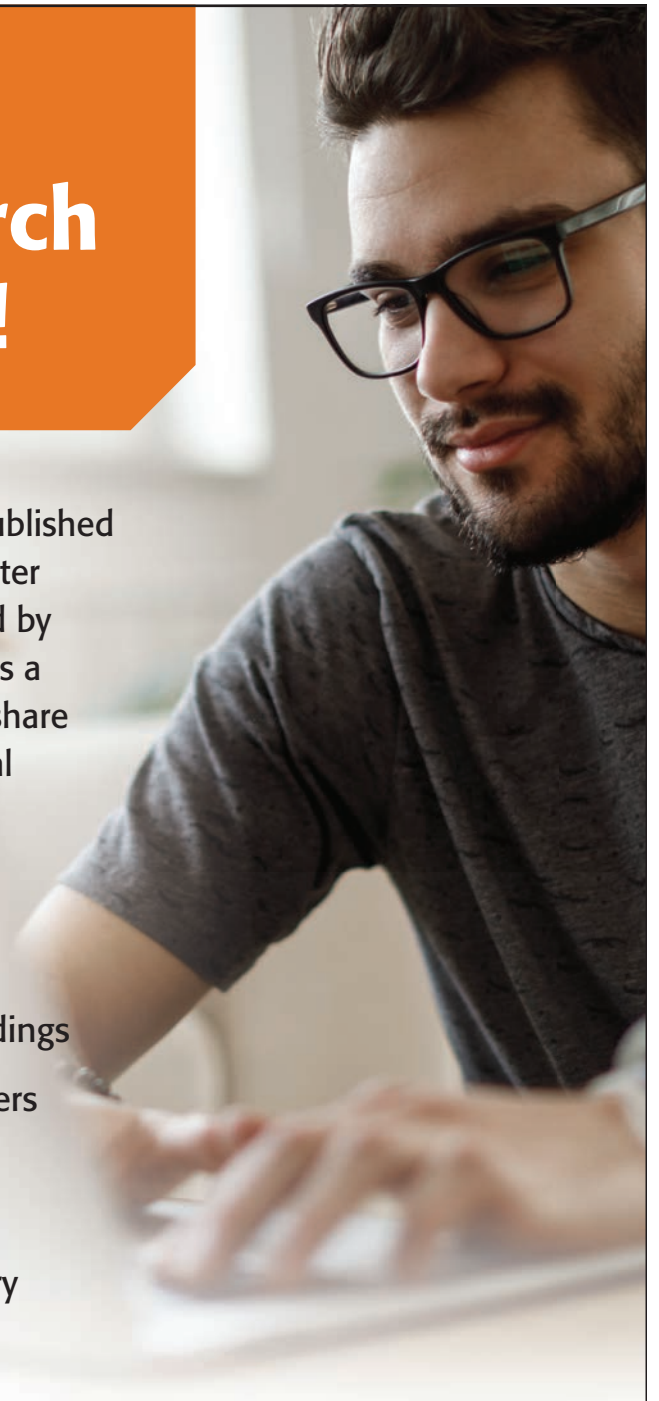
BENEFITS:

- Rapidly disseminate your research findings
- Gather feedback from fellow researchers
- Find potential collaborators in the scientific community
- Establish the precedence of a discovery
- Document research results in advance of publication

Upload your unpublished research today!

 Follow @TechRxiv_org
Learn more techrxiv.org

TechRxiv[™]
Powered by IEEE





President's Column

MTT-S Virtual Successes

■ Gregory Lyons

It is with great sadness that I must start this column by reporting to our IEEE Microwave Theory and Techniques Society (MTT-S) readership the passing of two Society stalwarts during the month of March 2021: Prof. Tatsuo Itoh (UCLA) and Prof. Tapan Sarkar (Syracuse). Their accomplishments were many, and their impact was great on the IEEE, the MTT-S, and the IEEE Antenna and Propagation Society (AP-S). They were leaders, educators, colleagues, mentors, and friends to many of us. Both provided us with an inspiration that will live long within the MTT-S.

Prof. Itoh was one of our cherished leaders and truly one of the pillars of our Society. He was a Life Fellow of IEEE, served as 1990 MTT-S president, and received the 2001 Nikola Tesla Award, IEEE Third Millennium Medal, and 2018 IEEE Electromagnetics Award. The MTT-S named our Best IEEE Microwave and Wireless



©SHUTTERSTOCK.COM/KRERKSTOCK

Components Letters Paper award after him. He was active as a voting Honorary Life Member of our MTT-S Administrative Committee (AdCom) until his passing. A biographical journal article captured his life from childhood through the evolution of his career [1]. Prof. Itoh wrote or co-wrote 48 books and chapters and nearly 1,500 papers, cited more than 63,000 times. The UCLA Samueli School of Engineering has created an online "In Memoriam" article for him [2], and an MTT-S "In Memoriam" column devoted to his life and work appeared in the June issue of *IEEE Microwave Magazine* [3].

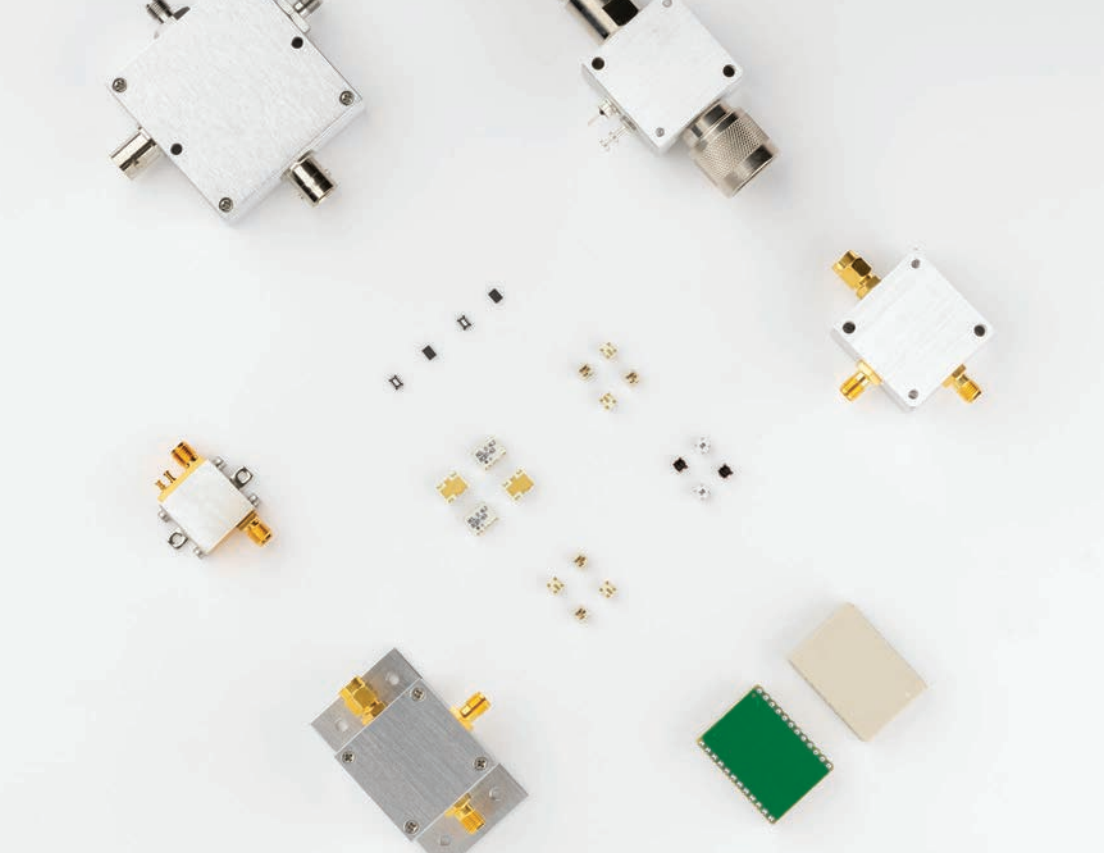
Prof. Sarkar was a key contributor to our field of interest and to the IEEE; he was the 2014 president of AP-S and helped establish a partner Society agreement among the MTT-S, AP-S, and IEEE Electromagnetic Compatibility Society. The MTT-S has a 40% membership overlap with the AP-S, and the two Societies continue to work together very effectively, especially on publications and conferences. Prof. Sarkar

also served as a vice president of the Applied Computational Electromagnetics Society and received the 2020 IEEE Electromagnetics Award. He authored or coauthored more than 380 papers, 32 book chapters, and 16 books. Prof. Sarkar's colleagues have



Gregory Lyons
(g.lyons@ieee.org),
2021 MTT-S
president, is with
Lincoln Laboratory,
Massachusetts
Institute of
Technology, Lexington,
Massachusetts, USA.

Digital Object Identifier 10.1109/MMM.2021.3071259
Date of current version: 1 June 2021



100 KHZ TO 28 GHZ

Bias Tees

Wideband, High-Current

- DC current up to 5A
- RF power up to 40W
- Mux-tees (bias tee + diplexer)
- Insertion loss as low as 0.15 dB
- New MMIC design covers 1.5 to 28 GHz



updated his Wikipedia article summarizing his career [4], and an MTT-S “In Memoriam” column will appear in an upcoming issue of *IEEE Microwave Magazine*.

2020/2021 Virtual Successes

The COVID-19 pandemic has gone on for over one year now. I can say with a great sense of pride that our MTT-S volunteers have risen to the challenge and done a fantastic job converting absolutely everything we had previously done in person into virtual events. We all have learned a lot along the way, and we have watched online virtual tools rapidly improve over this time. I wanted to share some of the best virtual successes as well as a few of the aspects of virtual events that we now understand much better.

IMS2020

The biggest initial virtual success for the MTT-S was accomplished by the Steering Committee team for the 2020 IEEE International Microwave Symposium (IMS2020), originally scheduled in Los Angeles for June 2020. IMS2020 General Chair Tim Lee; IMS Executive Committee “COVID Czar” JK McKinney; and IEEE Meetings, Conferences,

and Events (MCE) Administrator Elsie Vega deserve much of the credit for this success, turning IMS2020 into a 100% virtual event in August 2020, including a virtual exhibition. There were 8,611 total registered attendees for IMS2020. One significant difference from previous in-person IMS gatherings was a greater than 10 times increase in attendance from India and significant increases in attendance from a variety of other countries around the world. This demonstrates that virtual attendance reaches attendees who normally would not (or could not) travel to the IMS. This extended worldwide reach demonstrates that virtual content is an important consideration in planning for IMS beyond the pandemic.

MTT-S Webinars and Resource Center

The MTT-S began producing technical webinars in 2016 [5]. The webinar topics and content continue to be the responsibility of the MTT-S Education Committee. The MTT-S Marketing and Communications Committee (MarCom) hosts our webinars in collaboration with the ON24 webinar platform and our marketing partner, Naylor Association Solutions. In June 2020, the MTT-S launched our IEEE Resource Center online portal [6]. All of our past MTT-S webinars, as well as other educational digital content, are now hosted in the MTT-S Resource Center following live broadcast of the webinars.

Fortunately, all of our webinar and Resource Center infrastructure was in place prior to the COVID pandemic. This allowed the Education Committee to focus on increasing the number of webinars over a broad set of technical topics. The number of MTT-S webinars was increased to 18 in 2020. The webinar schedule for 2021 can be found at www.mtt.org [7] Previously broadcast webinars are available for free to MTT-S members in the MTT-S Resource Center hosted by www.ieee.org [8].

YP Live Talks

The MTT-S decided to go beyond standard technical webinars once the

pandemic began. We did so in a big way, providing a pair of Young Professional (YP) Live Talks with Astronaut Robert Thirsk (Figure 1) in May 2020 and with NASA JPL researcher Goutam Chattopadhyay (Figure 2) in June 2020, both hosted by MTT-S YP Tushar Sharma. These YP Live Talks saw wide viewership. The May 2020 talk had 350 live attendees and now stands at 11,000 total views. The June 2020 talk had 600 live attendees and now stands at 7,600 total views. The YP Live Talks combined technical content on an interesting subject (space and research) with discussions about personal experience, along with personal and career mentoring. For example, Robert Thirsk talked about living in isolation as an astronaut, a very appropriate mentoring topic for the beginning of a pandemic lockdown. The MTT-S will continue to host several webinars each year exploring topics that hold keen interest for our membership and that go beyond the boundaries of standard technical webinars.

Virtual Chapter Chair Meetings

Chapter Chair meetings (CCMs) went virtual starting in 2020. MTT-S Member and Geographic Activities (MGA) Committee Chair Nuno Borges Carvalho created a virtual format with an invited virtual talk and 2-min Chapter activities videos from various Chapters. The format has been a huge success with more attendees than typical for an in-person CCM (more than 200 live participants). In fact, the virtual CCMs have been so successful that MGA had to recommit to at least one in-person CCM every year versus all virtual CCMs! This has clearly been successful.

Virtual DML Talks

Distinguished Microwave Lecture (DML) talks also had to be converted to virtual talks. This conversion was quickly completed under the leadership of MTT-S Technical Coordination and Future Directions Committee Chair Dietmar Kissinger. A big advantage of the early conversion of each DML talk to virtual is that the DML talks are now



Figure 1. YP Live Talk: Astronaut Robert Thirsk.

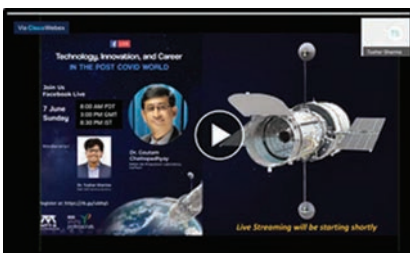


Figure 2. YP Live Talk: Goutam Chattopadhyay (NASA JPL).

TABLE 1. MTT-S 2020 virtual conferences.

Conference	Date	Platform	Attendees	Cost	Experience
WMCS (F)	May 2020	WebEx	200	IEEE provided	Good, once got used to
INMMIC (T)	July 2020	Zoom		University provided	Good
EPEPS (FC)	August 2020	Engagez	230	IEEE provided	Very Positive
RFIC (F)	August 2020	GTR		IMS2020 provided	Average
ARFTG (F)	August 2020	GTR		IMS2020 provided	OK for technical session
DIPED (T)	September 2020	Zoom		US\$125	Positive
WPTC (F)	November 2020	InfoVaya	400	US\$5,000	Considerably satisfactory
IRMMW-THz (T)	November 2020	Zoom/Remo	1000	US\$5,000	Good
IMBioC (F)	December 2020	Engagez	266	IEEE provided	Excellent

F: financially sponsored; FC: financially cosponsored; T: technically cosponsored; WMCS: IEEE Texas Symposium on Wireless and Microwave Circuits and Systems; INMMIC: International Workshop on Integrated Nonlinear Microwave and Millimetre-wave Circuits; EPEPS: IEEE Conference on Electrical Performance of Electronic Packaging and Systems; RFIC: Radio Frequency Integrated Circuits Symposium; ARFTG: Automatic Radio Frequency Techniques Group Microwave Measurement Conference; DIPED: IEEE Seminar/Workshop on Direct and Inverse Problems of Electromagnetic and Acoustic Wave Theory; WPTC: IEEE Wireless Power Transfer Conference; IRMMW-THz: International Conference on Infrared, Millimeter, and Terahertz Waves; IMBioC: IEEE International Microwave Biomedical Conference.

ready for hosting in the MTT-S Resource Center when appropriate.

2020/2021 Virtual Conferences

Starting in March 2020, all MTT-S conferences were converted to virtual format or hybrid format or postponed. MTT-S Meetings and Symposia Committee Chair Goutam Chattopadhyay has provided resources and information to MTT-S conference organizers to aid with this process, as has IEEE MCE with online resources: <https://ieeemce.org/covid/>.

The MTT-S converted 15 conferences to virtual format and nine conferences to hybrid format in 2020. So far this year (as of the end of March 2021), the MTT-S has converted seven conferences to virtual format and five conferences to hybrid format. Conference organizers and the MTT-S have learned a considerable amount about hosting virtual events. The results of a survey of 2020 MTT-S conference organizers are shown in Table 1. Virtual conference hosting tools have improved rapidly during the COVID pandemic. Many virtual conference organizers throughout IEEE report that smaller, regional conferences (no time zone issues) with exhibitions of up to 30 vendors have been very successful as virtual events. The virtual

conference format may continue beyond the end of the pandemic despite certain drawbacks of the virtual conference experience.

AdCom and TC Meetings

The MTT-S had to convert our AdCom and Technical Committee (TC) meetings to virtual formats. The biggest drawbacks are the limited interactive ability of virtual meeting tools, the need to limit the length of meetings and limit discussions, and the time zone issue with members around the world. Anonymous voting tools provided by IEEE worked well for our AdCom elections, and it was a new experience using the tools. Kudos to Elsie Vega for helping to make this happen smoothly.

WiM Meet Ups

Finally, new in 2021 are Women in Microwaves (WiM) networking Meet Ups. WiM is a subcommittee of the MTT-S MGA Committee. WiM Chair Sherry Hess took the lead this year by committing to holding a regular WiM event throughout the year. The first WiM Meet Up was held in March 2021 and was a success!

The MTT-S is a very active IEEE Society. I encourage you to visit our website www.mtt.org for more infor-

mation. If you would like to be involved as a volunteer, fill out a contact form at www.mtt.org/connectme, and we will make sure that you get connected.

References

- [1] P. H. Siegel, "Terahertz Pioneer: Tatsuo Itoh – 'Transmission lines and antennas: Left and right,'" *IEEE Trans. THz Sci. Technol.*, vol. 4, no. 3, pp. 298–306, May 2014. doi: 10.1109/TTHZ.2014.2312852.
- [2] "In memoriam: Professor Tatsuo Itoh, pioneer of microwave and millimeter-wave electronics," UCLA Samueli School of Engineering, Los Angeles, Mar. 2021. [Online]. Available: <https://samueli.ucla.edu/in-memoriam-professor-tatsuo-itoth-pioneer-of-microwave-and-millimeter-wave-electronics/>
- [3] "Tatsuo Itoh [In Memoriam]," *IEEE Microw. Mag.*, vol. 22, no. 6, pp. 82–84, June 2021.
- [4] "Tapan Sarkar." Wikipedia. https://en.wikipedia.org/wiki/Tapan_Sarkar
- [5] R. K. Gupta and M. Hamilton, "MTT-S Education Committee Launches successful 2016 webinar series [Education News]," *IEEE Microw. Mag.*, vol. 17, no. 11, pp. 84–91, Nov. 2016. doi: 10.1109/MMM.2016.2601539.
- [6] A. Abunjaileh, "The MTT-S Resource Center—Our new electronic portal [President's Column]," *IEEE Microw. Mag.*, vol. 21, no. 9, pp. 10–14, Sept. 2020.
- [7] "MTT-S webinars." IEEE Microwave Theory and Techniques Society. <https://mtt.org/mtt-s-webinars-schedule/>
- [8] Microwave Theory and Techniques Society (MTT-S) Resource Center. <https://resourcecenter.mtt.ieee.org>





MicroBusiness

Weddings, Funerals, and Lives on Hold

■ Fred Schindler

If you're a faithful reader of this magazine, or a frequent visitor to the www.mtt.org website, over the past couple of years you have seen memorials for many distinguished contributors to our technology and dedicated volunteers of our Society. As I write this, just in the past two weeks, I've learned of the passing of three more. While it's sad to see the deaths of so many of our leaders, I have fond memories of them, respect for their contributions, and thanks for their mentorship and support.

This past year under the COVID-19 pandemic has been difficult in many ways. The estimated deaths attributed to COVID-19 are currently over 2.7 million, which is certainly an undercount. The way the pandemic has stressed the medical infrastructure around the world has undoubtedly contributed to more disease, more suffering, and more death. Virtually every community has suffered a difficult year. In that, the IEEE Microwave Theory and Techniques Society (MTT-S) has had

plenty of company, even if it's not all attributable to COVID-19.

While there have been many deaths this past year, there have not been many funerals, or not funerals of the type we traditionally hold. Funerals have become private events, usually limited to immediate family. When my mother passed away nearly three years ago, we had a funeral and memorial services, including extended family, neighbors, friends, and colleagues. My dad passed away in January, during one of the pandemic's infectious peaks. Only a few family members attended the funeral, with some able to attend only via Zoom because of travel restrictions.

My dad lived to be nearly 99 years old, a long and full life. COVID-19 was not a factor in his death, and he was barely even aware that there was a pandemic underway. He was old, and his time had come. He and his generation are confronting normal human life expectancy.

My wife and I married nearly 40 years ago. For the next decade, we attended many weddings, as our generation

had come to the age and maturity when people tend to get married. After that, our invitations to weddings tailed off, since most of our siblings, cousins, and friends had by then been married.

During that time and for many years that followed, we also had very few funerals to attend. Our generation was still young enough that death was rare, and even our parents' generation was well below normal life expectancy.

With time, of course, that has changed. My children's generation is now at the age when they are getting married, so once again we have been getting invitations to weddings, only now they are for nieces and nephews. At the same time, our parents' generation has reached its life expectancy, so there are more funerals. Many of our colleagues,

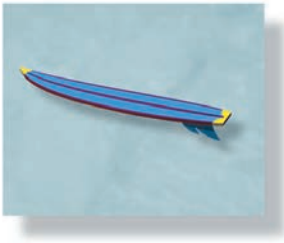
(continued on page 22)



©SHUTTERSTOCK.COM/NATNATNAT

Fred Schindler (m.schindler@ieee.org)
consults on management issues in the Boston,
Massachusetts, area.

Digital Object Identifier 10.1109/MMM.2021.3069603
Date of current version: 1 June 2021



Microwave Surfing

The Annual Quiz

■ Rajeev Bansal

It has been a year since I last visited my office and had a chance to browse through the printed copies of my IEEE magazines. Therefore, it was a treat to receive the inaugural, full-color, 512-page issue (January 2021) of *IEEE Journal of Microwaves* in my mailbox at home. As a new open-access publication of IEEE, it “both documents and celebrates the renaissance that we are now living through in microwave technology and applications” [1]. You can get your own free copy of the inaugural issue (while supplies last) by filling out a short survey at <https://mtt.org/publications/journal-of-microwaves/inaugural-issue/>. To introduce the wide range of topics covered in the first issue, I decided to put together this short quiz, based on some of the articles. It is now time to grab a pen and test your own knowledge of microwaves! No Googling allowed. The answers appear on the next page, so no peeking allowed either.



1. The term *microwaves* first appeared in American literature in the title of an article, “The Detection of Microwaves,” by the Italian engineer Nello Carrara, published in *Proceedings of the Institute of Radio Engineers* in the year _____.
 - a) 1922
 - b) 1932
 - c) 1942
 - d) none of the above.

2. The term *microwaves* as used by [1] covers the wavelength range _____.
 - a) from 3 cm to 3 mm
 - b) from 3 m to 3 μm
 - c) from 30 m to 30 μm
 - d) none of the above.
3. The most pervasive microwave field in the universe, the cosmic microwave background (CMB), peaks at a frequency of _____.
 - a) 1.6 GHz
 - b) 16 GHz
 - c) 160 GHz
 - d) none of the above.
4. Microwave pioneer _____ shared the 2006 Nobel Prize in Physics for the first complete measurement of the CMB blackbody spectrum and the first confirmed findings of CMB anisotropy.
 - a) Arno A. Penzias
 - b) John C. Mather
 - c) Robert W. Wilson
 - d) none of the above.
5. Microwave spectroscopy is the study of the interaction of a specimen with electromagnetic radiation as a function of the _____ of the radiation.
 - a) intensity
 - b) frequency
 - c) modulation
 - d) none of the above.

Rajeev Bansal (rajeev.bansal@uconn.edu) is with the University of Connecticut, Storrs, Connecticut, USA.

Digital Object Identifier 10.1109/MMM.2021.3069604
Date of current version: 1 June 2021

NOTE: An earlier version of this column appeared originally in the June 2021 issue of *IEEE Antennas and Propagation Magazine*.



6. _____, who liked to call himself the “Father of Radio,” invented the three-element vacuum tube.
- Lee de Forest
 - Reginald Aubrey Fessenden
 - Edwin Howard Armstrong
 - none of the above.
7. The specially built guidance computers for the Apollo missions, which culminated in the first human landing on the moon in 1969, used approximately 5,000 computer chips. The large Apollo order helped bring the cost of a computer chip down from US\$1,000 in 1960 to _____ in 1969.

- US\$15
- US\$1.58
- US\$7.28
- none of the above.

8. _____, best known for his pioneering work on very large-scale integration design techniques, was also responsible for the demonstration of the first microwave transistor (a gallium arsenide metal–semiconductor field-effect transistor).
- Gordon Moore
 - John Bardeen
 - Carver Mead
 - none of the above.
9. The Ginzburg-Landau theory provides a phenomenological understanding of how electromagnetic fields interact with superconductors. Landau received the Nobel Prize in Physics in 1962. Ginzburg _____.



- never won it
 - also won it in 1962
 - won it in 2003
 - none of the above.
10. The original purpose of the _____ integrals was to provide an accurate mathematical description of radio wave propagation over a lossy ground plane.
- Laplace
 - Hankel
 - Sommerfeld
 - none of the above.

Reference

[1] *IEEE J. Microw.*, vol. 1, no. 1, Jan. 2021.



Answers to the Annual Quiz

- b) 1932.
Source: P. H. Siegel, “Introduction to the *IEEE Journal of Microwaves*,” *IEEE J. Microw.*, vol. 1, no. 1, pp. 5–13, winter 2021. doi: 10.1109/JMW.2020.3035892.
- c) from 30 m to 30 μm .
Source: Inside the front cover of [1].
- c) 160 GHz. (It corresponds to radiation from a blackbody at a temperature of around 3 K.)
Source: P. H. Siegel, “Microwaves are everywhere: ‘CMB: Hiding in plain sight,’” *IEEE J. Microw.*, vol. 1, no. 1, pp. 14–24, winter 2021. doi: 10.1109/JMW.2020.3025246.
- b) John C. Mather. (Penzias and Wilson shared the 1978 Nobel Prize in Physics for their discovery of cosmic microwave background.)
Source: P. H. Siegel, “Microwave pioneers: John C. Mather ‘A singular purpose,’” *IEEE J. Microw.*, vol. 1, no. 1, pp. 25–31, winter 2021. doi: 10.1109/JMW.2020.3025239.
- b) frequency.
Source: D. R. Slocombe and A. Porch, “Microwaves in chemistry,” *IEEE J. Microw.*, vol. 1, no. 1, pp. 32–42, winter 2021. doi: 10.1109/JMW.2020.3029337.
- a) Lee de Forest.
Source: T. Lewis, “On the shoulders of giants: Reflections on the creators and uses of radio,” *IEEE J. Microw.*, vol. 1, no. 1, pp. 79–85, winter 2021. doi: 10.1109/JMW.2020.3034820.
- b) US\$1.58.
Source: T. Lewis, “On the shoulders of giants: Reflections on the creators and uses of radio,” *IEEE J. Microw.*, vol. 1, no. 1, pp. 79–85, winter 2021. doi: 10.1109/JMW.2020.3034820.
- c) Carver Mead.
Source: “Carver Mead: ‘It’s all about thinking,’ a personal account leading up to the first microwave transistor,” *IEEE J. Microw.*, vol. 1, no. 1, pp. 269–274, winter 2021. doi: 10.1109/JMW.2020.3028277.
- c) won it in 2003.
Source: S. M. Anlage, “Microwave superconductivity,” *IEEE J. Microw.*, vol. 1, no. 1, pp. 389–402, winter 2021. doi: 10.1109/JMW.2020.3033156.
- c) Sommerfeld.
Source: J. R. Mosig and K. A. Michalski, “Sommerfeld integrals and their relation to the development of planar microwave devices,” *IEEE J. Microw.*, vol. 1, no. 1, pp. 470–480, winter 2021. doi: 10.1109/JMW.2020.3032399.



Microwave Bytes

Iconic Circles

■ Steve C. Cripps

One hears the word “iconic” rather a lot these days; indeed, its overuse has become something of an irritation to me, especially when I am about to use it to describe something that probably deserves it. In older times, “icon” was used to describe some kind of a symbol, in particular something that we “click” with a mouse. The *Oxford English Dictionary* confirms this: “a small symbolic picture on a VDU screen that may be selected with a cursor to exercise an option that it represents.” As for the adjective form of the word, it says “of, pertaining to, or resembling an icon.” As such, the Smith chart has surely become the iconic trademark of the microwave engineer; and, given the number of business cards I have in my drawer that feature a Smith chart icon, this extends to encompass the entire microwave subject. Definitely a true icon.

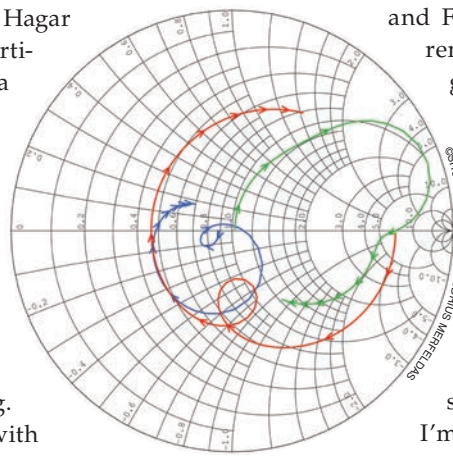
But after all these years, it seems a bit odd that in these columns, I have never said much about the Smith chart.

Steve C. Cripps (crippssc@cardiff.ac.uk)
is with the School of Engineering,
Cardiff University, Cardiff, CF10 3AT, U.K.

Digital Object Identifier 10.1109/MMM.2021.3069605
Date of current version: 1 June 2021

Ever since Phillip Hagar Smith’s seminal article [1], it has been a fruitful topic for authors, in particular those who wish to vandalize it in various ways, so finding anything new to say on the subject is a bit challenging. I certainly read with interest recent (and older) offerings in this magazine on the 3D version [2], [3] and comparisons with the art of Maurits Escher [4], not to mention the measurement of the Poincaré distance between impedances [5], should one ever need to know such a thing.

Back in the days when one could publish a short article in *IEEE Transactions on Microwave Theory and Techniques (TMTT)*, sometimes little more than a single column, there was a multitude of ideas for special Smith chart constructs that allegedly led to quick answers to specific problems. There are a few more esoteric applications; one such [6] actually makes a connection between the Smith chart



and Fermat’s last theorem. As a subject in general, however, it is, of course, another case of the computer simulation tool taking over the more laborious hours with pencil and compasses that predated such luxuries. So I’m doing my “old ways” talk already, and it’s getting a bit habitual. But I thought it might be at least entertaining to give some of my own recollections on the subject.

I well remember the very first lecture that introduced the Smith chart as “a polar plot of reflection coefficient.” In fact, this is not strictly correct. P.H. Smith was not the first person to represent a complex number in polar form; precisely who actually did has been a somewhat debated issue in the mathematical world, with both Euler and de Moivre being frequently cited in textbooks. Smith’s contribution was to take the polar reflection coefficient plane, bounded by the unity circle, but instead of plotting contours of constant

reflection coefficient amplitude, which would be concentric circles, he plotted the contours of constant resistance and constant reactance. We now know, of course, that these contours are also circles, with centers displaced from the origin, and it would be interesting to know whether Smith already knew this or whether he was the first person to derive these relationships.

These days, faced with such a problem, even my own first reaction would be to make a quick dash to Excel and plot a few dozen points to find out what the curves look like; on seeing that they looked like circles, I would then consider going back to “do the math,” which would often turn out to be surprisingly tricky. Smith, of course, did not have this luxury. Time and again throughout my life in microwaves, I have spent many hours chewing the end of a pencil (I actually usually use the kind with an eraser at the end, which, having much use, I opted for holding it in my teeth horizontally) trying to prove that some function or another traces a circle on the Smith chart, in the full knowledge already that it does. So, just for fun, let’s derive a Smith chart circle.

We take an impedance, $z = r + jx$, where r is fixed, and x is a variable.

This should be easy, right? The reflection coefficient, ρ , is given by

$$\rho = \frac{z-1}{z+1} = \frac{(r-1) + jx}{(r+1) - jx'}$$

where impedances are normalized to the characteristic impedance Z_0 .

Now, there may be folks around who look at this expression and can say, “Ah, yes, that’s a circle on the complex plane as x varies.” Indeed, I suspect there may have been more such folks hanging around microwave labs in the 1930s than there are now, but in any case, I am not one of them (on either count ☹️). One’s knee-jerk reaction is to establish the real and imaginary parts, whereby we can derive the x and y coordinates of the Smith chart trajectory, ρ_x and ρ_y ,

$$\rho_x = \frac{(r^2-1) + x^2}{(r+1)^2 + x^2}$$

$$\rho_y = \frac{2x}{(r+1)^2 + x^2}$$

and all we have to do is eliminate the varying parameter x to get the required function relating the x and y coordinates.

Not so easy?! I have to admit, I have found myself at this point many times when trying to prove some function is a circle on the Smith chart and given

up the quest, trying to satisfy myself with the Excel approach. As with many such mathematical problems, getting the solution is all a matter of setting the problem up “correctly” in the first place; if you get the first line wrong, you find yourself sinking ever more deeply into the mud.

The trick, in this case, is to stay with the expression for the impedance in terms of the corresponding reflection coefficients but now go straight into the x and y coordinates of ρ , so that

$$r + jx = \frac{(1 + \rho_x) + j\rho_y}{(1 - \rho_x) + j\rho_y}$$

Proceeding exactly as before, we get

$$r + jx = \frac{\{(1 - \rho_x^2) - \rho_y^2\} + 2j\rho_y}{(1 - \rho_x)^2 + \rho_y^2}$$

and taking real parts,

$$\rho_x^2 + \rho_y^2 - 2r\rho_x \frac{1-r}{1+r} = 0.$$

And now, we can use the venerable “completing the square” procedure (do they still teach that?!),

$$\left(\rho_x - \frac{r}{r+1}\right)^2 + \rho_y^2 = (1-r) + \frac{r^2}{1+r^2},$$

which, for sure, now look like circles, centered at

$$\frac{r}{1+r}$$

having a radius R given by

$$R^2 = (1-r) + \frac{r^2}{(1+r)^2}.$$

The contours of constant reactance, by a similar procedure, give circles centered at

$$\left(1, \frac{1}{x}\right),$$

having radius $(1/x)$.

So you can, in the future, always draw your own Smith chart using the aforementioned, as indicated in Figure 1.

Given the somewhat awkward forms of some of these results, one

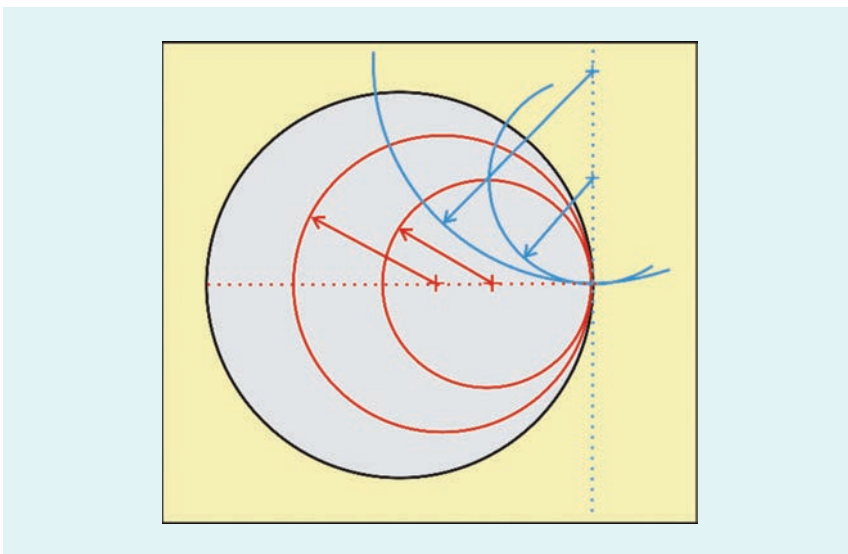


Figure 1. The location of constant resistance circles (red) and constant reactance circles (blue).

could speculate whether this was the motivation for Phillip Smith to present the results in a graphical form at a time when the only calculation aid was a hand-cranking mechanical contraption.

But, as I have said already, I have, at times, found myself going through similar mathematical gyrations to prove a result that is not usually found in a textbook. The first of these I encountered very early in my impedance-matching career and concerns the use of non-50-Ω transmission line elements; for the microwave designer, this is surely a frequent and useful technique, but its implementation seemed very laborious. The standard procedure was to renormalize your chart to the characteristic impedance of the matching section, read off the appropriate length by rotation about the pole, and then take the result and convert it back to the 50-Ω chart. Very cumbersome, and this was some years before it became possible to let the computer do the work and display the trajectory on the same 50-Ω chart throughout. The point being that, in the first instance, we don't actually know what length is needed if the element in question is just a part of a multielement network; it would be much better to do the whole process on a single 50-Ω chart.

I always suspected that the trajectory on the 50-Ω chart would still be a circle, and, as such, it should be fairly straightforward to derive formulae for the radius and center location of such circles for any selected impedance point. Surely, such a result would be a useful Smith chart construction, but I could not find it anywhere in the literature. My more senior colleagues at the time were more bemused than seriously interested (with one or two exceptions, I should say). It turned out, once again, to be a trickier derivation than I had reason to expect, and I think by the time I had come up with a reasonably acceptable solution, the CAD computer age, albeit only plotting Smith charts on a teleprinter, had rather reduced the original need. But given the widespread use of such elements, it still

seems to me that it is a construct that should be more well known. So, for posterity, if little else, let's do it.

We start with a non-50-Ω transmission line of characteristic impedance Z_{0L} and electrical length θ , terminated with an unmatched load Z_L . The reflection coefficient in the Z_{0L} system is given by

$$\rho_{L\theta} = \frac{Z_L - Z_{0L}}{Z_L + Z_{0L}} e^{-j2\theta},$$

which, for convenience, I will write in the form

$$\rho_{L\theta} = \rho_L e^{-j2\theta},$$

with ρ_L thus being the radius of a circle centered on the Z_L Smith chart.

We now convert this back into an impedance,

$$Z_{L\theta} = Z_L \frac{1 + \rho_L e^{-j2\theta}}{1 - \rho_L e^{-j2\theta}},$$

which now, in turn, we can express as a reflection coefficient back in the "home" impedance environment of Z_0 ,

$$\rho_{0\theta} = \frac{Z_L \frac{1 + \rho_L e^{-j2\theta}}{1 - \rho_L e^{-j2\theta}} - Z_0}{Z_L \frac{1 + \rho_L e^{-j2\theta}}{1 - \rho_L e^{-j2\theta}} + Z_0},$$

which, with yet more slick rearranging, can be written as

$$\rho_{z0} = \frac{1 + \gamma \rho_L e^{-j2\theta}}{\gamma + \rho_L e^{-j2\theta}}, \quad (1)$$

where γ is, interestingly, if only marginally so, a "reflection coefficient" based on the two characteristic impedances,

$$\gamma = \frac{Z_L - Z_0}{Z_L + Z_0}.$$

At this juncture, I should disclose that as I kept seeing expressions such as (1) and still not recognizing a circle with any certainty (albeit in the knowledge that it is), I discovered that there is, in fact, a theorem in complex function theory that comes to my assistance. In fact, (1) is a fairly simple example of what is termed a "bilateral transformation," which basically states

that any complex function z that traces out a circular locus on the z plane as one of its parameters is varied will still trace a circular locus on the w plane after being transformed by the function

$$w = \frac{a + bz}{c + dz},$$

where a , b , c , and d are any complex constants, and any appropriate textbook will give expressions for the corresponding radii and center locations (to be pedantic, which most math books usually are, this also absorbs the cases where the resulting loci can be straight lines, corresponding to circles with infinite radii). Although I may be appearing to deviate into yet another math class, it turns out that this theorem can be quite useful when analyzing passive networks, especially those including transmission lines, hence my initial encounter with it as another short *TMTT* article [2].

However, in this particular case, I can reveal a reasonably short path to a final proof, which involves a revisit of some basic, if now less familiar, results on complex numbers:

$$\begin{aligned} |z|^2 &= zz^*; \\ (z + z^*) &= 2 \operatorname{Re}(z); \\ |z + k|^2 &= (z + k)(z + k)^* \\ &= (z + k)(z^* + k), \end{aligned}$$

where k is real, and only the last result was perhaps, at first sight, the least familiar to me, albeit reasonably obvious, but actually the key to solving these kinds of problems.

So (1) can be rearranged to give

$$\rho_L e^{-j2\theta} = \frac{1 - \gamma \rho}{\rho - \gamma}$$

and taking magnitudes

$$\rho_L |\rho - \gamma| = |1 - \gamma \rho|.$$

Hence,

$$\rho_L^2 (\rho - \gamma)(\rho - \gamma)^* = (1 - \gamma \rho)(1 - \gamma \rho)^*.$$

And now, the really nifty step,

$$\rho_L^2 (\rho - \gamma)(\rho^* - \gamma) = (1 - \gamma \rho)(1 - \gamma \rho^*),$$

which rearranges into

$$\rho\rho^*(\gamma^2 - \rho_L^2) + (\rho + \rho^*)(\rho_L^2 - 1)\gamma = (\gamma^2 \rho_L^2 - 1),$$

and finally putting ρ into its Cartesian form, $\rho_X + j\rho_Y$,

$$\rho_Y^2 + \left(\rho_X + \frac{(\rho_L^2 - 1)}{(\gamma^2 - 1)} \right)^2 = (\gamma^2 \rho_L^2 - 1) + \left(\frac{(\rho_L^2 - 1)}{\gamma^2 - 1} \right)^2,$$

which, triumphantly, does indeed represent a circle centered on the real axis.

Although in the end a bit cumbersome, this result has some useful, “everyday” applications. For example, any chosen point on the standard chart has a family of circles passing through it, with centers located along the real axis, representing the matching trajectory of transmission lines having characteristic impedances ranging between the limiting cases of zero and infinity, as illustrated in Figure 2.

These extreme cases can be quickly identified as the existing Smith chart circles of series and shunt reactance; more realizable trajectories for transmission lines lie inside these boundaries. Furthermore, a graphical construction of any specific circle can be used to determine the cogni-

zant characteristic impedance retroactively by reading off the resistance values at the real axis intersection points. Figure 2 also reveals the range of impedances that can be matched to a given point using a single realizable transmission line element. I say “realizable” inasmuch as the “inaccessible” regions may well be within the range of an unrealizable transmission line, but I suspect even the most avid metamaterialist would have difficulty making a line with negative characteristic impedance ☹️.

Given that there is hardly a law against using more than one element to perform a matching task, I must admit that this particular result may appear somewhat academic, although it did happen to be the subject of one of those aforementioned short articles in *TMTT* and, in this case, featured the first time my name appeared in this most revered of journals, albeit as an acknowledgee [7].

I can still recall, with some detail, attending a meeting of the IEEE in London, sometime in the mid-1970s, when a speaker, Dr. (later Prof.) Rod Tucker, a colleague and later *TMTT* editor, showed that impedance contours of constant output power, measured using an output tuner on a GaAs FET,

were not circular but rather more elliptical. The general consensus, still prevalent today, was that this would be expected of a “nonlinear” device; at the time, and for some years later, I pondered the fact that if the device is backed off, even just a bit, from compression, it is still, de facto, operating in a linear fashion, but the contours remained “elliptical.”

I will not here repeat my own subsequent argument that emerged a few years, not to mention a few thousand miles, later as to why this appeared to be so [8]. Essentially, these constant power contours can be conceived to be the area enclosed between a constant resistance circle and a constant conductance circle, as depicted in Figure 3, thus giving a quasi-elliptical appearance. Although based on some simplifying assumptions, this basic construction has stood the test of time, despite numerous updates [9].

There is another related set of contours, which are also useful in PA design; these are the contours of constant impedance magnitude, which can be used to establish the onset of clipping. These are (of course) circles and are also illustrated in Figure 4, where a specific case of $20\ \Omega$ is highlighted and, in effect, represents the onset of clipping for a device having a $20\text{-}\Omega$ loadline value. The derivation turns out to be much more straightforward than the last one, and given that, in this case, it is worth recording that the contours do not represent the trajectory of a simple physical element. Essentially, if z is the chosen normalized impedance point, then

$$|z| = Z = \left| \frac{1 + \rho}{1 - \rho} \right|,$$

and proceeding as before,

$$Z^2(1 - \rho)(1 - \rho^*) = (1 + \rho)(1 + \rho^*),$$

which is a circle, centered at $(Z^2 + 1)/(Z^2 - 1)$, and radius R , given by $R^2 = ((Z^2 + 1)/(Z^2 - 1))^2 - 1$.

These curves have an interesting relationship with the power contours,

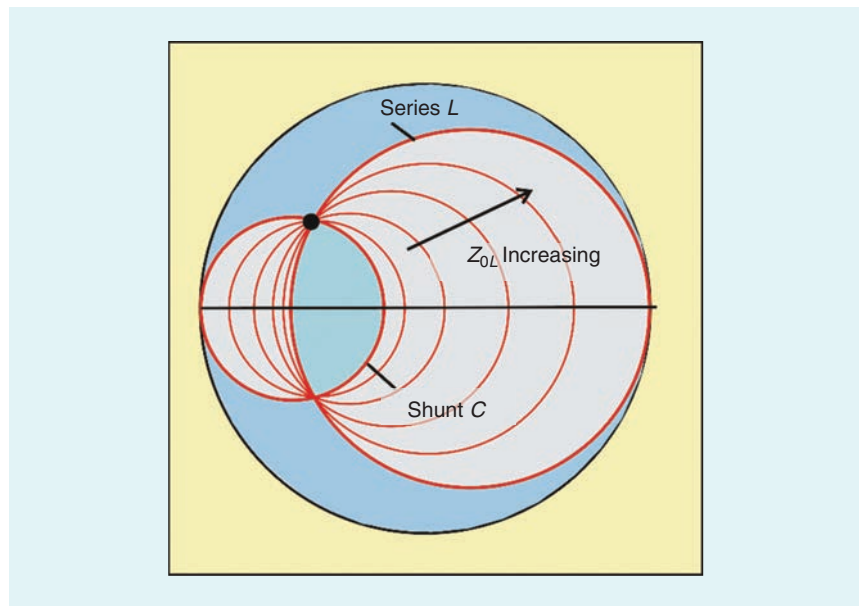


Figure 2. The trajectories of non-50- Ω transmission line matching elements.

as also shown in Figure 3. It has been commented, over the years and decades, that the right-hand arc of the power contour lies inside the clipping region, but the original argument was that in this region, the device drive is backed off, and the stipulated power will still be delivered with no clipping. More recently [9], we have shown that if the clipping action is taken into account, the right-hand arc is actually still “correct” at full drive—a little bit of serendipity there, I have to admit, nearly 40 years on.

Obviously, much of the foregoing has largely lost its immediate practical importance as far as the actual numerical calculations are concerned, with the computer now being used to determine and optimize element values. But the Smith chart still retains much value as a means of envisioning the behavior of matching sections and the physical behavior of measured devices. This has recently resurfaced in the increasing use of active load manipulation, or “load modulation,” in various PA configurations. Rather than devising a network that transforms a fixed 50-Ω termination, represented by a single point on the chart, into the desired impedance, the termination itself can be “modulated” through the use of an injected signal.

This is the basic action of the Doherty PA, although, in this case, the load modulation theoretically takes place along the real axis. The more recent load modulated balanced amplifier, or LMBA [10], is rather more versatile in that the termination can be moved to anywhere inside a concentric Smith chart circle, depending on the magnitude and phase of the control signal, as indicated by the shaded region in Figure 4. In principle, any point on the chart can be reached solely through a suitable setting of the control signal, whose magnitude defines the radius of the “patch.”

In fact, as shown in [10], the control signal power (CSP) is always fully recovered at the main amplifier output, but there may be some efficiency degradation due to the CSP

being generated at a lower efficiency. As such, a “hybrid” match is desirable, whereby the active modulation is augmented by a passive network. The designer is therefore confronted with a new twist on Smith chart mental gyrations; rather than moving a single point around, the whole load-modulated “patch” moves, as indicated in Figure 4.

But there is an additional dimension to the problem—the shape of the patch itself changes as well. In fact, given a circular patch, the bi-

linear transform theorem assures us that the circular shape will survive a transformation through any linear passive element, although its radius will likely change. So the Smith chart can once again be used to envisage the process: Figure 4 depicts a fairly simple case of a passive transmission line transformer as the passive matching element, in this case, the value of characteristic impedance that would be chosen to match the 50-Ω point to the optimum impedance at the center of the power contour.

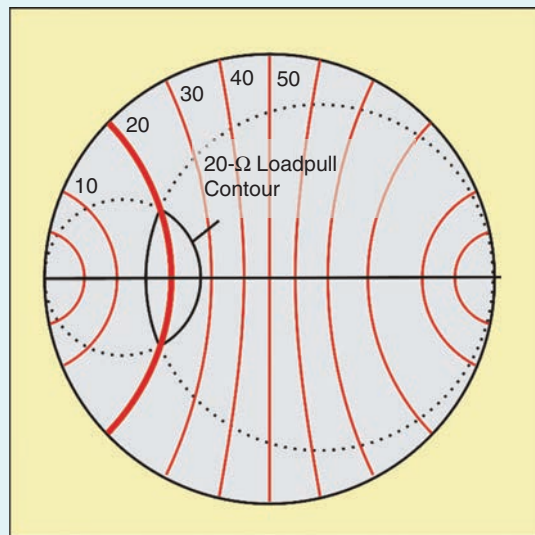


Figure 3. Impedance magnitude circles showing 20-Ω clipping and loadpull contours.

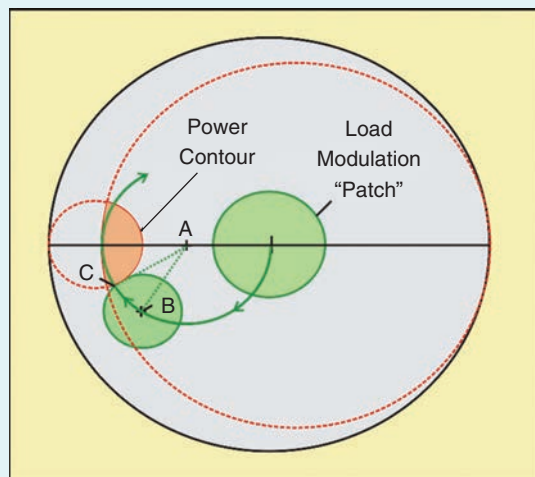


Figure 4. Impedance transformation including load modulation.

The key observation in Figure 4 is that the entire patch “swings” around the same center point A and will intersect the power contour (B) at a lower angle of rotation than would be the case for the single point represented by the unmodulated 50-Ω load (C). This translates directly into a substantial enhancement of the bandwidth, over which the response lies inside the power contour; Fano may not be defeated but is certainly bypassed. The Smith chart constructions can, as in times of old, be used to give precise quantitative information about the process, and the various touching circles offer some interesting geometry problems for those inclined. For those who are not so inclined, the computer will fill in the numerical detail.

The LMBA is still a developing subject, but it is interesting still to see the Smith chart right at the center of a new

research direction. For sure, the role of the Smith chart has gradually transitioned from a raw calculation aid into a valuable format for the visualization of device and network characteristics. It is ironic that the rapid calculation ability of the modern computer may have usurped the calculation function of the chart but has greatly enhanced its use as a meaningful display format—a true icon indeed.

References

- [1] P. H. Smith, “A transmission line calculator,” *Electronics*, vol. 12, no. 1, pp. 29–31.
- [2] C. Zelle, “A spherical representation of the Smith chart,” *IEEE Microw. Mag.*, vol. 8, no. 3, pp. 60–66, 2007. doi: 10.1109/MMW.2007.365060.
- [3] A. Muller et al., “The 3D Smith chart: From theory to experimental reality,” *IEEE Microw. Mag.*, vol. 21, no. 11, pp. 22–35, 2020. doi: 10.1109/MMM.2020.3014984.
- [4] M. H. Gupta, “Escher’s art, Smith chart, and hyperbolic geometry,” *IEEE Microw. Mag.*, vol. 7, no. 5, pp. 66–76, 2006. doi: 10.1109/MW-M.2006.247916.
- [5] T. Ohira, “Poincaré length,” *IEEE Microw. Mag.*, vol. 21, no. 3, pp. 120–121, 2020.
- [6] H. F. Matthys and R. F. Mathis, “Fermat’s last theorem and the Smith chart,” *Proc. IEEE*, vol. 57, no. 7, p. 65, 1966. doi: 10.1109/PROC.1966.4585.
- [7] P. I. Day, “Transmission line transformation between arbitrary impedances using the Smith chart,” *IEEE Trans. Microw. Theory Techn.*, vol. 23, no. 9, pp. 772–773, Sept. 1975. doi: 10.1109/TMTT.1975.1128674.
- [8] S. C. Cripps, “A theory for the prediction of GaAs FET load-pull contours,” in *Proc. IEEE Int. Microw. Symp. Dig.*, 1983, pp. 221–223. doi: 10.1109/MWSYM.1983.1130864.
- [9] R. Quaglia, D. J. Sheppard, and S. C. Cripps, “A reappraisal of optimum output matching conditions in microwave power transistors,” *IEEE Trans. Microw. Theory Techn.*, vol. 65, no. 3, pp. 838–845, 2017. doi: 10.1109/TMTT.2016.2627557.
- [10] D. J. Sheppard, J. R. Powell, and S. C. Cripps, “An efficient broadband reconfigurable power amplifier using active load modulation,” *IEEE Microw. Wireless Compon. Lett.*, vol. 26, no. 6, pp. 443–445, 2016. doi: 10.1109/LMWC.2016.2559503.



MicroBusiness *(continued from page 14)*

mentors, and managers have also come to that age.

But in this pandemic, our traditional rites-of-passage aren’t possible—there are no weddings or funerals. Life is on hold. Marriage is on hold. We have pending invitations to weddings that have been delayed until a time when the restrictions forced by the pandemic are likely to be behind us. For those couples, a key milestone in their lives has been postponed. Their lives have been delayed; so too have been the lives of most others.

When I think about schoolchildren—some spending a year in remote learning, not seeing their friends, and not having the childhood experiences we cherished—I wonder what the lasting impact on their lives will be. It will certainly vary. For the privileged few, with ample resources and sup-

port, the impact will be minimal. But for those that are already underprivileged, who don’t have an adequate support structure, whose circumstances are already fragile, how long will it take for them to recover from this setback? Will they ever?

Lives are on hold and our life expectancy, if anything, has decreased. So we have all lost a year that we will never recover. I think of all of the plans that we had made for the past year, almost all of them cancelled. The trips we had planned to take. The experiences we had planned to take in. The people we would have met. We won’t be able to recover the time we’ve lost. Will we be able to make up everything else that we’ve missed?

It’s been a difficult year for all of us. Everyone’s life has been on hold. For the young, major milestones have

been missed, delayed, or diminished. For this generation, the pandemic is dominating some of their formative years. It will have a lasting effect on the perspective that they carry with them going forward in life.

Our last milestone, at the end of life, has changed, too. Many have died without their families by them. Almost all have been marked by minimal, or diminished, celebrations of their lives. So many eminent members of our community have passed away over the past few years, starting even before the onset of the pandemic. During the pandemic, we haven’t been able to recognize their contributions and honor their memories as we would normally do. Their many contributions stay with us, and our fond memories persist. I toast them.





From the Guest Editors' Desk

Low-Noise Techniques

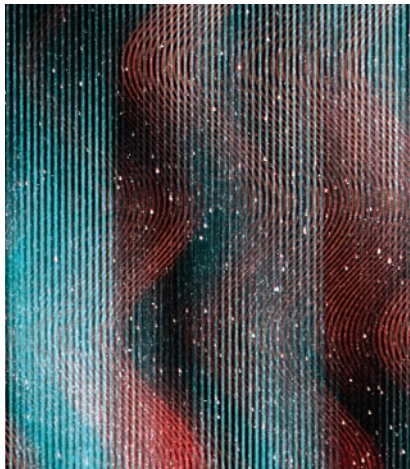
■ Fabrizio Bonani and Alfred E. Riddle

The focused issue we present here is sponsored by the IEEE Microwave Theory and Techniques Society (MTT-S) MTT-11 Technical Committee (TC) on Low-Noise Techniques. Each TC in the MTT-S is made up of international researchers with a variety of backgrounds and research interests. The low-noise TC changes on a regular basis and brings in researchers with new interests. Low-noise techniques cover everything from fundamental noise sources down to the quantum level and up to complete systems. Of course, nonlinear processes, semiconductor devices, and oscillator noise sources are also covered, as you will see in the articles in this issue. The goal of an MTT-S TC is to promote workshops and educational publications and to maintain an ever-improving knowledge base for the Society in a specific area.

We decided to focus attention on three different and interesting aspects

Fabrizio Bonani (fabrizio.bonani@polito.it) is with Polytechnico di Torino, Torino, 10129, Italy. Alfred E. Riddle (alfred.riddle@quanergy.com) is with Quanergy Systems, Inc., Sunnyvale, California, 94085, USA.

*Digital Object Identifier 10.1109/MMM.2021.3069614
Date of current version: 1 June 2021*

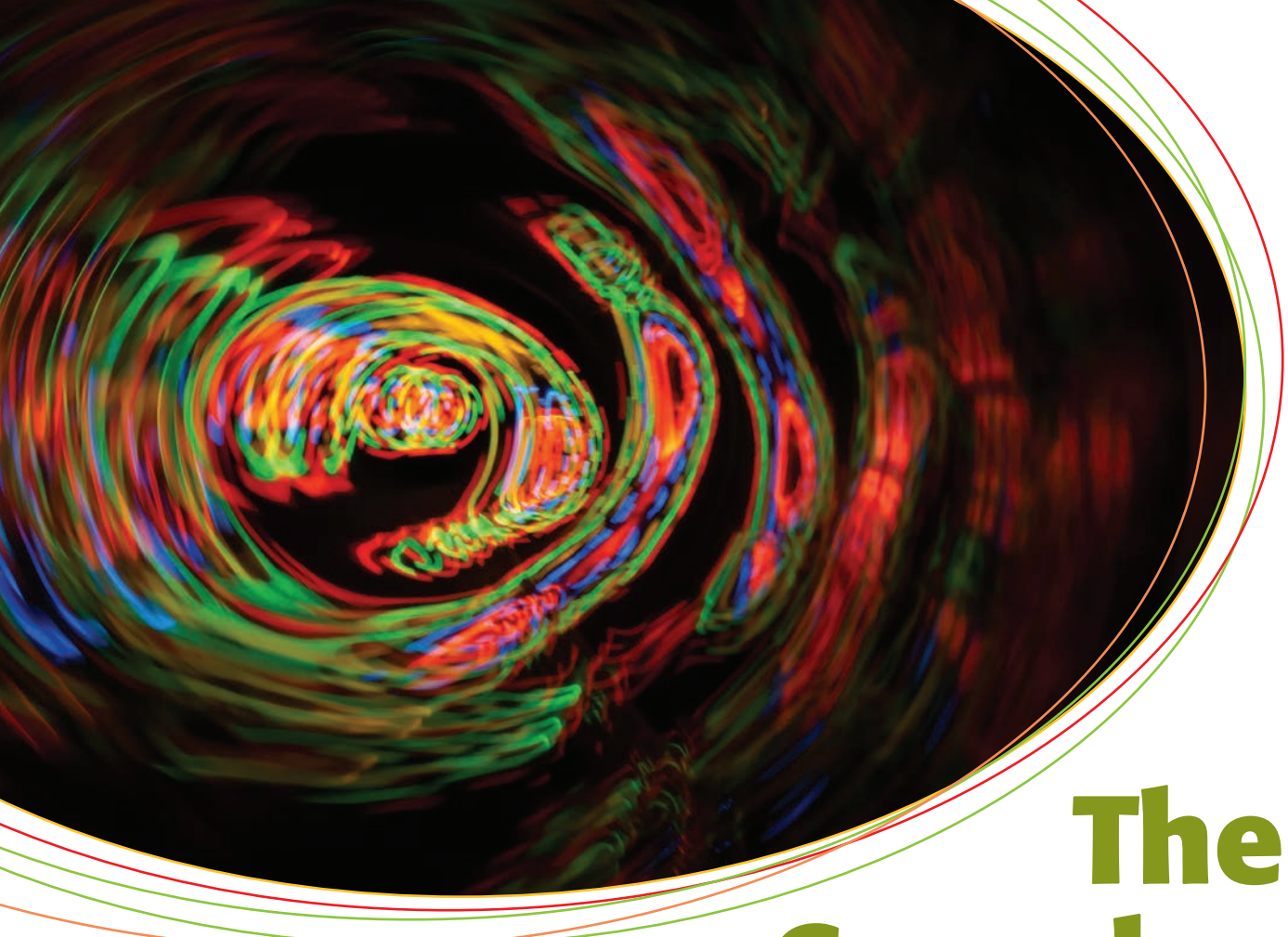


of the low-noise area, each chosen for its intrinsic complexity coupled with a widespread interest for microwave engineers. The first contribution, by Traversa et al., introduces the most recent approaches to one of the oldest, yet still active, areas of noise-related research: fluctuations in oscillators, which are autonomous nonlinear systems able to sustain a time-periodic signal even in the absence of external stimulations other than a dc energy source. This peculiar property has far-reaching consequences for the oscillator signal, in terms of both phase and amplitude noise. The second

contribution, by Boggione, provides a step-by-step introduction to the challenges in stationary noise characterization, from the customary case of two-port devices to the more advanced generalization to N -port networks. Novel techniques are also discussed, aimed at getting rid of the main characterization bottlenecks found in the standard procedures. Finally, noise simulation in nonlinear circuits, such as mixers, oscillators, buffer amplifiers, and standard low-noise amplifiers subject to large blocking signals, is the topic of the article by Rudolph and Apte. The review focuses on recent implementations in commercial circuit simulators, using the harmonic balance approach, of device noise models for the nonlinear regime with reference to the major technologies, namely, heterojunction bipolar transistors and field effect transistors.

We are confident that this focused issue, with contributions by members of the MTT-11 TC active in the respective research areas for several years, will be of interest to both the general reader and the low-noise specialist, helping them gain insight into these fascinating and practically important topics.





©SHUTTERSTOCK.COM/DMITRYSTESHENKO

The Complex World of Oscillator Noise

*Fabio L. Traversa, Michele Bonnin,
and Fabrizio Bonani*

The study of fluctuations in oscillators has been a classical research topic in mathematics, physics, and engineering since the first half of the 20th century [1]–[4]. Besides the intellectual fascination for mathematically difficult problems, the importance of the topic is deeply rooted in practical applications, mainly in the fields of RF and microwave electronics and also telecommunications. In fact, defining a precise frequency reference is fundamental for many applications, both electrical (e.g., transmitters and receivers) and optical (e.g., lasers). The broadening of the generated spectral line is mainly due to the phase-noise component of oscillator fluctuations, which consequently is the most commonly studied feature of oscillator noise (see [5] for a recent and exhaustive review). In a dual perspective, the definition of a precise time reference is also extremely important for digital applications,

*Fabio L. Traversa (ftraversa@memcpu.com) is with MemComputing Inc., San Diego, California, 92121, USA.
Michele Bonnin (michele.bonnin@polito.it) and Fabrizio Bonani (fabrizio.bonani@polito.it) are with the
Dipartimento di Elettronica e Telecomunicazioni, Politecnico di Torino, Torino, 10129, Italy.*

Digital Object Identifier 10.1109/MMM.2021.3069535

Date of current version: 1 June 2021

thus implying the necessity to keep under control the time jitter in clocked and in sampled systems. From a theoretical standpoint, phase noise and time jitter are simply two sides of the same coin, a manifestation of the oscillator's noisy behavior. As the microwave engineer is more often interested in the phase-noise characterization, we discuss only the latter. The time-jitter estimation is discussed, for instance, in [6].

Despite this long history, oscillator noise recently received a significant rejuvenation when a mathematically sound approach was proposed in [6] and [7] that takes care of some inconsistencies showed by classical approaches at vanishing offset frequencies. However, mathematical consistency is attained at the cost of a significant complexity of the corresponding noise theory. This makes it impossible to provide a direct link to simplified circuit analysis and, thus, to simple yet sufficiently accurate closed-form expressions that would make a direct connection to low-noise oscillator design rules, such as the celebrated Leeson formula [8], [9]. In other words, the use of advanced and mathematically sound theories is often confined to electronic design automation (EDA) tools for the CAD of oscillators.

The aim of this review is to introduce such modern approaches to oscillator (phase and amplitude) noise analysis and to discuss the relationship among them (avoiding as much as possible the corresponding mathematical subtleties), with the ultimate goal of clarifying their differences and connections.

Basics

The starting point of any oscillator noise theory is the set of equations that govern the state-space evolution of the circuit in the absence of any fluctuations, which in the simplest case is a set of ordinary differential equations (ODEs), such as

$$\frac{d\mathbf{x}}{dt} = \mathbf{f}(\mathbf{x}(t)), \quad (1)$$

where $\mathbf{x}(t)$ is the set of n variables describing the oscillator working point (WP), and \mathbf{f} is an n -size nonlinear function. Actually, circuit equations as implemented in circuit simulators generally take the form of a differential-algebraic equation system [10]. The treatment is mathematically more involved [11]; however, since the basic results are the same, we discuss here the simpler ODE case only. We consider here purely analog systems, in which \mathbf{f} is a smooth function. The case of mixed analog-to-digital circuits requires a more complex analysis because of the presence of jumps in the solution that prevent the direct exploitation of Floquet theory [12]–[14].

The oscillator is identified by a nonzero solution $\mathbf{x}_s(t)$ of (1) characterized by the property of being periodic; i.e., there is a period $T > 0$ such that $\mathbf{x}_s(t + T) = \mathbf{x}_s(t)$. Clearly, a well-designed oscillator should have a

From a theoretical standpoint, phase noise and time jitter are simply two sides of the same coin, a manifestation of the oscillator's noisy behavior.

strongly stable WP, meaning that a limited perturbation of the circuit should be rapidly absorbed by the oscillator, whose state should therefore plunge back on the limit cycle (orbit) $\mathbf{x}_s(t)$. Mathematically, this is guaranteed in the following way: the linear periodically time-varying (LPTV) system obtained by linearizing (1) around $\mathbf{x}_s(t)$ should be characterized by the unique structural Floquet exponent (FE) $\mu_1 = 0$ (see "A Floquet Theory Primer" for a brief introduction to Floquet theory) and also by the other $n - 1$ FEs all satisfying $\text{Re}\{\mu_i\} \ll 0$.

The presence of noise is translated into a dependency of the nonlinear function \mathbf{f} on a proper set of $m_w + m_c$ noise sources, represented by a stochastic vector $\xi_w(t)$ of size m_w , usually characterized as a set of uncorrelated white Gaussian noise processes [15] and by the low-frequency (typically, flicker) fluctuations characterized by m_c scalar, independent, and colored Gaussian noise sources $\xi_{cm}(t)$. In this way, the ODE system (1) is transformed into a stochastic ODE (S-ODE). As the noise sources are usually of limited magnitude, the customary procedure amounts to linearizing the perturbed S-ODE with respect to the noise sources, thus leading to a Langevin equation,

$$\frac{d\mathbf{x}}{dt} = \mathbf{f}(\mathbf{x}(t)) + \mathbf{B}_w(\mathbf{x}(t))\xi_w(t) + \sum_{m=1}^{m_c} \mathbf{B}_{wm}(\mathbf{x}(t))\xi_{cm}(t), \quad (2)$$

where $\mathbf{x}(t)$ is the set of perturbed circuit variables, now stochastic processes. Matrix \mathbf{B}_w , of size $n \times m_w$, represents the possible noise-source modulation of the white sources, while the m_c vectors \mathbf{B}_{wm} (of size n) are introduced to take into account the possible modulation of the colored sources.

At this point, the approaches available in the literature are different ways of tackling the solution of (2). The most obvious one is to directly solve the nonlinear S-ODE (most probably numerically) and find the corresponding second-order statistical characterization of the noisy circuit variables $\mathbf{x}(t)$, namely the two-time correlation matrix $\mathbf{R}_{\mathbf{x},\mathbf{x}}(t_1, t_2) = \langle \mathbf{x}(t_1)\mathbf{x}^\dagger(t_2) \rangle$, where $\langle \cdot \rangle$ represents the expectation operator and \dagger denotes the conjugate transpose. In many practical cases, noise is stationary, and thus $\mathbf{R}_{\mathbf{x},\mathbf{x}}(t_1, t_2) = \mathbf{R}_{\mathbf{x},\mathbf{x}}(t)$, where $t = t_2 - t_1$. Thus, according to the Wiener–Khinchin theorem [16], the same information can be more effectively represented by a frequency-domain function [the noise spectrum $\mathbf{S}_{\mathbf{x},\mathbf{x}}(\omega)$ or the power spectral

density (PSD)] that is the Fourier transform of $\mathbf{R}_{\mathbf{x},\mathbf{x}}(t)$. However, the direct numerical solution of an S-ODE is a tough task, particularly if the size n of the circuit is large and if an accurate determination of the statistical properties is sought. Therefore, this approach is used mainly as a reference solution for validating manipulations of (2), and it is mostly applied to low-dimensional test cases ($n = 2$ or 3 or slightly higher).

In most cases, the problem is tackled by decomposing the fluctuating solution into phase- and amplitude-noise components and by deriving (and solving) the corresponding S-ODEs. See the section "Solution Approaches: Phase–Amplitude Decomposition."

Finally, the noise sources are typically characterized as Gaussian stationary processes. The Gaussian assumption allows us to fully describe the statistical properties exploiting the average and the variance, i.e., the first two moments of the random process. In particular, here the white components ξ_w are assumed to be uncorrelated and of unit amplitude, as the source strength (and the possible correlation, if present) can be included in the modulating matrix $\mathbf{B}_w(t)$: $\mathbf{R}_{\xi_w, \xi_w}(t_1, t_2) = \mathbf{I}\delta(t_1 - t_2)$, so

that the corresponding PSD becomes $\mathbf{S}_{\xi_w, \xi_w}(\omega) = \mathbf{I}$, where \mathbf{I} is the identity matrix of size m_w . The uncorrelated colored noise sources represent important physical processes, such as flicker noise, and are characterized by the corresponding (here, scalar) PSD $S_{\xi_{cm}, \xi_{cm}}(\omega)$.

Phase Definition and Phase Noise

The nature of autonomous systems makes their operation rather involved. Practical oscillators are characterized by a time-periodic WP that is a stable periodic orbit $\mathbf{x}_s(t)$ (the limit cycle), i.e., a closed path in the state space continuously covered by the oscillator variables. Each point of the orbit is reached every T seconds, i.e., once per period of oscillation, and the actual operation of the circuit is characterized by the lack of a fixed time reference, meaning that, even if the oscillator correctly operates on the designed periodic solution, the starting point of the orbit, i.e., the value $\mathbf{x}_s(0)$, is randomly chosen by the peculiar initial conditions that are present at the time $t = 0$ of oscillator switch-on. More mathematically, given the WP $\mathbf{x}_s(t)$, the translated variables $\mathbf{x}_s(t + t_0)$ are also a solution of (1) for any t_0 . This

A Floquet Theory Primer

Floquet theory [11], [42] is the basis for the most advanced oscillator noise theories since it describes the input–output relationship of a linear periodically time-varying (LPTV) system of size n , such as

$$\frac{d\mathbf{y}}{dt} = \mathbf{A}(t)\mathbf{y}(t), \quad (S1)$$

where $\mathbf{A}(t) = \mathbf{A}(t + T)$ is a T -periodic matrix of size n . The Floquet theorem writes the solution of (S1) with initial condition $\mathbf{y}(0) = \mathbf{y}_0$ as

$$\mathbf{y}(t) = \mathbf{U}(t)\mathbf{D}(t)\mathbf{V}(0)\mathbf{y}_0, \quad (S2)$$

where $\mathbf{U}(t)$ and $\mathbf{V}(t)$ are two T -periodic invertible square matrices of size n such that $\mathbf{U}(t) = \mathbf{V}^{-1}(t)$, while matrix $\mathbf{D}(t)$ is diagonal:

$$\mathbf{D}(t) = \text{diag}\{\exp(\mu_1 t), \dots, \exp(\mu_n t)\}. \quad (S3)$$

The set of the n complex numbers μ_i defines the Floquet exponents (FEs) of (S1), while $\lambda_i = \exp(\mu_i T)$ are the corresponding Floquet multipliers (FMs).

Since $\mathbf{V}(t)\mathbf{U}(t) = \mathbf{I}_n$ (the identity matrix of size n), the columns $\mathbf{u}_i(t)$ of $\mathbf{U}(t)$ and the rows $\mathbf{v}_i^\dagger(t)$ of $\mathbf{V}(t)$ form a biorthogonal basis of \mathbb{R}^n . Function $\mathbf{u}_i(t)\exp(\mu_i t)$ is a solution of (S1) with initial condition $\mathbf{u}_i(0)$. On the other hand, $\mathbf{v}_i(t)\exp(-\mu_i t)$ is a solution of the adjoint system associated to (S1), i.e.,

$$\frac{d\mathbf{z}}{dt} = -\mathbf{A}^\dagger(t)\mathbf{z}(t), \quad (S4)$$

with initial condition $\mathbf{v}_i(0)$. Therefore, given the FE μ_i , $\mathbf{u}_i(t)$ is the associated direct Floquet eigenvector, while $\mathbf{v}_i(t)$ is the adjoint Floquet eigenvector. A geometrical interpretation can be found in [18]. The exponential dependence on μ_i implies that an oscillator has an asymptotically stable orbit if and only if all of the FEs μ_i ($i = 2, \dots, n$) have negative real parts or, equivalently, all of the FMs λ_i ($i = 2, \dots, n$) are found inside the unit circle of the complex plane.

A simple calculation [15] shows that the LPTV system associated to the linearization of an autonomous system around the oscillation noiseless WP $\mathbf{x}_s(t)$ always has $\mu_1 = 0$ as an FE, with the associated direct (normalized) Floquet eigenvector being the tangent to the oscillator limit cycle $\mathbf{u}_1(t) = \dot{\mathbf{x}}_s(t) / \|\dot{\mathbf{x}}_s(t)\|$ ($\dot{\cdot}$ denotes the time derivative). The corresponding adjoint Floquet eigenvector $\mathbf{v}_1(t)$ is the so-called perturbation projection vector, which plays the leading role in the assessment of phase noise [6], [18], [19]. However, the other FEs and eigenvectors are also of importance, both because they assess the stability of the circuit WP [43] and because they are required to express the oscillator amplitude noise [25]. The corresponding computation can be performed in both the time and frequency domains; see e.g., [36]–[38] and [44]–[46].

suggests that one should consider a decomposition of the perturbed oscillator solution $\mathbf{x}(t)$ by separating the variation along the orbit from that taking place in the $(n - 1)$ -dimensional space that is linearly independent of the first one.

The behavior along the limit cycle is characterized by the concept of orbit phase. The exact mathematical definition of phase in the case of a noisy oscillator is a rather complex task, especially if $n > 2$: it involves the concept of orbit isochron [17]–[19], and it is beyond the scope of this review. We simply state here that the oscillator phase is defined as the function such that, in the noiseless limit,

$$\Phi(t) = \Phi(\mathbf{x}_S(t)) = \omega_0 t, \quad (3)$$

where $\omega_0 = 2\pi f_0 = 1/T$ is the WP (angular) frequency, and it is generalized for the noisy oscillator to a stochastic process whose average is equal to $\Phi(t)$. The corresponding second-order statistical properties, i.e., the correlation function $R_{\Phi,\Phi}(t_1, t_2) = \langle \Phi(t_1)\Phi(t_2) \rangle$, define the concept of phase noise. The remaining $n - 1$ degrees of freedom required to fully characterize $\mathbf{x}(t)$ constitute the oscillator orbital—or amplitude—noise. As discussed in [20], for electronic oscillators, the WP is normally a strongly stable orbit. This implies that the orbital perturbations will eventually decay and that the instantaneous WP is attracted back toward the noiseless orbit. Amplitude noise is therefore negligible with respect to phase noise, thus explaining the focus of the literature (and the designer's efforts) on phase fluctuations. Nevertheless, there are examples of autonomous systems, e.g., some models of biological systems [21], [22], for which orbital fluctuations are not negligible [23]. Furthermore, even in the electronic circuit case, orbital contributions might become important far away from the oscillation harmonics, which in turn may impact the dynamic range of receivers operated in the presence of strong adjacent channels [24], [25].

Solution Approaches: Linearization

The solution of (2) is almost always found by leveraging the assumed small amplitude of the fluctuations induced by the noise sources, thus exploiting some degree of linearization. The simplest approach amounts to assuming that the effect of noise is a perturbation of the oscillator orbit:

$$\mathbf{x}(t) = \mathbf{x}_S(t) + \mathbf{x}_n(t), \quad (4)$$

where $\mathbf{x}_n(t)$ is a zero-average vector stochastic process of size n .

The standard approach proceeds by deriving a stochastic equation for $\mathbf{x}_n(t)$ based on the linearization of (2), either around a dc value \mathbf{x}_0 that approximates $\mathbf{x}_S(t)$ or directly around the oscillator limit cycle $\mathbf{x}_S(t)$. In the first case, the resulting system is linear time invariant

The solution of (2) is almost always found by leveraging the assumed small amplitude of the fluctuations induced by the noise sources, thus exploiting some degree of linearization.

(LTI), while in the second it becomes LPTV [24], [26]. The LTI analysis is extremely simple but has a very limited accuracy. It has been recognized as too crude for many applications, although in some specific cases, namely oscillators where little noise modulation takes place, the results might be in reasonably good agreement with those of experiments [5].

On the other hand, the LPTV approach is much more popular, thanks to a combination of the simplicity of the mathematical machinery and an often quite good accuracy in the results—at least not asymptotically close to the harmonics of the oscillation frequency ω_0 , where all linearized approaches yield a divergent spectrum [6]. The LPTV description was adopted in the classical work by Kurokawa [27] and has been generalized more recently within the framework of harmonic balance EDA tools, as described in [28], where the Kurokawa results are derived as a special case. The methodology derived in [28] decomposes the noise description exploiting two formulations, one used to estimate noise far away from the harmonics of ω_0 and the other very close to the harmonics, where the carrier modulation noise is defined. This sophisticated decomposition allows for accurate results even quite close to the nominal oscillation frequency, thus improving the applicability of the LPTV description and making it a common tool among designers.

Solution Approaches: Phase–Amplitude Decomposition

The path to the development of a well-founded, and ultimately more accurate, theory of noise in oscillators was initiated by the seminal work of Franz X. Kaertner, who proposed in [29] and [30] to decompose the noisy variables into a fluctuating term along the limit cycle (phase noise) and into amplitude noise, exploiting the decomposition illustrated in Figure 1 and expressed as

$$\mathbf{x}(t) = \mathbf{x}_S(t + \alpha(t)) + \delta\mathbf{x}(t). \quad (5)$$

The time-reference fluctuation $\alpha(t)$ is a zero-average (within the limit of negligible higher order terms of the α equation [15]) stochastic process that corresponds to phase noise

$$\Phi(t) = \omega_0(t + \alpha(t)), \quad (6)$$

while the amplitude fluctuations are represented by $\delta\mathbf{x}(t)$.

Of course, the decomposition in (5) is not uniquely defined; however, on the basis of the stability of the noiseless oscillator WP, the basic idea is to choose the definition so that $\delta\mathbf{x}(t)$ remains small irrespective of time t . Notice that, by contrast, the time fluctuation $\alpha(t)$ may be large without forcing the oscillator instantaneous WP to wander far away from the orbit $\mathbf{x}_S(t)$. In fact, as shown in [6], the time perturbation $\alpha(t)$ has a variance that grows unbounded linearly with time.

Taking for granted the decomposition (5), the available theories involve defining a stochastic equation that enables the evaluation of the statistical properties of $\alpha(t)$ and $\delta\mathbf{x}(t)$. Focusing on phase noise, we follow the most direct path; amplitude noise is simply neglected by setting $\delta\mathbf{x}(t) = 0$. However, this choice has to be made wisely, in the sense that the S-ODE that defines the time evolution of $\alpha(t)$ should be determined by guaranteeing that the corresponding orbital perturbation remains arbitrarily small. As discussed in [6] and [15], this implies that (2) has to be projected along the noiseless WP tangent, i.e., $d\mathbf{x}_S/dt$, whose versor is the Floquet eigenvector $\mathbf{u}_1(t)$ associated to the FE $\mu_1 = 0$ (see ‘‘A Floquet Theory Primer’’). As discussed in [30], this projection uniquely defines the phase and amplitude perturbations, as the corresponding equations are invariant with respect to linear changes of the state variables.

Although the projection along $\mathbf{u}_1(t)$ is mandatory to define the fluctuations along the orbit, the choice of the other Floquet eigenvectors as the remaining $n - 1$ base elements used to define the amplitude noise is not strictly necessary. However, as shown in [31], this choice guarantees that, even including the small amplitude noise, the defining equation for $\alpha(t)$ is left unchanged, thus preserving the results derived in [6] and [7]. Since the Floquet basis is not in general orthogonal, the projection operation requires the use of the

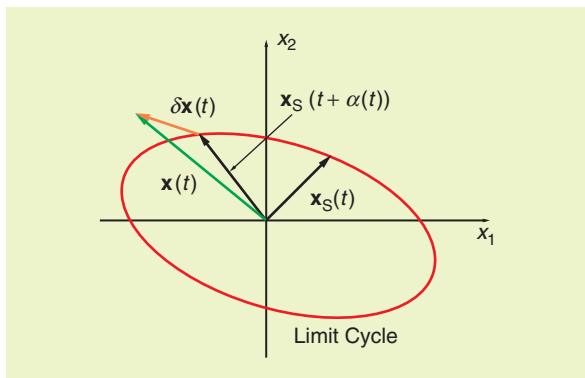


Figure 1. The graphical representation of the decomposition of the noisy oscillator variables into phase and amplitude fluctuations for a generic 2D system.

adjoint Floquet eigenvector $\mathbf{v}_1(t)$, also called the *perturbation projection vector (PPV)*. The resulting nonlinear S-ODE for the time fluctuation $\alpha(t)$ is [6]

$$\frac{d\alpha}{dt} = \mathbf{v}_1^\dagger(t + \alpha(t)) \mathbf{B}_w(t + \alpha(t)) \boldsymbol{\xi}_w(t) + \sum_{m=1}^{m_c} \mathbf{v}_1^\dagger(t + \alpha(t)) \mathbf{B}_{wm}(t + \alpha(t)) \boldsymbol{\xi}_{cm}(t). \quad (7)$$

Despite its nonlinear nature, this equation can be analyzed in detail (see [6] for white-noise sources and [7] for flicker-noise sources), and a general formulation for the resulting oscillator phase noise can be found whose characterization ultimately depends on the determination of the PPV, which therefore becomes the main quantity to be determined for phase-noise assessment. The detailed analysis in [6] and [7] shows that $\alpha(t)$ becomes asymptotically a Gaussian stationary stochastic process with variance fully defined by the harmonic components of the PPV and of the modulating functions

$$\sigma^2(t) = c_w t + \frac{1}{\pi} \sum_{m=1}^{m_c} |V_{0m}|^2 \int_{-\infty}^{+\infty} S_{\xi_{cm}, \xi_{cm}}(\omega) \frac{1 - e^{j\omega t}}{\omega^2} d\omega, \quad (8)$$

where

$$c_w = \frac{1}{T} \int_0^T \mathbf{v}_1^\dagger(t) \mathbf{B}_w(t) \mathbf{B}_w^\dagger(t) \mathbf{v}_1(t) dt \quad (9)$$

represents the contribution of white-noise sources, while colored noise is weighted by the magnitude of the dc component of $\mathbf{v}_1^\dagger(t) \mathbf{B}_{cm}(t)$,

$$V_{0m} = \frac{1}{T} \int_0^T \mathbf{v}_1^\dagger(t) \mathbf{B}_{cm}(t) dt. \quad (10)$$

The PSD of phase noise can also be expressed as a function of the same parameters. In fact, [7] shows that the spectrum of the asymptotic value of the autocorrelation function for $\mathbf{x}_S(t + \alpha(t))$ reads as

$$\mathbf{S}_{\mathbf{x}, \mathbf{x}}(\omega) = \sum_k \mathbf{X}_{S,k} \mathbf{X}_{S,k}^\dagger \mathbf{S}_k(\omega + k\omega_0), \quad (11)$$

where $\mathbf{X}_{S,k}$ is the amplitude of the k th harmonic of $\mathbf{x}_S(t)$ (assuming an exponential Fourier series), and

$$\mathbf{S}_k(\omega) = k^2 \frac{\omega_0^2}{\omega^2} \left[c_w + \sum_{m=1}^{m_c} |V_{0m}|^2 S_{\xi_{cm}, \xi_{cm}}(\omega) \right] \quad (12)$$

for $\omega \gg 0$, i.e., far away from the harmonics of ω_0 . However, close to the harmonics (i.e., for $\omega \approx 0$), a Lorentzian-shape contribution is recovered to avoid the nonphysical divergence for $\omega = 0$:

$$\mathbf{S}_k(\omega) = \frac{\omega_0^2 k^2 \left[c_w + \sum_{m=1}^{m_c} |V_{0m}|^2 S_{\xi_{cm}, \xi_{cm}}(\omega) \right]}{\frac{\omega_0^4 k^4}{4} \left[c_w + \sum_{m=1}^{m_c} |V_{0m}|^2 S_{\xi_{cm}, \xi_{cm}}(\omega) \right]^2 + \omega^2}. \quad (13)$$

Equation (12) is particularly interesting as it is consistent with well-known results concerning the scaling of noise sources by ω^2 on the phase-noise spectrum. The expression, however, is confined to a nonnegligible frequency offset from the ω_0 harmonics. Close to these harmonics, the spectrum (13) becomes Lorentzian, which is again an expected result [20]. Notice also that the magnitude of the phase-noise spectrum depends on the harmonic content of the PPV multiplied by the source modulation functions [see (9) and (10)].

A Comparison of [6], [30], and [32]

We now discuss briefly the differences among the approaches presented in references [6], [30], and [32]. A detailed comparison can be found in [33], where the PSDs are also presented. Notice that the same nonlinear S-ODE (7) was found in [30]; however, to find the phase-noise characterization, Kaertner made a zeroth-order approximation of the S-ODE, reducing it to the linear case:

$$\frac{d\alpha}{dt} = \mathbf{v}_1^\dagger(t) \mathbf{B}_w(t) \boldsymbol{\xi}_w(t) + \sum_{m=1}^{m_c} \mathbf{v}_1^\dagger(t) \mathbf{B}_{wm}(t) \boldsymbol{\xi}_{cm}(t). \quad (14)$$

Therefore, the results in [30] derive from an approximation of the correct phase equation (7), neglecting the α dependence on the right-hand side. Although this does not impair the general shape of the output spectrum, which retains exclusive dependence on both the spectral components of the PPV and the modulating functions and

the Lorentzian shape, the approximation becomes significant for the accurate description of specific behaviors, such as injection locking or power/ground interference analysis. See [34] and references therein for a discussion.

The comparison with the impulse sensitivity function (ISF) theory proposed in [32] (and summarized here in “The Impulse Sensitivity Function Theory”) is made more complex by the several ISF definitions that can be exploited.

- 1) The numerical ISF, defined in Appendix A of [32] as the phase fluctuation induced by a delta function perturbation in the oscillator variables calculated through time-domain simulations, corresponds to the PPV [34]. Therefore, since in [32] the phase fluctuation is obtained through a linear response theory, the time perturbation satisfies (14) (although in the original article, this relation is expressed in integral form), with the same limitations.
- 2) The closed-form ISF (see [32] and “The Impulse Sensitivity Function Theory”) corresponds to the projection along the direct Floquet eigenvector $\mathbf{u}_1(t)$, opposite to the correct use of the PPV, and thus may severely undermine the accuracy of the calculated phase variation.

Amplitude Noise

Projection of the full S-ODE along the other elements of the chosen basis yields a vector S-ODE having $\delta\mathbf{x}(t)$ as an

The Impulse Sensitivity Function Theory [32]

According to the definition given in [32], the impulse sensitivity function (ISF) $\Gamma(\omega_0\tau)$ “is a dimensionless, frequency- and amplitude-independent periodic function with period 2π which describes how much phase shift results from applying a unit impulse at time $t = \tau$.” This means that the ISF defined in this way corresponds to the impulse response of the linearized equations defining the phase perturbation. However, the operative definitions described in the original article lead to different relations with reference to the quantities as used in this review (we consider here, for the sake of simplicity, the white-noise sources only).

- 1) The closed-form ISF defined in Appendix B of [32] corresponds to the impulse response of the linearized equations defining the phase perturbation projected along the orbit tangent vector $\mathbf{u}_1(t)$:

$$\alpha(t) = \int_{-\infty}^t \mathbf{u}_1^\dagger(t) \mathbf{B}_w(t) \boldsymbol{\xi}_w(t) dt. \quad (S5)$$

Notice that the normalization of the unit tangent, as discussed in “A Floquet Theory Primer,” is necessary for establishing a direct relationship with the closed-form ISF.

- 2) The numerical ISF of [32] and “A Floquet Theory Primer” is defined in an incremental way by introducing an impulse perturbation into the circuit equations and determining the corresponding time evolution of the phase variation. As a consequence, it corresponds to the propagation of a deterministic source into a phase variation, which in turn was shown in [6] to be determined by the PPV:

$$\alpha(t) = \int_{-\infty}^t \mathbf{v}_1^\dagger(t) \mathbf{B}_w(t) \boldsymbol{\xi}_w(t) dt. \quad (S6)$$

As a final remark, we point out that the correct use of the ISF should be within the nonlinear stochastic ordinary differential equation (S-ODE) (7) and not by exploiting the Kaertner approximation (14). The latter corresponds directly to (S6), while (S5) leads to a different S-ODE:

$$\frac{d\alpha}{dt} = \mathbf{u}_1^\dagger(t) \mathbf{B}_w(t) \boldsymbol{\xi}_w(t). \quad (S7)$$

The amplitude ISF basically amounts to selecting the Floquet subspace that primarily influences the amplitude fluctuation, thus corresponding to an approximation of the full theory in [25].

unknown, whose solution characterizes the amplitude noise of the oscillator. Details on the projection procedure and of the intricacies related to the use of Itô calculus can be found in [15] and [35]. In the simplest case, i.e., treating $\delta\mathbf{x}(t)$ as a linear perturbation of the limit cycle affected by phase noise, some of the present authors were able to prove that $\mathbf{x}_S(t + \alpha(t))$ and $\delta\mathbf{x}(t)$ become asymptotically uncorrelated stochastic processes, while the corresponding amplitude-noise PSD depends on the remaining $n - 1$ FEs and Floquet eigenvectors [25]. The formulas are very complex but nevertheless easily implementable into EDA tools, provided that the relevant Floquet quantities have been accurately determined [36]–[38].

Notice that the same S-ODE for amplitude noise discussed in [25] and [31] was already derived in [30]. Although the solution outlined in [30] is based on the linear phase equation (14) as opposed to the nonlinear equation (7), the resulting spectra show, as in [25], that only the FEs characterized by a magnitude of the real part much lower than ω_0 provide a significant contribution.

Amplitude noise was also tackled in [24], where the amplitude ISF is defined properly, extending the concept of ISF used for phase-noise characterization. The amplitude ISF basically amounts to selecting the Floquet subspace that primarily influences the amplitude fluctuation, thus corresponding to an approximation of the full theory in [25].

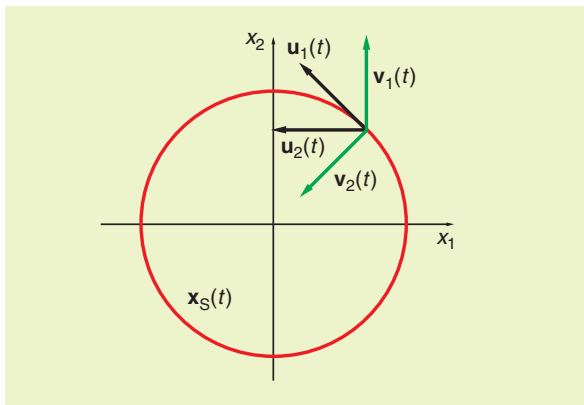


Figure 2. A representation of the limit cycle for the simple 2D oscillator (15), along with the direct and adjoint Floquet eigenvectors (shown here for $t = \pi/8$).

Finally, we remark that a careful treatment of the amplitude-noise elimination leads to the presence of higher-order terms in the phase-noise equation (see [15] and [39] and the references therein), which also influences the noiseless oscillation frequency.

A Simple 2D Example

As an example, we consider an extremely simple autonomous system, the 2D oscillator proposed in [40], written here in Cartesian coordinates:

$$\dot{x}_1 = x_1 - x_2 - (x_1 + x_2)\sqrt{x_1^2 + x_2^2} + \epsilon\xi_1 \quad (15a)$$

$$\dot{x}_2 = x_1 + x_2 + (x_1 - x_2)\sqrt{x_1^2 + x_2^2} + \epsilon\xi_2, \quad (15b)$$

where ϵ is a parameter introduced to modulate the magnitude of the unit white Gaussian noise sources ξ (in other words, we set the colored noise sources to zero). The WP is defined by the solution of (15) for $\epsilon = 0$:

$$\mathbf{x}_S(t) = \begin{bmatrix} x_{S1}(t) \\ x_{S2}(t) \end{bmatrix} = \begin{bmatrix} \cos(2t) \\ \sin(2t) \end{bmatrix}. \quad (16)$$

This very simple example allows us to evaluate analytically the FEs and eigenvectors. The structural FE $\mu_1 = 0$ is characterized by the direct eigenvector $\mathbf{u}_1(t)$ and by the PPV $\mathbf{v}_1(t)$,

$$\mathbf{u}_1(t) = \begin{bmatrix} -\sin(2t) \\ \cos(2t) \end{bmatrix}, \quad \mathbf{v}_1(t) = \begin{bmatrix} \cos(2t) - \sin(2t) \\ \cos(2t) + \sin(2t) \end{bmatrix}, \quad (17)$$

while for the second FE we find $\mu_2 = -1$ and

$$\mathbf{u}_2(t) = \frac{1}{2} \begin{bmatrix} -\cos(2t) - \sin(2t) \\ \cos(2t) - \sin(2t) \end{bmatrix}, \quad \mathbf{v}_2(t) = 2 \begin{bmatrix} -\cos(2t) \\ -\sin(2t) \end{bmatrix}. \quad (18)$$

For both eigenspaces, we have chosen to normalize to one the direct eigenvector, while for the adjoint $\mathbf{v}(t)$ the biorthogonality condition $\mathbf{u}_j^\dagger(t)\mathbf{v}_j(t) = 1$ was imposed. The four Floquet eigenvectors are shown in Figure 2. Notice that \mathbf{u}_1 and \mathbf{u}_2 are not orthogonal (though linearly independent) and neither are the PPV and \mathbf{v}_2 . On the other hand, the couples $(\mathbf{u}_1, \mathbf{v}_2)$ and $(\mathbf{u}_2, \mathbf{v}_1)$ are orthogonal.

Therefore, the correct time perturbation S-ODE (7) reads

$$\frac{d\alpha}{dt} = [\cos(2(t + \alpha(t))) - \sin(2(t + \alpha(t)))]\epsilon\xi_1(t) + [\cos(2(t + \alpha(t))) + \sin(2(t + \alpha(t)))]\epsilon\xi_2(t), \quad (19)$$

both for the rigorous theory in [6] and for the numerical ISF [32], while the approximated theory in [30] (and the original implementation of [32] with the numerical ISF) culminate in solving (14):

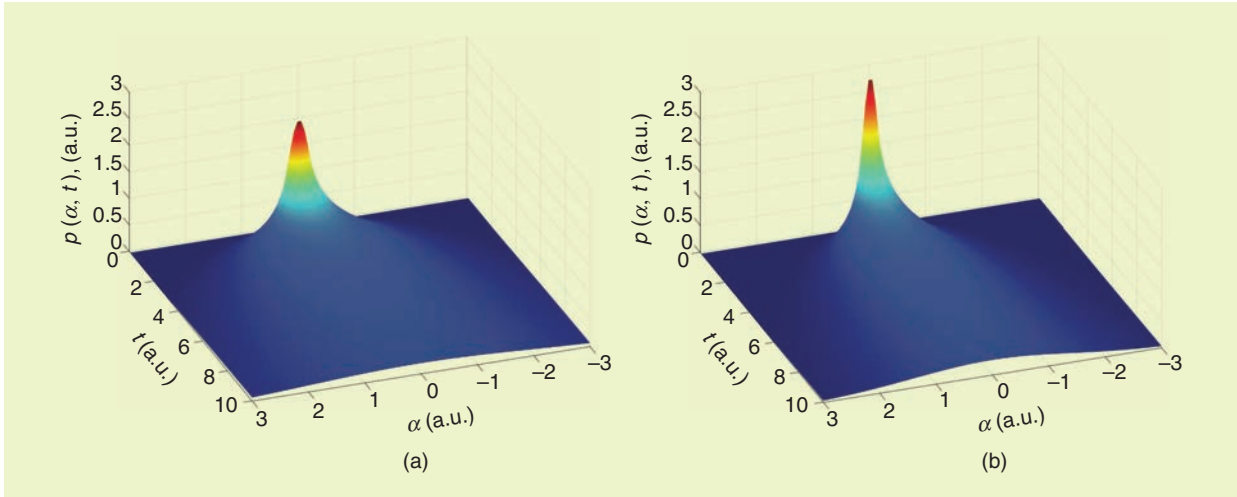


Figure 3. A representation of the probability density function $p(\alpha, t)$ for the oscillator (15) according (a) to the noise model in (19) and (20) and (b) to the closed-form ISF (21). In both cases, $\epsilon^2 = 0.2$ was assumed. a.u.: arbitrary units.

$$\frac{d\alpha}{dt} = [\cos(2t) - \sin(2t)]\epsilon\xi_1(t) + [\cos(2t) + \sin(2t)]\epsilon\xi_2(t). \quad (20)$$

Finally, the use of the closed-form ISF leads to the Langevin equation

$$\frac{d\alpha}{dt} = -\sin(2t)\epsilon\xi_1(t) + \cos(2t)\epsilon\xi_2(t). \quad (21)$$

The classical approach to studying S-ODEs, such as the previous time-perturbation equations, amounts to converting them into the corresponding Fokker–Planck equation [41], which defines the evolution of the probability density function $p(\alpha, t)$ for process $\alpha(t)$, the advantage being that such an equation is entirely within the standard functions domain (i.e., no stochastic processes are involved). The derivation of the Fokker–Planck equation equivalent to (19), (20), and (21) leads to the same diffusion-type equation:

$$\frac{\partial p}{\partial t} = D \frac{\partial^2 p}{\partial \alpha^2}, \quad (22)$$

where, however, $D = \epsilon^2$ for (19) and (20), while $D = \epsilon^2/2$ for (21). This very simple behavior is due to the extreme symmetry of system (15): as clearly visible in (17) and (18), the components of the Floquet vectors exhibit a constant phase shift as a consequence of the rotational invariance of (15). The same argument also justifies the unexpected equivalence of the two approaches from [6] and [30], which is clearly peculiar to this specific case.

The solution of (22) is a Gaussian random process,

$$p(\alpha, t) = \frac{1}{\sqrt{4\pi Dt}} e^{-\frac{\alpha^2}{4Dt}}, \quad (23)$$

yielding a variance for the time perturbation equal to $\sigma^2(t) = 2Dt$ (linearly increasing with time, as expected). Therefore, the approaches (19) and (20) are characterized by a phase noise $\sigma^2(t) = 2\epsilon^2 t$, while the closed-form ISF model (21) leads to a Gaussian process with variance $\sigma^2(t) = \epsilon^2 t$, i.e., half of the correct result. A comparison of the models is shown in Figure 3.

Conclusions

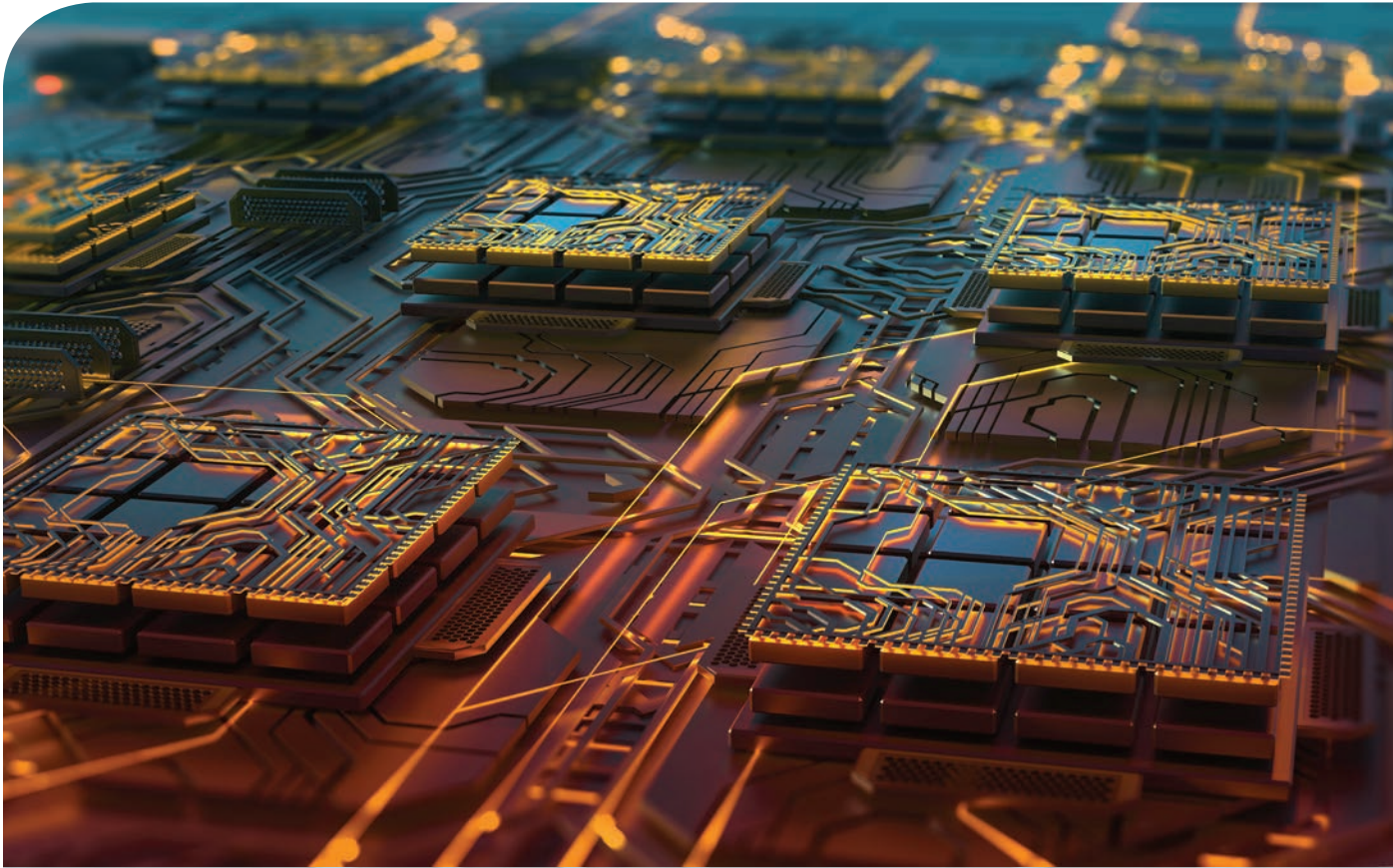
We have reviewed the available approaches to oscillator noise analysis currently implemented in modern EDA tools for low-noise oscillator design. Starting from the common ground of Floquet analysis for the linearized system obtained as a result of the perturbation of the autonomous system equations around the noiseless WP, the approaches are presented in a unified way. They are then discussed with the aim of pointing out the common elements and the major differences.

References

- [1] M. A. Garstens, "Noise in nonlinear oscillators," *J. App. Phys.*, vol. 28, no. 3, pp. 352–356, Mar. 1957. doi: 10.1063/1.1722745.
- [2] W. A. Edson, "Noise in oscillators," *Proc. IRE*, vol. 48, no. 8, pp. 1454–1466, 1960. doi: 10.1109/JRPROC.1960.287573.
- [3] E. Hafner, "The effects of noise in oscillators," *Proc. IEEE*, vol. 54, no. 2, p. 179, 1966. doi: 10.1109/PROC.1966.4631.
- [4] M. Lax, "Classical noise V. Noise in self-sustained oscillators," *Phys. Rev.*, vol. 160, no. 2, pp. 290–307, 1967. doi: 10.1103/PhysRev.160.290.
- [5] E. Pankratz and E. Sánchez-Sinencio, "Survey of integrated-circuit-oscillator phase-noise analysis," *Int. J. Circuit Theory Appl.*, vol. 42, no. 9, pp. 871–938, Sept. 2014. doi: 10.1002/cta.1890.
- [6] A. Demir, A. Mehrotra, and J. Roychowdhury, "Phase noise in oscillators: A unifying theory and numerical methods for characterization," *IEEE Trans. Circuits Syst. I, Fundam. Theory Appl.*, vol. 47, no. 5, pp. 655–674, May 2000. doi: 10.1109/81.847872.
- [7] A. Demir, "Phase noise and timing jitter in oscillators with colored-noise sources," *IEEE Trans. Circuits Syst. I, Fundam. Theory Appl.*, vol. 49, no. 12, pp. 1782–1791, Dec. 2002. doi: 10.1109/TCSI.2002.805707.

- [8] D. Leeson, "A simple model of feedback oscillator noise spectrum," *Proc. IEEE*, vol. 54, no. 2, pp. 329–330, 1966. doi: 10.1109/PROC.1966.4682.
- [9] J.-C. Nallatamby, M. Prigent, M. Camiade, and J. Obregon, "Phase noise in oscillators – Leeson formula revisited," *IEEE Trans. Microw. Theory Tech.*, vol. 51, no. 4, pp. 1386–1394, Apr. 2003. doi: 10.1109/TMTT.2003.809187.
- [10] K. Kundert, A. Sangiovanni-Vincentelli, and J. White, K. Kundert, A. Sangiovanni-Vincentelli, and J. White, Eds., *Steady-State Methods for Simulating Analog and Microwave Circuits*, Boston: Kluwer, 1990.
- [11] A. Demir, "Floquet theory and non-linear perturbation analysis for oscillators with differential-algebraic equations," *Int. J. Circuit Theory Appl.*, vol. 28, no. 2, pp. 163–185, 2000. doi: 10.1002/(SICI)1097-007X(200003/04)28:2<163::AID-CTA101>3.0.CO;2-K.
- [12] F. Bizzarri, A. Brambilla, and G. S. Gajani, "Steady state computation and noise analysis of analog mixed signal circuits," *IEEE Trans. Circuits Syst. I, Reg. Papers*, vol. 59, no. 3, pp. 541–554, Mar. 2012. doi: 10.1109/TCSI.2011.2167273.
- [13] F. Bizzarri, A. Brambilla, and G. S. Gajani, "Extension of the variational equation to analog/digital circuits: Numerical and experimental validation," *Int. J. Circuit Theory Appl.*, vol. 41, no. 7, pp. 743–752, Oct. 2012. doi: 10.1002/cta.1864.
- [14] D. K. Agrawal, F. Bizzarri, A. Brambilla, and A. A. Seshia, "Numerical verification of an analytical model for phase noise in MEMS oscillators," *IEEE Trans. Ultrason., Ferroelect., Freq. Control*, vol. 63, no. 8, pp. 1204–1207, Aug. 2016. doi: 10.1109/TUFFC.2016.2575364.
- [15] F. L. Traversa, M. Bonnin, F. Corinto, and F. Bonani, "Noise in oscillators: A review of state space decomposition approaches," *J. Comput. Electron.*, vol. 14, no. 1, pp. 51–61, 2015. doi: 10.1007/s10825-014-0651-3.
- [16] C. Gardiner, *Handbook of Stochastic Methods for Physics, Chemistry and the Natural Sciences* (Springer series in Synergetics), 3rd ed., Berlin: Springer-Verlag, 2004.
- [17] J. Guckenheimer, "Isochrons and phaseless sets," *J. Math. Biol.*, vol. 1, no. 3, pp. 259–273, Sept. 1975. doi: 10.1007/BF01273747.
- [18] T. Djuurhuus, V. Krozer, J. Vidkjaer, and T. Johansen, "Oscillator phase noise: A geometrical approach," *IEEE Trans. Circuits Syst. I, Reg. Papers*, vol. 56, no. 7, pp. 1373–1382, July 2009. doi: 10.1109/TCSI.2008.2006211.
- [19] O. Suvak and A. Demir, "On phase models for oscillators," *IEEE Trans. Comput.-Aided Design Integr. Circuits Syst.*, vol. 30, no. 7, pp. 972–985, July 2011. doi: 10.1109/TCAD.2011.2113630.
- [20] K. Kundert, "Introduction to RF simulation and its application," *IEEE J. Solid-State Circuits*, vol. 34, no. 9, pp. 1298–1319, Sept. 1999. doi: 10.1109/4.782091.
- [21] A. Winfree, *The Geometry of Biological Time*, 2nd ed. New York: Springer-Verlag, 2000.
- [22] K. Wedgwood, K. Lin, R. Thul, and S. Coomber, "Phase-amplitude descriptions of neural oscillator models," *J. Math. Neurosci.*, vol. 3, no. 1, p. 2, 2013. doi: 10.1186/2190-8567-3-2.
- [23] M. Bonnin, "Amplitude and phase dynamics of noisy oscillators," *Int. J. Circuit Theory Appl.*, vol. 45, no. 5, pp. 636–659, 2016. doi: 10.1002/cta.2246.
- [24] A. Hajimiri and T. Lee, *The Design of Low Noise Oscillators*. Dordrecht: Kluwer, 1999.
- [25] F. L. Traversa and F. Bonani, "Oscillator noise: A nonlinear perturbative theory including orbital fluctuations and phase-orbital correlation," *IEEE Trans. Circuits Syst. I, Reg. Papers*, vol. 58, no. 10, pp. 2485–2497, Oct. 2011. doi: 10.1109/TCSI.2011.2123531.
- [26] A. Suárez, *Analysis and Design of Autonomous Microwave Circuits*. Hoboken: Wiley, 2009.
- [27] K. Kurokawa, "Some basic characteristics of broadband negative resistance oscillators," *Bell Syst. Tech. J.*, vol. 48, no. 6, pp. 1937–1955, 1969. doi: 10.1002/j.1538-7305.1969.tb01158.x.
- [28] V. Rizzoli, F. Mastroi, and D. Masotti, "General noise analysis of nonlinear microwave circuits by the piecewise harmonic balance technique," *IEEE Trans. Microw. Theory Tech.*, vol. 42, no. 5, pp. 807–819, May 1994. doi: 10.1109/22.293529.
- [29] F. X. Kaertner, "Determination of the correlation spectrum of oscillators with low noise," *IEEE Trans. Microw. Theory Tech.*, vol. 37, no. 1, pp. 90–101, Jan. 1989. doi: 10.1109/22.20024.
- [30] F. X. Kaertner, "Analysis of white and $f^{-\alpha}$ noise in oscillators," *Int. J. Circuit Theory Appl.*, vol. 18, pp. 485–519, 1990. doi: 10.1002/cta.4490180505.
- [31] F. L. Traversa and F. Bonani, "Asymptotic stochastic characterization of phase and amplitude noise in free-running oscillators," *Fluctuation Noise Lett.*, vol. 10, no. 2, pp. 207–221, June 2011. doi: 10.1142/S021947751100048X.
- [32] A. Hajimiri and T. Lee, "A general theory of phase noise in electrical oscillators," *IEEE J. Solid-State Circuits*, vol. 33, no. 2, pp. 179–194, Feb. 1998. doi: 10.1109/4.658619.
- [33] A. Suarez, S. Sancho, S. V. Hoeye, and J. Portilla, "Analytical comparison between time- and frequency-domain techniques for phase-noise analysis," *IEEE Trans. Microw. Theory Techn.*, vol. 50, no. 10, pp. 2353–2361, Oct. 2002. doi: 10.1109/TMTT.2002.803457.
- [34] S. Srivastava and J. Roychowdhury, "Analytical equations for nonlinear phase errors and jitter in ring oscillators," *IEEE Trans. Circuits Syst. I, Reg. Papers*, vol. 54, no. 10, pp. 2321–2329, Oct. 2007. doi: 10.1109/TCSI.2007.905637.
- [35] M. Bonnin, F. Corinto, and M. Gilli, "Phase noise, and phase models: Recent developments, new insights and open problems," *Nonlinear Theory Its Appl., IEICE*, vol. 5, no. 3, pp. 365–378, 2014.
- [36] F. L. Traversa and F. Bonani, "Frequency domain evaluation of the adjoint Floquet eigenvectors for oscillator noise characterization," *IET Circuits Devices Syst.*, vol. 5, no. 1, pp. 46–51, 2011. doi: 10.1049/iet-cds.2010.0138.
- [37] F. L. Traversa and F. Bonani, "Improved harmonic balance implementation of Floquet analysis for nonlinear circuit simulation," *AEU - Int. J. Electron. Commun.*, vol. 66, no. 5, pp. 357–363, May 2012. doi: 10.1016/j.aeue.2011.09.002.
- [38] F. L. Traversa and F. Bonani, "Selective determination of Floquet quantities for the efficient assessment of limit cycle stability and of oscillator noise," *IEEE Trans. Comput.-Aided Design Integr. Circuits Syst.*, vol. 32, no. 2, pp. 313–317, Feb. 2013. doi: 10.1109/TCAD.2012.2214480.
- [39] M. Bonnin and F. Corinto, "Phase noise and noise induced frequency shift in stochastic nonlinear oscillators," *IEEE Trans. Circuits Syst. I, Reg. Papers*, vol. 60, no. 8, pp. 2104–2115, Aug. 2013. doi: 10.1109/TCSI.2013.2239131.
- [40] G. Coram, "A simple 2-D oscillator to determine the correct decomposition of perturbations into amplitude and phase noise," *IEEE Trans. Circuits Syst. I, Fundam. Theory Appl.*, vol. 48, no. 7, pp. 896–898, July 2001. doi: 10.1109/81.933331.
- [41] H. Risken, *The Fokker-Planck Equation. Methods of Solution and Applications*, 2nd ed., Berlin: Springer-Verlag, 1986.
- [42] M. Farkas, *Periodic Motions*. New York: Springer-Verlag, 1994.
- [43] F. Cappelluti, F. L. Traversa, F. Bonani, S. Donati Guerrieri, and G. Ghione, "Large-signal stability of symmetric multi-branch power amplifiers exploiting Floquet analysis," *IEEE Trans. Microw. Theory Tech.*, vol. 61, no. 4, pp. 1580–1587, Apr. 2013. doi: 10.1109/TMTT.2013.2248017.
- [44] A. Demir and J. Roychowdhury, "A reliable and efficient procedure for oscillator PPV computation, with phase noise macro-modeling applications," *IEEE Trans. Comput.-Aided Design Integr. Circuits Syst.*, vol. 22, no. 2, pp. 188–197, Feb. 2003. doi: 10.1109/TCAD.2002.806599.
- [45] F. L. Traversa, F. Bonani, and S. Donati Guerrieri, "A frequency-domain approach to the analysis of stability and bifurcations in nonlinear systems described by differential-algebraic equations," *Int. J. Circuit Theory Appl.*, vol. 36, no. 4, pp. 421–439, 2008. doi: 10.1002/cta.440.
- [46] A. Brambilla, G. Gruosso, and G. Storti Gajani, "Determination of Floquet exponents for small-signal analysis of nonlinear periodic circuits," *IEEE Trans. Comput.-Aided Design Integr. Circuits Syst.*, vol. 28, no. 3, pp. 447–451, Mar. 2009. doi: 10.1109/TCAD.2009.2013285.





©SHUTTERSTOCK.COM/YURCHANKA SIARHEI

A Brief Walk Through Noise

Luciano Boglione

As the title suggests, I am inviting the reader to take a brief walk with me and discuss the interesting subject of microwave noise. My goal is to provide some highlights on this subject, from its basic pillars based on physics to the latest engineering publications. A solid understanding of noise cannot but stand on the shoulders of

the physicists who have continually been looking at overcoming the limitations of any theoretical model to explain nature. Names like Brown, Einstein, and Nyquist must be mentioned before focusing on the applications of those ideas, which started more than 100 years ago: How do you describe noise when considering microwave circuits? How do you characterize noisy microwave circuits nowadays?

Luciano Boglione (l.boglione@ieee.org) is with the U.S. Naval Research Laboratory, Washington, DC, 20375, USA.

Digital Object Identifier 10.1109/MMM.2021.3069536

Date of current version: 1 June 2021

The answers in this article will not describe minute mathematical details. Like any discussions during a stroll, the examples I offer may bias the conversation toward familiar grounds. Indeed, I will tell you about two interesting applications I have been working on: leveraging the size of a particular class of devices to determine their noise performance and characterizing noisy networks with $N \geq 2$ ports because differential circuits fall into this class.

It should not come as a surprise, then, that this article is neither a tutorial nor a technical article in their respective strict senses. The reader will not learn the details that a graduate class would teach but will learn enough to have a better idea of the subject and hopefully enjoy the time taken for this walk. Despite the obvious bias and limitations, I hope that this article will also inspire the reader to learn more about noise or even start focused research on the subject. With this disclaimer in mind, it's time to take our walk.

Physics Background

Noise was a subject of research well before the first man-made electromagnetic waves traveled across the Atlantic [1]. The description of random motion is attributed to Robert Brown [2]. A Scottish botanist with a keen interest in using microscopes, his observations from a particular plant (Figure 1) published in 1828 became famous:

This plant was *Clarkia pulchella*, of which the grains of pollen, taken from anther full grown, but before bursting, were filled with particles or granules of unusually large size, varying from nearly 1/4000th to about 1/5000th of an inch in length, and of a figure between cylindrical and oblong, perhaps slightly flattened, and having rounded and equal extremities. While examining the form of these particles immersed in water, I observed many of them very evidently in motion; their motion consisting not only of a change of place in the fluid, manifested by alterations in



Figure 1. A *Clarkia pulchella*, the plant in which Robert Brown observed random motion of particles. (Source: https://species.wikimedia.org/wiki/Clarkia_pulchella.)

their relative positions, but also not infrequently of a change of form in the particle itself; a contraction or curvature taking place repeatedly about the middle of one side, accompanied by a corresponding swelling or convexity on the opposite side of the particle. In a few instances the particle was seen to turn on its longer axis. These motions were such as to satisfy me, after frequently repeated observation, that they arose neither from currents in the fluid, nor from its gradual evaporation, but belonged to the particle itself.

Scientists came to realize that Brownian motion is evidence of the existence of atoms, a concept that was beginning to be accepted by the physics community of the time. Brownian motion was eventually explained in stochastic terms by another soon-to-be-famous scientist, Albert Einstein [3].

The adoption of electrical communications at the dawn of the 20th century brought the issue of noise to the forefront of science and engineering, as it became obvious that signals are degraded as they travel from a transmitter to a receiver. Through the gift of scientific lenses and time travel, it is easy to say now that research in blackbody radiation during the early 1900s was essential to understanding noise [4].

A blackbody is defined as an idealized, perfectly opaque material that absorbs all of the incident radiation at all frequencies f , reflecting none [5]. Rayleigh and Jeans [6], [7] could determine that the power density exchanged by a blackbody at temperature T (K) in unit bandwidth B of 1 Hz around its center frequency f_0 is

$$P^{\text{RJ}} = kT \text{ (W)}(\text{Hz})^{-1}. \quad (1)$$

This familiar expression carries two important consequences:

- It fits measured data well as long as the frequency under consideration is well below the optical region at room temperature.
- The total energy in a bandwidth B goes to $+\infty$ as the bandwidth increases.

The second issue came to be known as the ultraviolet catastrophe because (1) fails as frequencies approach the optical domain. Indeed, (1) just did not make sense. Something was obviously incorrect in the scientific understanding of the problem.

Max Planck proposed a powerful answer in 1901 [8] to go beyond the ultraviolet catastrophe and bring the total energy over $B \rightarrow +\infty$ to a finite value by making a crucial assumption before carrying out the same sequence of logical steps that yields (1). Planck assumed that the possible mode energies are not continuously distributed; rather, they are quantized and must satisfy a new constraint $E = nhf$, where n is a number of photons, or discrete particles of light, each having energy

hf . With that unconventional idea, the spectral power a blackbody emits turns out to be

$$P^{\text{PK}} = kT \cdot \frac{\frac{hf}{kT}}{\exp\left(\frac{hf}{kT}\right) - 1} \text{ (W) (Hz)}^{-1}, \quad (2)$$

where the additional dimensionless fraction is called the *Planck factor*. The Planck factor is numerically very close to 1 as long as the condition $hf \ll kT$ is satisfied—which is indeed the case up to $f = kT/h \approx 6$ THz at $T = 290$ K. In other words, $P^{\text{PK}} \approx P^{\text{RJ}}$ for all (microwave) intents and purposes, and considerable error occurs only at very high (optical) frequencies or at very low temperatures of operation [9].

Blackbody radiation is important because it is needed when dealing with cosmic background radiation, astronomy, and other fascinating subjects. However, its importance goes well beyond a list of scientific topics. Planck's hf assumption at the core of (2) draws the line between classical and quantum mechanics. While providing a tool to describe nature's behavior, where every previous tool had failed, Planck took the first step into a brand new way of interpreting nature.

But, wait a minute. What was the logical basis or the inspiration for Planck to make the very unusual hf assumption? To my limited knowledge, nobody knows for sure. A strike of genius? A lucky guess? Who knows. What we know is that it works. And very well. At the end of the day, research is indeed 1% inspiration and 99% perspiration.

Noise Formalism

Another piece of the noise puzzle must be introduced before talking about noise and techniques for its measurement: How is noise handled when analyzing an electrical circuit? The basic answer came from Nyquist in 1928 [11], when he demonstrated, with arguments very similar to those used by Rayleigh, Jeans, and Planck, that the noise spectral power a resistor can exchange under thermodynamic equilibrium is kT . The result is important because it provides the link between blackbody radiation and a resistor. As Figure 2 illustrates, a resistor can effectively model a blackbody by associating its temperature to an equivalent value T_{eq} . Furthermore, the spectral power associated with a blackbody implies an exchange of power between the blackbody and the external environment. The power exchanged is the maximum power the body can exchange—in equivalent words, it is the available power associated with the equivalent resistor at the ambient temperature it happens to be.

The available power is a well-defined concept in circuit theory. If a blackbody at temperature T can be modeled by a resistor R at that temperature,

then a Thevenin or Norton equivalent circuit can be defined, respectively, through the very definition of available power,

$$kBT = \begin{cases} \frac{\overline{ee^{\dagger}}}{4R_{\text{TH}}} \rightarrow V_{\text{TH}} = \sqrt{\overline{ee^{\dagger}}} = \sqrt{4kTB R_{\text{TH}}} \\ \frac{\overline{ii^{\dagger}}}{4G_{\text{N}}} \rightarrow I_{\text{N}} = \sqrt{\overline{ii^{\dagger}}} = \sqrt{4kTB G_{\text{N}}} \end{cases}, \quad (3)$$

where $R_{\text{TH}} = \Re\{Z_{\text{TH}}\}$ and $G_{\text{N}} = \Re\{Y_{\text{N}}\}$.

The doors to an analytical description of noise in electrical circuits are now open because any one-port noisy network can be described by a Thevenin or Norton equivalent circuit, as depicted in Figure 2. Its source represents either a noise voltage or current generator that yields the equivalent available power kT to a conjugate match, as described by (3).

Experience tells us that no dc component is generated by a noisy resistor because, on average, no current or voltage is detected at the source nodes. The root mean square value of a random process is often shown as $\overline{ee^{\dagger}}$ or other equivalent forms that imply an average of a random quantity e . When the noise power spectrum is constant over a frequency, as in (3), the noise is called *white*. Other types of noise exist [12] that may require a dc current to be detectable, such as in the case of shot noise. Whatever the type, the basic concepts outlined previously to analyze a noisy circuit in a small bandwidth B still hold.

The extension to linear networks with $N \geq 2$ ports is straightforward once it becomes clear that a multitude of possible combinations between input and output signals exists [13]–[16]. We call the relationship between input and output signals a representation of the network. Let's focus our thoughts on a two-port

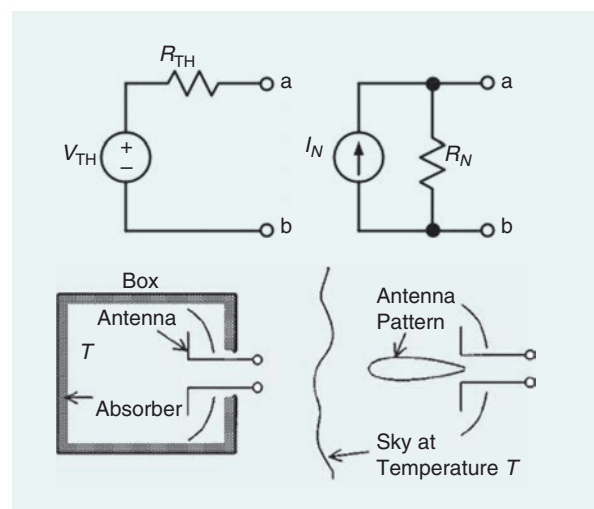


Figure 2. The equivalent behavior between a resistance, an antenna enclosed in a blackbody, and an antenna observing the sky, all at the same temperature T [10].

The question of transforming a set of noise parameters in a given representation to another one can be reduced to a simple problem involving linear transformations.

network, and let's use matrix algebra since linearity is assumed.

For any choice of input \mathbf{x} and output \mathbf{y} signals, a small-signal matrix \mathbf{M} will link the signals. Additionally, experience tells us that the output vector will also carry a noise signal \mathbf{n} and its associated noise power when no input signal is entering the network, represented as

$$\mathbf{y} = \mathbf{M}\mathbf{x} + \mathbf{n}. \quad (4)$$

The noise power available by the network will be described by

$$\overline{\mathbf{nn}^\dagger} = \mathbf{C}_n = \begin{bmatrix} C_{11} & C_{12} \\ C_{21} & C_{22} \end{bmatrix}, \quad (5)$$

where $C_{12} = C_{21}^\dagger$. Indeed, this matrix is Hermitian and nonnegative definite (i.e., its determinant is such that $\det\{\mathbf{C}_n\} \geq 0$). The diagonal elements are real numbers and are associated with the noise power carried by the output signals \mathbf{y} . For instance, in an impedance Z representation, the output signals are the voltages at the two ports, as demonstrated in a particular instance of a two-port network in Figure 3. Hence, $C_{11} = \overline{v_{n1}v_{n1}^\dagger}$ and $C_{22} = \overline{v_{n2}v_{n2}^\dagger}$.

The off-diagonal elements in (5) are complex numbers and conjugates of each other. They are associated with the correlation between the two equivalent sources represented by the noise vector \mathbf{n} in (4). For example, if the network had only one physical noise source internally, as in the case of Figure 3, the observable output noise signal observed at the input and output port may not be statistically independent—in this case, the input and output noise sources v_{n1} and v_{n2} are fully correlated with $C_{12} = R$, the value of the

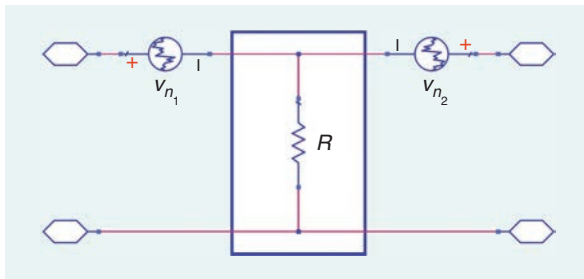


Figure 3. A noisy resistor as a two-port network in impedance Z representation.

resistor itself. In general, the output noise signals are partially correlated, and the off-diagonal elements carry the correlation information. The actual value of the correlation parameter ρ is calculated from (5) as $\rho = C_{12}/\sqrt{|C_{11}||C_{22}|}$. In the case of Figure 3, $\rho = +1$.

We call the numbers constituting the complex correlation matrix (5) *noise parameters*. In the case of a two-port network, there are four real numbers in (5), namely, C_{11} , C_{22} , $\Re\{C_{12}\}$, and $\Im\{C_{12}\}$. Data sheets often report the noise parameters in terms of the set F_{\min} , R_n , $|\Gamma_{S_{\text{opt}}}|$, and $\angle\Gamma_{S_{\text{opt}}}$, which is an equivalent set of noise parameters [17].

The question of transforming a set of noise parameters in a given representation to another one can be reduced to a simple problem involving linear transformations. The transformation tables found in books such as [17] or [18] can be easily expressed by a matrix-based approach that provides the same information in a very concise form. The benefit of this approach is the fact that it can be easily worked out by hand calculation and implemented in commercial software that is readily available.

Indeed, it is relatively straightforward to link two representations of the same network,

$$\mathbf{y}_{\text{old}} = \mathbf{M}_{\text{old}} \mathbf{x}_{\text{old}} + \mathbf{n}_{\text{old}} \quad (6)$$

and

$$\mathbf{y}_{\text{new}} = \mathbf{M}_{\text{new}} \mathbf{x}_{\text{new}} + \mathbf{n}_{\text{new}}, \quad (7)$$

with a linear transformation matrix $\mathbf{C}_{\text{old} \rightarrow \text{new}}$ [19], [20] such that

$$\begin{aligned} \mathbf{y}_{\text{new}} &= \mathbf{C}_{\text{old} \rightarrow \text{new}} \mathbf{y}_{\text{old}} \\ &= \mathbf{C}_{\text{old} \rightarrow \text{new}} \mathbf{x}_{\text{old}} + \mathbf{C}_{\text{old} \rightarrow \text{new}} \mathbf{n}_{\text{old}}. \end{aligned} \quad (8)$$

By considering (5) and applying standard matrix algebraic techniques,

$$\overline{\mathbf{n}_{\text{new}}\mathbf{n}_{\text{new}}^\dagger} = \mathbf{C}_{\text{old} \rightarrow \text{new}} \overline{\mathbf{n}_{\text{old}}\mathbf{n}_{\text{old}}^\dagger} \mathbf{C}_{\text{old} \rightarrow \text{new}}^\dagger \quad (9)$$

is obtained. Note that we have dropped any reference to a two-port network as much as possible while walking through the transformation procedure. Indeed, the reader should realize that the noise formalism described previously applies to any N -port networks, and we will still call noise parameters the elements of the $N \times N$ correlation matrix \mathbf{C}_n .

What Makes a Good Receiver?

Before talking about noise measurement techniques, we need to understand what can be measured. The main goal of any RF circuit, broadly speaking, is to support the transmission and recovery of information from a transmitter to a receiver. The information is appropriately carried by a signal $s(t)$ through a channel—be that a cable,

an optical fiber, or free space. The receiver, however, will also pick up an additional unwanted signal $n(t)$ that shows up as crackling noise out of your low-tech radio receiver when no signal of interest $s(t)$ is present.

We will call the unwanted signal “noise” and assume that the receiver processes both $s(t)$ and $n(t)$ linearly because the signals, either alone or combined, don’t push the receiver into saturation. The nature of the signal $n(t)$ will determine the characteristic of this noise. In this context, we are a little fuzzy, and the implication is that $n(t)$ is effectively white noise rather than a powerful interfering signal booming through your speakers.

The ratio of the power S associated with signal $s(t)$ with the power N associated with the noise $n(t)$ is the signal-to-noise ratio, typically referred to as SNR. The higher this ratio, the smaller the noise power compared to the signal of interest’s power. In other words, an overwhelming strength of $s(t)$ compared to the noise strength will make its recovery by the receiver easier.

The issue is that every subcomponent of the receiver, such as the amplifiers, mixers, and filters, will also introduce their own noise and conspire to make the recovery of $s(t)$ more challenging. Why? Because the SNR found at the output of each component is reduced by the amount of noise power that the component is delivering to the next stage: the higher the noise, the lower the SNR and the more challenging the recovery of the information that the signal is carrying. This is particularly true when the signal of interest has just been detected by the antenna and input into the first stage of the receiver chain, like the one illustrated in Figure 4. Indeed, any noise added by the first couple of stages of the receiver chain may significantly affect the output SNR. Once the signal has reached the following stages, the noise added should be essentially negligible compared to the signal of interest $s(t)$.

Maintaining a sufficiently large SNR is a key feature of any receiver and a fundamental challenge for RF designers at both the system and circuit levels. What are the options to accomplish this goal? One can 1) amplify the input signal, 2) make sure that each subcomponent introduces as little noise as possible, or 3) do a combination of the two approaches. Of course, the devil is in the details.

Assume that the input SNR_i delivered by the antenna into the receiver is known. The first component after a receiver antenna should be a low-noise amplifier (LNA), as exemplified in Figure 4. Both the input signal S and noise N powers feeding the LNA will be amplified the same way—indeed, the incoming noise is usually some orders

of magnitude smaller than the signal, so the tradeoff described here is acceptable. If the LNA was noiseless, SNR_o at the output would have the same value as SNR_i at the input. Unfortunately, the LNA introduces its own noise power to the receiver, which effectively increases the output noise N_o power level at its output port and reduces SNR_o.

Indeed, for any linear component, it is true that SNR_o ≤ SNR_i, where the equality holds only in the (ideal) case of lossless components. The ratio of input to output SNR is called *noise factor*—or *noise figure* when expressed in decibels,

$$F = \frac{SNR_i}{SNR_o} \geq 1. \quad (10)$$

The closer to one the noise figure, the better the receiver. Recalling that available powers are always used when dealing with noise, (10) can be rewritten as

$$F = \frac{S_i/N_i}{S_o/N_o} = \frac{N_o}{G_{av}N_i}, \quad (11)$$

where $G_{av} = S_o/S_i$ is the available gain of the linear network—the LNA in this case. Friis [21] showed that the first element of a chain of linear circuits can set the noise performance of the entire chain if it also provides (sufficient) gain,

$$F_{tot} = F_A + \frac{F_B - 1}{G_A} + \frac{F_C - 1}{G_A G_B} + \dots, \quad (12)$$

where the subscript A refers to the first component in the chain, B to second component, C to the third component, and so on. For example, A is the LNA, B is the attenuator, and C is the mixer in Figure 4. G_A and G_B are the available gains of the first two networks, and all quantities are dimensionless numbers, not decibels.

Note that, if G_A is large, then $F_{tot} \approx F_A$, and the first stage effectively sets the overall noise figure of the receiver. On the other hand, if the first stage of the receiver is a passive element, for example, a filter or a circulator, its noise factor is the inverse of its available gain (i.e., its loss $L = 1/G_{av} = F$) [22], [23], and the cascaded noise factor is $F_{tot} = F_A F_B$. In other words, the noise figure increases by the value of the network’s attenuation if a passive component is inserted first in the receiver chain.

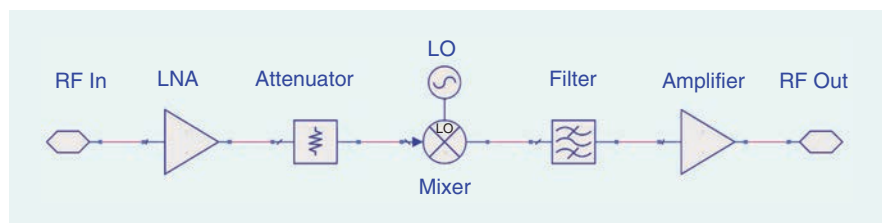


Figure 4. The receiver chain design: the LNA must be the first stage of the chain to achieve good noise performance. LO: local oscillator.

In the design of Figure 4, we needed the attenuator right after the amplifier for system performance reasons: not the ideal choice, perhaps, but life is full of compromises.

Measuring Microwave Noise

Noise Figure

A microwave noise figure meter measures the noise power of the device under test (DUT) over frequency and typically displays its noise figure. The instrument must control a noise source connected at the input of the DUT to deliver N_i and make the measurement and the proper calculations. An example of a modern noise figure meter is seen in Figure 5. At its core, it consists of a receiver tuned at frequency f_o that detects the noise power N_o delivered by the DUT within a known bandwidth B . The receiver makes use of (11) to calculate F from the measurement of N_o after de-embedding the noise contribution of the receiver itself with (12).

The source that injects the noise power N_i is modeled by (3) and equals kBT_o . Note that the input noise power depends on the ambient temperature T_o , which must be 290 K by definition for a correct determination of the DUT's noise figure [24]. In other words, some mathematical manipulations supported by the theory outlined here may be needed to present the correct noise figure value from the raw measurement data.

The available gain G_{av} of the DUT must be known to determine the noise figure correctly according to (11). The determination of G_{av} used to be a bottleneck for noise figure meters because a standard noise figure meter could determine only the transducer power gain G_T of a network with an imperfectly matched output port rather than its available power gain G_{av} [17]. The issue of a mismatched port is key when dealing with noise because, as noted previously, the noise power is defined as available power: the determination of G_{av} is just one way this issue manifests itself in the



Figure 5. A modern noise figure meter integrated as a personality of a vector network analyzer.

practical world. Clever solutions were demonstrated to determine G_{av} based solely on noise figure measurements [25], [26]. Nowadays, the noise figure measurement is just one of many integrated features of a vector network analyzer that make it possible to determine G_{av} through the measurement of the DUT's scattering parameters and some math [27], [28].

As mentioned, the measurement of the noise figure relies on a power measurement at the output of the DUT after all of the necessary calibrations. The instrument measures the noise power level N_o that is detected at the output of a linear DUT when a noise source is injecting a known amount of noise power N_i at the DUT's input port. The measured output power N_o consists of the two contributions referred to the DUT's input port,

$$N_o = G_{av} \cdot (N_i + N_{i,int}), \quad (13)$$

where 1) N_i is the available noise power that the DUT delivers to its output port when injected at its input port, and 2) $N_{i,int}$ is the available noise power that the DUT generates internally.

Note that (13) applies at the known frequency f_o , which can be swept to measure N_o over a range of frequencies. Expression (13) also shows that N_o is linearly dependent on N_i , which means that, for a known and fixed gain G_{av} at f_o , the output power N_o will intercept the horizontal axis at negative $N_{i,int}$ when plotting N_o versus N_i . Given that (1) linearly connects power and temperature, two values of N_i are sufficient to determine $N_{i,int}$: for each value of N_i corresponding to a hot and cold source at equivalent temperature $T_{i,h}$ and $T_{i,c}$, respectively, an output power measurement is executed to determine $T_{o,h} = N_{o,h}/kB$ and $T_{o,c} = N_{o,c}/kB$. Simple algebraic manipulations of (13) yield

$$T_{i,int} = \frac{T_{i,h} - T_{i,c} \cdot Y}{Y - 1}, \quad (14)$$

where $Y = T_{o,h}/T_{o,c}$ is the ratio of the measured output noise powers $N_{o,x}$ when the source $N_{i,x}$ is hot ($x = h$) and cold ($x = c$), respectively.

This procedure determines the equivalent noise temperature $T_{i,int}$ of the DUT and is called the *Y-factor measurement* [29]. It relies on two noise power measurements, each described by (13), and the calculation described by (14). Strictly speaking, the available gain of the DUT is not required in (14) because two points of the straight line described by (13) are used to determine $N_{i,int}$. If G_{av} is determined independently (through scattering parameters measurement, for example), then one power measurement is sufficient to determine $N_{i,int}$ with (13). This measurement approach is called a *cold-source technique* [28], as any unheated (i.e., "cold") termination at room temperature will do

the trick. The temperature $T_{i,int}$ in (14) is the equivalent noise temperature T_{eq} of the DUT because it describes the noise temperature of a source that would deliver the same noise power from the output port of the DUT if the DUT were noiseless.

A standard implementation of a noise source consists of a break-down diode that generates a known amount of power when turned on (Figure 6). Although the source presents an input impedance very close to $50\ \Omega$, an additional attenuator between the diode and DUT can improve the Y-factor measurement when the source is hot (diode on) or cold (diode off). The ability for the source to be hot and cold is described by the excessive noise ratio (ENR),

$$ENR = \frac{T_h - T_c}{T_o}. \quad (15)$$

The cold temperature T_c can be often assumed to be equal to $T_o = 290\text{ K}$ in a lab environment. The fact that temperatures in Kelvin are involved in noise power measurements makes relative errors less a concern. For instance, using $T_o = 300\text{ K}$ instead of $T_o = 290\text{ K}$ yields an error in N_i less than $3.5\% \approx 100 \cdot (300 - 290)/290$. Modern noise sources can download the ENR data directly to the noise figure meter via a cable connection.

The Noise Parameters

The noise figure is a straightforward measurement, but it will not provide the entire picture of the DUT's noise performance. For instance, F depends on the choice of source impedance because both the noise power and available gain in (11) are functions of the source impedance value. Typically, microwave equipment operates in a $50\text{-}\Omega$ system, and noise figures are measured with a $50\text{-}\Omega$ source impedance. In the absence of specific information, it is safe to assume that an F_{50} noise figure measurement has been made. On the other hand, the correlation matrix (5) stemming from the noise vector \mathbf{n} in (4) fully describes the total amount of noise power that the network can deliver from its ports independently of the port terminations.

The noise figure can be calculated if the correlation matrix is known. Researchers reported in [14] and [15] that

$$F(Z_S) = 1 + \frac{z_S^\dagger C_{DUT}^Z z_S}{4N_i R_S} \quad (16)$$

in a chain (transmission) representation, where $Z_S = R_S + jX_S$ is the source impedance and $z_S^\dagger = [1\ Z_S]$. Expansion of (16) in admittance representation yields the noise figure expression used by Lane [30],

$$F(Y_S) = F_{min} + \frac{R_n}{G_S} |Y_S - Y_{Sopt}|^2. \quad (17)$$

Lane cast (17) in terms of a linear expression in the four noise parameters, F_{min} , R_n , $G_{Sopt} = \Re\{Y_{Sopt}\}$, and

$B_{Sopt} = \Im\{Y_{Sopt}\}$, which he then determined by executing a least square approximation on $N \geq 4$ noise figure measurements executed for N corresponding values of the source admittance Y_S . This is the bare-bones description of the Lane method, which is clearly understandable from (16): C_{DUT} is a matrix of four unknowns, and z_S is the "knob" that can be varied to collect a number of measurements of noise figure F as a function of the source impedance. How do you set the value of Y_S ? In other words, what is required by the real world to implement the knob? The knob is implemented by inserting a microwave tuner between the noise source and the input port of the DUT. A desired Y_S is obtained by setting the tuner in the corresponding position at the measurement frequency.

The Lane procedure can determine the noise parameters of any linear network at the frequency of interest. However, its implementation comes with some unfortunate overhead. First of all, it requires a tuner in front of the DUT. In the microwave range, these tend to be bulky, as Figure 7 illustrates. The



Figure 6. Standard noise sources in the microwave range. The most recent offering (top) will carry the ENR information electronically and provide it to the instrument automatically via USB cable.

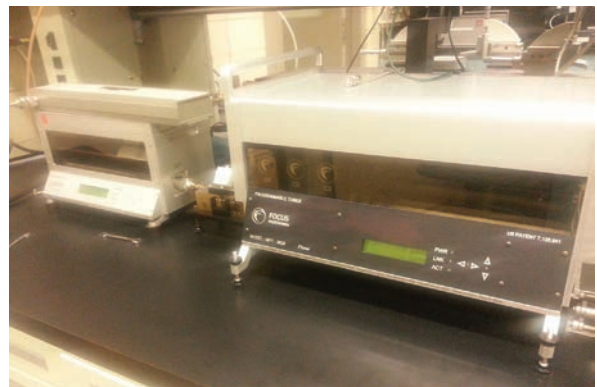


Figure 7. Commercially available tuners in the GHz range. The tuner in the foreground is a harmonic tuner as it can control the fundamental and one of its first two harmonics simultaneously.

tuner itself will also introduce its own noise into the signal chain, which must be de-embedded from the measurement.

The noise contribution is different for every position yielding the desired Y_S , which means that proper bookkeeping is required during measurement to de-embed the tuner's noise contribution from the measured noise power at each position of the tuner. Tuners are also relatively narrow band, confining the measurement to the tuner's frequency band of operation and requiring the use of multiple tuners to cover a broad frequency range. Considering that the noise parameters are coveted for active devices at the wafer level, the measurement setup and execution become quite an endeavor. If you have experienced this measurement, then you know; if you haven't, you have been warned.

On-Wafer Noise Parameter Measurement

Can the standard Lane procedure be simplified in some aspects to make it easier to implement? This is the question. A possible answer tailored for on-wafer active devices—the type of DUTs that circuit designers most benefit from by determining their noise parameters—has been found by giving a fresh look at (16): Is there another knob hidden in the expression that can keep Y_S constant (thereby removing the need for a tuner) while affecting the noise figure measurement? The answer, as you may suspect at this point, is indeed positive—yes, there is [32]–[34]. The hidden knob is the size of the transistor; for field-effect transistor (FET) devices, the size is the width of the gate finger, and bipolar transistors are sized in terms of the emitter area. Integrated circuit designers size the transistor to meet their specifications, so scalable models have been investigated and delivered to the designer community for a long time [35]. The question becomes: How is the

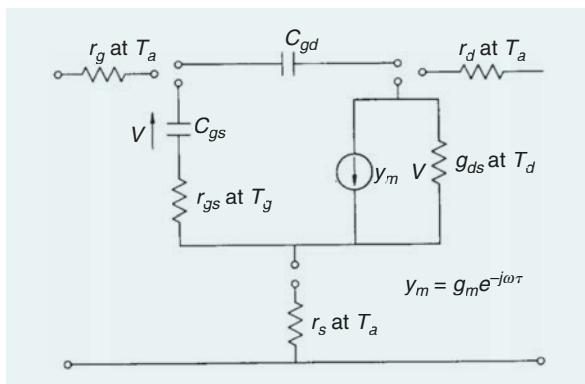


Figure 8. An intrinsic model with equivalent temperatures associated with lossy components as reported in [31, Figure 1]. T_a is the ambient temperature. Note that [31] makes use of lower-case letters for the model's noisy components.

noise performance of the device affected by its size? To answer this question, let's focus on FET devices.

A well-established device model has been described in [31], and it has been used for FETs extensively. The model is scalable [36], and the noise performance of the device at a fixed bias point is described by two noisy resistors, R_{gs} and R_{ds} , at equivalent temperatures T_{gs} and T_{ds} , respectively, that are located in the intrinsic part of the device sketched out in Figure 8. The remarkable feature of this model is that the noise sources associated with R_{gs} and R_{ds} have been proven experimentally over and over again to be uncorrelated. More specifically, the noise correlation matrix turns out to be

$$C_{DUT}^H = 4N_o \begin{bmatrix} t_{gs} \frac{r_{gs}}{W} & 0 \\ 0 & t_{ds} \frac{W}{r_{ds}} \end{bmatrix} \quad (18)$$

in hybrid representation, where $N_o = kT_0B$; W is the size (width) of the FET device; r_{gs} and r_{ds} are the resistances per unit width (i.e., $r = R \cdot W$); and t_{gs} and t_{ds} are the equivalent noise temperatures of the two resistors R_{gs} and R_{ds} normalized to $T_0 = 290$ K. Note that it is customary to use lower-case letters for passive components normalized to size. This convention is pointed out here because the Pospieszalski noise model in Figure 8 used lower-case letters for the components of his model.

Does it make sense? The short answer is yes, but let me explain it a little better. Firstly, let me remind the reader that (18) applies specifically to FET devices. Secondly, circuit representations are equivalent, so using the hybrid representation provides a diagonal correlation matrix (18) that visually describes the fact that the two noise sources in the device model are uncorrelated. The dependence on size does not show its proportionality with W because the hybrid representation is not the best choice for that purpose. The best choice is the admittance representation, which would yield $C_{DUT}^Y \propto W$, but it would also have nonzero off-diagonal elements. However, this is not an issue: as explained in the "Noise Formalism" section, a conversion matrix can be obtained that links the two representations,

$$C_{DUT}^Y = C_{H-Y} C_{DUT}^H C_{H-Y}^\dagger \quad (19)$$

The conversion matrix C_{H-Y} is a complicated function of size W , but the important fact is that it is a known function of size. With that in mind, (18) can be inserted in an expression equivalent to (16) with the help of an appropriate transformation matrix similar to (19). When the expression linking the noise figure and C_{DUT}^H has been worked out for a device of known size W , the coefficients of t_{gs} and t_{ds} are known functions of the device model components and size. If $n = 1, 2, \dots$,

$N \geq 2$ devices of different size W_n are available for measurement, a linear system of equations can be built and a least squares solution calculated to yield the values of t_{gs} and t_{ds} from the noise figure measurements.

When (18) is completed with the calculated t_{gs} and t_{ds} values, the noise parameters in any other representations can be easily calculated by hand or within a circuit simulator. For instance, Figure 9 presents the experimental validation of the sized-based noise characterization extraction procedure. The data were obtained from noise figure measurements over frequency on a set of gallium nitride FETs biased at the same V_{gs} and constant drain current density J_{ds} . The bottom row of plots in Figure 9 shows the ratio $y = (F_{\min} - 1) \Re\{Y_S\}/W$, which is the linear combination of t_{gs} and t_{ds} . Note that it effectively untangles the noise figure measurements over frequency.

Note that a source tuner is not required, and the source impedance can be kept constant at 50Ω to measure the noise figure, which makes it really unique [37] because it does not rely on the assumptions that other approaches employ [38]. For instance, it could be applied to extract noise parameters of devices at very low temperatures or over bias.

Indeed, the size-based procedure effectively removes the bottlenecks mentioned previously by exploiting the scalability of on-wafer devices. Finally, the procedure makes it easy to assess the noise parameters of active devices either in a production environment or in an R&D facility. In production, the fact that only F_{50} measurements are required makes the procedure faster and can provide added value to either designers or customers by delivering measurement-based noise parameters along with standard scattering parameter information. In an R&D facility, noise parameters can finally be known as part of the device development information rather than a complicated, time-consuming effort penciled out toward the bottom of a long to-do list.

The research behind this effort centered on FET devices and its recent results [39]–[41] are directed toward developing a general approach that allows us to extract the four noise parameters of any scalable devices from measurement, similar to what a vector network analyzer does with scattering parameters. Compelling results have been obtained [42] along the way of developing a solution—which is what makes research interesting.

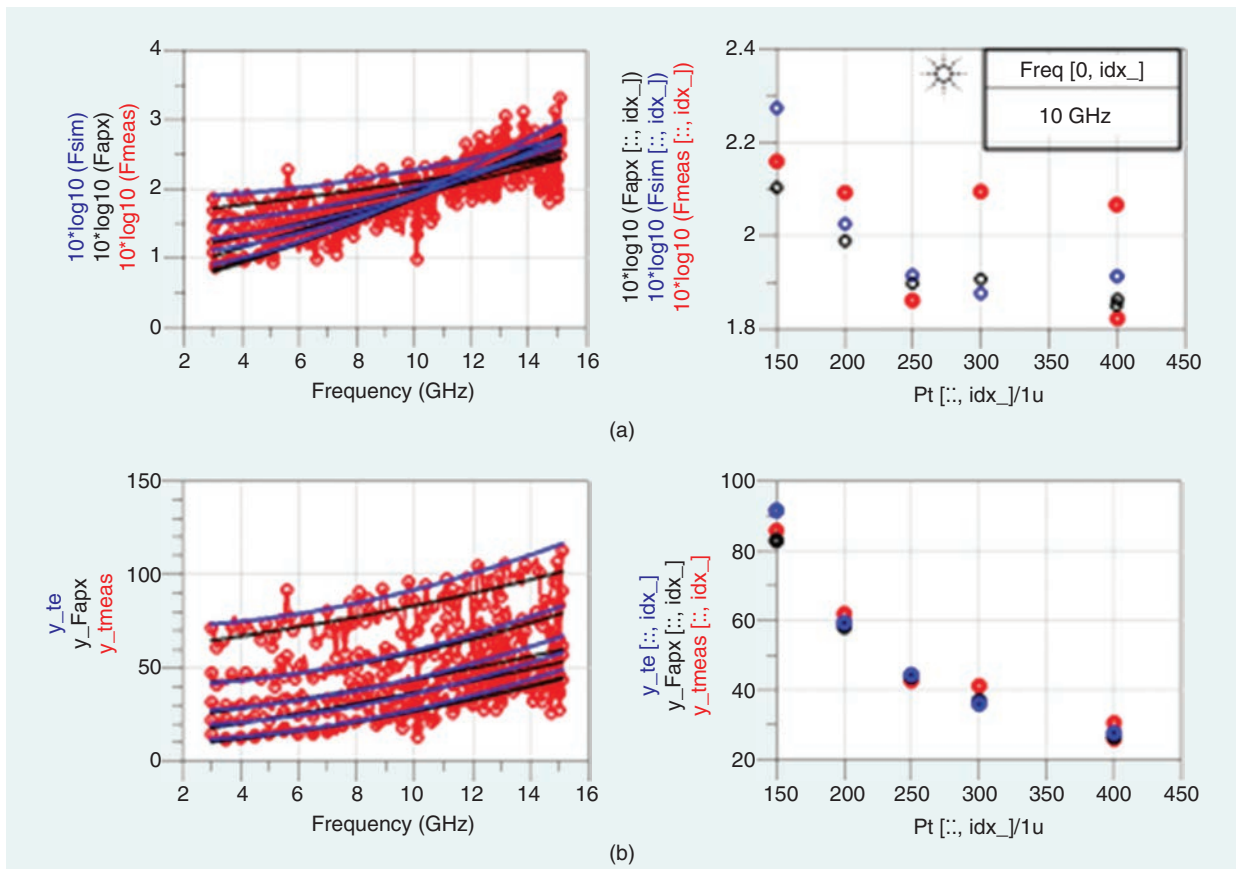


Figure 9. Extracted equivalent noise temperatures versus (a) data versus frequency for various sizes and (b) data versus size at constant frequency (10 GHz) [33].

Differential Circuits

When considering differential networks [43], a typical image that comes to mind is a network with four ports considered in pairs: two ports form the input port, and two ports form the output port. The signals that travel through those ports have the property that they are perfectly out of phase between each other, leaving the common-mode signal for later consideration.

Let me take a step back and offer some considerations from a slightly different perspective. A differential signal can be defined invoking the concept of linearity: when two single-ended ports are considered together, then the sum and difference of the voltages and currents found at those ports will define two new voltages and currents. More specifically, the common-mode signal and the differential-mode signal may be expressed as

$$\begin{cases} V_c = \frac{V_2 + V_1}{2} & I_c = \frac{I_2 + I_1}{2} \\ V_d = V_2 - V_1 & I_d = I_2 - I_1 \end{cases} \quad (20)$$

or, for that matter, by combining single-ended scattering waves to obtain mixed-mode scattering waves.

The new voltages and currents (the *signals*, to be a little more generic in our terminology) defined by (20) yield some interesting consequences. The difference of two single-ended signals (i.e., the differential signal) does not require a ground node since it effectively defines the new signal with respect to one of the two single-ended signals. Additionally, if it happens that the single-ended signals are out of phase (say, $V_1 = V_2 e^{-j\pi} = -V_2$), then the sum of the two signals (i.e., the common signal) is equal to zero.

The absence of a ground node makes a differential signal V_d very attractive to use in a noisy environment. Assume that both single-ended voltage signals $V_{se,2}$ and $V_{se,1} = -V_{se,2}$ are noisy, with uncorrelated noise ($\overline{v_{se,1} v_{se,2}^\dagger} = 0$). Then, the noise on the differential port is

$$\overline{v_d^2} = \overline{(v_{se,2} - v_{se,1})(v_{se,2} - v_{se,1})^\dagger} = \overline{|v_{se,2}|^2} + \overline{|v_{se,1}|^2},$$

and the signal power is proportional to

$$|V_d|^2 = |V_{se,2} - V_{se,1}|^2 = |2V_{se,2}|^2 = 4|V_{se,2}|^2.$$

Making the simplifying assumption that the single-ended noise voltages have the same noise characteristics ($\overline{|v_{se,1}|^2} = \overline{|v_{se,2}|^2}$), then the SNR is

$$\frac{|V_d|^2}{\overline{v_d^2}} = 2 \frac{|V_{se,2}|^2}{\overline{|v_{se,2}|^2}} \mapsto SNR_d = 2 \cdot SNR_{se}.$$

In other words, the SNR_d for the differential signal is 3 dB higher than the SNR_{se} for the single-ended signal—and every decibel counts in a noisy environment.

Measuring Noise in Differential Circuits

So how do we measure the noise performance of a noisy differential circuit? Alternatively—and equivalently—how do we measure the noise performance of a four-port linear network? Making a differential noise measurement is challenging for a number of reasons.

Equipment

Microwave equipment is inherently single-ended equipment, as Figure 5 and 6 illustrate. They always have a node called a *ground* to which voltage signals are referred and simulators often associate with node number zero. It would be nice to have differential sources as promptly available as single-ended ones, but then common-mode sources ought to be made available as well. Rather than wishing for that solution, we will take full advantage of the fact that the system we are considering is linear and leave the arduous task of making mixed-mode signals and noise sources for future considerations.

Setup

A differential setup can be as cumbersome to characterize as in the single-ended case. Everything that is done in the single-ended case (for example, the calibration of the receiver and determination of the DUT's available gain) should be done in the differential case, without forgetting the common-mode signal as well. Complications arise from the fact that we are considering a linear four-port network, and careful attention to all of the details must be paid. Indeed, whether the network has four single-ended ports or four mixed-signal ports (differential and common modes at the input and output ports), the DUT still has four ports.

Differential measurements are executed routinely [44], [45] by adding to the setup the proper components that can provide a differential signal. A common component in use for mixed-mode measurement setups like the one depicted in Figure 10 is a balun [23], [46], [47], a reciprocal three-port device that can ideally transform a single-ended signal into a differential signal. The main issue with a three-port network in this context is that the inversion of its matrix to de-embed its contribution is impossible. Why? To give a sense of the reason as to why the de-embedding of a three-port network is not feasible, consider that de-embedding essentially means that a matrix \mathbf{M} can be preceded by another matrix \mathbf{M}^{-1} such that the cascaded effect is to remove the effect of the matrix \mathbf{M} ,

$$\mathbf{M}^{-1}\mathbf{M} = \mathbf{1}. \quad (21)$$

In the case of a two-port network, this process is well defined. In the case of a three-port network, the

mathematical inversion implies that the differential- and common-mode signals from the two mixed-mode input ports can be transformed into one single-ended signal at the third port and then reconstructed uniquely to the two output ports—not an easy task.

Terminations

Well-defined terminations are key for meaningful small-signal measurement. When a vector network analyzer is used to measure the scattering parameters, great care should be taken to make sure that the DUT sees $50\ \Omega$ at the measurement planes and at all other network ports. This is true whether a single-ended or a mixed-mode measurement is made. In other words, if one were to measure a four-port network in terms of differential and common mixed-signal modes, the ports must see the required mixed-mode termination at the mixed-mode ports that are not excited (for example, 100 and $25\ \Omega$ at the differential- and common-mode ports, respectively).

When a balun is inserted between the source and differential DUT, a conversion between differential- and common-mode signals may exist in the mixed-mode scattering parameter matrix. If the DUT has some differential-mode reflections, some of this power will be converted into a common-mode signal, which will impinge on the common-mode port of the same DUT. If the DUT's common-mode input impedance is not its characteristic impedance ($25\ \Omega$ in our example), a reflection will take place that will convert again to the differential mode. Of course, the common-mode impedance at the DUT's input port may depend on the common-mode load termination, which depends on the

output balun. Unless the proper terminations are placed at the proper plane and handled correctly, the picture gets very complicated very fast.

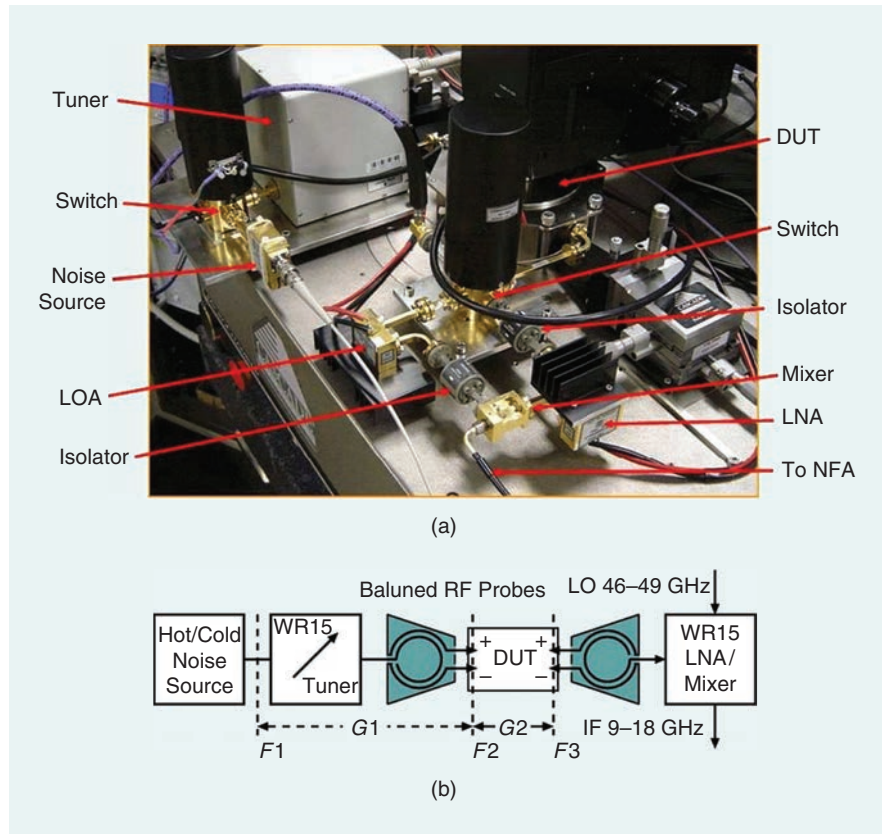


Figure 10. The (a) details and (b) basic scheme test setup for differential noise figure measurement at 60 GHz [44]. LOA: local oscillator amplifier; NFA: noise figure analyzer; WR: rectangular waveguide; IF: intermediate frequency.

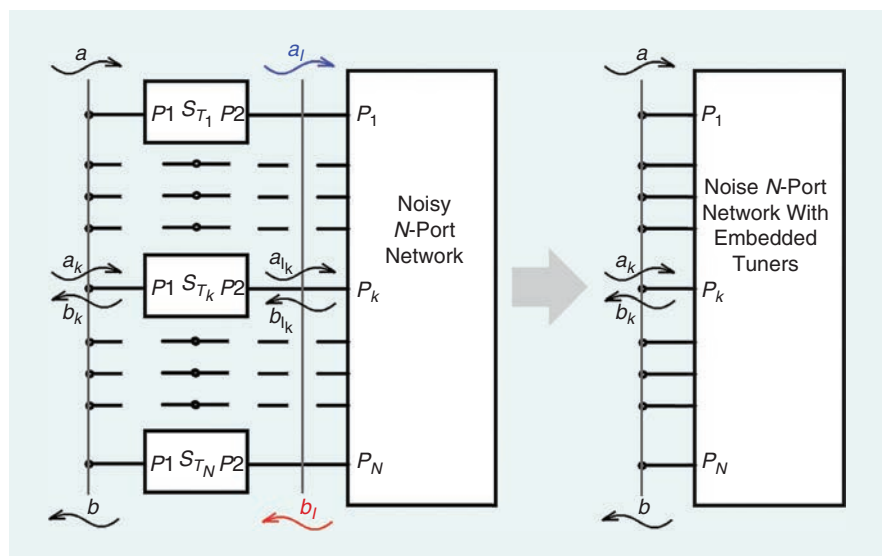


Figure 11. The new framework of [48] that generalizes the Lane approach to the case of linear networks with N ports.

performance essentially becomes a linear algebra exercise [43].

The framework has been described in [48], and it is sketched out in Figure 11. In [48], the Lane approach is generalized to the case of N -port linear networks so that it is possible to determine the $N \times N$ correlation matrix. Its reduction to practice is illustrated in Figure 12, where a commercially available differential amplifier ADI5565 board has been characterized. The differential- and common-mode noise parameters in Table 1 are calculated from the measured single-ended 4×4 correlation matrix with the proper mixed-mode termination in place.

The theory of [48] highlights interesting details that are hidden in the Lane procedure tailored to the case of a two-port network. For example, only $N - 1$ tuners are required to determine the N^2 real values associated with the noise correlation parameter matrix. This is also the case of a two-port network, as only the source tuner is required to extract the four real-valued noise parameters. If the number of settings for each of the $(N - 1)$ tuners is the same, then Figure 13 indicates that three settings per tuner are needed to characterize $2 \leq N \leq 6$ port networks and only two settings to characterize $N \geq 7$ port networks.

This approach naturally delivers an overestimated system of equations because the number of measurements increases exponentially faster than the number N^2 of unknowns in the correlation matrix: a minimum of 3^N measurements in the case of $2 \leq N \leq 6$ port networks or 2^N measurements in the case of $N \geq 7$ port

networks. For example, this approach applied to an $N = 4$ -port network with $N^2 = 16$ unknown real valued noise parameters yields a minimum of $3^N = 81$ measurements. However, similarly to the Lane procedure, additional settings above the minimum number required by Figure 13 could be used.

Finally, note that this procedure is applicable to any network with N ports, be it an on-wafer device or a printed circuit board with SMA connectors because the knob that is used in (16) is the equivalent of the source impedance of the two-port network case, not the correlation matrix itself, as described in the "On-Wafer Noise Parameter Measurement" section.

Conclusions

The article walked the reader from standard concepts to advanced techniques in microwave noise characterization to hopefully allow an appreciation of the benefits of the new approaches to the challenge of measuring noise. A circuit analysis for dealing with noise has been used to highlight new techniques in measuring noise that try to remove the bottlenecks found in standard procedures. Measuring noise parameters of active devices by exploiting the devices' scalable performance, as reflected in a well-accepted noise model, has been described.

The extension of the standard tuner-based noise parameter extraction from two-port to N -port networks has also been sketched out to support an alternative and exact determination of the noise performance of mixed-mode networks such as differential amplifiers. The common denominator through most of the article is to make use of linear algebra to build a suitable mathematical framework that can help inspire new techniques to determine the noise performance of microwave networks.

Acknowledgment

This work was supported by the U.S. Office of Naval Research, Arlington, Virginia. Opinions, interpretations, conclusions, and recommendations are of the authors and are not necessarily endorsed by the U.S. Government.

References

- [1] J. E. Brittain, "Electrical engineering Hall of Fame: Guglielmo Marconi," *Proc. IEEE*, vol. 92, no. 9, pp. 1501–1504, 2004. doi: 10.1109/JPROC.2004.832946.
- [2] R. Brown, "A brief account of microscopical observations, made in the months of June, July, and August, 1827 on the particles contained in the pollen of plants; and on the general existence of active molecules in organic and inorganic bodies," *Phil. Mag.*, vol. 4, no. 21, pp. 358–371, 1828. doi: 10.1080/14786442808674769.
- [3] A. Einstein, "Investigations on the theory of, the brownian movement," in *Annalen der Physik*. New York: Dover, 1956, pp. 549–560.
- [4] C. C. Jones, R. J. Jones, and P. C. Jones, "Discussion of black body radiation and entropy," *Proc. SPIE*, vol. 1157, Jan. 1990. doi: 10.1117/12.978575.

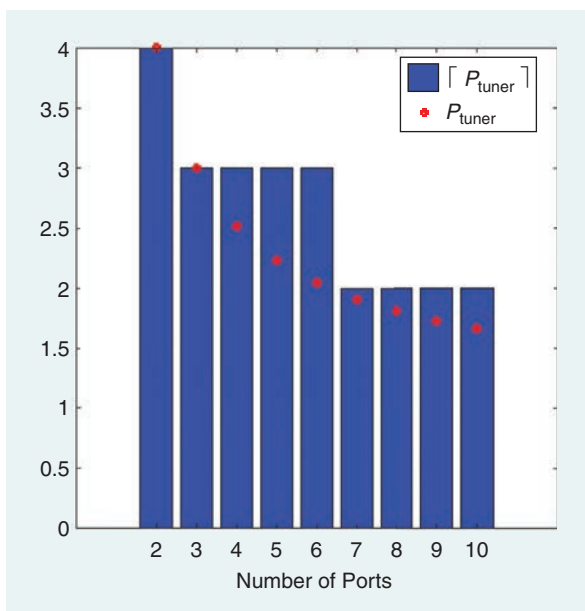
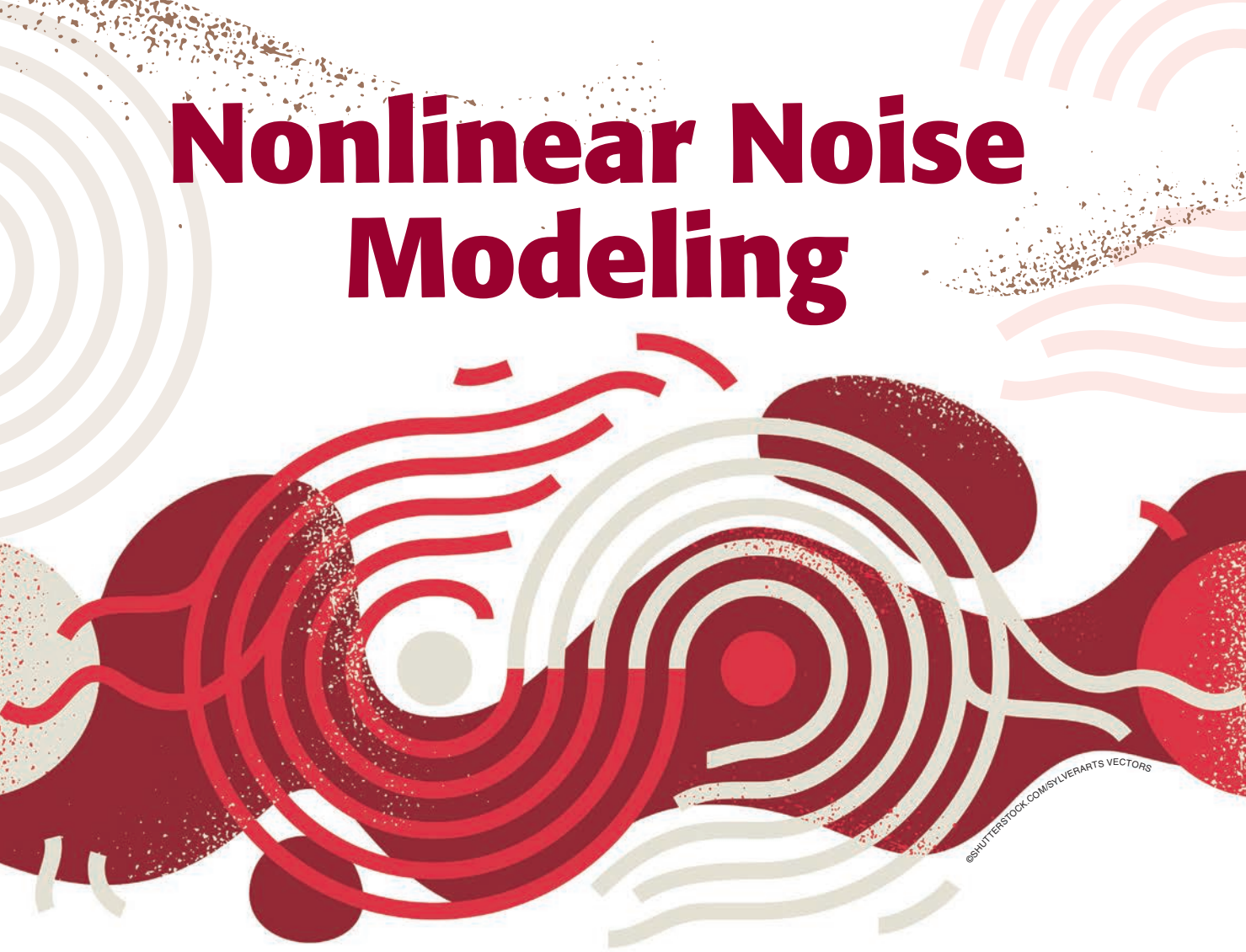


Figure 13. The number of settings for each tuner as a function of the number of ports N . The theoretical value (red dot) must be approximated by the next integer (blue bars) [48].

- [5] F. T. Ulaby, R. K. Moore, and A. K. Fung, *Microwave Remote Sensing: Active and Passive*. Reading, MA: Addison-Wesley, 1981, Chs. 4.3.2, p. 192.
- [6] J. H. Jeans, "The dynamical theory of gases and of radiation," *Nature*, vol. 72, no. 1857, pp. 101–102, June 1905. doi: 10.1038/072101d0.
- [7] J. H. Jeans, "A comparison between two theories of radiation," *Nature*, vol. 72, no. 1865, pp. 293–294, July 1905. doi: 10.1038/072293d0.
- [8] M. Planck, "On the law of distribution of energy in the normal spectrum," *Annalen der Physik*, vol. 4, p. 553, 1901.
- [9] A. Kerr and J. Randa, "Thermal noise and noise measurements—A 2010 update," *IEEE Microw. Mag.*, vol. 11, no. 6, pp. 40–52, Oct. 2010. doi: 10.1109/MMM.2010.937732.
- [10] J. D. Kraus, *Radio Astronomy*, 2nd ed., Cygnus-Quasar Books, 1982.
- [11] H. Nyquist, "Thermal agitation of electric charge in conductors," *Phys. Rev.*, vol. 32, no. 1, pp. 110–113, July 1928. doi: 10.1103/PhysRev.32.110.
- [12] S. A. Maas, *Noise in Linear and Nonlinear Circuits*. Norwood, MA: Artech House, 2005.
- [13] H. A. Haus, "Representation of noise in linear two ports," *Proc. IRE*, vol. 48, no. 1, pp. 69–74, Jan. 1960. doi: 10.1109/JRPROC.1960.287381.
- [14] H. Hillbrand and P. H. Russer, "An efficient method for computer aided noise analysis of linear amplifier networks," *IEEE Trans. Circuit Theory*, vol. 23, no. 4, pp. 235–238, Apr. 1976. doi: 10.1109/TCS.1976.1084200.
- [15] H. Hillbrand and P. H. Russer, "Correction to 'An efficient method for computer aided noise analysis of linear amplifier networks,'" *IEEE Trans. Circuits Syst.*, vol. 23, no. 11, p. 691, Nov. 1976. doi: 10.1109/TCS.1976.1084145.
- [16] D. A. Frickey, "Conversion between S, Z, Y, h, ABCD and T parameters which are valid for complex source and load impedances," *IEEE Trans. Microw. Theory Techn.*, vol. 42, no. 2, pp. 205–211, Feb. 1994. doi: 10.1109/22.275248.
- [17] G. Gonzalez, *Microwave Transistor Amplifiers: Analysis and Design*, 2nd ed., Englewood Cliffs, NJ: Prentice Hall, 1996.
- [18] J. Engberg and T. Larsen, *Noise Theory of Linear and Nonlinear Circuits*. Hoboken, NJ: Wiley, 1995.
- [19] S. W. Wedge and D. B. Rutledge, "Wave techniques for noise modelling and measurement," *IEEE Trans. Microw. Theory Techn.*, vol. 40, no. 11, pp. 2004–2011, Nov. 1992. doi: 10.1109/22.168757.
- [20] L. Bogleione, R. D. Pollard, and V. Postoyalko, "Analytical behaviour of the noise resistance and the noise conductance for a network with parallel and series feedback," *IEEE Trans. Microw. Theory Techn.*, vol. 45, no. 2, pp. 301–304, Feb. 1997. doi: 10.1109/22.557617.
- [21] H. T. Friis, "Noise figure of radio receivers," *Proc. IRE*, vol. 32, no. 7, pp. 419–422, July 1944. doi: 10.1109/JRPROC.1944.232049.
- [22] S. W. Wedge and D. B. Rutledge, "Noise waves and passive linear multiports," *IEEE Microw. Compon. Lett.*, vol. 1, no. 5, pp. 117–119, May 1991. doi: 10.1109/75.89082.
- [23] D. Pozar, *Microwave Engineering*. Hoboken, NJ: Wiley, 2004.
- [24] "Ire standards on methods of measuring noise in linear two-ports, 1959," in *Proc. IRE*, vol. 48, pp. 60–68, Jan. 1960. doi: 10.1109/JRPROC.1960.287380.
- [25] M. Sannino, "Computer-aided simultaneous determination of noise and gain parameters of microwave transistors," in *Proc. 1979 9th Euro. Microw. Conf.*, pp. 692–696.
- [26] G. Martines and M. Sannino, "Determination of microwave transistor noise and gain parameters through noise-figure measurements only," *IEEE Trans. Microw. Theory Techn.*, vol. 30, no. 8, pp. 1255–1259, 1982. doi: 10.1109/TMTT.1982.1131233.
- [27] "Fundamentals of RF and microwave noise figure measurements," Agilent Tech., Palo Alto, CA, Application Note 57-1, 5952-8255E, Aug. 2010.
- [28] "High-accuracy noise figure measurements using the PNA-X series network analyzer," Keysight Tech., Palo Alto, CA, Application Note 5990–5800EN, 2010.
- [29] "Noise figure measurement accuracy: The Y-factor method," Agilent Tech., Palo Alto, CA, Application Note 5952–3706E.
- [30] R. Q. Lane, "The determination of device noise parameters," *Proc. IEEE*, vol. 57, no. 8, pp. 1461–1462, Aug. 1969. doi: 10.1109/PROC.1969.7311.
- [31] M. W. Pospieszalski, "Modeling of noise parameters of MESFET's and MODFET's and their frequency and temperature dependence," *IEEE Trans. Microw. Theory Techn.*, vol. 37, no. 9, pp. 1340–1350, Sept. 1989. doi: 10.1109/22.32217.
- [32] L. Bogleione, "A noise parameters extraction procedure suitable for on-wafer device characterization," *Proc. 2012 IEEE Int. Semicond. Conf. Dresden-Grenoble (ISCDG)*, pp. 135–138. doi: 10.1109/ISCDG.2012.6360037.
- [33] L. Bogleione, "A novel extraction procedure to determine the noise parameters of on-wafer devices," in *Proc. 2013 IEEE MTT-S Int. Microw. Symp. Digest (MTT)*, pp. 1–4. doi: 10.1109/MWSYM.2013.6697733.
- [34] L. Bogleione, "A novel theoretical analysis for the determination of the noise parameters applicable to millimeter-wave frequencies," *Int. J. Numer. Model., Electron. Netw., Devices Fields*, vol. 28, no. 6, pp. 649–658, 2015. doi: 10.1002/jnm.2045.
- [35] J. Gao, *RF and Microwave Modeling and Measurement Techniques for Field Effect Transistors*. Zurich: SciTec, 2010.
- [36] B. Hughes, J. Perdomo, and H. Kondoh, "12 GHz low-noise MMIC amplifier designed with a noise model that scales with MODFET size and bias," *IEEE Trans. Microw. Theory Techn.*, vol. 41, no. 12, pp. 2311–2316, Dec. 1993. doi: 10.1109/22.260722.
- [37] L. Bogleione, "Noise temperature extraction procedure for characterization of on-wafer devices," in *Proc. 2020 94th ARFTG Microw. Meas. Symp. (ARFTG)*, pp. 135–138. doi: 10.1109/ARFTG47584.2020.9071780.
- [38] P. J. Tasker, W. Reinert, B. Hughes, J. Braunstein, and M. Schlechtweg, "Transistor noise parameter extraction using a 50 ohm measurement system," in *Proc. IEEE MTT-S Int. Microw. Symp.*, 1993, pp. 1251–1254.
- [39] A. Caddemi, E. Cardillo, G. Crupi, L. Bogleione, and J. Roussos, "Microwave linear characterization procedures of on-wafer scaled GaAs pHEMTs for low-noise applications," *Electronics*, vol. 8, no. 11, p. 1365, 2019. doi: 10.3390/electronics8111365.
- [40] L. Bogleione, J. Roussos, A. Caddemi, E. Cardillo, and G. Crupi, "Device noise parameter characterization: Towards extraction automation," in *Proc. IEEE Microw. Meas. Conf. (ARFTG)*, Jan. 2020, pp. 1–4. doi: 10.1109/ARFTG47584.2020.9071780.
- [41] A. Caddemi, L. Bogleione, E. Cardillo, G. Crupi, and J. A. Roussos, "Cross-laboratory experimental validation of a tunerless technique for the microwave noise parameters extraction," *IEEE Trans. Microw. Theory Techn.*, vol. 69, no. 3, pp. 1733–1739, 2021. doi: 10.1109/TMTT.2020.2999780.
- [42] L. Bogleione, "On the determination of device noise parameters versus size," *IEEE Trans. Microw. Theory Techn.*, vol. 68, no. 10, pp. 4169–4176, 2020. doi: 10.1109/TMTT.2020.3015472.
- [43] A. Ferrero and M. Pirola, "Generalized mixed-mode S-parameters," *IEEE Trans. Microw. Theory Techn.*, vol. 54, no. 1, pp. 458–463, Jan. 2006. doi: 10.1109/TMTT.2005.860497.
- [44] L. F. Tiemeijer, R. M. T. Pijper, and E. van der Heijden, "Complete on-wafer noise-figure characterization of 60-gHz differential amplifiers," *IEEE Trans. Microw. Theory Techn.*, vol. 58, no. 6, pp. 1599–1608, June 2010. doi: 10.1109/TMTT.2010.2049167.
- [45] M. Robens, R. Wunderlich, and S. Heinen, "Differential noise figure de-embedding: A comparison of available approaches," *IEEE Trans. Microw. Theory Techn.*, vol. 59, no. 5, pp. 1397–1407, May 2011. doi: 10.1109/TMTT.2010.2103093.
- [46] N. Marchand, "Transmission line conversion transformers," *Electronics*, pp. 142–145, Dec. 1944.
- [47] L. Bogleione and J. Goodman, "Analysis of tunable Marchand baluns," in *Proc. IEEE Radio Freq. Integr. Circuits (RFIC) Symp.*, June 1–3 2014, pp. 115–118. doi: 10.1109/RFIC.2014.6851673.
- [48] L. Bogleione, "Generalized determination of device noise parameters," *IEEE Trans. Microw. Theory Techn.*, vol. 65, no. 10, pp. 4014–4025, Oct. 2017. doi: 10.1109/TMTT.2017.2709320.



Nonlinear Noise Modeling



Matthias Rudolph and Anisha M. Apte

Noise is a random signal, a perturbation of dc bias and RF signals. It is usually necessary that digital electronics provide a low bit error rate or error vector magnitude to guarantee the reliable digital transmission of data. Microwave electronics are commonly expected to amplify or mix these digital signals with high linearity and without adding significant noise, which translates to the requirement of a 10-dB signal-to-noise ratio (SNR) in a communication system. In the case of a nonlinear circuit, it might not always be

clear how noise could be an issue at all. Firstly, the signal is several tens of decibels larger than in the small-signal domain. Secondly, one might consider nonlinear distortions to be the first limiting factor.

So why bother about the noise that still remains as a small-signal quantity? Indeed, if nonlinear distortion products disturb the signal quality, the carrier-to-interference ratio becomes more important than the SNR. But there are important applications where the small perturbation due to noise is able to degrade the performance.

Matthias Rudolph (rudolph@b-tu.de) is with Brandenburg University of Technology, Cottbus, D-03046, Germany, and with Ferdinand-Braun-Institut für Höchstfrequenztechnik, Berlin, D-12489, Germany.

Anisha M. Apte (anisha_apte@ieee.org) is with Synergy Microwave Corporation, Paterson, New Jersey, USA.

Digital Object Identifier 10.1109/MMM.2021.3069538

Date of current version: 1 June 2021

The first example is a mixer circuit. These circuits commonly use field-effect transistors (FETs) or diode switches to generate new frequencies. Due to the non-linearity of the mixer circuit, the input signal is mixed with a large-signal local oscillator (LO) signal at frequency f_{LO} to obtain an output signal at the sum or difference of the frequencies. For example, an intermediate frequency (IF) signal at f_{IF} can be upconverted to the RF range to $f_{RF} = f_{IF} + f_{LO}$. Although this circuit is highly nonlinear, it is used to convert a small-signal input to a small-signal output at a different frequency. For the circuit to work, large-signal operation is essential, but input and output signals are small-signal quantities where the SNR is important.

A second example is the oscillator. A transistor's output signal is partly fed back to the input at one specific frequency f_{LO} to generate even higher output signal levels, which are eventually limited by the transistor saturation power. As we need a significant output power at f_{LO} and like a good efficiency, the transistor will be driven in the strongly nonlinear domain. But, if the zero crossings of the output voltage are inspected to determine the oscillation frequency, even a noise signal of very low power levels is capable of introducing a certain jitter, that is, phase noise that translates to a broadening of the spectral line at f_{LO} .

Even in the case of linear amplifiers, large-signal noise can become important, as discussed in the "Linear

Noise Simulation" section. The two short examples, mixer and oscillator circuits, should be enough to exemplify the importance of noise effects in nonlinear circuits in general.

Linear Noise Simulation

Noise is an electrical signal. Once its origin is characterized and described by a current or voltage source, one could, in principle, apply small-signal circuit analysis to determine the noise levels at the input and output ports. Fortunately, the physical and mathematical derivations yield a rather simple description for the common types of noise observed in electronics. What we need to know are the autocorrelation and cross-correlation functions of the noise sources, which translate to the spectral power densities.

In the case of the thermal noise of a resistor, for example, its equivalent noise current source is given by $\langle |i_R|^2 \rangle = 4kT\Delta fG$, with the Boltzmann constant k , temperature T , bandwidth Δf , and admittance G . If the noise performance of a two-port needs to be calculated and it contains this resistor as a noise source, one can determine how a current i_R translates into short circuit port currents i_1 and i_2 at port 1 and 2, respectively. It is quite straightforward to calculate $\langle |i_1|^2 \rangle$, $\langle |i_2|^2 \rangle$, and $\langle i_1 i_2^* \rangle$ from these currents. The last term characterizes the correlation of the two noise currents, which is a complex number. (See "Linear Two-Port Noise Spectra.")

Linear Two-Port Noise Spectra

A linear two-port exhibits noise power that is measurable, independent of whether or not a signal source is applied or not. The spectra observed are sketched in Figure S1. At low frequencies, flicker noise and burst noise are observed and yield an almost $1/f$ slope in the power spectrum when approaching zero frequencies. Lorentz-type spectra can also be observed that show a cutoff frequency. These spectra are the superposition of fluctuations that involve slow processes, such as the capture and release of carriers at traps, and fluctuations in carrier mobility.

At a corner frequency ω_f , the noise spectrum approaches a constant noise floor, the so-called white noise. White noise can be thermal noise or shot noise due to carriers crossing a barrier as in a diode. The corner frequency ω_f depends on the type of transistor. It is higher in field-effect transistor devices, where the current flows in parallel to an interface or surface so that generation and recombination are stronger than in bipolar devices, where the current flows mainly through the bulk semiconductor. Note that, in thermal equilibrium, the device will receive the same amount of power from its environment as it emits in terms of noise. Also, a purely

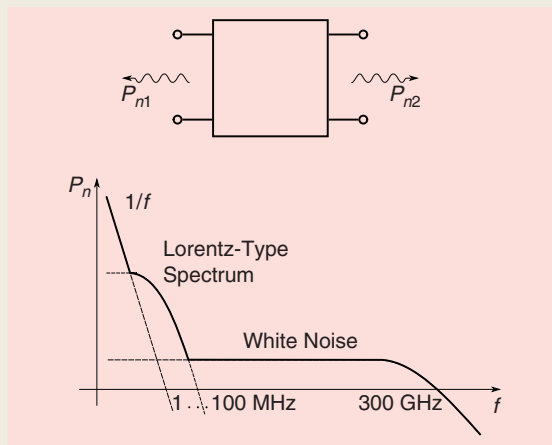


Figure S1. A noisy two-port and the typical noise spectrum measured at one of the ports.

white spectrum (constant over all frequencies) or perfect $1/f$ spectrum contradicts physics as either would provide infinite power. White noise, if it is of a thermal nature, for example, shows a low-pass characteristic, as predicted by quantum physics, which needs to be accounted for beyond 300 GHz at room temperature.

Four values (two real and one complex quantity) therefore describe the terminal noise performance of the two-port. It is not required to determine the short circuit noise currents. Also, open-circuit noise voltages or the four noise parameters can be used. Through the correlation-matrix approach, the different descriptions can be transformed into each other; in addition, the noise performance of a combination of two-ports is easily determined [1], [2]. (See “Linear Two-Port Noise Parameters.”)

A simulator could calculate the small-signal and noise performance of a larger system by combining the noise correlation matrices of all parts of the system. The basis of an accurate simulation is, of course, a good noise model.

Linear Noise Modeling

A linear noise model looks like a small-signal model with additional noise sources. To derive the model, it is required to know the physical origin of the noise and derive the resulting noise observed at the device terminals. In the case of an FET, for example, Pucel [3] took a physical model of the static electron transport in the channel, superimposed microscopic thermal noise sources distributed along it, and integrated all of the contributions to the terminal short circuit noise currents. The result is

a description of the terminal short circuit noise sources, derived on the assumption that the drain-source dc current is affected by thermal noise. The equivalent circuit is illustrated in Figure 1. As we can see, it is just the usual small-signal equivalent circuit with two terminal noise current sources, defined by

$$\langle i_g^2 \rangle_{\text{Pucel}} = 4k\Delta f T \frac{(\omega C_{gs})^2}{g_m} \cdot R, \quad (1)$$

$$\langle i_d^2 \rangle_{\text{Pucel}} = 4k\Delta f T g_m \cdot P, \quad (2)$$

$$\langle i_g i_d \rangle_{\text{Pucel}} = 4k\Delta f T \cdot C^* \cdot \sqrt{RP} \quad (3)$$

with the three fitting parameters P , R , and $C \approx -j$. The rest of the parameters are the angular frequency ω , Boltzmann constant k , device temperature T in

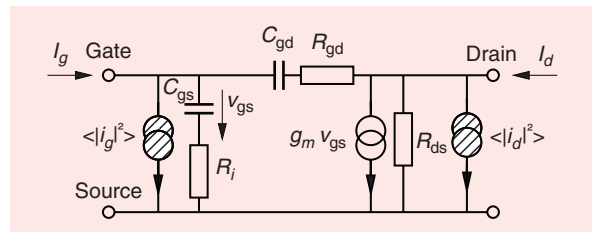


Figure 1. An intrinsic noise model of the gallium nitride (GaN) FET according to Pucel.

Linear Two-Port Noise Parameters

The signal-to-noise ratio at the output of the device SNR_{out} is worse than at the input (SNR_{in}) due to the noise of the two-port. In small-signal analysis, the noise exhibited by the two-port is a property of the two-port and independent of the external circuitry. The noise factor $F = SNR_{\text{in}}/SNR_{\text{out}} \geq 1$ is used to characterize it, e.g., in the case of amplifiers or transistors, when the input and output ports are defined. An important part of the definition is that the source is considered to provide thermal noise at temperature $T_0 = 290$ K. The noise figure NF (i.e., the noise factor F in dB) depends on the source termination, as shown in Figure S2. If the source reflection coefficient Γ_s (or source admittance $Y_s = G_s + jB_s$) is not matched, a part of the noise exhibited by the input port will get reflected and propagated through the two-port, thus adding to the noise exhibited at the output port. The noise signals observed at the two ports are random but not completely independent of each other if the noise can be traced back to the same physical origins within the two-port.

For correlated noise, the selection of Γ_s may lead to a positive or destructive superposition of the two noise waveforms. At the same time, the mismatch at the input varies the gain of the two-

port. As a consequence, one finds an optimum source admittance, $Y_{\text{opt}} = G_{\text{opt}} + jB_{\text{opt}}$, for which the noise factor reaches its minimum value $F = F_{\text{min}}$. The increase of the noise factor due to mismatch is characterized by an equivalent noise resistance R_N . These four noise parameters, F_{min} , R_N , G_{opt} , and B_{opt} , are characteristic properties of a linear two-port, similar to its Y-parameters. Just as with the Y-parameters, many equivalent expressions based on Z- or S-parameters exist. Note that noise matching and power matching are commonly different.

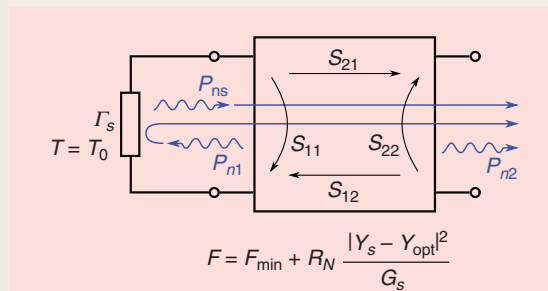


Figure S2. The dependence of the noise figure on the input termination with reflection coefficient Γ_s and admittance $Y_s = G_s + jB_s$. The source exhibits thermal noise at $T_0 = 290$ K.

Kelvin, bandwidth Δf , transconductance g_m , and gate-source capacitance C_{gs} .

An alternative approach was proposed by Pospieszalski [4], who attributed thermal noise to the two resistances that are present in the equivalent circuit (Figure 2). The gate-source resistance R_{gs} and the drain-source resistance R_{ds} are considered to exhibit noise according to their respective temperatures T_g and T_d . While T_g should be equal to the device temperature, T_d is usually in the range of more than 1,000 K, as it describes the electrons in the channel.

Although the two noise models were derived based on quite different assumptions, it is possible to transform one into the other [5]. The assumptions required are usually valid: $C \approx -j$ is implied already in Pucel's derivation since it describes the coupling of the noise from the channel to the gate through C_{gs} . We should also have some headroom in frequency and stay well below the transit frequency so that $(\omega C_{gs} R_{gs})^2 \ll 1$, $(\omega C_{gs})^2 \ll 1$ and $g_m \approx g_{m0}$ hold. Under these assumptions, the model parameters of one model can be derived from the other model through

$$R = \frac{T_g}{T_0} R_{gs} g_m, \quad (4)$$

$$P = \frac{T_d}{T_0} \frac{1}{R_{ds} g_m} + R, \quad (5)$$

$$C = -j \sqrt{\frac{R}{P}}. \quad (6)$$

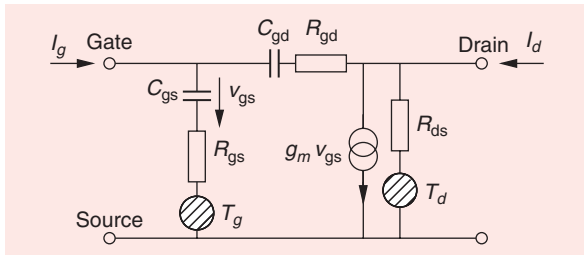


Figure 2. An intrinsic noise model of the GaN FET according to Pospieszalski.

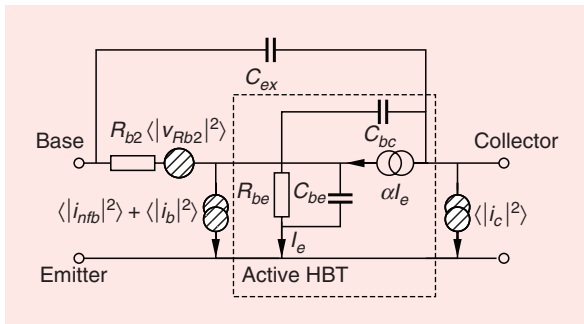


Figure 3. An intrinsic noise model of the HBT.

For bipolar transistors, van der Ziel [6] took a similar approach as Pucel for FETs to determine the white noise model. He considered the electron transport in the base, superimposed microscopic noise sources distributed along the base describing the random diffusion process, and determined how these microscopic noise sources would add to short circuit noise currents at the emitter and collector side of the transistor. He also showed that an alternative approach considering shot noise at both p-n junctions, which is correlated through the base transit time, yields the same result. Figure 3 depicts the small-signal equivalent circuit of a heterojunction bipolar transistor (HBT). It consists of the part inside the dashed box, known as the active HBT, that describes the base and the two p-n junctions. Since the base and collector contacts require some lateral access to the device, an extrinsic base-collector p-n capacitance C_{ex} and a resistance of the base layer R_{b2} are added.

Since the currents through the two p-n junctions are correlated and due to the rearrangement of the current sources away from the p-n junctions to the base and collector terminals, the two shot noise sources read

$$\begin{aligned} \langle |i_b|^2 \rangle &= 2q\Delta f (I_{be} + |1 - e^{-j\omega\tau}|^2 I_c) \\ \langle |i_c|^2 \rangle &= 2q\Delta f I_c \\ \langle i_b i_c^* \rangle &= 2q\Delta f (e^{j\omega\tau} - 1) I_c \end{aligned} \quad (7)$$

with the electron charge q , base-emitter and collector dc currents I_{be} , I_c , the correlation time constant τ , bandwidth Δf , and angular frequency ω [8], [9]. In addition to the white noise sources, the equivalent circuit shows the noise source $\langle |i_{ntb}|^2 \rangle$ that describes the $1/f$ -shaped low-frequency flicker noise at the base-emitter junction.

Noise in Nonlinear Circuits

Leaving the small-signal domain, e.g., by increasing the input power of an amplifier, one observes two basic effects: quantities such as gain or matching change from their small-signal value and, eventually, new frequencies are generated due to nonlinearity. It is, therefore, to be expected that similar effects are observed in terms of noise, too. (See "Noise in an Ideal Nonlinear Circuit.")

One issue that is often overlooked concerns the noise figure, which can be quite different in large-signal operation from its small-signal value. The noise figure NF is commonly used to characterize the impact of white RF noise on the signal quality and is given in decibels as the ratio of SNR at the input to the SNR at the output of a two-port. The NF is well suited to characterize the noise contribution of an amplifying element, but the usual way of measuring it

is constrained to small signals. The common Y-factor measurement method even excites the device under test only by “hot” and “cold” noise sources without any additional signal at all. If the noise figure is required in nonlinear operation, one commonly relies on simulation.

Another issue is frequency conversion in nonlinear circuits. Figure 4 highlights the effect. The noise of any device shows a $1/f$ frequency dependence at low frequencies, which is Hooge and generation-recombination noise. The corner frequency is far below the microwave range so that the $1/f$ noise is not relevant for small-signal, low-noise amplification. But, in the case of a nonlinear circuit, the noise will undergo a mixing process with any large-signal frequency, resulting in noise sidebands.

A circuit that combines all types of nonlinear behavior is the oscillator. An oscillator can be considered to be a broadband amplifier with a frequency-selective feedback loop, and it is a highly nonlinear frequency-generating circuit. It might be beneficial to have a look at the empirical Leeson [10] formula that explains the noise spectrum $\mathcal{L}(f_m)$ in a bandwidth of 1 Hz at a certain frequency offset f_m from the oscillation frequency f_0 . (See “Oscillator Phase Noise.”) A more complete description of the phase-noise phenomenon is given through the enhanced formula [12]

$$\mathcal{L}(f_m) = 10 \log \left\{ \left[1 + \frac{f_0^2}{(2f_m Q_{\text{load}})^2 (1 - Q_{\text{load}}/Q_0)^2} \right] \cdot \left(1 + \frac{f_c}{f_m} \right) \frac{FkT_0}{2P_{\text{sav}}} + \frac{2kT_0 R K_0^2}{f_m^2} \right\}. \quad (8)$$

Noise in an Ideal Nonlinear Circuit

With noise being an electrical signal, it experiences frequency translation processes in nonlinear circuits in the same way as any other electrical signal. The differences to be considered for the RF signal are that the noise commonly originates from another source, such that the transfer functions for the RF and noise signals differ. Leaving this aside for the moment, the spectrum of the noise differs significantly from the RF signal spectrum. At RF frequencies, the noise observed is constant so that a frequency translation shows basically no effect. But, other than the RF signal, noise always comes with a low-frequency flicker noise component, increasing roughly according to a $1/f$ law in baseband.

The hypothetical example of an RF signal superimposed with a standard noise floor being frequency converted through an ideal mixer is illustrated in Figure S3. Since all of the input frequencies ω_i get converted, according to the local oscillator (LO) frequency ω_{lo} , to frequencies $\omega_o = \omega_i \pm \omega_{lo}$, we observe noise sidebands due to the upconverted flicker noise around the LO frequency. This example is hypothetical since, in reality, the LO signal provides phase noise and the mixer itself also provides flicker noise. In actuality, noise sidebands are observed for all mixing products at the output together with flicker noise in the baseband.

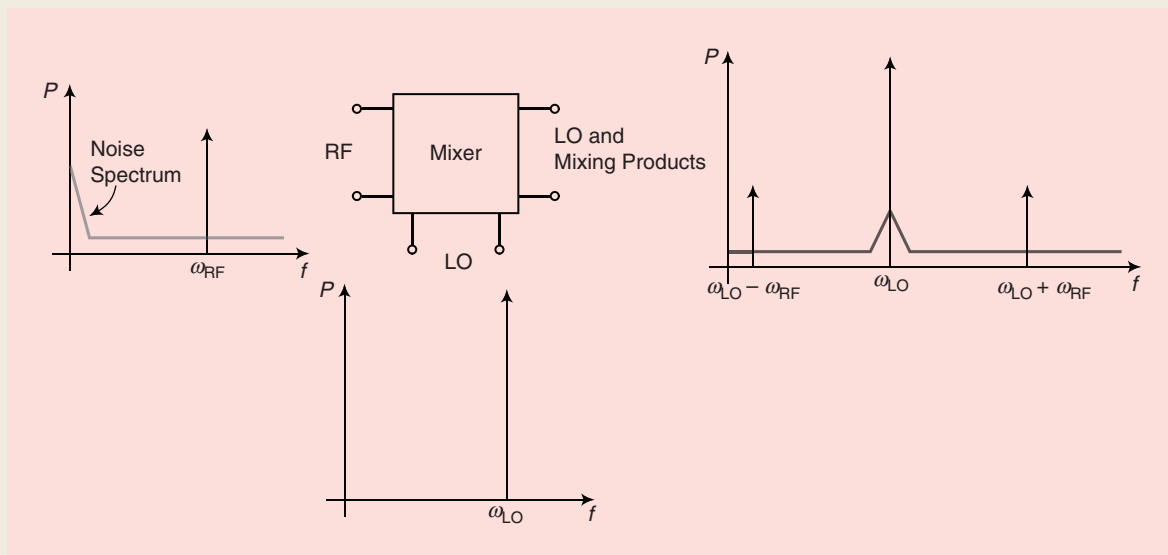


Figure S3. The idealized frequency conversion of noise and an RF signal by a hypothetical noiseless mixer and LO signal.

Since phase noise is given relative to the average output power P_{sav} , the formula gives the ratio of thermal noise kT_0 multiplied by the large-signal noise factor F to P_{sav} . The linear and dimensionless F needs to be inserted here instead of the previously discussed NF , which is given in decibels. The ratio is multiplied with two factors. The second factor describes the $1/f$ slope of the noise observed below a certain corner frequency f_c . The first term accounts for the frequency-selective feedback network. It is considered to be a resonant circuit with a bandwidth dependent on the loaded quality factor Q_{load} and its unloaded equivalent Q_0 . The noise is filtered accordingly. The second term in the brackets accounts for the additive noise introduced by the tuning diode, with R being the equivalent noise resistance of the tuning diode (typically 200–10,000 Ω) and the oscillator voltage gain K_0 [2].

While a large-signal noise figure can hardly be measured, it is possible to characterize how a certain transistor performs in terms of phase noise when driven by a large signal. The measurement setup resembles more or less the setup of a phase-noise measurement system, with the difference that the device under test is open loop and a carrier signal has to be provided at the input.

Noise in nonlinear operation affects, for example, the following types of circuits:

- oscillators show phase noise, as discussed
- mixers work with small-signal RF and IF but are nonlinearly driven by the LO
- buffer amplifiers amplifying oscillator signals work in the large-signal domain and may degrade the phase noise

- a low-noise amplifier (LNA) that is subject to a jamming signal at a different frequency is also driven nonlinearly although still considered a small-signal amplifier at the receiver frequency.

Before we address the simulation of these types of circuits, it is necessary to discuss how the physical noise sources interact with large signals.

Noise Sources and Large Signals

Thermal noise depends only on electrical signals through self-heating. Power dissipation P_{diss} in a device is given by the product of current and voltage, but the relation of self-heating to dissipated power follows the same law as the voltage following the current in an RC low pass. Thus, at dc and low frequencies, the device temperature T_j will be given by $T_j = T_a + R_{th}P_{diss}$. But, beyond a certain cutoff frequency, the junction temperature will no longer follow the electrical signals. Since the thermal time constant is usually around 1 μs (or longer) in a monolithic microwave integrated circuit (MMIC), it is a good approximation for most microwave or mm-wave circuits to assume that only the dc components contribute to noise.

Shot noise at a p-n junction, on the other hand, is given by $\langle |i_s|^2 \rangle = 2qI\Delta f$, with the electron charge q , current I , and bandwidth Δf . The formula is derived based on the assumption that the current consists of the series of current pulses that carry the total charge of q across the p-n junction in an infinitesimally short time. No cutoff frequency is observed since the shape of the current pulses resembles Dirac pulses reasonably well and the Fourier transform of a Dirac is the constant function. The point is that the sum of the pulses

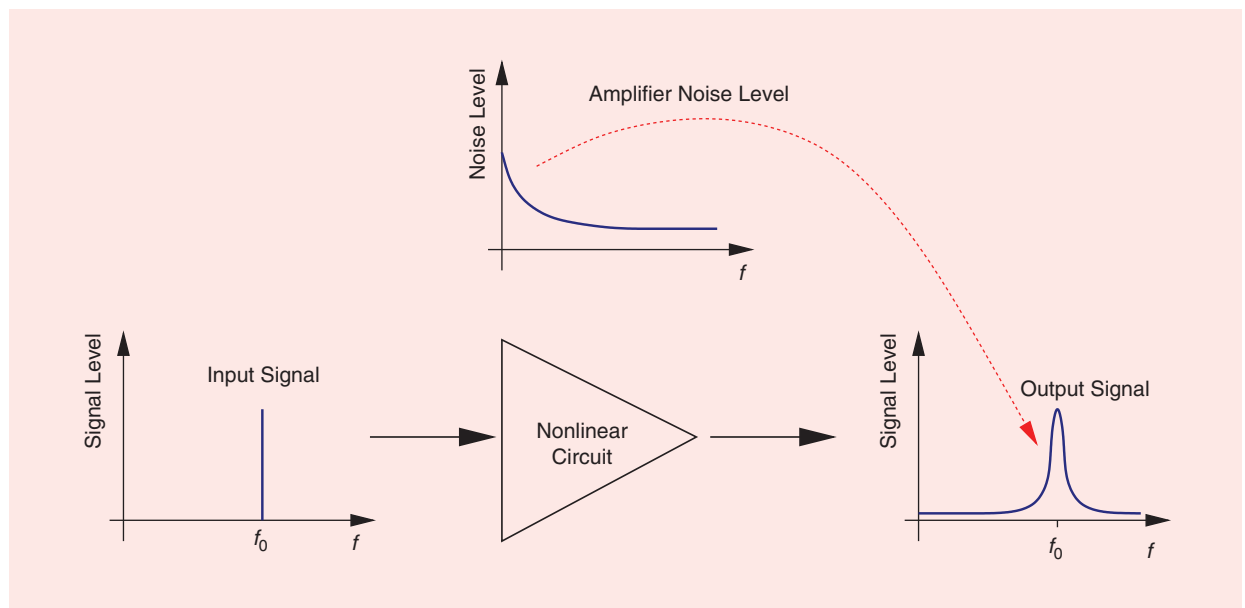


Figure 4. The upconversion of low-frequency noise in a nonlinear circuit.

is the current; thus, when an RF large-signal current is applied, the effective value of this current will add to I . The current driving the noise is, therefore, no longer the dc component but the sum of the dc and all harmonic large-signal currents. The spectrum of the noise, however, will not change as it is determined by the individual Dirac-shaped pulse.

Toward lower frequencies, the noise is observed to increase approximately according to a $1/f$ law. Generation and recombination of carriers are one source of this so-called flicker noise. Traps in the semiconductor capture and release electrons, which superimposes a random telegraph signal on the current. Capture and release can be considered to happen instantaneously, but characteristic time constants are observed for the times the electrons are kept and for the times the trap remains empty. The noise spectrum measured for a single type of trap is Lorentz shaped and calculated as

$$\langle |i_{gr}|^2 \rangle = \frac{K}{1 + (\omega/\omega_k)^2} I^a, \quad (9)$$

with the fitting factors K and a , current I , angular frequency ω , and cutoff frequency ω_k defined by the average time the electron remains in the trap and how long the trap remains empty.

It is important to note that the low-pass-like shape of the spectrum is not caused by a process that can be considered to be slow in the sense that it will not follow RF signals. Capture and release happen instantaneously and thereby might well be related to an RF large-signal current.

The issue is highlighted in Figure 5. Let's consider a semiconductor resistor [Figure 5(a)]. If we force a dc current through it, flicker noise will be observed with a $1/f$ -like frequency dependence [Figure 5(b)]. What happens in the case of a pure RF large-signal current [Figure 5(c)]? If the noise is controlled by dc currents only, nothing will be measured. But, if RF large-signal current noise also controls the noise, noise sidebands will be observed at the RF frequency due to the upconversion of the flicker noise [7].

It is important to note that the upconversion in this case happens within the noise process and that no nonlinear circuit is involved. The intensity of the random telegraph signal of the traps is controlled by the current density, which means, in this case, multiplying a low-pass signal with an RF carrier. Voilà: upconverted $1/f$ noise.

In conclusion, in the large-signal domain, RF signals also have a direct impact on noise sources. Device temperature changes and RF currents can trigger noise processes. In the following sections, we discuss how harmonic-balance circuit simulators commonly calculate noise and

how to implement noise sources and then address relevant nonlinear circuits and what they need to simulate their noise performance.

Harmonic-Balance Simulators and Nonlinear Noise

Simulating noise takes a number of steps in the frequency domain. To calculate the noise figure in an S-parameter simulation, the simulator needs to take the following steps:

- 1) Determine the dc bias point.
- 2) Linearize the nonlinear model at the dc bias point to get the Y-parameter matrix of the circuit.
- 3) Calculate the noise sources based on the bias point and operation temperature.
- 4) Calculate the S-parameters from the Y-parameter matrix.
- 5) Calculate the noise figure from the Y-parameter matrix and noise sources.

In the case of a nonlinear harmonic-balance simulation, the noise simulation follows a similar pattern, which is known from mixer analysis as large-signal/small-signal analysis. This type of analysis assumes that a known large

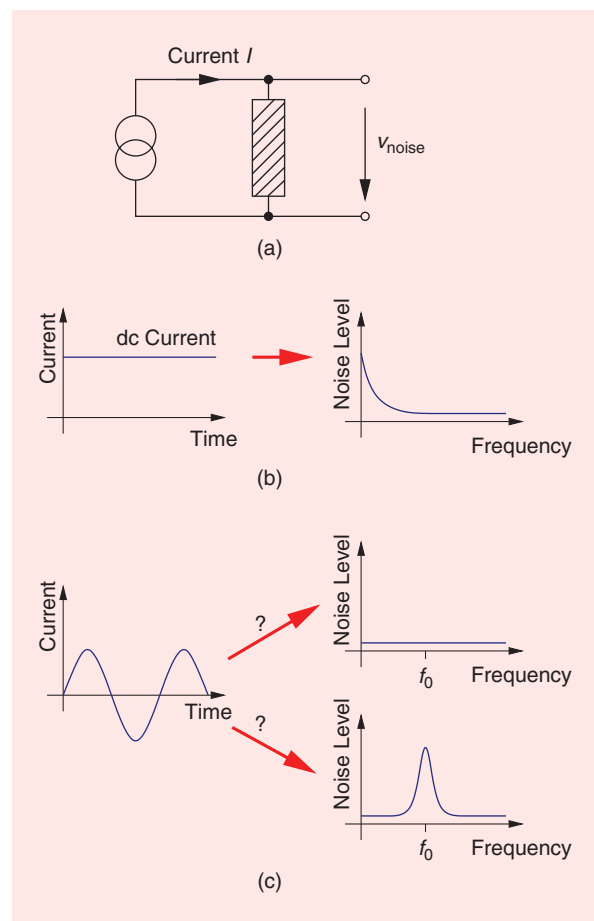


Figure 5. The upconversion of low-frequency noise in a nonlinear circuit. (a) A semiconductor resistor excited (b) by a dc signal and (c) by a high-amplitude RF signal.

signal controls the nonlinear behavior of the circuit, while a small signal superimposes only small perturbations. Simulating noise under this assumption proceeds according the following steps:

- 1) Determine the large-signal currents and voltages and the dc bias point through harmonic-balance simulation.
- 2) Consider the dynamic large-signal solution to be a time-varying bias point.
- 3) Linearize the nonlinear model around the time-varying bias point to get a time-varying Y-parameter matrix of the circuit.
 - a) Calculate the time-varying derivative of the current and charge functions.
 - b) Fourier transform the solution to get a Y-parameter-type conversion matrix (containing fundamental and harmonics of the Fourier transformed admittance).
- 4) Calculate the noise sources based on the dc bias point and operation temperature.
- 5) Calculate the noise figure from the conversion matrix and noise sources.

This scheme of calculating the noise in a nonlinear circuit assumes that only dc currents excite noise sources, but it accounts for frequency conversion. Thus, flicker noise gets transformed to noise sidebands at all large-signal harmonics.

If one needs to have the large-signal current drive the noise source, it is required to implement it through

a subcircuit, as depicted in Figure 6. Instead of, e.g., implementing a flicker noise source,

$$\langle |i'|^2 \rangle = \frac{K}{1 + (\omega/\omega_k)^2} I^a, \quad (10)$$

using a built-in noise source, which will lead to the simulator setting $I = I_{DC}$, a subcircuit is defined consisting of a normalized noise source feeding a noise,

$$\langle |i''|^2 \rangle = \frac{K}{1 + (\omega/\omega_k)^2}, \quad (11)$$

to a $1-\Omega$ resistor and a nonlinear source feeding a current,

$$i'' = \sqrt{I(t)^a}, \quad (12)$$

to another $1-\Omega$ resistor. Sensing the voltages $v_a(t)$ and $v_b(t)$ across these resistors and using them to define a controlled current source,

$$i''' = v_a(t) \cdot v_b(t) \cdot (A^2/V^2), \quad (13)$$

will realize a noise source controlled by the instantaneous large-signal current. Thus, if the current consists of dc and harmonics, flicker noise will be observed in the baseband together with noise sidebands at the large-signal RF frequencies. Note that upconverted flicker noise would be observed even if the dc current is zero or if the circuit still shows linear behavior despite the large-signal excitation.

Noise sources of this type are commonly called *cyclostationary noise sources* since we treat the large-signal excitation like a periodic time-varying bias point in the analysis.

Bias-Dependent Linear Noise Models

On the basis of the discussion so far, we can move on to define a transistor noise model for nonlinear circuit simulation. Taking a linear noise model as the starting point, it is basically required to replace the small-signal model with a large-signal model and to define its noise sources depending on actual dc currents

and the transistor temperature, assuming that the cyclostationarity discussed previously is a second-order effect.

Bias-Dependent HBT Noise Model

A large-signal equivalent circuit for the intrinsic HBT is illustrated in Figure 7. Comparing it to the small-signal model from Figure 3 reveals a switch from T to π -topology, as the current source is now

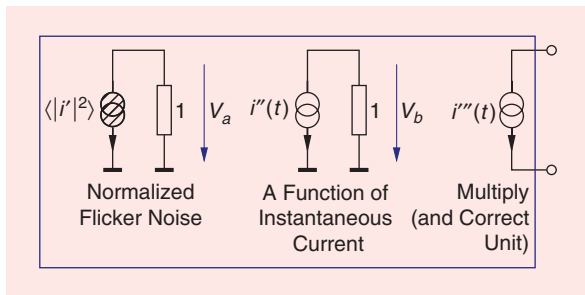


Figure 6. Implementing a cyclostationary noise source.

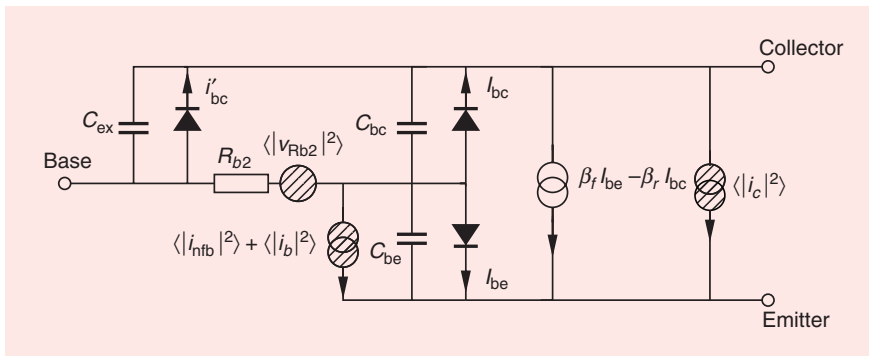


Figure 7. A large-signal HBT noise model.

describing the collector–emitter current instead of the base–collector current and all linear elements are now replaced by large-signal elements: charge and current sources. In the figure, charge sources are drawn as capacitances, and diode symbols are used to indicate that the p–n junction currents indeed display the expected I – V characteristics. The noise sources are still at the same branches as in the small-signal case and still follow the same relation as given in (7).

The white noise of the intrinsic HBT is still defined by the thermal noise of the base resistance and by the shot noise of the two p–n junctions. However, the dc currents and the temperature are now determined first by a large-signal simulation. The only critical issue is the correlation of the two shot-noise sources, which is expressed by the time constant τ . While τ can be considered to be a fitting factor in the small-signal model, we need a physics-based understanding and mathematical description in the large-signal case to predict its bias dependence.

A first-order approximation is to assume that $\omega\tau \ll 1$ holds and that the correlation term can be neglected altogether. This assumption is the basis of the Fukui noise model [14], and it has been the standard case in bipolar junction transistor and HBT large-signal noise models since its publication.

But this assumption doesn't hold in many of today's devices. Figure 8 depicts the measured minimum noise figures of two indium gallium phosphide/gallium arsenide (InGaP/GaAs) devices of different base and collector width. The measurement is denoted by the dots, while the dashed lines are simulated assuming $\omega\tau \approx 0$, which significantly overestimates the minimum noise figure toward higher frequencies. In contrast, a large-signal model accounting for the correlation, shown as solid lines, is able to significantly improve the model agreement. While this finding is valid for the device with wider base and collector layers, correlation proves to be low enough to be neglected in the other device. Unfortunately, it is not easy to predict whether correlated shot-noise sources are required to simulate devices of a given process. Similar conclusions were drawn for silicon germanium (SiGe) HBTs [15].

The issue with implementing τ in a nonlinear model is that it shows a distinct bias dependence; see Figure 9 for the previously discussed device. The extracted values of τ are about 65% of the base and collector transit times. Therefore, knowledge of the transit time and a

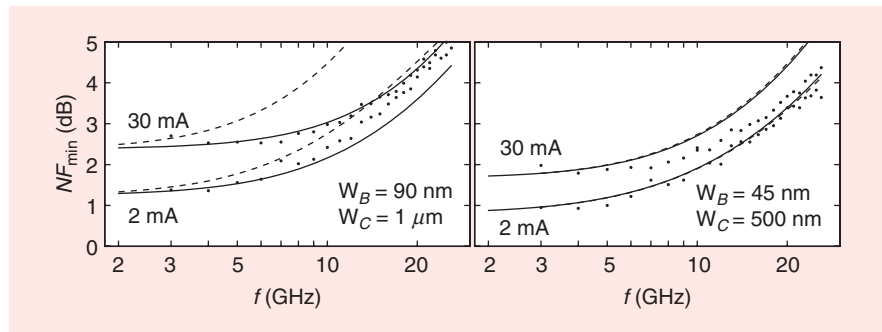


Figure 8. The noise parameters of $3 \times 30\text{-}\mu\text{m}^2$ InGaP/GaAs HBTs from wafers with different base and collector layer thickness (W_B, W_C) at $V_{CE} = 1\text{ V}$. The measured values (\bullet), values simulated with the large-signal noise model ignoring shot-noise correlation ($- -$), and values simulated with the noise model providing a dedicated large-signal description of the correlation time constant τ ($-$) [13].

constant fitting factor are all that need to be known to implement bias-dependent correlated shot noise.

Flicker noise is also important in HBTs since these are the devices of choice for the design of oscillators. HBTs provide lower flicker-noise corner frequencies than FETs. Flicker noise is significant at interfaces, and,

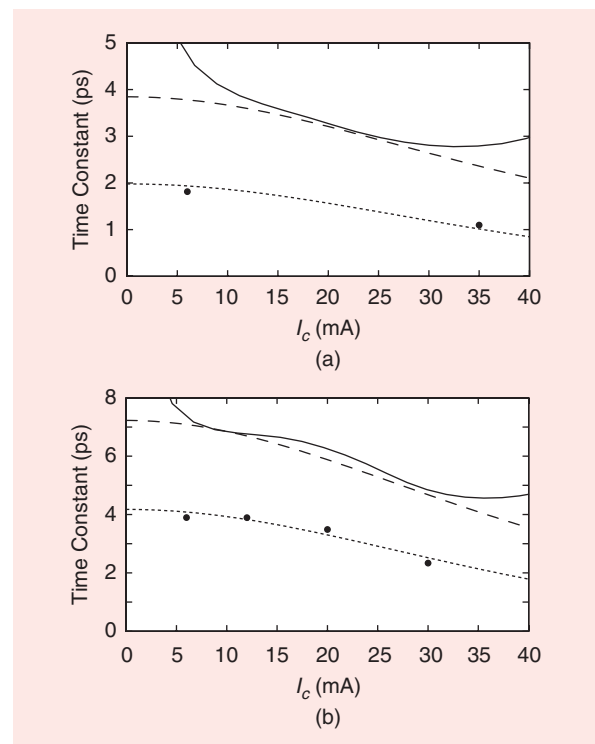


Figure 9. The time constants for a $3 \times 30\text{-}\mu\text{m}^2$ HBT at (a) $V_{CE} = 1\text{ V}$ and (b) $V_{CE} = 4\text{ V}$. The correlation time constant τ determined from noise measurement (\bullet), the total intrinsic time constant of current gain α determined from S -parameter measurement ($-$), the base and collector transit time τ_b and τ_c , approximated by formulas of the FBH large-signal model ($- -$), and 65% of calculated τ_c estimated from FBH large-signal model formulas (\cdots) (from [13]).

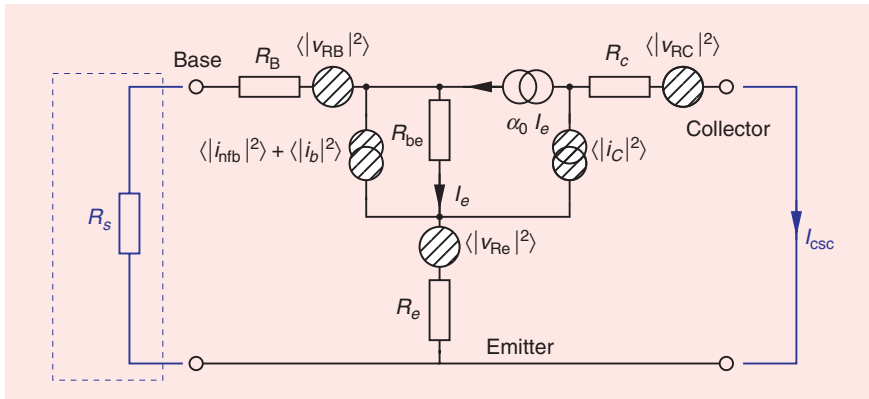


Figure 10. A simplified equivalent circuit for the low-frequency range to explain baseband flicker noise.

since the FET channel is commonly located along an interface, these devices exhibit much higher flicker noise compared to HBTs, where the current flows mainly through the bulk.

Flicker noise is present everywhere in a semiconductor device. Figure 10 portrays a simplified equivalent circuit for the measurement of the short circuit noise source at low frequencies. It includes access resistances but omits all capacitances and access inductances, as their contribution should be low at frequencies below 1 MHz.

For HBTs, the most important source is located at the base-emitter junction. The noise spectrum follows the law given in (9). Figure 10(a) illustrates a measurement of an InGaP/GaAs HBT. A step, as expected from the corner frequency of a Lorentz spectrum, is visible at about 100 kHz; below 1 kHz, an additional increase according to a $1/f$ law is observed. The figure illustrates the measurement and simulation at three currents, and the model predicts the bias and frequency dependence well. This noise source is traditionally the only flicker

Residual Phase Noise

The term “residual phase noise,” as we understand it here, is used to describe the phase noise added to a carrier signal by an amplifier. A basically linear amplifier can add to the phase noise if the carrier signal’s amplitude is fluctuating. The amplitude noise gets translated into phase noise due to the amplitude-modulation to phase-modulation (AM-to-PM) conversion of the amplifier. Low AM-to-PM conversion is therefore advisable for oscillator-buffer amplifiers. The article describes a second source of residual phase noise that is observed due to cyclostationary noise when a fairly linear GaAs transistor is driven by a rather large signal.

noise source accounted for in bipolar transistor models.

However, if the model provides only this noise source, it might not be able to predict the noise if the HBT is connected to a source impedance different from the measurement condition. In our case, if the source resistance is changed from a very high value (10,000 Ω) to a very low value (10 Ω), the model fails, as seen in the blue line in Figure 11(b). The reason is that the low source resistance can be considered to effectively short

circuit the base-emitter flicker noise current. Thus, at least a second flicker noise source is present, and it is assumed that the emitter cap layer, acting as a ballasting resistance, adds additional flicker noise, which now becomes visible. The red curve shows the performance of the model with two sources [11].

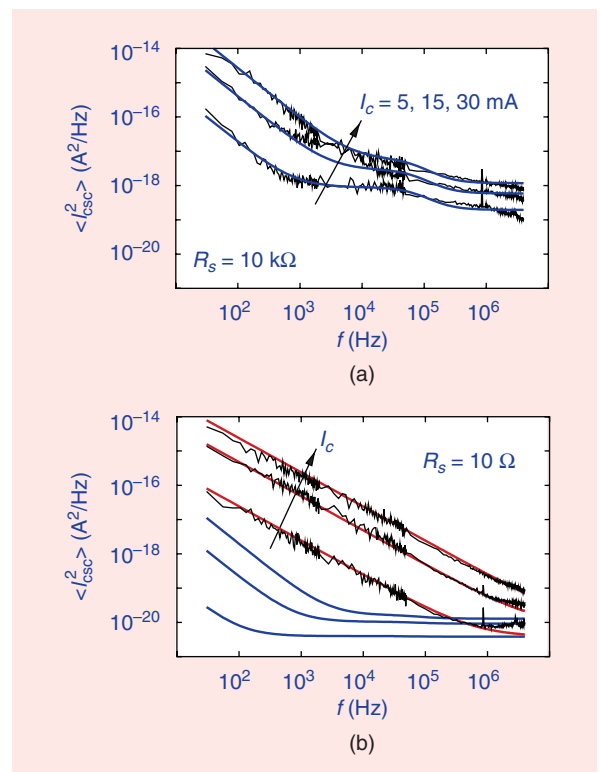


Figure 11. A measured short circuit flicker-noise current spectrum for a $3 \times 30\text{-}\mu\text{m}^2$ InGaP/GaAs HBT, measured and modeled as shown in Figure 10, with the source resistance R_s as given in the graphs. (a) High-impedance source measurement (black lines) simulation with full model (blue). (b) Low-impedance measurement (black curve) simulation with base-emitter flicker noise source only (blue curve) and full noise model (red curve).

Example: SiGe HBT Oscillator With Buffer Amplifier

SiGe HBTs are the devices of choice for oscillator design. Due to their low flicker-noise corner frequency, the transistors exhibit the lowest phase noise in oscillators. A typical oscillator design includes a buffer amplifier that boosts the output power and isolates the oscillator output from the initially unknown or varying load impedance.

From the standpoint of noise simulation, we face a number of challenging noise processes. In the oscillator, flicker noise gets upconverted to the oscillation frequency due to a mixing process in the nonlinearly driven transistors. This upconverted noise is the main contribution to the phase noise close to the oscillation frequency. The buffer amplifier is commonly operated in saturation for maximum output power and good efficiency. Thus, it is also in nonlinear operation, and its noise figure can be expected to exceed the linear spot-noise figure significantly due to the higher peak currents and gain compression [12], [36]. In the buffer amplifier, flicker noise also gets upconverted due to nonlinearities. A third effect that degrades noise performance is AM-to-PM conversion, i.e., that the buffer amplifier translates fluctuations in the oscillator amplitude into phase noise.

However, all of these mechanisms are caused by the nonlinear circuit operation and can indeed be

simulated by standard harmonic-balance simulators and models. We will look into GaAs devices later on, where this statement becomes questionable. But, for silicon or SiGe bipolar transistors, it seems that nonlinear noise modeling is applicable.

As an example, a 100-MHz crystal oscillator with a buffer amplifier is built and simulated. The oscillation frequency is kept rather low to focus on the nonlinear noise behavior, which could easily be shadowed by lines and parasitics at gigahertz frequencies. The design was carried out using a BFG540W packaged SiGe HBT by Infineon and the SPICE model parameter set provided by the manufacturer. The circuit schematic of the crystal oscillator is portrayed in Figure 12, while Figure 13 illustrates the buffer amplifier. The buffer amplifier is in a common-base configuration to take advantage of its good noise properties and high reverse isolation. Its simulated 1-dB compression point is at -12 dBm at the input, while the oscillator is simulated to provide 5 dBm of output power. The amplifier is thus operated in saturation.

Simulation with Ansoft Harmonica (now Ansys Designer) is compared to the measurement in Figure 14. The simulation also shows the effect of a crystal filter at the output of the circuit as used in the measurement, which reduces the noise far from the carrier. Taking into account that all passives are represented by ideal models and that the manufacturer's transistor model parameter set was used

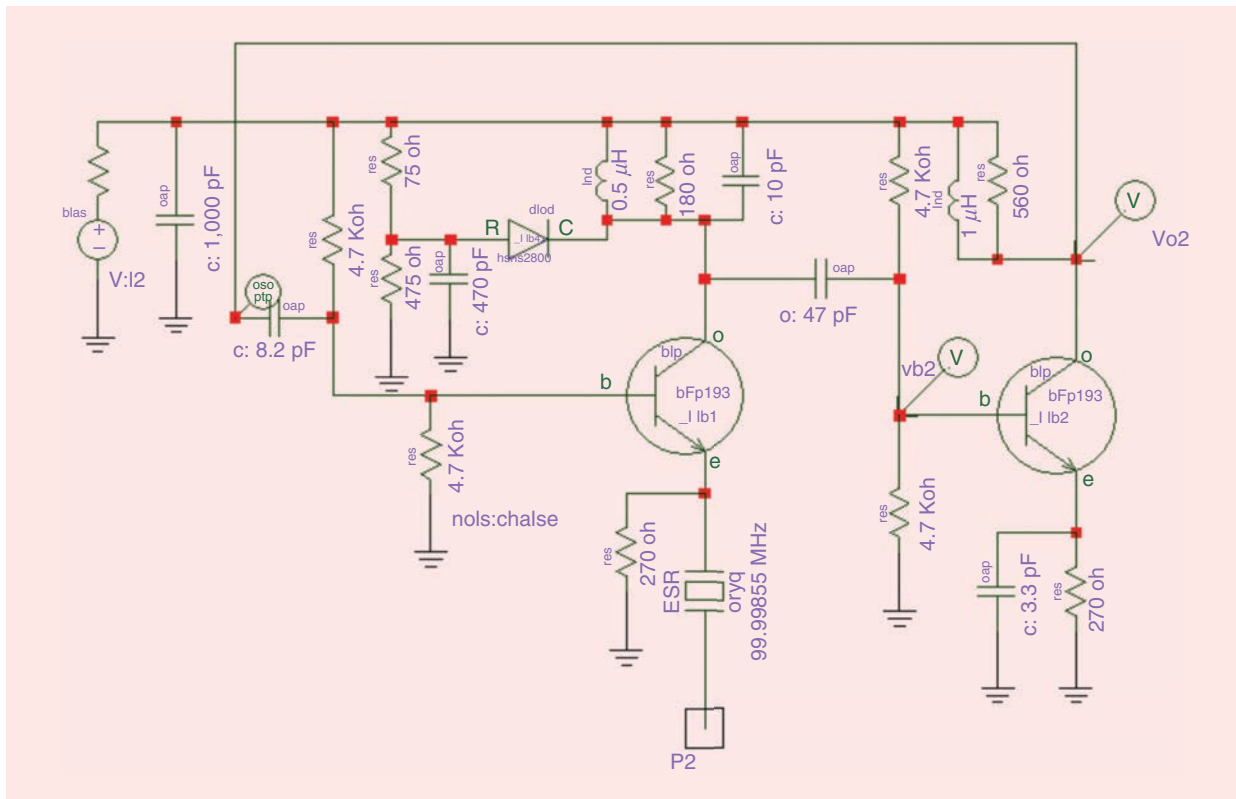


Figure 12. A 100-MHz crystal oscillator.

Oscillator Phase Noise

An oscillator is a nonlinear device that results in an upconversion of the low-frequency flicker noise to the oscillation frequency, broadening its spectrum.

To explain the frequency dependence of the phase noise, we can rely on the simple model depicted in Figure S4. For the oscillator operating in steady state, it is possible to model all of the noise caused by a single source, adding a noise voltage V_{in} to the input of the amplifier. The rest of the oscillator is modeled as a feedback system with a broadband amplifier providing a gain G considered to be constant for the frequencies of interest and a frequency selective feedback through a bandpass with transfer function $H(j\omega)$. We assume that the bandpass is narrow band, providing a bandwidth (BW) $2\omega_Q$, and is mainly comprised of a resonator with quality factor Q . As noise is broadband, it exists inside and outside the passband. Inside the passband, the transfer function is given by

$$V_{out} = \frac{G}{1 + G \cdot H(j\omega)} \cdot V_{in}. \quad (S1)$$

At the oscillation frequency, an output voltage V_{out} is observed, even without excitation voltage V_{in} , so that

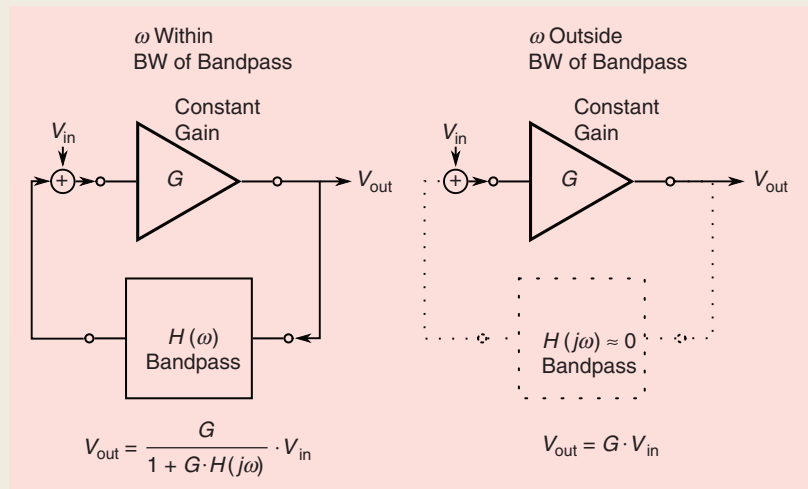


Figure S4. A simple model explaining the origin of oscillator phase noise.

$G \cdot H(j\omega_c) = -1$ holds. Phase noise is observed close to the carrier frequency ω_c , with $\omega_c + \omega_m \approx \omega_c$. The loop gain can be linearized by a Taylor series,

$$G \cdot H(\omega_c + \omega_m) \approx -1 - \frac{\partial[G \cdot H(\omega)]}{\partial\omega} \Big|_{\omega=\omega_c} \cdot \omega_m. \quad (S2)$$

Taking advantage of the approximation, we get

$$V_{out} = \frac{G}{\frac{\partial[G \cdot H(\omega)]}{\partial\omega} \Big|_{\omega=\omega_c}} \cdot \frac{1}{\omega_m} \cdot V_{in}, \quad (S3)$$

without fine tuning to the devices under test, it has to be stated that the agreement of the two curves is indeed extremely good. This holds especially true for the technically more interesting offset frequencies of 100 Hz–100 kHz, where even the simulation is too pessimistic [37]. (See “Oscillator Phase Noise.”)

Bias-Dependent FET Noise Model

Bias-dependent FET noise modeling is more complicated since the complex physics of the charge transport in the channel also control the noise performance. As a result, small-signal noise models come with three (R , P , C) or two (T_g , T_d) fitting parameters. Even a single temperature only of the Pospieszalski model, T_g , is linked to the device temperature.

For CMOS devices, a number of physics-based, bias-dependent noise models exist that require a good knowledge of physical parameters, such as electron velocity and charge density in the channel. Based on

these parameters, different formulations for the bias-dependence of the R , P , and C parameters are derived, e.g., in [16]–[18].

For III-V devices, the physics are more complex and the technology less well controlled. Thus, the bias dependence of the Pucel [19] and Pospieszalski [20] noise models is realized by fitting functions. It is a drawback of this solution, however, that it still requires knowledge of small-signal quantities, such as C_{gs} , g_m , or R_{ds} , while the large-signal model is formulated in terms of currents and charges.

To get around the issues concerning R_{ds} , the authors proposed defining the drain noise source of the Pospieszalski model depending on I_{ds} instead. The following formulation was chosen:

$$\begin{aligned} \langle i_{cn}^2 \rangle &= 4k\Delta f T_d \\ &\stackrel{!}{=} 2q\Delta f X'_d I_{ds}, \end{aligned} \quad (14)$$

for frequencies close to ω_c . Within the passband of the feedback loop, we can conclude that noise is multiplied by $1/\omega_m$ in voltage or $1/\omega_m^2$ in power. Outside of the feedback passband, feedback is blocked, and the noise is amplified according to the amplifier gain G .

Resulting phase-noise spectra are shown in Figure S5. Consider that the flicker noise of a transistor within the oscillator has a corner frequency ω_f . This noise gets upconverted to the oscillation frequency ω_c . The slope of the phase noise now depends on which frequency is higher, ω_f or ω_Q . For $\omega_m > \omega_Q$, the phase noise is determined by the upconverted noise and shows the frequency slope as in the baseband. Within the BW, the slope is weighted by $1/\omega^2$. This leads to spectra

$\propto 1/\omega^3$ for the upconverted flicker noise within the BW of the resonator and to spectra $\propto 1/\omega^2$ for white noise within the BW of the resonator. Outside the BW of the resonator, the frequency dependence of the noise spectra is not altered so that spectra

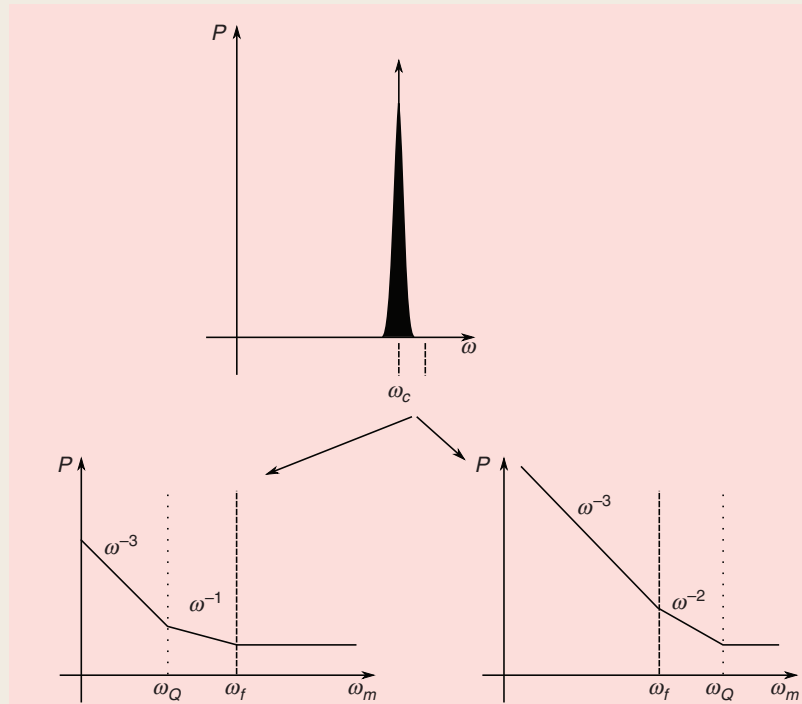


Figure S5. The phase-noise spectra of oscillators.

$\propto 1/\omega$ for the upconverted flicker noise outside and frequency-independent white noise are observed. The figure shows the typical shapes of phase noise. A more detailed interpretation of the spectra provides Leeson's formula [see (8)].

with the electron charge q and the noise bandwidth Δf . The drain temperature T_d is replaced by the fitting factor X'_d . Note that this approach is simply a reformulation of the noise source without any physical explanation. But, in measurement, it turned out that the new fitting parameter X'_d depends only on the current I_{ds} , which is easily described by a simple formula like

$$X'_d = NP_1 - NP_2 \cdot (\tanh(NP_3 \cdot I_{ds}) + \tanh(NP_4 \cdot I_{ds})), \quad (15)$$

with fitting parameters NP_1 – NP_4 (Figure 15).

Example: GaN LNA Subject to a Blocking Signal

LNAs may receive not only the signal of a very low power level at the desired frequency but also unwanted blocking or jamming signals at frequencies nearby. Band-selection filters between antennas and LNAs attenuate out-of-band signals. However, a large-signal

jammer may still drive an LNA into nonlinear operation, even though the received signal is amplified in the small-signal domain.

A number of investigations were published addressing the measurement of noise and gain of an LNA in the presence of a blocking signal. Most authors measured the residual phase noise to derive the noise figure from the white noise floor far from the large-signal frequency [21]–[25]. This type of measurement resembles a phase-noise measurement, but, instead of the oscillator phase noise, the phase noise of an amplifier is measured with a carrier signal injected from a signal source.

Another approach enables the measurement of all four noise parameters through a classical source-pull noise measurement while, at the same time, a jamming signal is injected at a higher frequency [26]. The results of these studies can be briefly summarized as follows:

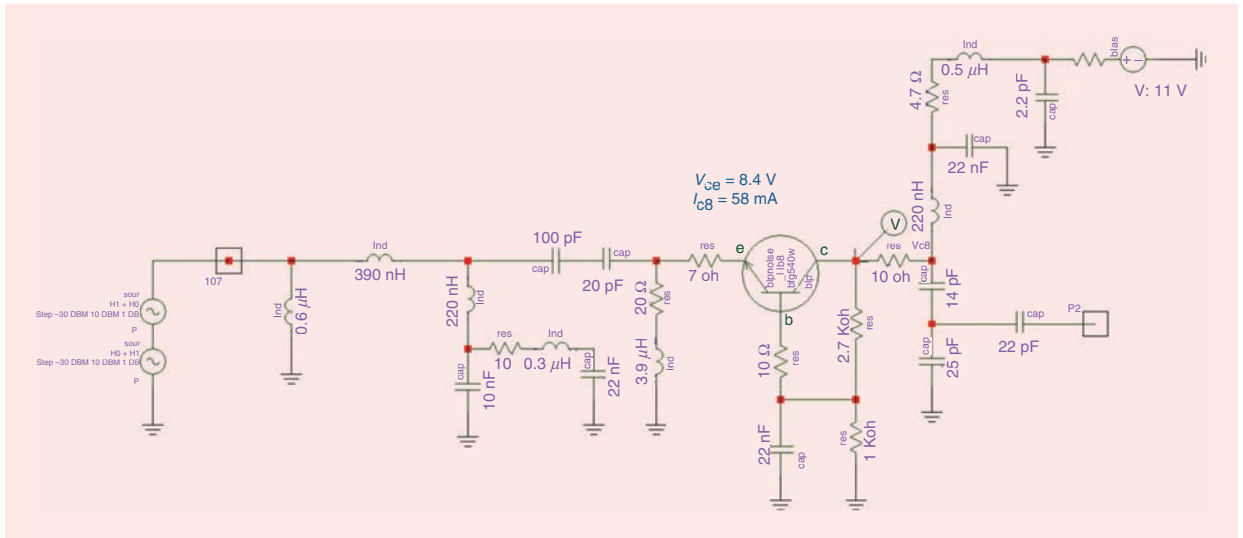


Figure 13. A common-base buffer amplifier for the 100-MHz crystal oscillator in Figure 12.

- The noise figure increases with the jamming signal power. Figure 16 illustrates a measurement of two different commercial LNAs.
- A sharp increase in the noise figure is observed once the LNA is driven into compression.
- The increase in noise figure cannot be explained by the reduction of the LNA gain alone [24]. Assuming that the noise powers provided by the signal source and by the device are independent of the input power, it is possible to approximate the noise figure based on its small-signal value and gain,

$$F_{50} = \frac{SNR_{in}}{SNR_{out}} = \frac{P_{Nout}}{P_{Nin} \cdot G}$$

$$\Rightarrow F_{50}(P_{in}) \approx F_{50}(0) \cdot \frac{G(0)}{G(P_{in})}, \quad (16)$$

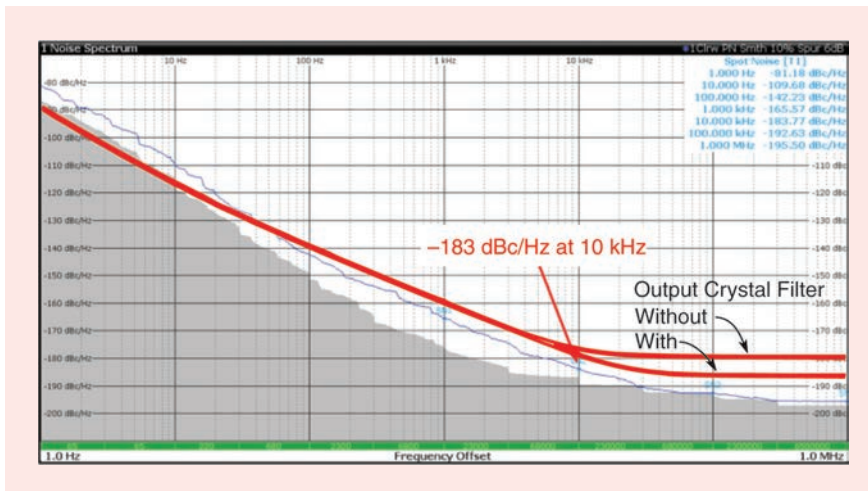


Figure 14. The measured and simulated phase-noise spectrum of the oscillator (Figure 12) with the buffer amplifier (Figure 13).

where the index 50 denotes the noise figure in a 50-Ω system. From this analysis, one would expect that NF_{50} increases by 1 dB if the gain drops by 1 dB.

Figure 16 depicts the measured NF_{min} of two LNAs at 4 GHz as a function of 10-GHz blocking signal power. The devices differ in terms of the small-signal noise figure and in terms of the 1-dB compression points (P_{1dB}). The device with the lower small signal NF_{min} provides a lower P_{1dB} (squares), which causes the noise figure to be much more susceptible to blocking signal power [26].

To investigate how this behavior could be simulated, we measured the 50-Ω noise figure (NF_{50}) of a $4 \times 125\text{-}\mu\text{m}$ GaN high-electron mobility transistor (HEMT) on silicon-carbide substrate in 25-μm technology from the Ferdinand-Braun-Institut [29] on-wafer, using the setup described in [26]. The result is displayed in Figure 17 [27], [28]. Two types of nonlinear noise models were investigated: a bias-dependent Pucel model (dashed lines) and a bias-dependent Pospieszalski model (solid lines).

For comparison, the analytical approximation (16) is plotted as well (dashed line). This approximation is too pessimistic for the bias point shown here. The measured noise figure (symbols) increases in a much less pronounced way and at higher blocking powers. The nonlinear simulation results follow the measured noise figure very well.

Both models contain empirical descriptions of the bias dependence of the parameters R , P , and C or T_g and T_d . In the simulation, the dc bias and temperature under the large-signal conditions are calculated to determine the intrinsic noise sources. Thus, the only difference to a small-signal noise analysis is a possible change in bias and temperature, and the noise may undergo mixing processes just like every other electrical signal in the nonlinear circuit.

This analysis shows that a bias-dependent noise description is sufficient to predict white noise even in the nonlinear case. As observed for the small-signal case, both models work well despite their different physics-based derivation and model topology. An important fact for this finding to hold true is that the blocking and signal frequencies are spaced in a way that the blocking signal's phase noise sidebands fade away and do not affect the signal frequency. The examples given in the "Truly Nonlinear Noise Models" section will address the question of phase noise in III-V devices, especially how flicker noise gets upconverted in large-signal operation.

Truly Nonlinear Noise Models

The models presented so far were bias-dependent rather than truly nonlinear since the noise sources were determined from the static bias point and temperature that is reached in steady-state nonlinear operation.

A truly nonlinear noise model will need to account for more: it has to predict the upconversion of flicker noise independent of the circuit nonlinearity. The following examples highlight that bias-dependent modeling is often not sufficient. Specifically, in a circuit that works without dc current, the model would predict no phase-noise sidebands at all. So let us look into the measurement and simulation of a resistive GaAs HEMT mixer.

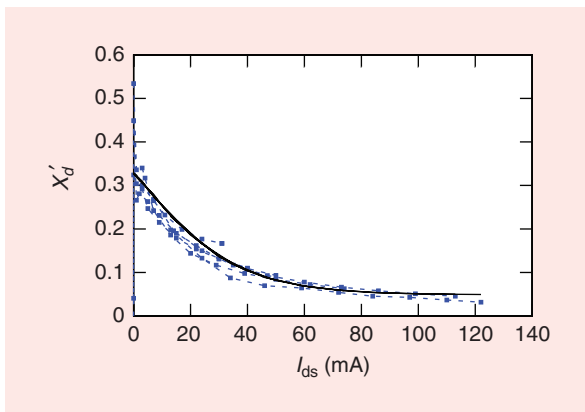


Figure 15. The bias dependence of an alternative Pospieszalski noise model drain parameter X'_d for a $4 \times 125\text{-}\mu\text{m}$ GaN high-electron mobility transistor (HEMT).

Example: GaAs HEMT Resistive Mixer

A resistive mixer in its simplest form is a single FET used as a switch. Applying an LO signal to the gate turns the HEMT into a switch that is periodically opened and closed and thereby chops any small signal applied to the drain, generating mixing products. Since the drain-source dc voltage is kept at zero volts, no dc currents are flowing, and a traditional model would predict no flicker noise contribution by the HEMT. Figure 18 describes the equivalent circuit of the investigated structure. The switch lets the drain dc voltage float or shorts it to the ground. In the case of a floating dc drain voltage, leakage of the LO signal leads to a drain-source dc current promoting flicker noise, but forcing $V_{DS} = 0\text{ V}$ prevents this effect. This example is taken from the first work known to the authors that experimentally proved

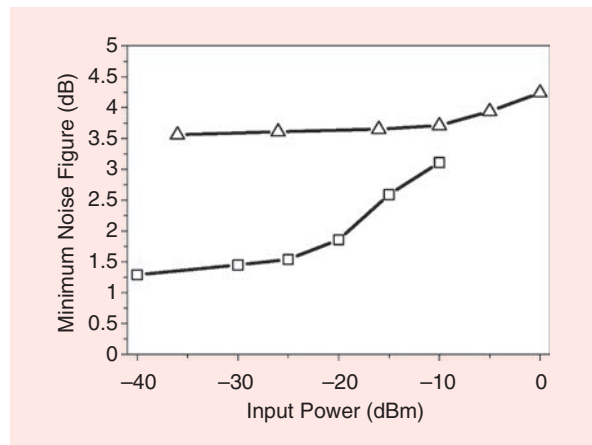


Figure 16. The measured NF_{min} of two LNAs at 4 GHz as a function of 10-GHz blocking signal power. The 1-dB compression points of the two LNAs are -13 dBm (squares) and -6 dBm (triangles) [26].

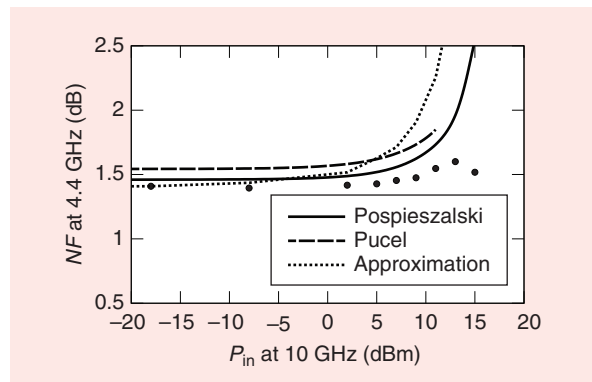


Figure 17. The measured NF_{50} of a $4 \times 125\text{-}\mu\text{m}$ GaN HEMT at $V_{DS} = 4\text{ V}$, $I_{DS} = 50\text{ mA}$. Noise was measured at 4.4 GHz as a function of 10-GHz blocking signal power. The measurement (bullets) is compared to simulations using bias-dependent Pospieszalski (solid line) and Pucel (dashed line) models and with the analytical approximation according to (16) [28].

the existence of cyclostationary noise in a circuit and proposed the respective flicker-noise model [30].

Measurement of the spectral power density at a 1-kHz offset from the LO frequency is depicted in Figure 19 as a function of the LO frequency. It is observed that noise is reduced by suppressing the HEMT dc current, but only by 5–10 dB, not to zero. The simulation required the implementation of a cyclostationary HEMT flicker-noise source. It is worthwhile to note that, in the absence of a dc current, flicker noise upconversion happens entirely through the noise process, i.e., inside the noise source.

Example: GaAs HBT Oscillators

Phase noise is the main limiting factor in oscillators, and it is therefore imperative to predict it well in circuit simulation. Phase noise arises from upconverted flicker noise that is generated and upconverted in the nonlinearly driven transistor. While it seems that bias-dependent noise models work well for silicon

bipolar and heterobipolar devices, it turned out that noise upconversion is not predicted well in GaAs HBTs. Two enhancements to the flicker-noise model were required for reliable oscillator phase-noise simulation: at least two flicker noise sources are needed, as discussed earlier, and these noise sources are required to be implemented as cyclostationary noise sources [31]–[33]. These empirical publications considering measurement and harmonic-balance simulation are supported by a number of investigations based on numerical physical semiconductor simulation [34], [35].

To investigate the flicker noise behavior of InGaP/GaAs HBTs, we measured the residual phase noise (see “Residual Phase Noise”) of a $3 \times 3\text{-}\mu\text{m}^2$ device from the foundry of the Ferdinand-Braun-Institut [31]. The measurement was carried out in the setup described in [21], which is capable of measuring the phase noise of a device under an open-loop condition, controlling the carrier frequency and power injected into the device.

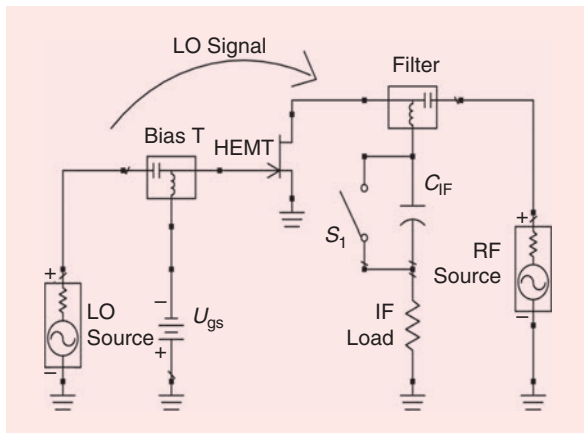


Figure 18. A single-ended resistive FET mixer for theoretical and experimental low-frequency noise investigations [30].

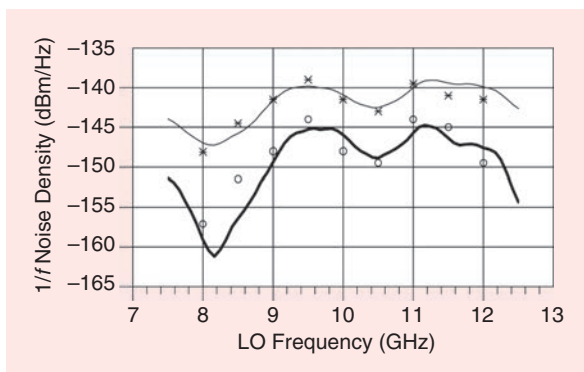


Figure 19. Power spectral density at 1 kHz, LO power = 0 dBm. The thick lines are simulations with a dc path (circles: measurement), and the thin lines are simulations without a dc path (stars: measurement) [30].

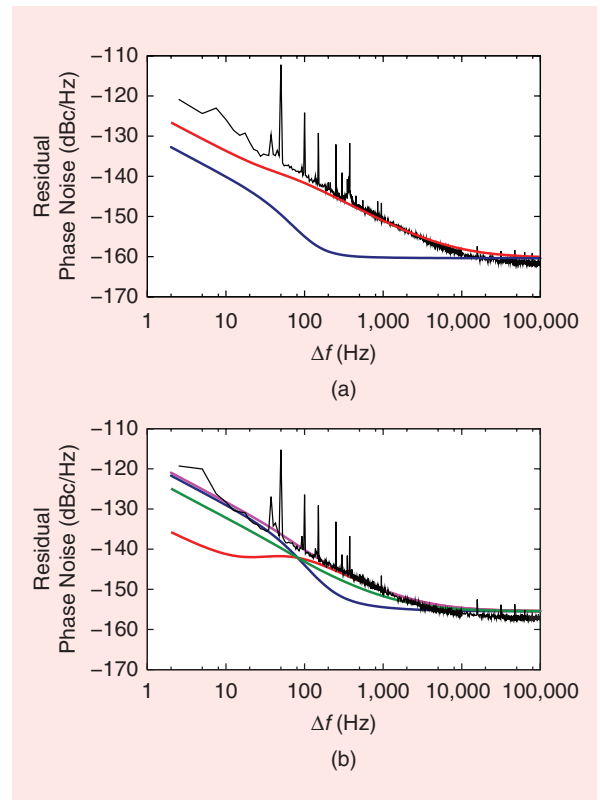


Figure 20. The measured and simulated residual phase noise of $3 \times 30\text{-}\mu\text{m}^2$ HBT with available input power (a) $P_m = -11$ dBm and (b) $P_m = -16$ dBm. $V_{ce} = 3$ V, $I_c = 30$ mA, and $f = 3.5$ GHz. The measurements (black curves) are compared to simulations using conventional low-pass, low-frequency noise sources (blue), cyclostationary sources (red), partly correlated cyclostationary sources (magenta), and superposition of cyclostationary and low-pass sources (green) [7], [31].

Figure 20 describes the result of the investigation [31]. The device is driven with an input power of -16 and -11 dBm, which is not enough to drive it into compression. Thus, it could be expected that the upconversion of the baseband flicker noise due to the HBT nonlinearity alone (blue curve) should lead to a low noise level. At least in Figure 20(a), it is observed that the model underestimates the residual phase noise by 10–20 dB. Implementing cyclostationary noise sources adds an independent second mechanism of phase-noise sideband generation. The red curve shows a simulation relying on cyclostationary sources. This phase-noise sideband is the result of the cyclostationary noise undergoing a mixing process due to device nonlinearities. The figure shows that a cyclostationary noise source is indeed required to predict the phase noise in InGaP/GaAs HBTs.

However, this might not be as easy, as Figure 20(b) indicates, for a slightly different measurement condition. For this measurement, the cyclostationary noise source implementation fails for offset frequencies below 100 Hz, while the standard implementation yields good results. The only reason that the cyclostationary implementation could ever yield lower residual phase noise is that the upconverted baseband flicker noise and the noise source's phase-noise sideband cancel out in the mixing process. The magenta and green curves show the approaches to solve the issue. For the magenta curve, the cyclostationary noise source is defined in a way that the noise sideband and the baseband flicker noise are partly uncorrelated. While this works fine, there is no physical theory backing this approach. The green curve simply assumes two noise sources: a standard implementation and a cyclostationary implementation in parallel, which yields an expected 3-dB offset to the magenta curve. However, whether a flicker noise source is observed to be best described through a cyclostationary source or through the standard description depends on the nonlinear processes in the semiconductor [7], and it is not unlikely that both types are observed in parallel.

In practice, however, it seems that, for the simulation of GaAs HBT oscillators, cyclostationary noise sources are required [32], [33], while no reports are found in the literature suggesting that it might also be necessary for SiGe oscillators as well. As an example, a result from [33] is cited in Figure 21. It illustrates the measured phase noise of a 4.2–4.5-GHz voltage-controlled oscillator MMIC (black lines) together with simulations based on cyclostationary flicker noise sources (green lines), which still show a certain discrepancy with increasing frequency offset from the carrier. Additionally, implementing cyclostationary shot-noise sources finally yields an almost perfect fit.

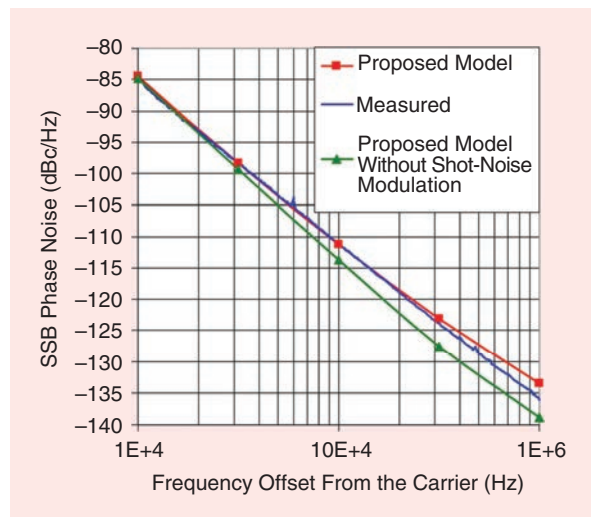


Figure 21. The phase noise spectrum of a 4.2–4.5-GHz voltage-controlled oscillator MMIC. The measurements (black curve) are compared to simulations with cyclostationary flicker noise sources (green curve) and cyclostationary flicker and shot-noise sources (red curve) [33].

Regarding oscillator phase noise, it can be concluded that the tools required for accurate simulation are the standard harmonic-balance simulator and transistor models that include cyclostationary noise source formulations to a certain extent. The question, however, of which transistor requires which type of model depends on the technology and can hardly be stated a priori.

Conclusions

Predicting noise through circuit simulation is crucial in nonlinear circuits, such as low-noise and buffer amplifiers, oscillators, or mixers. The first prerequisite to achieving this goal is a nonlinear circuit simulator capable of simulating noise in the nonlinear domain. Fortunately, mainstream harmonic-balance simulators are able to calculate how a small-signal quantity such as noise gets transferred from a defined source through a nonlinear circuit, including frequency-conversion effects.

The challenge remains of defining noise sources as a part of a transistor model description. A circuit designer needs to check carefully whether a nonlinear model includes an appropriate description of the noise behavior. In many cases, however, traditional noise models that reflect the bias dependence of the noise are sufficient and enable accurate simulation. However, especially for III-V devices, a dedicated cyclostationary implementation of the noise sources is required, which is, so far, not accounted for in transistor models provided with circuit simulators.

Acknowledgment

The authors would like to thank Dr. Ulrich L. Rohde for fruitful discussions and continuous support of their work.

References

- [1] H. Hillbrand and P. Russer, "An efficient method for computer aided noise analysis of linear amplifier networks," *IEEE Trans. Circuits Syst.*, vol. 23, no. 4, pp. 235–238, 1976. doi: 10.1109/TCS.1976.1084200.
- [2] G. D. Vendelin, A. M. Pavio, and U. L. Rohde, *Microwave Circuit Design: Using Linear and Nonlinear Techniques*, 3rd ed. Hoboken, NJ: Wiley, 2021.
- [3] R. A. Pucel, H. A. Haus, and H. Statz, "Signal and noise properties of gallium arsenide microwave field-effect transistors," *Adv. Electron. Electron Phys.*, vol. 38, pp. 195–265, 1975. doi: 10.1016/S0065-2539(08)61205-6.
- [4] M. W. Pospieszalski, "Modeling of noise parameters of MESFETs and MODFETs and their frequency and temperature dependence," *IEEE Trans. Microw. Theory Techn.*, vol. 37, no. 9, pp. 1340–1350, Sept. 1989. doi: 10.1109/22.32217.
- [5] P. Heymann, M. Rudolph, H. Prinzler, R. Doerner, L. Klapproth, and G. Böck, "Experimental evaluation of microwave field-effect-transistor noise models," *IEEE Trans. Microw. Theory Techn.*, vol. 47, no. 2, pp. 156–163, Feb. 1999. doi: 10.1109/22.744290.
- [6] A. V. Der Ziel, "Noise in junction transistors," *Proc. IRE*, vol. 46, pp. 1019–1038, June 1958. doi: 10.1109/JRPROC.1958.286840.
- [7] M. Rudolph and F. Bonani, "Low-frequency noise in nonlinear systems," *IEEE Microw. Mag.*, vol. 10, no. 1, pp. 84–92, Feb. 2009. doi: 10.1109/MMM.2008.930678.
- [8] M. Rudolph, R. Doerner, L. Klapproth, and P. Heymann, "An HBT noise model valid up to transit frequency," *IEEE Electron Device Lett.*, vol. 20, no. 1, pp. 24–26, Jan. 1999. doi: 10.1109/55.737562.
- [9] M. Rudolph and P. Heymann, "Comparative study of shot-noise models for HBTs," in *Proc. Eur. Microw. Integr. Circ. Conf. (EuMIC)*, 2007, pp. 191–194. doi: 10.1109/EMICC.2007.4412681.
- [10] D. B. Leeson, "A simple model of feedback oscillator noise spectrum," *Proc. IEEE*, vol. 54, no. 2, pp. 329–330, Feb. 1966. doi: 10.1109/PROC.1966.4682.
- [11] P. Heymann, M. Rudolph, R. Doerner, and F. Lenk, "Modeling of low-frequency noise in GaInP/GaAs hetero-bipolar transistors," in *Proc. IEEE MTT-S Int. Microw. Symp. Dig.*, 2001, vol. 3, pp. 1967–1970. doi: 10.1109/MWSYM.2001.967295.
- [12] U. L. Rohde, A. K. Poddar, and G. Böck, *Modern Microwave Oscillators for Wireless Applications: Theory and Optimization*. Hoboken, NJ: Wiley, 2005.
- [13] M. Rudolph, F. Korndörfer, P. Heymann, and W. Heinrich, "Compact large-signal shot-noise model for HBTs," *IEEE Trans. Microw. Theory Techn.*, vol. 56, no. 1, pp. 7–14, Jan. 2008. doi: 10.1109/TMTT.2007.911944.
- [14] H. Fukui, "The noise performance of microwave transistors," *IEEE Trans. Electron Devices*, vol. ED-13, no. 3, pp. 329–341, Mar. 1966. doi: 10.1109/T-ED.1966.15689.
- [15] J. Herricht et al., "Systematic compact modeling of correlated noise in bipolar transistors," *IEEE Trans. Microw. Theory Techn.*, vol. 60, no. 11, pp. 3403–3412, Nov. 2012. doi: 10.1109/TMTT.2012.2216284.
- [16] C. H. Chen and M. J. Deen, "Channel noise modeling of deep sub-micron MOSFETs," *IEEE Trans. Electron Devices*, vol. 49, no. 8, pp. 1484–1487, Aug. 2002. doi: 10.1109/TED.2002.801229.
- [17] J. C. J. Paasschens, A. J. Scholten, and R. van Langevelde, "Generalizations of the Klaassen-Prins equation for calculating the noise of semiconductor devices," *IEEE Trans. Electron Devices*, vol. 52, no. 11, pp. 2463–2472, Nov. 2005. doi: 10.1109/TED.2005.857189.
- [18] A. S. Roy and C. C. Enz, "Compact modeling of thermal noise in the MOS transistor," *IEEE Trans. Electron Devices*, vol. 52, no. 4, pp. 611–614, Apr. 2005. doi: 10.1109/TED.2005.844735.
- [19] B.-U. Klepser, C. Bergamaschi, M. Schefer, C. G. Diskus, W. Patrick, and W. Bachtold, "Analytical bias dependent noise model for InP HEMT's," *IEEE Trans. Electron Devices*, vol. 42, no. 11, pp. 1882–1889, 1995. doi: 10.1109/16.469392.
- [20] L. Klapproth, A. Schaefer, and G. Böck, "A bias dependent HEMT noise model," in *Proc. IEEE MTT-S Int. Microw. Symp. Dig.*, 1997, vol. 2, pp. 881–884. doi: 10.1109/MWSYM.1997.602940.
- [21] G. Cibiel, L. Escotte, and O. Llopis, "A study of the correlation between high-frequency noise and phase noise in low-noise silicon-based transistors," *IEEE Trans. Microw. Theory Techn.*, vol. 52, no. 1, pp. 183–190, Jan. 2004. doi: 10.1109/TMTT.2003.821271.
- [22] A. Hati, D. A. Howe, F. L. Walls, and D. Walker, "Noise figure vs. PM noise measurements: A study at microwave frequencies," in *Proc. IEEE Int. Frequency Contr. Symp.*, 2003, pp. 516–520. doi: 10.1109/FREQ.2003.1275144.
- [23] A. Hati, D. A. Howe, F. L. Walls, and D. K. Walker, "Merits of PM noise measurement over noise figure: A study at microwave frequencies," *IEEE Trans. Ultrason., Ferroelectr., Freq. Control*, vol. 53, no. 10, pp. 1889–1894, Oct. 2006. doi: 10.1109/TUFFC.2006.121.
- [24] N. Garmendia and J. Portilla, "Study of PM noise and noise figure in low noise amplifiers working under small and large signal conditions," in *Proc. IEEE MTT-S Int. Microw. Symp. Dig.*, 2007, pp. 2095–2098. doi: 10.1109/MWSYM.2007.380300.
- [25] M. Janković, J. Breitbarth, A. Brannon, and Z. Popović, "Measuring transistor large-signal noise figure for low-power and low phase-noise oscillator design," *IEEE Trans. Microw. Theory Techn.*, vol. 56, no. 7, pp. 1511–1515, July 2008. doi: 10.1109/TMTT.2008.924350.
- [26] C. Chambon, L. Escotte, S. Gribaldo, and O. Llopis, "C-band noise-parameter measurement of microwave amplifiers under nonlinear conditions," *IEEE Trans. Microw. Theory Techn.*, vol. 55, no. 4, pp. 795–800, Apr. 2007. doi: 10.1109/TMTT.2007.893676.
- [27] M. Rudolph, L. Escotte, and R. Doerner, "Modeling nonlinear white noise in GaN HEMT devices," *Frequenz*, vol. 69, nos. 1–2, pp. 47–55, Dec. 2014. doi: 10.1515/freq-2014-0121.
- [28] M. Rudolph, L. Escotte, and R. Doerner, "GaN HEMT noise model performance under nonlinear operation," in *Proc. 44th Eur. Microw. Conf. (EuMIC)*, 2014, pp. 1416–1419. doi: 10.1109/EuMC.2014.6986711.
- [29] M. Rudolph, R. Doerner, E. Ngnintedem, W. Heinrich, "Noise modeling of GaN HEMT devices," in *Proc. 12th Eur. Microw. Integr. Circuits Conf. (EuMIC)*, 2012, pp. 159–162.
- [30] M. Margraf and G. Boeck, "Analysis and modeling of low-frequency noise in resistive FET mixers," *IEEE Trans. Microw. Theory Techn.*, vol. 52, no. 7, pp. 1709–1718, July 2004. doi: 10.1109/TMTT.2004.830486.
- [31] M. Rudolph, F. Lenk, O. Llopis, and W. Heinrich, "On the simulation of low-frequency noise upconversion in InGaP/GaAs HBTs," *IEEE Trans. Microw. Theory Techn.*, vol. 54, no. 7, pp. 2954–2961, July 2006. doi: 10.1109/TMTT.2006.877055.
- [32] J.-C. Nallatamby, M. Prigent, M. Camiade, A. Sion, C. Gourdon, and J. J. Obregon, "An advanced low-frequency noise model of GaInP/GaAs HBT for accurate prediction of phase noise in oscillators," *IEEE Trans. Microw. Theory Techn.*, vol. 53, no. 5, pp. 1601–1612, May 2005. doi: 10.1109/TMTT.2005.847050.
- [33] P. A. Traverso, C. Florian, M. Borgarino, and F. Filicori, "An empirical bipolar device nonlinear noise modeling approach for large-signal microwave circuit analysis," *IEEE Trans. Microw. Theory Techn.*, vol. 54, no. 12, pp. 4341–4352, Dec. 2006. doi: 10.1109/TMTT.2006.885991.
- [34] F. Bonani, S. Donati Guerrieri, and G. Ghione, "Physics-based simulation techniques for small- and large-signal device noise analysis in RF applications," *IEEE Trans. Electron Devices*, vol. 50, no. 3, pp. 633–644, Mar. 2003. doi: 10.1109/TED.2003.810477.
- [35] J. E. Sanchez, G. Bosman, and M. E. Law, "Two-dimensional semiconductor device simulation of trap-assisted generation-recombination noise under periodic large-signal conditions and its use for developing cyclostationary circuit simulation models," *IEEE Trans. Electron Devices*, vol. 50, no. 5, pp. 1353–1362, May 2003. doi: 10.1109/TED.2003.813448.
- [36] U. L. Rohde, E. Rubiola, and J. C. Whitaker, *Microwave and Wireless Synthesizers: Theory and Design*, 2nd ed. Hoboken, NJ: Wiley, 2021.
- [37] A. Poddar, U. Rohde, and A. Apte, "How low can they go?: Oscillator phase noise model, theoretical, experimental validation, and phase noise measurements," *IEEE Microw. Mag.*, vol. 14, no. 6, pp. 50–72, Sept./Oct. 2013.



IEEE Microwave and Wireless Components Letters

Special Issue on

Radar and Microwave Sensor Systems

Submission date: 1 September 2021, Publication date: January 2022

Motivation:

This Special Issue is devoted to technical papers on radar and sensor systems in the microwave and millimeter-wave bands. Massive technological progress has been made in recent years at the microwave device and component level, enabling new research directions on sophisticated microwave and millimeter-wave systems. Among the most significant fields of application for such systems has been sensor technology, with a major emphasis on radar systems. Interest in automotive sensing, wireless human-computer interaction, biometric measurements, industrial monitoring, and target tracking among many other applications has driven this interest. Advances in device and component technology are supporting system design concepts that treat the microwave hardware as a co-design element of the system, along with signal processing and antenna design. Such co-design is of particular importance in radar and sensor systems, where a rapidly increasing number of wireless devices and an increasingly crowded spectrum necessitates the design and use of specialized signals (both temporal waveform designs and spatial beamforming) to maintain and improve sensor performance. Systems designed for general broad applicability are becoming more challenging to implement, while specialized systems that co-design the aperture, microwave hardware, and signal processing are becoming increasingly relevant. Technologies such as digital array radar, distributed and networked sensors, computational imagers, high-sensitivity Doppler radars, and integrated millimeter-wave radar, to name only a few, have supported system-level developments. This Special Issue is intended to highlight advancements in these and other microwave system-level technologies.

Topics of interest include, but are not limited to:

- *Microwave and millimeter-wave radar and sensor system design and demonstration:* radar and sensor demonstrations, beamforming systems, passive and networked radar, joint radar and communication systems, joint sensing and communications systems, synthetic aperture radar, new and emerging sensor system implementations.
- *Millimeter-wave imaging systems:* active and passive phased arrays, MIMO arrays, interferometric systems, signal processing for imaging systems, calibration.
- *Distributed, networked and cooperative radar:* network architectures, repeaters, coherent and non-coherent networks, cooperative sensor systems, distributed MIMO.
- *Hardware/software co-design:* MIMO antenna arrays, angle estimation, hardware-supported signal processing approaches, modulation schemes for MIMO sensing systems.
- *Millimeter-wave sensor MMICs and components:* MMICs and circuits using solid state and non-solid state technologies, multi-channel transceivers, power amplifier, complex systems on chip, signal cancelling chips for duplex systems, integrated antennas.
- *Experimental demonstrations of novel modulation schemes for sensing and radar applications:* digital modulation, OFDM, PMCW, chirp sequence systems, non-linear modulations, novel waveform design and demonstration.
- *Applications of radar and microwave sensor systems:* automotive and industrial applications, wireless human-computer interaction, biometric measurements, industrial monitoring, target tracking, remote sensing, new and emerging sensor applications.

Authors must consult the link <https://mtt.org/publications/microwave-and-wireless-components-letters/author-information-letters/> for submission instructions.

Guest Editors

Prof. Christian Waldschmidt
University of Ulm

Prof. Jeffrey Nanzer
Michigan State University

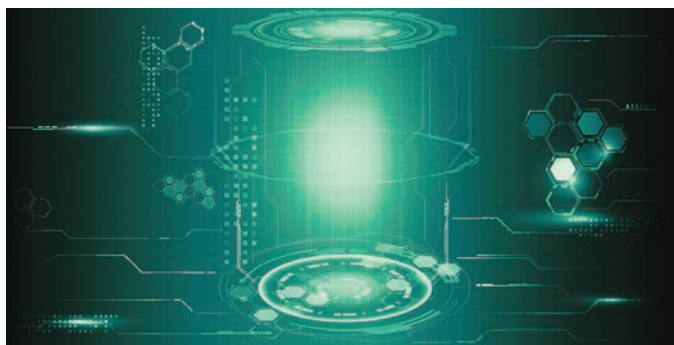


Application Notes

The Fairy Tale of Simple All-Digital Radars: How to Deal With 100 Gbit/s of a Digital Millimeter-Wave MIMO Radar on an FPGA

■ **Benedikt Schweizer, Alexander Grathwohl, Gilberto Rossi, Philipp Hinz, Christina Knill, Simon Stephany, Herman Jalli Ng, and Christian Waldschmidt**

Driven by the demand for automotive assistance and safety systems, millimeter-wave (mm-wave) radars have received a lot of attention in the last decade, leading to highly sophisticated radar sensors being used in a large variety of different applications from automotive and industrial sensing to security. These sensors are mostly based on frequency-modulated continuous wave (FMCW) or chirp-sequence modulation schemes. However, a disruptive develop-



©SHUTTERSTOCK.COM/ALLEACHDAY

ment is observable in the field of mm-wave radars: the focus is on digital radars! The digital signal generation not only allows the flexible adoption of modulation parameters during operation but even enables the use of multiple waveforms and modulation schemes. Since the

transmit (Tx) signal is designed precisely in terms of time and spectrum utilization, it further enables simplified cooperation between sensors. This helps to avoid interference [1]–[3] and enables the operation of multiple sensors in a sensor network [4]. Additionally, unfiltered and uncut channel information is available at the receiver such that interference detection and its precise characterization are simplified [5], and the existence of other radars may even be exploited in the form of passive radar operation [6]. This development is closely related to the evolution of orthogonal frequency-division multiplexing (OFDM) and phase-modulated continuous wave (PMCW) as modulation formats since those schemes can benefit most from a digital implementation. At the same time, the analog front-end hardware is simplified, and the combination

Benedikt Schweizer (benedikt.schweizer@uni-ulm.de), Alexander Grathwohl (alexander.grathwohl@uni-ulm.de), Gilberto Rossi (gilberto.rossi1@gmail.com), Philipp Hinz (philipp.hinz@uni-ulm.de), Christina Knill (christina.knill@uni-ulm.de), Simon Stephany (simon.stephany@uni-ulm.de), and Christian Waldschmidt (christian.waldschmidt@uni-ulm.de) are with the Institute of Microwave Engineering, Ulm University, Ulm, 89081, Germany. Herman Jalli Ng (herman-jalli.ng@hs-karlsruhe.de) is with the Karlsruhe University of Applied Sciences, Karlsruhe, 76133, Germany.

Digital Object Identifier 10.1109/MMM.2021.3069602
Date of current version: 1 June 2021

of independent front- and back-end blocks modularizes radar design.

Yet there are reasons why this development is still research. The lack of affordable high-speed data converters, which are required to have a sufficiently good range resolution, is an important point to mention here, as well as the necessity of a digital processing engine that can handle the immense amount of data that need to be processed. For a sampling rate of 1 GHz, four in-phase/quadrature (I/Q)-channels, and a resolution of 14 bits, the data rate is about 112 Gb/s for both the transmitter and receiver. This leads to 14 GB of receive (Rx) data per second, which, even for a short radar frame with a duration of 10 ms, sums up to 140 MB! Consequently, recent publications have mostly focused on optimized signal processing [7]–[12] and the development of suitable transceiver monolithic microwave integrated circuits (MMICs) [13]–[16], while the systems that have been realized and used to verify the concepts are rather bulky and rely on software-based offline processing [17], [18]. Only a few examples exist that take the next step toward a complete system. In [19], a compact software-defined radar including data converters is presented. A system capable of real-time processing of small-bandwidth OFDM signals is published in [20], and a sophisticated integrated PMCW radar system-on-chip (SoC) that implements analog-to-digital converters (ADCs) and range processing on-chip is shown in [21]. Yet all of those approaches have in common that they are restricted to small bandwidths or require at least partial offline processing. The most advanced SoC is presented in [22], where the complete PMCW processing is integrated in an application-specified IC (ASIC).

Fortunately, technological development does not stop and suitable devices with high sampling-rate data converters are finally available [23], [24], allowing the realization of an all-digital radar. In the following, we present a highly flexible all-digital 4×4 multiple-input, multiple-output (MIMO) mm-wave radar prototype. It fulfills functional automotive-grade specifications and is capable of real-time evaluation of OFDM and PMCW signals. The core of the system is a Xilinx RFSoc (radio frequency SoC) with integrated high-speed data converters, and the setup serves as an experiment and research platform. The article describes all hardware and software building blocks, starting with system aspects, the front-end hardware, and details of the radar MMICs. The modulation formats OFDM and PMCW and their signal processing chains are explained, and the implementation in a hardware description language on the field programmable gate array (FPGA) is shown. Details on the digital design methodologies are given, and adoptions in the signal processing chain compared to a software implementation are highlighted with an emphasis on

how to cope with the high data rates. The functionality of the whole system is verified with measurements of a stationary scene and of an approaching car for both PMCW and OFDM.

System Overview

Radar systems consist of an analog RF front end and a digital processing back end. Whereas in classical radar design, the challenge is to create a high-end front end that is supported by a relatively simple back end, it is the other way around for digital radars: the front end is a simple frequency conversion and amplification stage, but the back end requires a large number of high-speed data converters and immense processing capabilities. Consequently, the core of the system shown in Figure 1 is a Xilinx ZCU111 RFSoc evaluation board [23]. It combines a classical FPGA SoC with integrated ARM processing cores with eight high-speed ADCs and eight digital-to-analog converters (DACs). Two separate double data rate 4 (DDR4) memory banks are connected to the processing system (PS) and to the programmable logic (PL). With this system it is possible to generate wideband signals of up to 4-GHz bandwidth. After mixing and amplification in the front end, they are transmitted at 77 GHz and sampled and evaluated with the RFSoc again. The system overview in Figure 2 shows that the RFSoc is connected to an RF front end with eight single-channel transceiver MMICs. Due to the limited number of ADC and DAC channels, only four of the eight available Tx and Rx channels can be used in I/Q configuration. To select those channels based on the requirements of a specific application and to route them to the ADCs and DACs, an adapter board connects the front end and the RFSoc. The adapter board is also used for baseband amplification of the Rx signal, low-pass filtering, and ac coupling. The antenna arrays are exchangeable by use of a waveguide transition between the front end and the antenna board.

Analog Front End

The analog front end is designed such that it offers maximum flexibility to serve as an experimental platform, allowing the investigation of all possible aspects of

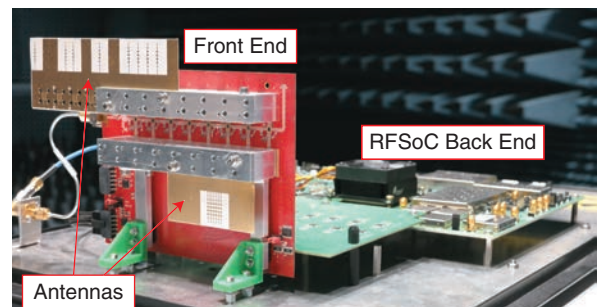


Figure 1. A photo of the whole digital radar system.

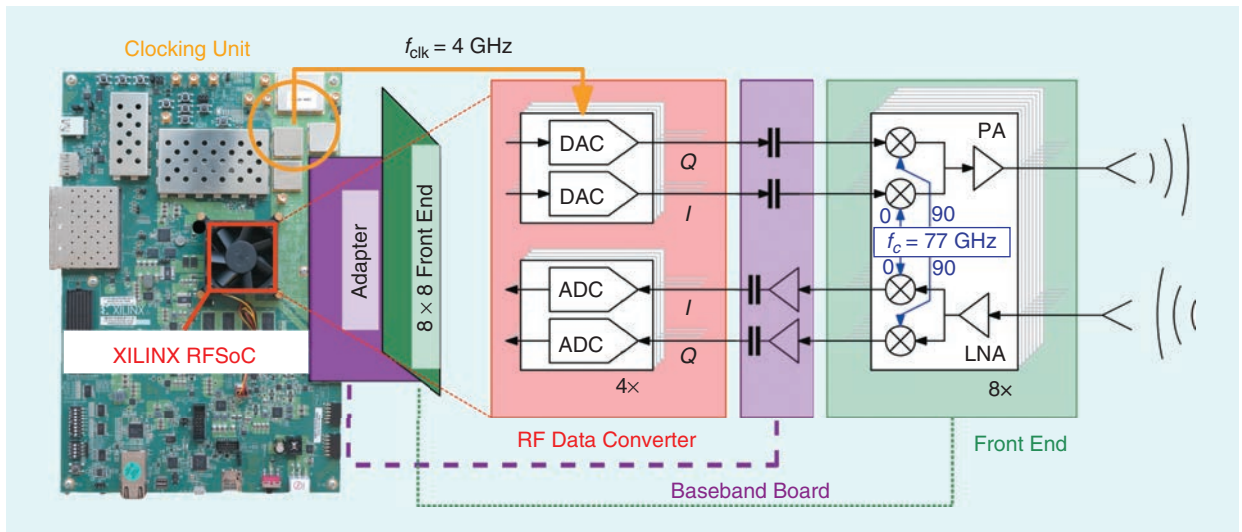


Figure 2. A schematic depiction of the whole system consisting of a Xilinx RFSOC with integrated RF data converters, baseband board for MMIC selection, and ac coupling and amplification as well as a front end with eight transceiver MMICs (left to right). PA: power amplifier; LNA: low-noise amplifier.

digital radars (Figures 3 and 4). Eight fully integrated radar transceiver MMICs featuring one Tx and one Rx channel are used [14], [25]. The transmitters with a maximum output power of 19.2 dBm include a vector modulator and a power amplifier that has a linear gain of 23.4 dB with an output-referred 1-dB compression point of 17.3 dBm at 79 GHz. The receivers have an input-referred 1-dB compression point of -10 dBm and offer a total conversion gain of 27.5 dB with a noise figure of 7.2 dB. The board is supplied with an external local oscillator (LO) signal at 19.25 GHz, which is doubled on the printed circuit board (PCB) with a frequency multiplier to provide the 38.5-GHz input signal for the transceivers. The signal is amplified and doubled in the MMICs once again to reach the desired 77-GHz carrier frequency. Additionally, an amplified version of the input LO signal at 38.5 GHz is provided as an output as well, allowing a daisy-chained LO arrange-

ment of the chips [26]. In this way, it is guaranteed that all MMICs have a similar and sufficiently high LO input power, and a multistage distribution network is omitted. In the radar transceiver chips, the baseband signals are converted to the RF carrier and fed to the antennas. For maximum flexibility in array design, the antenna PCBs are connected via low-loss waveguide board-to-board transitions [27]–[29]. To process the data with a simple and efficient fast Fourier transform (FFT)-based angle estimation technique, a 4 × 4 uniform linear array with an Rx antenna spacing of $\lambda/2$ and a Tx antenna spacing of 2λ is used. The virtual array corresponds to the Kronecker product of the Tx and Rx antenna arrays and contains 16 elements. It has a width of 7.5λ , and its ambiguity-free region is $\pm 90^\circ$. The antenna elements themselves are series-fed tapered patch antennas with 12-dBi gain and 3-dB beamwidths of $\pm 40^\circ$ and $\pm 7^\circ$ in azimuth and elevation, respectively [30]. To minimize the

Tx–Rx leakage, the MMICs are used as either Tx or Rx, and the Tx and Rx arrays are placed on separate antenna PCBs. This allows a high amplification of the Rx baseband signal to deliver the required input power to the ADCs.

Digital Radar Signal Processing

Compared to analog frequency-modulated radars, digital signal generation offers the possibility to realize modulation schemes such as OFDM and PMCW, which are instantaneously wideband.

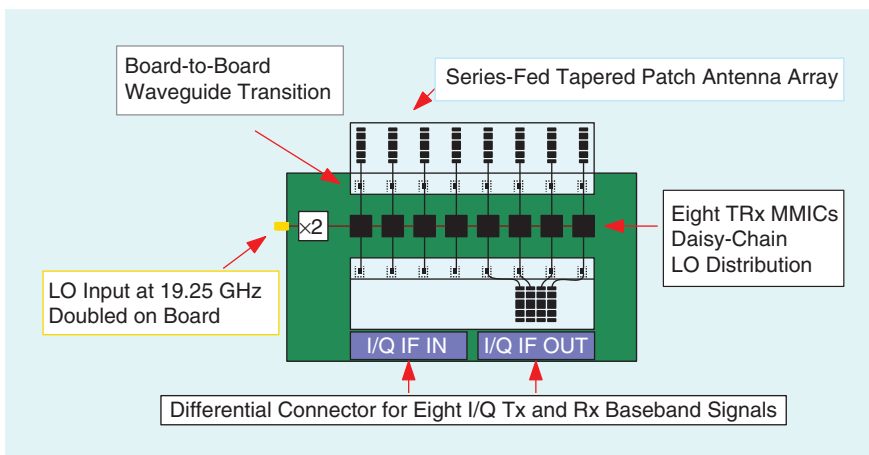


Figure 3. An analog front end with a description of the relevant parts. TRx: transceiver.

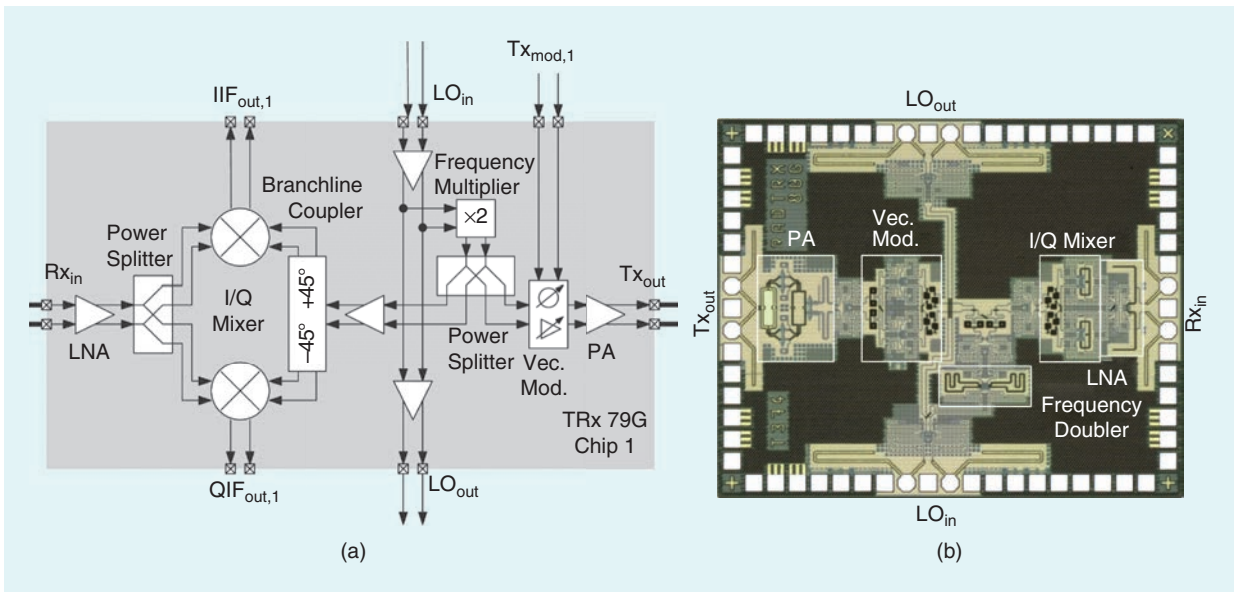


Figure 4. A (a) schematic and (b) photo of the transceiver MMIC with Tx vector modulator (Vec. Mod.) and Rx I/Q mixer. The carrier frequency is supplied at $f_c/2$ and doubled internally. Both images are from [25]. IIF: in-phase intermediate frequency; QIF: quadrature intermediate frequency.

Both schemes employ a coded waveform, leading to a large processing gain and making it more robust against interference artifacts [5], [31] and hardware errors [7], [32], [33]. In Figure 5, the modulation principle, the time-domain baseband signal, and the spectra of both approaches are illustrated. During evaluation, the time of flight of the signal is estimated, yielding the distance of targets. Extracting the Doppler frequency from a series of consecutive transmissions yields the target's radial velocity. Whereas the extraction of a Doppler shift is commonly realized with a discrete Fourier transform (DFT), the two schemes differ with respect to the range processing. In the following, the basic signal characteristics and the processing of both OFDM and PMCW are briefly summarized.

OFDM Radar

OFDM [34], [35] is a multicarrier scheme. The signal consists of a large number N of orthogonal sinusoids, the so-called subcarriers. Their frequencies are equally spaced by Δf , and the subcarriers are orthogonal if the symbol duration equals $T = 1/\Delta f$. These sinusoids are modulated with phase codes, for example, quadrature phase shift keying (QPSK) symbols,

and transmitted simultaneously, forming a noise-like signal in time domain, as depicted in Figure 5. The signal can be conveniently generated and evaluated in the frequency domain using so-called modulation symbols that contain the initial phase of each subcarrier. Such an OFDM symbol with phase codes d_n is described by

$$x(t) = \sum_{n=0}^{N-1} d_n e^{j2\pi n \Delta f t} \text{rect}\left(\frac{t}{T}\right). \quad (1)$$

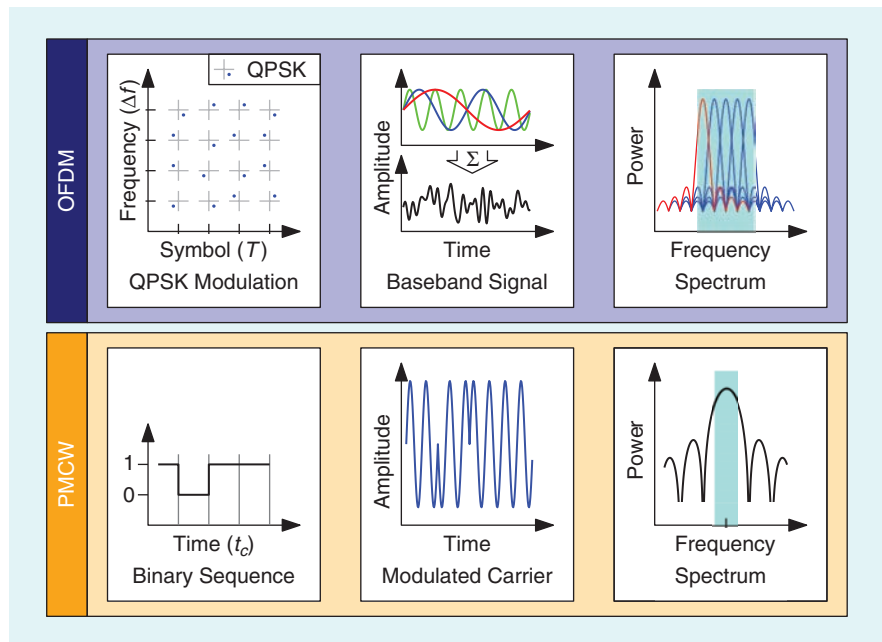


Figure 5. Comparison of OFDM and PMCW waveforms: modulation, waveform, and spectrum.

A series of M symbols with different phase codes $d_{n,m}$ is transmitted consecutively to form one frame, which makes it possible to measure the distance and the Doppler frequency of multiple objects. To prevent intersymbol interference, a cyclic prefix is added before each symbol. In practice, a 2D modulation symbol matrix is generated in the time-frequency domain containing the Tx phase codes. At the receiver, the difference compared to the transmitted modulation symbols is evaluated [36]. This is done with an inverse FFT (IFFT) along the frequencies (n) to extract the frequency-dependent phase rotation, which corresponds to the time of flight and, hence, the distance of the target. To extract the velocity information, an FFT along the OFDM symbols is used. For MIMO operation, where the separation of all Tx signals at the receiver is required, OFDM offers the possibility to use a special form of frequency-division multiplexing based on subcarrier interleaving. Only a subset of the available subcarriers is used on each transmitter, making them orthogonal and perfectly distinguishable at the receiver [37], as visualized in

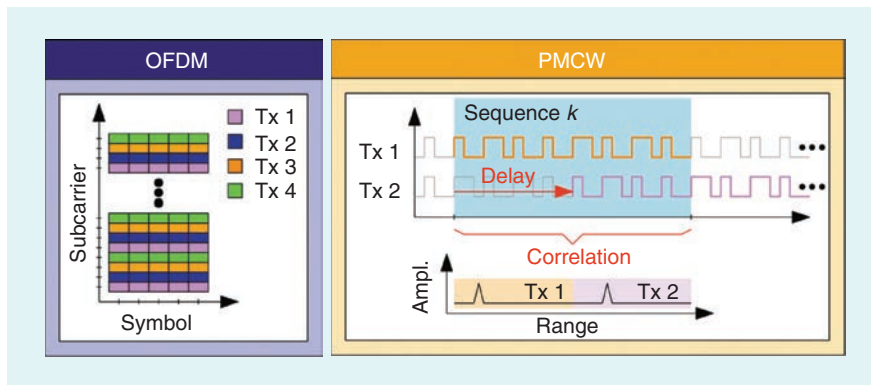


Figure 6. MIMO schemes for OFDM and PMCW in this work. OFDM offers subcarrier interleaving, where a set of subcarriers is assigned to each Tx antenna. PMCW uses a delayed binary sequence. During evaluation of the Rx signal, the Tx signals are separated in the range profile.

Figure 6. The parameters of the OFDM implementation are given in Table 1.

PMCW Radar

For the single-carrier scheme PMCW [16], [21], [38], the phase of the RF carrier is directly modulated with a binary sequence with a fast chip rate f_{chip} yielding the signal bandwidth $B = 1/f_{\text{chip}}$, as illustrated in Figure 5. To estimate the distance of a target, the received signal is correlated with delayed versions of the binary sequence. The correlation result should yield a maximum for the actual distance and zero for all other delays; that is, the sequence should have good circular autocorrelation properties. Since the level of the correlation sidelobes determines the noise level in the range-velocity map and limits the dynamic range of the radar, the choice of the binary sequence is crucial for a good radar performance. Suitable sequences are maximum length sequences (MLS, or M-sequence) [39], almost perfect autocorrelation sequences (APAS) [40], [41], and zero correlation zone (ZCZ) sequences [42]–[44]. MLS have a flat autocorrelation

sidelobe level of -1 , and APAS and ZCZ offer perfect correlation properties for most of the delays, as shown in Figure 7.

For MIMO operation, different realizations of one type of sequence can be assigned to the Tx's to be transmitted simultaneously, realizing code division multiplexing. Since the receivers need to differentiate from among all Tx codes, excellent cross-correlation properties are required as well. However, codes that fulfill both requirements for all delays do not exist. An alternative is using time-shifted

TABLE 1. The modulation parameters of the OFDM radar at 77 GHz used in this work.

Subcarriers	N	1,984
Symbols	M	2,048
Bandwidth	B	958.75 MHz
Subcarrier spacing	Δf	488.28 kHz
Duration of cyclic prefix	T_{cp}	0.512 μs
Duration of OFDM symbol	T_{OFDM}	2.56 μs
Measurement duration	T_{meas}	5.24 ms
Unambiguous range (four Tx)	R_{ua}	76.75 m
Range resolution	ΔR	0.155 m
Unambiguous velocity	v_{ua}	± 380 m/s
Velocity resolution	Δv	0.37 m/s

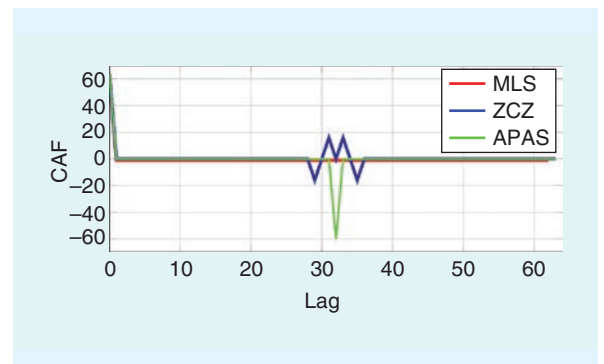


Figure 7. The cyclic autocorrelation function (CAF) properties of MLS, APAS, and ZCZ sequences. MLS have a constant sidelobe level of -1 ; APAS and ZCZ have ideal autocorrelation properties except for a few lags.

versions of one binary sequence to benefit from the good autocorrelation properties for Tx separation as well [45]. For velocity estimation, the sequence is transmitted M times consecutively. Since the duration of one sequence is on the order of a few μs , each sequence samples the Doppler frequency at that time instance. To extract the Doppler frequency, a DFT is performed on all resulting range profiles over time. Due to the short sequence duration and fast sampling rate, the unambiguous areas are maximized, making PMCW suitable for automotive applications. For stationary and slowly moving scenes, it is also possible to accumulate some range profiles before velocity estimation to reduce data rates and computational effort [21]. Table 2 summarizes the parameterization of the PMCW scheme used in this work.

Digital Design Challenges

The main challenge for a real-time implementation of any digital modulation format is the need to process the immense amount of data at rates of up to 100 Gbit/s. Consequently, a suitable digital system architecture is required that can handle the high data rate. In general, two contrary design methodologies can be distinguished.

Memory-Centric Approach

The first step of this straightforward approach is to store all received data in the PL-attached external DDR4 memory. The procedure offers maximum flexibility for the evaluation of an arbitrary number of receivers with the most resource-efficient digital design: since the Rx signal is first stored in DDR4 memory, the processing of single channels can be done sequentially, using the available time before the next frame starts. In this way, processing blocks are reused, for example, for multiple channels, making this concept the most resource-efficient one. At the same time, the computational delay is increased, lowering the maximum achievable frame rate. This methodology is only applicable if the combined data rate of all Rx channels is lower than the available memory bandwidth. This method is used for the PMCW implementation to present a resource-efficient solution.

Streaming Approach

In order to minimize the number of memory accesses and maximize the frame rate, the received data can be processed in a streaming manner. The idea is to process all incoming data immediately, which is often combined with a pipelining concept and parallelization. This method is suitable for designs where each processing step reduces the amount of data such that the final result can be stored in memory with a smaller data rate. Radar usually fulfills this requirement, at least for the first processing steps: although, in gen-

eral, 2D streaming FFTs are realizable, it is not that trivial for large matrix sizes as they occur for digital radars, easily exceeding $2,000 \times 2,000$ complex values. Hence, for the 2D radar evaluation (range and velocity), streaming processing is possible for range evaluation. Before the final processing step, the range profiles need to be stored in the external DDR4 memory. This method is used for the OFDM implementation in the following. Due to the parallelism and avoidance of unnecessary memory operations, this approach delivers a high-performance solution at the cost of significantly increased hardware usage.

The OFDM Implementation

Since the whole processing of OFDM [46] is based on large DFTs, the main task is to implement efficient streaming FFTs. To have a subcarrier spacing of about 500 kHz at a sampling rate of 1 GHz, the FFT length is chosen to be 2,048. A good realization is seen in using four standard Xilinx IP FFTs with length 512 in a four-butterfly (4BF) structure [47]. This is additionally advantageous since the data format for the converter input and output requires four samples per clock cycle. This parallelism reduces the digital clock to a suitable rate of 250 MHz.

The general setup is shown in Figure 8. Based on pseudorandom QPSK modulation symbols created by a linear feedback shift register, the Tx signal is realized by an inverse streaming FFT in a 4BF structure that directly prepends the required prefix. To have four orthogonal Tx signals for MIMO operation, the modulation symbols are distributed in an interleaving fashion to four parallel 4BF-IFFT instances such that a unique Tx signal for each of the four antennas is realized. At the receiver, each antenna receives the superposition of all four delayed Tx signals. After a streaming 4BF-FFT, all modulation symbols contain valid data, being a combination of the transmitted modulation symbol and the channel information. The transmitted modulation symbols need to be removed by a spectral division. This step is realized on the output stream of the first 4BF-FFT. The range estimation is thereafter done on each Tx-dependent subset

TABLE 2. The modulation parameters of the PMCW radar at 77 GHz used in this work.

Sampling frequency	f_s	1 GHz
Sequence length	L	2,047
Sequence type		M-sequence
Number of sequences	M	2,048
Measurement duration	T_{meas}	4.1 ms
Unambiguous range	R_{ua}	307 m
Range resolution	ΔR	0.15 m
Unambiguous velocity	v_{ua}	± 476 m/s
Velocity resolution	Δv	0.46 m/s

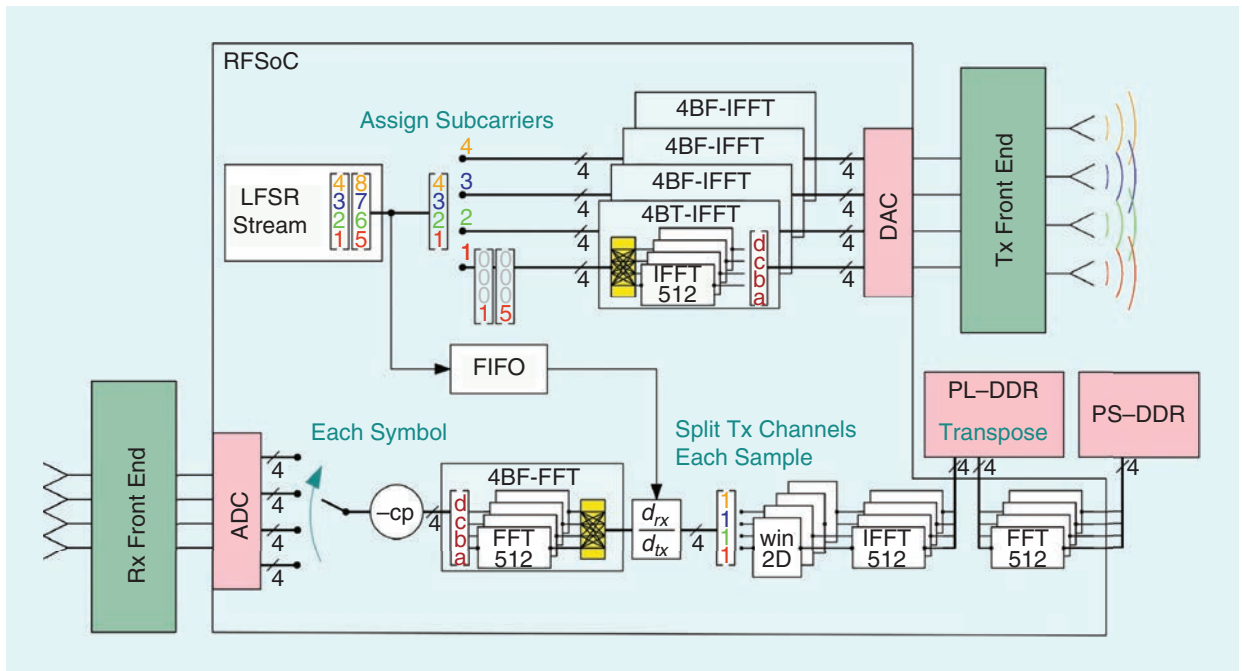


Figure 8. A depiction of the OFDM processing implementation. The index 4 at connection lines refers to four complex numbers. FIFO: first in, first out; LFSR: linear feedback shift register; cp: cyclic prefix; win: window function.

TABLE 3. Implementation details for the OFDM radar.

	Theory	Realization
Frame rate		94 Hz
Unambiguous range	76.75 m	76.75 m
Range cells	512	256
Maximum range	79.36 m	39.68 m
Unambiguous velocity	± 380 m/s	± 95 m/s
Velocity cells	2,048	512
Maximum velocity	± 380 m/s	± 95 m/s
Digital signal processing slices		1,587
Lookup tables		221,402

Reductions compared to theoretical values arise from quasi-RX TDM for velocity and from a reduced number of range cells that are stored.

of modulation symbols in parallel, yielding four range profiles with 512 values each. At this point, the data rate is reduced by a factor of two since the range profiles are cut to a length of 256. These profiles are stored block-wise in DDR4 memory such that the velocity estimation can start as soon as the range processing has finished for the first values of the last symbol. Finally, four range-velocity maps are available for each receiver.

Since this receiver block is rather large and the unambiguously measurable velocity is sufficiently high to be reduced by a factor of four while still meeting the automotive requirements, the receiver block is implemented only once, realizing a quasi-Rx time-division multiplexing (TDM). Although this sounds rather

disadvantageous, this method is chosen to demonstrate the functionality of the OFDM-specific MIMO multiplexing approach based on subcarrier interleaving. All phase errors arising from different sampling points in time and frequency are compensated for afterward [8], [48]. The application of the previously mentioned concept realizes an all-digital radar with a measurement bandwidth of almost 1 GHz and a frame duration of about 5 ms. The dynamic range of the digital processing back end is above 110 dB, and a maximum frame rate of 95 Hz for range-velocity calculation in 4×4 MIMO operation is possible. This high frame rate comes at the cost of extensive use of digital logic and is possible by consequently applying stream processing, pipelining, and parallelization. The achieved parameters are summarized in Table 3. Note that the unambiguous velocity is reduced by a factor of four compared to the theoretical value due to Rx switching, and the maximum range is defined by the number of range cells that are stored.

The functionality is verified with static measurements of two corner reflectors in an anechoic chamber. A non-coherent integration of all 16 virtual range-velocity maps is shown in Figure 9(a), where the corner reflectors can clearly be recognized in addition to the crosstalk. The corresponding direction of arrival (DOA) estimation realized in the PS of the RFSoc is given in Figure 9(b).

The PMCW Implementation

For PMCW, the main task is the realization of a digital correlation block that delivers the correlation results

for all delays in multiples of the chip duration of the sequence. To achieve an efficient implementation, the module was designed in high-level synthesis, based on C code of the mathematical definition of a correlation for the desired number of delays. To achieve good Tx channel separation, one M-sequence with 2,047 values is used at a chip rate of 1 GHz, and time-shifted versions are transmitted on each antenna, as can be seen in Figure 10. To realize a maximally efficient and flexible design, all Rx data are first stored in the external PL-attached DDR4 memory. One correlation instance processes all virtual channels sequentially, making the design very resource efficient at the cost of a long calculation time. However, the frame rate may be increased by reducing the number of range cells for which the correlation is calculated. This corresponds to a reduction of the maximum range. The results of the correlation are thereafter stored in the external memory again. Finally, a parallelized FFT is used to perform the Doppler estimation. This implementation features about 1 GHz of analog bandwidth, and the maximum 4×4 MIMO frame rate is 10 Hz for a maximum distance of 70 m and 34 Hz for 20 m, respectively. It could be easily doubled using a second correlation block, if desired. In contrast to the OFDM implementation, all Rx channels are processed such that the unambiguously measurable velocity is maximized.

The design functionality is demonstrated in Figure 11 for the same static scene as before. Just as for OFDM, the DOA estimation is realized on the ARM processing cores using an FFT algorithm. The corresponding angle estimation is given in Figure 11(b), and Table 4 summarizes the implementation details.

Measurement Examples

With the earlier mentioned concepts, an all-digital mm-wave radar fulfilling functional automotive requirements is realized. To demonstrate the performance, snapshots of an approaching car passing the radar as shown in

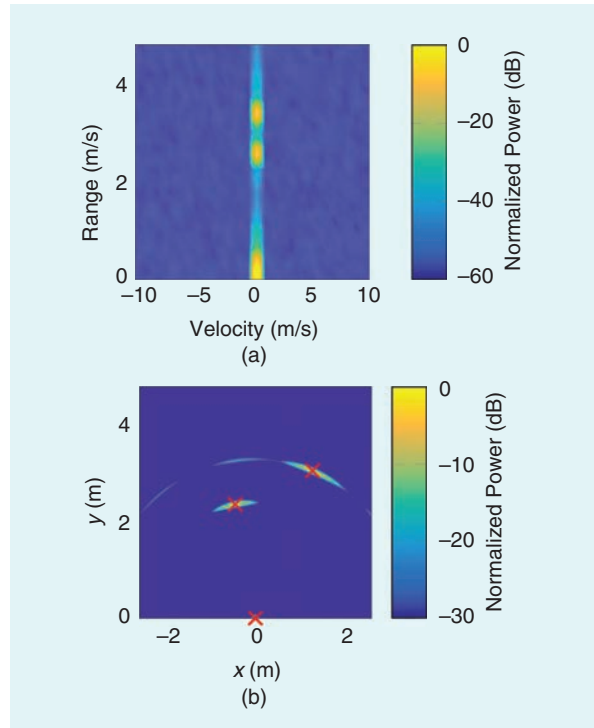


Figure 9. Anechoic chamber measurements with two targets. (a) OFDM: range-velocity map. (b) OFDM: DOA estimation.

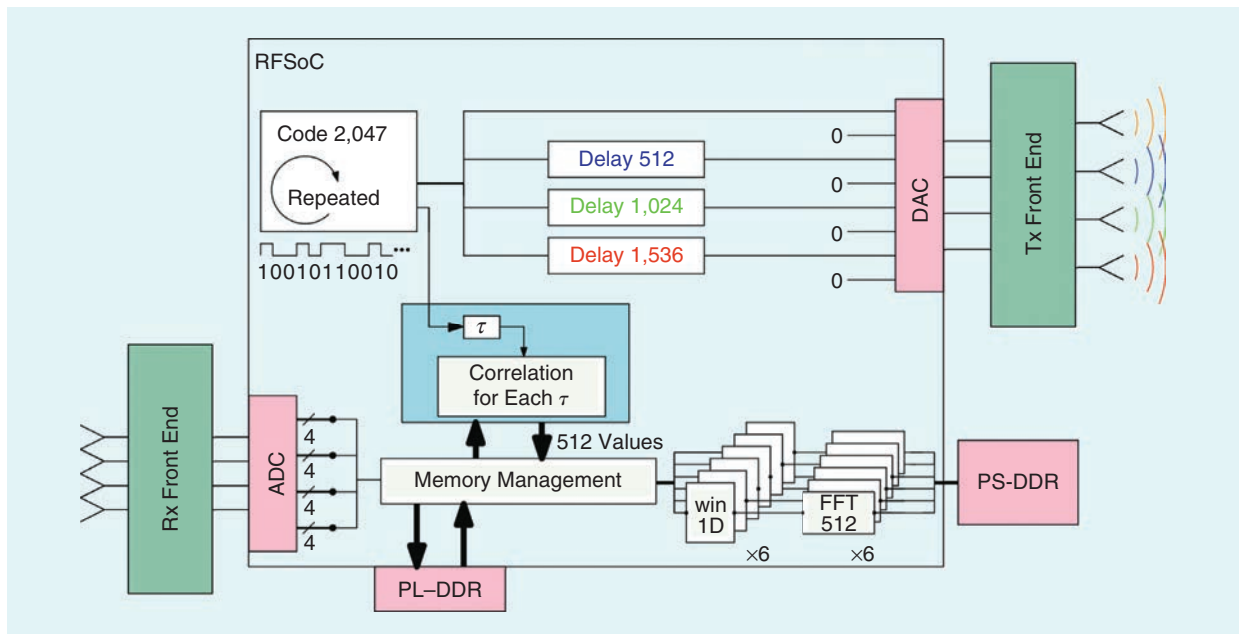


Figure 10. A depiction of the PMCW processing implementation.

Figure 12 are presented in Figures 13 and 14. The radar is tilted by approximately 20° toward the car lane. Based on a constant false alarm rate detector, reflection points of the targets are identified in the range-velocity map, and the angle estimation is performed on each of them such that the contour of the car is visible in the angular picture [49].

Conclusions

The advantages of digital radars are frequently highlighted, leading to the impression that the realization of such a sensor is simple. However, when it comes to applications that require a large bandwidth, not only

is the absence of high-speed data converters a problem, but it is also challenging to deal with data rates that easily exceed 100 Gb/s. With recently available RFSoc modules, it is now possible to realize research and development platforms for digital radars. For the first time, this allows designers to characterize and optimize all components involved in such systems. This includes evaluating suitable transceiver MMICs, baseband processing architectures, and modulation formats, just to mention the aspects that have been addressed.

The article also emphasizes that sophisticated digital designs are required to realize the radar processing in

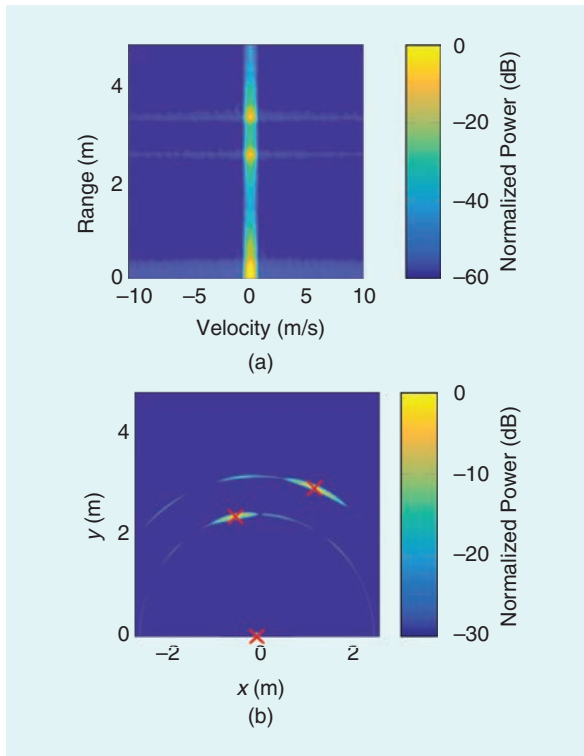


Figure 11. PMCW verification measurements in an anechoic chamber with two targets. (a) PMCW: Range-velocity map. (b) PMCW: DOA estimation.

TABLE 4. Implementation details for the realized PMCW radar back end.

	Theory	Mode 1	Mode 2
Frame rate		10 Hz	34 Hz
Range cells	2,047	512	128
Maximum range	307 m	77 m	20 m
Velocity cells	2,048	512	
Maximum velocity	±476 m/s	±117 m/s	
Digital signal processing slices		40	
Lookup tables		136,509	

The limited maximum range and velocity are no physical quantities but arise from the reduced number of cells that are processed and stored.



Figure 12. A measurement scene of the approaching car.

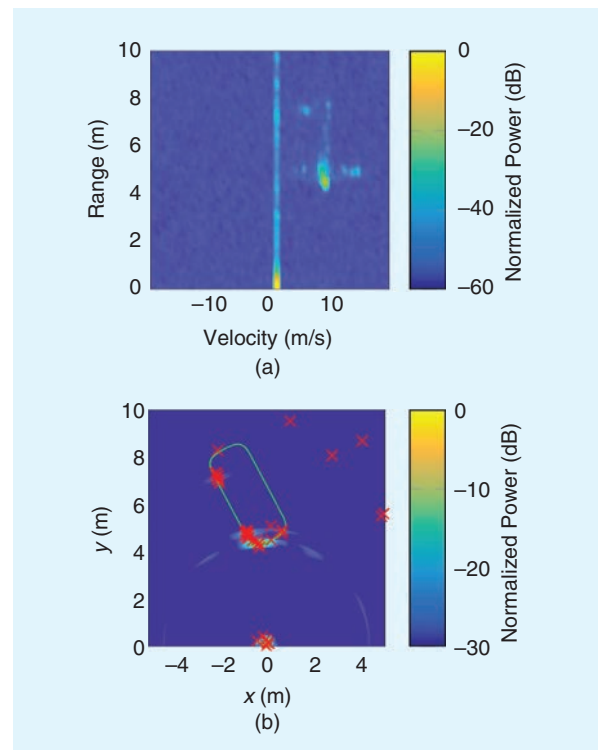


Figure 13. OFDM measurements of an approaching car. Range-velocity map and DOA estimation with estimated contour of the vehicle. (a) OFDM: Range-velocity map. (b) OFDM: DOA estimation.

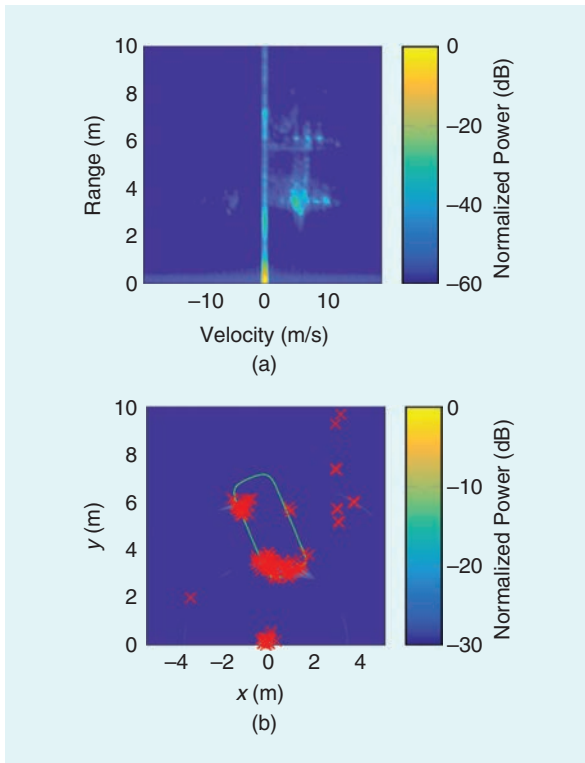


Figure 14. PMCW measurements of an approaching car. Range-velocity map and DOA estimation with estimated contour of the vehicle. (a) PMCW: Range-velocity map. (b) PMCW: DOA estimation.

real time. Although high-performance FPGAs offer a huge amount of logic slices, they are also a costly solution. During the development of a product, it is essential to partition the processing chain in a sensible way by identifying which functions are best implemented in an ASIC, on low- and high-performance FPGAs, or even on dedicated digital signal processor chips or modules for machine learning and artificial intelligence. This choice will strongly be driven by the application: in high-volume markets such as automotive, highly integrated solutions will dominate; in industrial applications, on the other hand, FPGAs might still be favorable due to the short development time and flexibility of the system.

The evolution of digital radars may further be accelerated by the development of 5G and 6G communication standards. They use similar carrier frequencies and modulation schemes and rely on the same homodyne system concept. This enables radar to use hardware developed for the high-volume communications market and to benefit from algorithms used in communications, for example, digital predistortion.

While many years and countless engineering hours have been spent on the optimization of FMCW and chirp-sequence radars, the development of all-digital radars is still in its infancy. This article shows that

there is still great potential in digital realizations; it simply needs to be exploited.

We expect radar design to change: where mostly sophisticated RF engineers were required in the past, an interdisciplinary team working closely together will be needed to handle the challenges presented by digital radars.

Acknowledgments

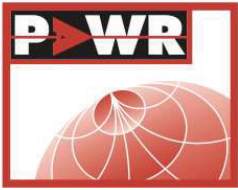
We gratefully thank Xilinx and Missing Link Electronics for providing us with a ZCU111 evaluation board and design support as well as IHP Microelectronics for the radar transceiver MMICs. This work was supported in part by the German Federal Ministry of Education and Research (BMBF) through the research project Radar4FAD—Universal Radar Modules for Fully Automated Driving.

References

- [1] Y. L. Sit and T. Zwick, "MIMO OFDM radar with communication and interference cancellation features," in *Proc. IEEE Radar Conf.*, May 2014, pp. 265–268. doi: 10.1109/RADAR.2014.6875596.
- [2] G. Hakobyan, K. Armanious, and B. Yang, "Interference-aware cognitive radar: A remedy to the automotive interference problem," *IEEE Trans. Aerosp. Electron. Syst.*, vol. 56, no. 3, pp. 2326–2339, June 2019. doi: 10.1109/TAES.2019.2947973.
- [3] C. Aydogdu et al., "Radar interference mitigation for automated driving: Exploring proactive strategies," *IEEE Signal Process. Mag.*, vol. 37, no. 4, pp. 72–84, July 2020. doi: 10.1109/MSP.2020.2969319.
- [4] D. Werbunat, B. Meinecke, B. Schweizer, J. Hasch, and C. Waldschmidt, "OFDM-based radar network providing phase coherent DOA estimation," *IEEE Trans. Microw. Theory Techn.*, 2020. doi: 10.1109/TMTT.2020.3026041.
- [5] C. Knill, B. Schweizer, P. Hügler, and C. Waldschmidt, "Impact of an automotive chirp-sequence interferer on a wideband OFDM radar," in *Proc. 15th Eur. Radar Conf. (EuRAD)*, Sept. 2018, pp. 34–37. doi: 10.23919/EuRAD.2018.8546524.
- [6] S. Schieler et al., "OFDM waveform for distributed radar sensing in automotive scenarios," in *Proc. 16th Eur. Radar Conf. (EuRAD)*, Oct. 2019, pp. 225–228.
- [7] A. Bourdoux, M. Bauduin, and C. Desset, "IQ imbalance robust OFDM radar waveform," in *Proc. 15th Eur. Radar Conf. (EuRAD)*, Sept. 2018, pp. 297–300. doi: 10.23919/EuRAD.2018.8546643.
- [8] B. Schweizer, C. Knill, D. Schindler, and C. Waldschmidt, "Stepped-carrier OFDM-radar processing scheme to retrieve high-resolution range-velocity profile at low sampling rate," *IEEE Trans. Microw. Theory Techn.*, vol. 66, no. 3, pp. 1610–1618, Mar. 2017. doi: 10.1109/TMTT.2017.2751463.
- [9] C. Knill, F. Roos, B. Schweizer, D. Schindler, and C. Waldschmidt, "Random multiplexing for an MIMO-OFDM radar with compressed sensing-based reconstruction," *IEEE Microw. Wireless Compon. Lett.*, vol. 29, no. 4, pp. 300–302, Apr. 2019. doi: 10.1109/LMWC.2019.2901405.
- [10] B. Nuss, J. Mayer, S. Marahrens, and T. Zwick, "Frequency comb OFDM radar system with high range resolution and low sampling rate," *IEEE Trans. Microw. Theory Techn.*, vol. 68, no. 9, pp. 3861–3871, Sept. 2020. doi: 10.1109/TMTT.2020.2988254.
- [11] C. Pfeffer, R. Feger, and A. Stelzer, "A stepped-carrier 77-GHz OFDM MIMO radar system with 4GHz bandwidth," in *Proc. Eur. Radar Conf. (EuRAD)*, Sept. 2015, pp. 97–100. doi: 10.1109/EuRAD.2015.7346246.
- [12] J. Overdevest, F. Jansen, F. Uysal, and A. Yarovsky, "Doppler influence on waveform orthogonality in 79GHz MIMO phase-coded automotive radar," *IEEE Trans. Veh. Technol.*, vol. 69, no. 1, pp. 16–25, Jan. 2020. doi: 10.1109/TVT.2019.2951632.
- [13] D. Schindler et al., "Dual-channel single sideband transmitter in 45nm CMOS SOI for a 70GHz OFDM radar," in *Proc. 15th Eur. Radar Conf. (EuRAD)*, Sept. 2018, pp. 521–524.

- [14] H. J. Ng, R. Hasan, and D. Kissinger, "A scalable four-channel frequency-division multiplexing MIMO radar utilizing single-sideband delta-sigma modulation," *IEEE Trans. Microw. Theory Techn.*, vol. 67, no. 11, pp. 4578–4590, Nov. 2019. doi: 10.1109/TMTT.2019.2930499.
- [15] D. Guermandi et al., "A 79GHz binary phase-modulated continuous-wave radar transceiver with TX-to-RX spillover cancellation in 28nm CMOS," in *Proc. IEEE Int. Solid-State Circuits Conf. (ISSCC)*, Feb. 2015, pp. 1–3. doi: 10.1109/ISSCC.2015.7063072.
- [16] V. Giannini et al., "A 79GHz phase-modulated 4GHz-BW CW radar transmitter in 28nm CMOS," *IEEE J. Solid-State Circuits*, vol. 49, no. 12, pp. 2925–2937, Dec. 2014. doi: 10.1109/JSSC.2014.2355819.
- [17] D. Schindler, B. Schweizer, C. Knill, J. Hasch, and C. Waldschmidt, "An integrated stepped-carrier OFDM MIMO radar utilizing a novel fast frequency step generator for automotive applications," *IEEE Trans. Microw. Theory Techn.*, vol. 67, no. 11, pp. 4559–4569, Nov. 2019. doi: 10.1109/TMTT.2019.2916822.
- [18] G. Hakobyan, M. Girma, X. Li, N. Tammireddy, and B. Yang, "Repeated symbols OFDM-MIMO radar at 24GHz," in *Proc. Eur. Radar Conf. (EuRAD)*, Oct. 2016, pp. 249–252.
- [19] C. Pfeffer, R. Feger, M. Jahn, and A. Stelzer, "A 77-GHz software defined OFDM radar," in *Proc. 15th Int. Radar Symp. (IRS)*, June 2014, pp. 1–5. doi: 10.1109/IRS.2014.6869235.
- [20] T. Multerer, M. Vossiek, U. Prechtel, and V. Ziegler, "Spectrum-efficient real-time OFDM MIMO radar for moving target detection in medium-range applications," in *Proc. IEEE MTT-S Int. Conf. Microw. Intell. Mobility (ICMIM)*, Apr. 2018, pp. 1–4. doi: 10.1109/ICMIM.2018.8443563.
- [21] D. Guermandi et al., "A 79-GHz 2×2 MIMO PMCW radar SoC in 28-nm CMOS," *IEEE J. Solid-State Circuits*, vol. 52, no. 10, pp. 2613–2626, Oct. 2017. doi: 10.1109/JSSC.2017.2723499.
- [22] V. Giannini et al., "A 192-virtual-receiver 77/79GHz GMSK code-domain MIMO radar system-on-chip," in *Proc. IEEE Int. Solid-State Circuits Conf. (ISSCC)*, Feb. 2019, pp. 164–166. doi: 10.1109/ISSCC.2019.8662386.
- [23] B. Farley, J. McGrath, and C. Erdmann, "An all-programmable 16-nm RFSoc for digital-RF communications," *IEEE Micro*, vol. 38, no. 2, pp. 61–71, Mar. 2018. doi: 10.1109/MM.2018.022071136.
- [24] S. Devarajan et al., "A 12-b 10-GS/s interleaved pipeline ADC in 28-nm CMOS technology," *IEEE J. Solid-State Circuits*, vol. 52, no. 12, pp. 3204–3218, Dec. 2017. doi: 10.1109/JSSC.2017.2747758.
- [25] M. Kucharski, A. Ergintav, W. A. Ahmad, M. Krstić, H. J. Ng, and D. Kissinger, "A scalable 79-GHz radar platform based on single-channel transceivers," *IEEE Trans. Microw. Theory Techn.*, vol. 67, no. 9, pp. 3882–3896, Sept. 2019. doi: 10.1109/TMTT.2019.2914104.
- [26] H. J. Ng, M. Kucharski, W. Ahmad, and D. Kissinger, "Multi-purpose fully differential 61- and 122-GHz radar transceivers for scalable MIMO sensor platforms," *IEEE J. Solid-State Circuits*, vol. 52, no. 9, pp. 2242–2255, Sept. 2017. doi: 10.1109/JSSC.2017.2704602.
- [27] Z. Tong and A. Stelzer, "A vertical transition between rectangular waveguide and coupled microstrip lines," *IEEE Microw. Wireless Compon. Lett.*, vol. 22, no. 5, pp. 251–253, May 2012. doi: 10.1109/LMWC.2012.2192719.
- [28] E. Topak, J. Hasch, and T. Zwick, "Compact topside millimeter-wave waveguide-to-microstrip transitions," *IEEE Microw. Wireless Compon. Lett.*, vol. 23, no. 12, pp. 641–643, Dec. 2013. doi: 10.1109/LMWC.2013.2284824.
- [29] P. Hügler, F. Roos, M. Scharfel, M. Geiger, and C. Waldschmidt, "Radar taking off: New capabilities for UAVs," *IEEE Microw. Mag.*, vol. 19, no. 7, pp. 43–53, Nov. 2018. doi: 10.1109/MMM.2018.2862558.
- [30] C. Vasanelli, R. Batra, A. D. Serio, F. Boegelsack, and C. Waldschmidt, "Assessment of a millimeter-wave antenna system for MIMO radar applications," *IEEE Antennas Wireless Propag. Lett.*, vol. 16, pp. 1261–1264, Nov. 2017. doi: 10.1109/LAWP.2016.2631889.
- [31] S. Alland, W. Stark, M. Ali, and M. Hegde, "Interference in automotive radar systems: Characteristics, mitigation techniques, and current and future research," *IEEE Signal Process. Mag.*, vol. 36, no. 5, pp. 45–59, Sept. 2019. doi: 10.1109/MSP.2019.2908214.
- [32] W. V. Thillo, V. Giannini, D. Guermandi, S. Brebels, and A. Bourdoux, "Impact of ADC clipping and quantization on phase-modulated 79GHz CMOS radar," in *Proc. 11th Eur. Radar Conf. (EuRAD)*, Oct. 2014, pp. 285–288. doi: 10.1109/EuRAD.2014.6991263.
- [33] B. Schweizer, D. Schindler, C. Knill, J. Hasch, and C. Waldschmidt, "On hardware implementations of stepped-carrier OFDM radars," in *Proc. IEEE/MTT-S Int. Microw. Symp. (IMS)*, June 2018, pp. 891–894. doi: 10.1109/MWSYM.2018.8439179.
- [34] S. B. Weinstein and P. M. Ebert, "Data transmission by frequency-division multiplexing using the discrete Fourier transform," *IEEE Trans. Commun. Technol.*, vol. 19, no. 5, pp. 628–634, Oct. 1971. doi: 10.1109/tcom.1971.1090705.
- [35] N. Levanon, "Multifrequency radar signals," in *Proc. IEEE Int. Radar Conf.*, May 2000, pp. 683–688. doi: 10.1109/RADAR.2000.851916.
- [36] C. Sturm, E. Pancera, T. Zwick, and W. Wiesbeck, "A novel approach to OFDM radar processing," in *Proc. IEEE Nat. Radar Conf.*, June 2009, no. 3, pp. 9–12. doi: 10.1109/RADAR.2009.4977002.
- [37] C. Sturm, Y. L. Sit, M. Braun, and T. Zwick, "Spectrally interleaved multi-carrier signals for radar network applications and multi-input multi-output radar," *IET Radar, Sonar Navigat.*, vol. 7, no. 3, pp. 261–269, Mar. 2013. doi: 10.1049/iet-rsn.2012.0040.
- [38] W. Menzel, J. Buechler, and J. Taech, "An experimental 24GHz radar using phase modulation spread spectrum techniques," in *Proc. 28th Eur. Microw. Conf.*, Oct. 1998, vol. 2, pp. 56–60. doi: 10.1109/EUMA.1998.338125.
- [39] H. J. Ng, R. Feger, and A. Stelzer, "A fully-integrated 77-GHz UWB pseudo-random noise radar transceiver with a programmable sequence generator in SiGe technology," *IEEE Trans. Circuits Syst. I*, vol. 61, no. 8, pp. 2444–2455, Aug. 2014. doi: 10.1109/TCSI.2014.2309774.
- [40] J. Wolfmann, "Almost perfect autocorrelation sequences," *IEEE Trans. Inf. Theory*, vol. 38, no. 4, pp. 1412–1418, July 1992. doi: 10.1109/18.144729.
- [41] W. Van Thillo, P. Giffroé, V. Giannini, D. Guermandi, S. Brebels, and A. Bourdoux, "Almost perfect auto-correlation sequences for binary phase-modulated continuous wave radar," in *Proc. Eur. Microw. Conf.*, Oct. 2013, pp. 1803–1806. doi: 10.23919/EuMC.2013.6687029.
- [42] P. Z. Fan, N. Suehiro, N. Kuroyanagi, and X. M. Deng, "Class of binary sequences with zero correlation zone," *IET Electron. Lett.*, vol. 35, no. 10, pp. 777–779, May 1999. doi: 10.1049/el:19990567.
- [43] H. Torii, M. Nakamura, and N. Suehiro, "A new class of zero-correlation zone sequences," *IEEE Trans. Inf. Theory*, vol. 50, no. 3, pp. 559–565, Mar. 2004. doi: 10.1109/TIT.2004.825399.
- [44] H. Haderer, R. Feger, C. Pfeffer, and A. Stelzer, "Millimeter-wave phase-coded CW MIMO radar using zero- and low-correlation-zone sequence sets," *IEEE Trans. Microw. Theory Techn.*, vol. 64, no. 12, pp. 4312–4323, Dec. 2016. doi: 10.1109/TMTT.2016.2613530.
- [45] A. Bourdoux, U. Ahmad, D. Guermandi, S. Brebels, A. Dewilde, and W. V. Thillo, "PMCW waveform and MIMO technique for a 79GHz CMOS automotive radar," in *Proc. IEEE Radar Conf. (Radar-Conf)*, May 2016, pp. 1–5. doi: 10.1109/RADAR.2016.7485114.
- [46] B. Schweizer, S. Stephany, and C. Waldschmidt, "A software-defined radar using Xilinx' RFSoc," in *Proc. 3rd Workshop on Programmable Process. Autonom./Connected Veh.*, July 2019, pp. 99–107.
- [47] J. W. Cooley and J. W. Tukey, "An algorithm for the machine calculation of complex Fourier series," *Math. Comput.*, vol. 19, no. 90, pp. 297–301, Aug. 1965. doi: 10.1090/S0025-5718-1965-0178586-1.
- [48] T. Multerer, U. Prechtel, M. Vossiek, and V. Ziegler, "Systematic phase correction for direction-of-arrival estimation in spectrally interleaved OFDM MIMO radar," *IEEE Trans. Microw. Theory Techn.*, vol. 67, no. 11, pp. 4570–4577, Nov. 2019. doi: 10.1109/TMTT.2019.2921321.
- [49] C. Vasanelli et al., "Calibration and direction-of-arrival estimation of millimeter-wave radars: A practical introduction," *IEEE Antennas Propag. Mag.*, vol. 62, no. 6, pp. 34–45, 2020. doi: 10.1109/MAP.2020.2988528.





IEEE Topical Conference on RF/Microwave Power Amplifiers for Radio and Wireless Applications



Paper Deadline
25 July 2021

<https://www.radiowirelessweek.org/>

Steering Committee

General Chair

Kevin Chuang, *MaxLinear*

General Co-Chair

Alexander Koelpin, *Hamburg University of Technology*

Technical Program Chair

Changzhi Li, *Texas Tech. University*

Finance Chair

Holger Maune, *Technical University of Darmstadt*

PAWR Co-Chairs

Václav Valenta, *European Space Agency*

Roberto Quaglia, *Cardiff University*

WiSNet Co-Chairs

Rahul Khanna, *Intel*

Paolo Mezzanotte, *University of Perugia*

SiRF General Chair

Saeed Zeinolabedinzadeh, *Arizona State University*

SHaRC Co-Chairs

Markus Gardill, *Julius-Maximilians-University Würzburg*

Maximilian C. Scardelletti, *NASA Glenn Research Center*

Executive Committee Chair

Rashaunda Henderson, *University of Texas Dallas*

Conference Management

Elsie Vega, *IEEE*

Deidre Artis, *IEEE*

Call For Papers

The 2022 IEEE Topical Conference on RF/Microwave Power Amplifiers for Radio and Wireless Applications (PAWR 2022) will be a part of 2022 IEEE Radio and Wireless Week (RWW 2022) which will be held during week of 16 January 2022 in Las Vegas, NV, USA.

RWW 2022 will also feature:

- IEEE Radio and Wireless Symposium (RWS)
- 22nd Topical Meeting on Silicon Monolithic Integrated Circuits in RF Systems (SiRF)
- IEEE Topical Conference on Wireless Sensors and Sensor Networks (WiSNet)
- IEEE Space Hardware and Radio Conference (SHaRC)
- Special Sessions, Short Courses, and Design Competition

Each of these events will be organized separately, with their own call for papers found at <http://www.radiowirelessweek.org/>.

Power amplifiers are often the most critical component of RF/microwave communications systems and consequently the focus of intense research to achieve increased linearity and power efficiency. New forms of power amplification are being developed to meet the needs of the wireless communication equipment industry and the world's demand for greater information transmission. PAWR 2022 will feature tracks on RF/microwave Power Amplifiers. Papers featuring innovative work are solicited in (but not limited to) the following areas of RF/microwave power amplifier technology:

- High Power/Wideband Active Devices
- Power Amplifiers for Mobile, Avionics and Space
- Modeling and Characterization
- Advanced Circuit Design and Topologies
- Green Power Amplifier Technology
- Integration Technology
- Packaging and Reliability
- Linearization and Efficiency Enhancement Techniques
- Applications, Novel Architectures and System Analysis

PAWR2022 Chair

Václav Valenta, *European Space Agency*

PAWR2022 Co-Chair

Roberto Quaglia, *Cardiff University*

Authors of papers presented at RWW 2022 will be invited to submit an expanded version to the **IEEE T-MTT Mini-Special Issue**.

Paper submission instructions can be found at <http://www.radiowirelessweek.org/>. Submissions should be formatted according to the submission review template available on the RWW website. Authors should indicate preference for oral or poster presentation. All submissions must be received by **25 July 2021**. All accepted papers will be published in a digest and included in the IEEE Xplore® Digital Library. Submissions will be evaluated based on novelty, significance of the work, technical content, interest to the audience, and quality of writing.



Women in Microwaves

Women in Microwaves at MIKON: (Not) for the First Time

■ **Malgorzata Celuch**

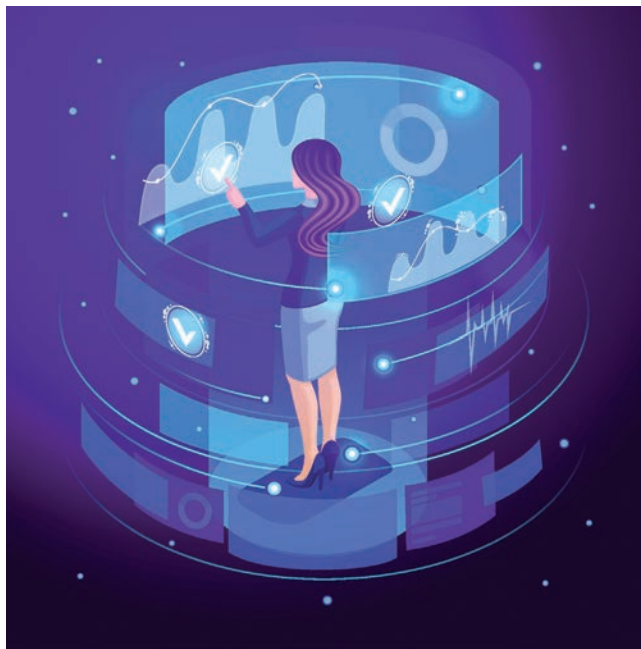
“At MIKON, there have always been women in microwaves, but there has never been a Women in Microwaves (WiM) event.” I thought this catchy phrase would open the doors to organizing an inaugural event as part of Microwave and Radar Week (MRW) 2020 [1]. And it did! We had a WiM session on 5 October, and over the following three days we ran an IEEE kiosk hosting the IEEE Microwave Theory and Techniques Society (MTT-S) and IEEE Women in Engineering (WiE) materials. The MRW event was attended by 120 on-site and 120 online participants: a good record during a time of pandemic!

Who Are We?

In January 2020, a new board was elected for the IEEE Poland Section’s WiE Affinity

Malgorzata Celuch (mceluch@qwed.eu) is with QWED, Warsaw, 02-078, Poland.

*Digital Object Identifier 10.1109/MMM.2021.3070815
Date of current version: 1 June 2021*



©SHUTTERSTOCK.COM/PROKOPEVA IRINA

Group. The WiE had been active in Poland over the previous decade, which was nicely illustrated by the International Leadership Summit [2] held at a UNESCO World Heritage site in Krakow in September 2017 (the first-ever IEEE WiE Summit in IEEE Region 8). However, a microwave component was missing, with “electrical and electronics” in the title of the summit

dominated by “computer and networks engineering” in the practical scope.

The 2020 elections brought a change. Dr. Katarzyna Wasielewska (from the State University of Applied Sciences, Elblag, Poland, and currently a postdoctoral researcher with the Department of Signal Theory, Telematics, and Communications, Universidad de Granada, Spain) ensures personal and thematic continuity with earlier activities, while the two new members (Dr. Marzena Olszewska-Placha and myself, both of QWED, www.qwed.eu, Warsaw, Poland) represent the MTT-S.

So whom do we actually represent? Electronic engineering is less popular among Polish girls than, for example, biotechnologies. And, without digging into the official statistics (which still remains to be done), my memories of university tell me that we had 40% female students in informatics while only 10% were in radioelectronics. That was back in the 1980s; if I observed any

IEEE Transactions on Microwave Theory and Techniques

Special Issue

AI- and Machine Learning-Based Technologies for Microwaves

Submission deadline: 22 February 2022. Expected publication date: August 2022

Machine learning (ML) and AI have experienced phenomenal success in the past decade in signal processing, image and speech recognition, robotics, autonomous systems and more. This success is also coupled with the expanding applications of machine learning and AI in broad areas of science and engineering. The microwave community is among the earliest in exploring machine learning and artificial neural networks (ANN) for wireless and wireline electronic device, circuit and system designs. In recent years, there is a significant increase in the interests and activities in applying machine learning and AI not only at device/circuit level modeling and design, but also at system and higher-level applications. Stimulated research and applications leads to novel methodologies of microwave oriented machine learning techniques, such as new ANN, support vector machine and Gaussian process based approaches, automated modeling, deep learning; in addition to an expanding scope of microwave problems that are addressed by machine learning and AI, from electromagnetic structural modeling and design, multi-physics modeling, microwave filter/multiplexer design, GaN HEMT modeling, PA behavioural modeling, digital predistortion design, oscillator design, SIW diagnosis, MEM sensor modeling, design of high-speed VLSI packages and microsystems, wireless power transfer, MIMO transmitter design and more. Further applications of machine learning at system level are creating breakthrough capabilities of microwave systems, such as electromagnetic-based image reconstruction for medical or security applications, and dynamic spectrum allocation for next generation wireless systems.

This special issue will bring the subject into focus, creating a forum for researchers and engineers. The special issue aims to stimulate in-depth overviews, thought-provoking formulations, novel methodologies and applications. Topics include, but are not limited to:

- Electromagnetic modeling, optimization and uncertainty quantification using machine learning
- Machine learning and AI methods for modeling GaN HEMTs, HBT and other nonlinear devices
- Novel machine learning/AI paradigm and knowledge-based methods to microwave design
- Evolutionary algorithms for microwave design optimization
- Machine learning and AI oriented multi-physics modeling for microsystems and power devices
- Machine learning methods for SIC/SIW modeling and diagnosis
- ANN for signal and power integrity analysis in IC interconnects, packages, and microsystems
- Machine learning methods in design of microwave filters/multiplexers, such as waveguide filters, SIW filters, dielectric resonator filters, reconfigurable filters, and more
- Application of machine learning to modeling of sensors, and MEM devices
- Application of machine learning to VCO design, PA modeling and digital predistortion design
- Machine learning for transmitter/receiver design including MIMO transmitters and more
- Application of machine learning for modeling and design for wireless power transfer
- Machine learning for electromagnetic/microwave-based image reconstruction, sensing, gesture recognition, and applications for health-monitoring, medical or security systems
- Machine learning for radar detection, object localization and application in autonomous systems,
- Intelligent RF system design, machine learning for signal detection and classification, spectrum monitoring, dynamic spectrum allocation, and channel optimization; AI in wireless systems, modulation identification, and RF fingerprinting
- Novel applications of machine learning and AI for wireless systems from megahertz to terahertz.

Authors should consult <https://www.mtt.org/author-information-transactions/> for submission instructions.

Guest Editor: Prof. Q.J. Zhang, Carleton University, Ottawa, Canada, Qijun.zhang@carleton.ca

change over the next 30 years of teaching electromagnetics at the Warsaw University of Technology (WUT), the percentage has only been going down. I recall being one of three females in a student group of 30: 20 years later, Marzena was the only one in her group.

Today, we have neither the means nor intention to cheer a cohort of young women into becoming electromagnetic nerds or integrated circuit designers. We believe, however, in the power of diversity: as I used to say to my students, “Electromagnetic waves are everywhere.” There are many fascinating things to be done in the megahertz (MHz)-to-terahertz (THz) range. Our own team at QWED may serve as an illustration. With a staff of 15 (50% of whom are in R&D), we develop and commercialize Quick-Wave electromagnetic and multiphysics software; design, manufacture, and sell microwave resonators for material measurements; and contribute to research and industrial projects in the gigahertz (GHz) characterization of semiconductor and energy materials, space and defense technologies, and the microwave processing of foods [3]. And there is still so much to be done!

Perhaps I should also add that half of the QWED team is made up of women (Figure 1), which is unusual for *any* high-tech small and medium-size enterprise (SME) and particularly for a microwave SME. Our secret is probably in trying to maintain a family atmosphere—a sense of permanence and continuity. The core team comes from the Institute of Radioelectronics at WUT, where we studied and taught, under the leadership of Prof. Wojciech Gwarek, IEEE Fellow (2001) and recipient of MTT-S Pioneer Award (2011) for the development and practical use of the electromagnetic modeling methods that formed the foundations of QWED.

We maintain harmonious relations with WUT, through joint research and student internships. To sum up some of our experiences and also appeal to young engineers and those with a greater



Figure 1. The women at QWED 2020.

affinity for informatics, Marzena gave her presentation “Computer Multiphysics Simulations—A Must-Have for Emerging Technologies” at a recent IEEE Day and IEEE Student Meeting Champions League session [4] (see [5] for the slides). However, this came after our WiM activities’ inauguration at MIKON.

Why MIKON?

MIKON is a traditional microwave conference with more than 50 years of history. It first took place in 1969 with a focus on the Polish microwave

community but gradually attracted the international community with its high scientific standards (as well as the added social benefits). Since the 1990s, MIKON has been run under the auspices of the IEEE, and, since 2004, it has been part of MRW—which also comprises radar, semiconductor, and signal processing events. Major credit for these wonderful developments goes to Prof. Jozef Modelski, MIKON chair 1994–2006, MRW chair since 2004, and past president and Honorary Life Member of the MTT-S.

We chose MIKON for our first public WiM event not only due to its long history and prominence but also because of our personal connection and memories. At MIKON 2010, Marzena received her first research award for best M.Sc. thesis. My first attendance and contribution to MIKON took place back in 1991 [6], and here I share a few memories of the occasion. That conference was held in the 17th century castle of Rydzyna, which inspired cultural and social exchanges in addition to scientific communications. I shall never forget a social evening when Prof. João Costa Freire played guitar, Prof. Andre Vander Vorst performed a repertoire of Jacques Brel, and Prof. Tatsuo Itoh sang a Japanese song *a capella* (I contribute this small piece to the memory of Prof. Tatsuo Itoh, whom the MTT community sadly lost a few weeks



Figure 2. The introduction of the WiM session by Prof. Jozef Modelski (Marzena Olszewska-Placha is seated on the left, and the author stands on the right).

prior to the writing of this column.). I left Rydzyna with a bunch of new research ideas and a refreshed vision of academic life, where people of very diverse backgrounds could interact on so many topics. At that time, I was formally on maternity leave and not quite sure how my professional life could further evolve. Poland was in a period of political and economic changes, resulting in my predicted monthly salary from the university not covering even a week of babysitting for my son. MIKON 1991 certainly give me new motivation and courage to face these challenges, which is probably one of the best things a conference can do for a woman debating whether or not to stay in the engineering field. I felt it was worth offering a similar experience to a new generation of women in microwaves, and I also felt that the MIKON setting would add a golden touch to our first WiM event.

The WiM Session Itself

To those surprised by the fact that we actually managed to have an in-person meeting in the midst of the pandemic, let me explain that MIKON 2020 luckily fit into a kind of transfer window after the traditional vacation period and just before the second wave of infections emerged. Travel restrictions had just been relaxed, and flights from several European countries reopened, allowing, for example, our guests from France and Germany to attend.

Prof. Modelski introduced the WiM session (Figure 2). Keynote talks were presented remotely (see Figure 3) by the first and second female presidents of the IEEE MTT-S: Past President Prof. Dominique Schreurs and President-Elect Prof. Rashaunda Henderson. Dr. Agnieszka Konczykowska, IEEE Fellow, served as the senior panelist. On-site support was provided by Prof. Daniel Pasquet (MTT-S AdCom member) and Dr. Volker Ziegler (AIRBUS Central R&T, Germany).

The overall challenges faced by women in science and engineering were subsequently discussed, and the audience (including three female

apprentice engineers of QWED) contributed with problems to be considered in further WiE activities. In particular, we found that, while the term *microwaves* somewhat disturbs or even terrifies novices (or, in the best case, is associated with a domestic oven), there are other relevant terms likely to raise curiosity and interest in the field.

Two of them are *computer simulations* and *emerging technologies*, which were merged in the title of Marzena's presentation [7], which builds upon the MIKON dissemination experience.

The WiM/MTT-S kiosk was open and visible throughout the week (Figure 4). During the banquet, we thanked the organizers for hosting



Figure 3. The on-site (and some of the online) participants of the WiM session during MIKON 2020. Seated in the middle are Marzena Olszewska-Placha (left) and the author; standing behind are Prof. Daniel Pasquet (left) and Dr. Volker Ziegler; and onscreen are MTT-S President-Elect Rashaunda Henderson (left) and IEEE Fellow Dr. Agnieszka Konczykowska.



Figure 4. The WiE kiosk at MIKON-MRW 2020.



Figure 5. The author during the MRW banquet.

the WiM session (Figure 5) and agreed to organize similar events at the next MRW (Gdansk, 2022). Additional photos of the event can be found at <https://www.qwed.eu/mikon2020wie.html>.

What Comes Next?

As the IEEE Poland Section WiE affinity group, we hope to use our best efforts, competencies, and personal experiences to promote microwave engineering among women and help promote women in microwave engineering and beyond, in the seven spheres of life and society. The talks Marzena prepared [5] will be given at subsequent editions of IEEE Day and the IEEE Student Meeting Champions League, for which QWED will also become partner, with a view of promoting the MHz-to-THz theme in students' projects. I am honored to be invited by the Education Subcommittee of the MTT-S AdCom to present a webinar in September 2021 [8].

References

- [1] "Microwave and Radar Week 2020, Warsaw." Oct. 5–7, 2020. www.mrw2020.org
- [2] "IEEE women in engineering international leadership summit Krakow 2017." IEEE. <https://wie.ieee.org/ieeewieilspoland2017/>
- [3] U. Erle, P. Pesheck, and M. Lorence, *Development of Packaging and Products for Use in Microwave Ovens*, 2nd ed. Amsterdam, The Netherlands: Elsevier, 2020.
- [4] "IEEE student meeting 13.01.2021." IEEE. 2020. <https://ieeep1/?q=node/204>
- [5] M. Olszewska-Placha, "Computer multiphysics simulations: A must-have for emerging technologies," QWED. https://www.qwed.eu/nanobat/IEEE_StudentMeeting2021_presentation.pdf
- [6] M. Olszewska, "Design of dual reflector antenna operating in 5.2–5.8 frequency range," M.Sc. thesis, Warsaw Univ. Technol., 2010.
- [7] W. Gwarek and M. Celuch-Marcysiak, "Time-domain analysis of two- and three-dimensional microwave circuits," in *Proc. Int. Microwave Conf. MIKON-91*, Rydzyna, May 1991, pp. 56–80.
- [8] M. Celuch, "Modelling-based measurements of materials for application in 5G and energy sectors," webinar scheduled for Sept. 14, 2021 (as part of a monthly series sponsored by the Education Subcommittee in the MTT-S AdCom).



Introducing IEEE Collabratec™

The premier networking and collaboration site for technology professionals around the world.

IEEE Collabratec is a new, integrated online community where IEEE members, researchers, authors, and technology professionals with similar fields of interest can **network** and **collaborate**, as well as **create** and manage content all in one place!

Learn about IEEE Collabratec at iee-collabratec.ieee.org





IEEE Space Hardware and Radio Conference

16-19 January 2022, Caesars Palace Hotel, Las Vegas, NV USA



IEEE



<https://www.radiowirelessweek.org/>

Paper Deadline
25 July 2021

Steering Committee

General Chair

Kevin Chuang, *MaxLinear*

General Co-Chair

Alexander Koelpin, *Hamburg University of Technology*

Technical Program Chair

Changzhi Li, *Texas Tech. University*

Finance Chair

Holger Maune, *Technical University of Darmstadt*

PAWR Co-Chairs

Václav Valenta, *European Space Agency*

Roberto Quaglia, *Cardiff University*

WiSNet Co-Chairs

Rahul Khanna, *Intel*

Paolo Mezzanotte, *University of Perugia*

SiRF General Chair

Saeed Zeinolabedinzadeh, *Arizona State University*

SHaRC Co-Chairs

Markus Gardill, *Julius-Maximilians-University Würzburg*

Maximilian C. Scardelletti, *NASA Glenn Research Center*

Executive Committee Chair

Rashaunda Henderson, *University of Texas Dallas*

Conference Management

Elsie Vega, *IEEE*

Deidre Artis, *IEEE*

Call For Papers

The 2022 IEEE Space Hardware and Radio Conference (SHaRC 2022) will be a part of 2022 IEEE Radio and Wireless Week (RWW 2022) which will be held during the week of 16 January 2022 in Las Vegas, NV, USA.

RWW 2022 will also feature:

- IEEE Radio and Wireless Symposium (RWS)
- 22nd Topical Meeting on Silicon Monolithic Integrated Circuits in RF Systems (SiRF)
- IEEE Topical Conference on Wireless Sensors and Sensor Networks (WiSNet)
- IEEE Topical Conference on RF/Microwave Power Amplifiers for Radio and Wireless Applications (PAWR)
- Special Sessions, Short Courses, and Design Competition

Each of these events will be organized separately, with their own call for papers found at <http://www.radiowirelessweek.org/>.

The IEEE Space Hardware and Radio Conference (IEEE SHaRC) addresses new concepts, novel implementations, as well as emerging applications for space-based hardware for communications, earth observation, and other novel disruptive services. To meet recent needs, there has been a renaissance of interest and investment in space- and suborbital-based systems especially for high-data-rate communications networks. These new global satellite networks are disruptive, rely on new system and subsystem design paradigms, and are an enabler for many novel applications. The IEEE Space Hardware and Radio Conference provides a forum for discussions on this new frontier.

Papers featuring innovative work are solicited in (but not limited to) the following areas of the space hardware and systems:

- Cubesat, Micro- and Small-Satellite Hardware and Systems
- Satellite, High-Altitude Balloon and UAV Systems, Networks & Concepts
- Ground Stations, Terrestrial Systems and Mobile Communications Integration
- Space Electronics & Radiation Effects
- Antennas, Antenna Arrays and Multi-Antenna Systems
- Communication Systems, Inter-Satellite- and High-Data-Rate Links
- Mission Concepts, Large Constellations, Orbital Configurations & Operations
- Geolocation & Satellite Navigation
- Sensing and Earth Observation
- Frequency Spectrum Allocations, International Regulations & Standards

SHaRC 2022 Chair

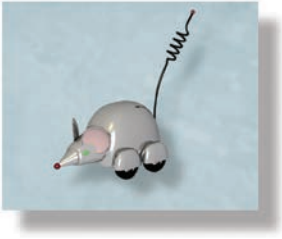
Markus Gardill, *Julius-Maximilians-University Würzburg*

SHaRC 2022 Co-Chair

Maximilian C. Scardelletti, *NASA Glenn Research Center*

Authors of papers presented at RWW 2022 will be invited to submit an expanded version to the **IEEE T-MTT Mini-Special Issue**.

Paper submission instructions can be found at <http://www.radiowirelessweek.org/>. Submissions should be formatted according to the submission review template available on the RWW website. Authors should indicate preference for oral or poster presentation. All submissions must be received by **25 July 2021**. All accepted papers will be published in a digest and included in the IEEE Xplore® Digital Library. Submissions will be evaluated based on novelty, significance of the work, technical content, interest to the audience, and quality of writing.



New Products

■ Ken Mays, Editor

Products listed in *IEEE Microwave Magazine* are restricted to hardware, software, test equipment, services, applications, and publications for use in the science and practice of RF/microwave or wireless engineering. Product information is provided as a reader service and does not constitute endorsement by IEEE or the IEEE Microwave Theory and Techniques Society. Absolute accuracy of listings cannot be guaranteed. Contact information is provided for each product so that interested readers may make inquiries directly.

Please submit "New Products" column information to microwave.newproducts@ieee.org.

Welcome to a further installment of the "New Products" column in *IEEE Microwave Magazine*. In this issue, we present six new items that may be of interest to the RF/microwave and wireless communities.

High-Power 8-GHz GaN Variable-Fence Microwave Comb Generator

Ultraview has announced a new class of microwave comb generator featuring previously unattainable output power levels, low jitter, and spectral content programmability. Based on a custom ultrahigh-repetition-rate gallium nitride (GaN) differential pulser

Digital Object Identifier 10.1109/MMM.2021.3069621
Date of current version: 1 June 2021

integrated circuit, the palm-sized Ultracomb-8G is powered from any USB3.0/3.1 port through which the user can program comb amplitude, comb picket spacing, and low-/high-frequency spectral weighting.

Comb picket spacing can be software-programmed to any frequency from 10 MHz to 2 GHz in single-ended-output mode (10–50 MHz in differential output mode) in 0.01-Hz steps, generated by an onboard LMX2594 synthesizer driven from an internal 150-femtosecond (fs) jitter reference clock

or external 10–500-MHz reference. The unit can also be programmed in 1:1 clock mode, enabling the pulse repetition rate of the comb generator (and the comb tooth spacing) to be the same as the external reference/clock input. Its differential outputs enable direct antenna connections without the use of a balun as well as a 3-dB-higher total output level.

The Ultracomb-8G has the additional unique ability to create strings of pulses with widths varying from 100 picoseconds (ps) to 800 ps, enabling it to generate relatively flat combs with usable energy to 10 GHz or, alternatively, combs with much

higher power but with most of the energy concentrated below 2 GHz. This is useful, for example, in antenna testing, in which low-frequency antennas can be tested over very long ranges or transmission through lossy media while retaining the ability to test over a wider bandwidth when using shorter ranges.

Announcing a new class of microwave comb generator featuring previously unattainable output power levels, low jitter, and spectral content programmability.



The Design and Analysis Frontier of Electronic Packaging

30th Conference on Electrical Performance of Electronic Packaging and Systems

October 17th to 20th, 2021



Call for Papers



EPEPS is the premier international conference on advanced and emerging issues in electrical modeling, measurement, analysis, synthesis, and design of electronic interconnections, packages, and systems. It also focuses on new methodologies and CAD/design techniques for evaluating signal, power, and thermal integrity and ensuring performance in high-speed, RF, and wireless designs. EPEPS is jointly sponsored by IEEE Electronics Packaging Society, IEEE Microwave Theory and Techniques Society and IEEE Antennas and Propagation Society. Submitted papers should describe new technical contributions related to the area of electrical performance of high-performance interconnect systems, covering:

- System-level, board-level, package-level and on-chip interconnects
- High-speed channels, links, backplanes, serial and parallel interconnects, SerDes
- RF/microwave/mm-wave packaging structures and components, antenna-in-package and RFIC co-design, mixed signal modules and wireless switches
- Signal and thermal integrity
- Power integrity and power distribution networks
- Low power mobile and personal applications
- Memory and DDR interfaces
- Jitter and noise management
- Electronic packages and microsystems
- Heterogeneous integration, 2.5D/3D interconnects and packages, TSVs and MCMs
- Electromagnetic (EM) and EM interference modeling, simulation algorithms, tools, and flows
- Macro-modeling and model order reduction as it applies to electrical analysis
- Advanced and parallel CAD techniques for signal, power, and thermal integrity analysis
- Measurement and data analysis techniques for system-level and on-chip structures
- High volume testing for electronic packages.

Submission Deadline: July 11, 2021

Conference Chairs:

Jose Hejase, jhejase@nvidia.com

Zhen Peng, zvpeng@illinois.edu

For more information/contact: epeps-admin@illinois.edu

Submission Format: 2-column, 3-page PDF format only.

Selected papers will be invited for a special issue in *IEEE Transactions on Components, Packaging, and Manufacturing Technology*. Information for authors can be found at www.epeps.org. Submitted manuscripts should be camera ready and compliant with the general standards of the IEEE, including appropriate referencing. Noncompliant manuscripts will not be considered for review.

Location: EPEPS 2021 will be a virtual event due to continuing COVID-19 repercussions worldwide.

Tutorials: EPEPS offers tutorials on state-of-the-art topics including latest advances: on CAD software tool techniques for package/PCB design, SI and PI modeling, high-speed SerDes simulation, high precision measurement techniques and novel interconnect design.

IEEE Education Credits: IEEE offers professional development hours (PDHs) and continuing education units (CEUs) for attending the EPEPS program.

Simulation Benchmarking: EPEPS 2021 organizers invite paper submissions covering simulation tool development advances which utilize benchmarks established and released publicly by the IEEE TC-EDMS Packaging Benchmarks Committee (<http://www.packaging-benchmarks.org/>).

Exhibits: EPEPS offers an excellent array of vendor exhibits. EPEPS is an exciting forum for vendors to demonstrate their state-of-the-art tools to attendees. Interested vendors can contact the conference administration for more details.

Conference Website: www.epeps.org

At the narrowest pulsewidth setting, and with a 500-million pulse per second (mp/s) pulse repetition frequency (500-MHz picket spacing), each generated picket below 3 GHz has a greater than +10-dBm power level. Even up to 6 GHz, each picket has greater than 0-dBm power. The picket at 8 GHz has a level of -7.5 dBm. At 1,250 mp/s, the first three pickets are each more than +15 dBm. The unit can generate a comb with 200-MHz spacing and flat with 0 dBm/picket power to 3 GHz, -3 dBm at 5.4 GHz, and -11 dBm at 8 GHz. GUI software, with full Qt source, is included for Windows 10, Mac OS X, Linux Mint 18, and RHEL/Centos 7.x.



Learn more about Ultraview and its products at www.ultraviewcorp.com.

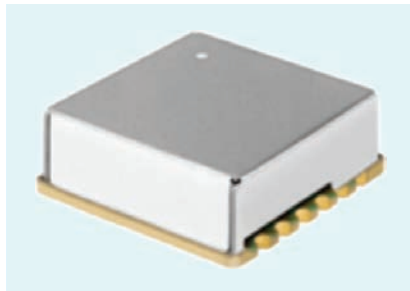
High-Performance, Low-Noise Ku Band PLO

Z-Communications has announced a new Restriction of Hazardous Substances in Electrical and Electronic Equipment (RoHS)-compliant fixed-frequency phase-locked loop model that can enhance any application needing premium performance while operating in the Ku-band region. The SFS14000H-LF is a plug-and-play phase-locked oscillator (PLO) allowing for quick and simple integration into any system design. It is specified to produce a fixed signal output at 14.0 GHz while locked to an external 100-MHz reference oscillator source. This simple-to-use PLO features unmatched low-phase noise performance of -93 dBc/Hz, -96 dBc/Hz, and -116 dBc/Hz at the 1-, 10-, and 100-kHz offsets, respectively.

The SFS14000H-LF is designed to deliver an output power of -3 dBm

into a 50-Ω load while operating off a voltage-controlled oscillator voltage supply of 5 V dc and drawing 85 mA and a phase-locked loop voltage of 3.3 V dc while drawing 40 mA. This product features a typical harmonic suppression of -20 dBc and spurious suppression of -65 dBc. It is housed in Z-Communications's standard SFS-L1 package measuring 1.0 in × 1.0 in × 0.22 in. The SFS14000H-LF is also a good choice for an automated surface mount assembly and is available in tape and reel packaging.

The SFS14000H-LF is well suited for radar applications requiring operation over the temperature range of -40 to 85 °C. For further information on this model or any other product from Z-Communications, please contact their Applications Department via email at applications@zcomm.com or via phone at +1 858-621-2700.



Ultraportable Handheld Microwave Spectrum Analyzers Supporting 6–20 GHz

SAF Tehnika has expanded its Spectrum Compact family of ultraportable handheld microwave spectrum analyzers with the introduction of a model that supports 6–20 GHz. The new Spectrum Compact delivers high durability at an affordable price point, making it a useful tool for field engineers and technicians responsible for link planning, installation, site acceptance, maintenance, and troubleshooting of wireless networks.

This product features a typical harmonic suppression of -20 dBc and spurious suppression of -65 dBc.

The 6–20-GHz spectrum analyzer has high sensitivity of -110 dBm at 30-kHz resolution bandwidth, long battery life of up to 4 h, and instant-on functionality for quick startup and operation, and it is designed in a rugged, ultracompact form factor that measures only 5.31 in × 3.27 in × 1.34 in (135 mm × 83 mm × 34 mm) and weighs 20.11 oz. (0.57 kg). It is a good choice for mobile carriers, telecommunications professionals, Internet service providers, and contractors responsible for regulatory and compliance, drone applications, and satellite operation.

The Spectrum Compact family has been designed to address the challenges of field applications. Similar to all Spectrum Compact models, the 6–20-GHz handheld spectrum analyzer has a resistive touchscreen for operation with gloves as well as high contrast and full display modes for easy readability in bright light environments. Durable thumbscrews for the waveguide adapter connections help the Spectrum Compact withstand harsh environments. Spectrum traces can be saved in the integrated 8 GB of memory for offline analysis, investigation, and reporting using the Spectrum Manager PC software.

The 6–20-GHz instrument extends the frequency range for the Spectrum Compact family. Included in the series are portable E-band (70–87-GHz) and V-band (56–71-GHz) handheld spectrum analyzers.

Spectrum Compact devices are well suited for mobile operators, carriers, and tower installation crews deploying 5G networks; wireless Internet service providers; local government institutions; public safety departments; and critical network infrastructure owners. Field engineers and technicians can use the ultraportable handheld microwave spectrum analyzer to conduct site surveys, radio parameter verification, antenna alignment,

The 22nd IEEE Topical Meeting on Silicon Monolithic Integrated Circuits in RF Systems

16-19 January 2022, Caesars Palace Hotel, Las Vegas, NV USA

Paper Deadline
25 July 2021



Radio and Wireless Week

<https://www.radiowirelessweek.org/>



Conference Chair

Saeed Zeinolabedinzadeh
Arizona State University

Technical Program Chair

Roe Ben-Yishay
ON Semiconductor

Technical Program Co-Chair

Robert Schmid
Johns Hopkins Applied Physics Lab

Publication Chair

Aleks Dyskin
Inxpect

Publicity Chair

Ickhyun Song
Oklahoma State University

International Liaison - Asia

Chien-Nan Kuo
National Chiao Tung University

International Liaison - Europe

Mehmet Kaynak

IHP Microelectronics

Executive Committee

Julio Costa

Qorvo

Mehmet Kaynak

IHP Microelectronics

Eric Kerherve

University of Bordeaux

Dietmar Kissinger

Ulm University

Chien-Nan Kuo

National Chiao Tung University

Donald Lie

Texas Tech University

Sergio Pacheco

NXP Semiconductors

Nils Pohl

Ruhr-Universität Bochum

Jae-Sung Rieh, Korea University

Hao Li, Infineon Technologies

Hasan Sharifi

HRL Labs

Václav Valenta, ESA / ESTEC

Monte Miller

NXP Semiconductors

Ahmet Cagri Ulusoy

Karlsruhe Institute of Technology

Vadim Issakov

University Magdeburg

Yi-Jan Emery Chen

National Taiwan University

Venkata Koushik Malladi,

NXP Semiconductors

Call for Papers

IEEE Topical Meetings on Silicon Monolithic Integrated Circuits in RF Systems have been at the forefront of moving Silicon technologies into microwave, millimeter-wave and THz applications – a development now widely accepted, and of great importance. RF CMOS and Si/SiGe BiCMOS technologies are well established in commercial and defense applications.

SiRF 2022 will mark the 22nd topical meeting on SiRF, with a renewed emphasis on promoting a dialogue between IC designers and researchers promoting non-standard technologies, exploiting the maturity of Silicon processes, but addressing the challenges of tomorrow. The three days of SiRF 2022 will chronicle recent advances in our dynamic field, and provide the platform for developing new ideas, and candid exchange, facilitated by SiRF's single-session format. As in past years, a line-up of reputed invited speakers will stimulate our discussions, with an emphasis on emerging technologies.

For more details, visit: <http://www.radiowirelessweek.org/sirf-home>

SiRF 2022 solicits papers in the following focus areas:

1. RF, Millimeter-wave and THz Integrated Circuit Front ends

- Integrated Transceivers and Transceiver sub-systems
- MIMO and Phased Array Integrated Circuits
- Ultra-Wideband Front ends and Building Blocks
- Emerging Technologies, 5G and 6G Front ends
- mmW & THz Imaging Circuits
- System-on-Chip and System-on-Package
- Smart Antennas and Integrated Meta-Surfaces
- RF, mmW and THz Circuit Building Blocks
- Reconfigurable Radio Front ends
- Wireless Sensors and Sensor Systems
- Low Power RFIC for Biomedical Applications

2. Wireline Communication Circuits and Building Blocks

- Wideband Transmitter, Receiver and Transceivers
- High Frequency Oscillators and Signal Generators
- PLLs and Frequency Synthesizer Integrated Circuits
- Clock and Data Recovery Circuits
- Precise Timing Circuits
- High-Speed Modulators and Drivers

3. High Speed Data Converters & Mixed Signal Circuits

- Nyquist Rate and Oversampling A/D and D/A Converters
- Embedded & Application-Specific A/D and D/A Converters
- Analog to Information Conversion
- Time-to-Digital Converters
- Analog Circuits and Building Blocks
- Digitally Assisted Analog Circuits and Analog Calibration
- MEMS/sensor Interface Circuits

4. Silicon Photonics and Electronic-Photonic Integrated Circuits

- Wideband Electronic-Photonic Circuits
- Electronic-Photonic Modulators
- Electronic-Photonic Receives
- Wideband TIAs and Drivers
- LIDARS
- Optical PLLs
- Radio Over Fiber Circuits

5. Devices, Technology, Modeling and Materials

- Advanced RF CMOS and SiGe BiCMOS Devices
- Si-Based Heterostructures
- Through-Silicon Via Integration
- RF MEMs and Micromachining
- Advanced Device Modeling
- Advanced Packaging
- Epitaxy
- Strain Engineering
- Characterization and Stability Issues
- Smart Materials
- Nano Technologies Including CNT, Nanowire and Graphene

6. Measurement and Modeling

- Multi-Physics Modeling
- EM Simulation of Complex RFICs
- Robust Measurement and De-Embedding
- Built-In Self-Test
- Self-Calibration

MEETING DETAILS

SiRF 2022 will be held during Radio and Wireless Week in Las Vegas, NV, along with the Radio and Wireless Symposium (RWS), the Topical Conference on Power Amplifiers for Wireless and Radio Applications (PAWR), the Topical Meeting on Wireless Sensors and Sensor Networks (WisNet), and the Space Hardware and Radio Conference (SHARC).

Authors of papers presented at RWW 2022 will be invited to submit an expanded version to the **IEEE T-MTT Mini-Special Issue**.

Paper submission instructions can be found at <http://www.radiowirelessweek.org/>. Submissions should be formatted according to the submission review template available on the RWW website. Authors should indicate preference for oral or poster presentation. All submissions must be received by **25 July 2021**. All accepted papers will be published in a digest and included in the IEEE Xplore® Digital Library. Submissions will be evaluated based on novelty, significance of the work, technical content, interest to the audience, and quality of writing.

interference detection, line-of-sight verification, signal strength mapping, and interference hunting.



SAF Tehnika has developed a free virtual demo of Spectrum Compact for viewing at https://saftehnika.com/en/sc_emulator.

Samtec Compression-Mount PCB Connectors With Reach to 65 GHz

Samtec now offers compression-mounted printed circuit board (PCB) connectors for microwave applications up to 65 GHz. The solderless vertical launch allows for easy, field replaceable, cost-effective assembly to the board. Connector interfaces include 1.85 mm (65 GHz), 2.40 mm (50 GHz), and 2.92 mm (40 GHz), with microstrip and stripline options available.



Threaded coupling provides superior repeatability with high mechanical stability. Mating cable assemblies are also available. Connectors that are 1.35 mm (90 GHz) are coming soon.

For more information, please visit samtec.com/PrecisionRF.

Microwave Cable Assemblies Applicable Up to 110 GHz

Rosenberger, the long-recognized RF and microwave technology supplier, has developed a comprehensive portfolio of standard flexible microwave cable assemblies, with and without armoring (crush resistance with armor 80 N/mm) and characterized by excellent phase and amplitude stability as well as high electrical and mechanical stability.

The standard cable assemblies' range covers ultralow-loss and high-phase-stable variants for 18, 26.5, 40, 50, and 70 GHz. For stringent test and measurement applications, where metrology grade performance is required, Rosenberger offers vector network analyzer test cables with performance up to as high as 110 GHz. Custom-designed cable assemblies can also be ordered on request.

A product flyer with detailed information is available for download at <https://www.rosenberger.com/product/microwave-cable-assemblies/>.



Four-Way Splitter/Combiner Passes DC and 40–65 GHz

Mini-Circuits' model ZC4PD-E40653+ is a four-way, dc pass power splitter/combiner with a wide frequency range of 40–65 GHz. Well suited for millimeter-wave testing and coverage in 5G cellular wireless networks, it handles as much as 12-W input power as a splitter, with excellent amplitude unbalance of typically 0.2 dB between channels. The typical insertion loss per channel above the nominal 6-dB power split is 2.1 dB at 40–50 GHz and 2.6 dB at 50–65 GHz. The typical isolation between channels is 28 dB at 40–50 GHz and 26 dB at 50–65 GHz. Voltage standing-wave ratio at all ports is typically 1.16:1 or lower, while phase unbalance from a 0° split among channels is within $\pm 3.5^\circ$ at 40–50 GHz and $\pm 4.9^\circ$ at 50–65 GHz. The RoHS-compliant, 50- Ω splitter/combiner has female 1.85-mm coaxial connectors and measures 1.854 in \times 1.00 in \times 0.50 in (47.10 mm \times 25.40 mm \times 12.70 mm). It can pass as much as 334-mA dc current and is designed for operating temperatures from -55 to $+100^\circ\text{C}$.



For information, please visit <https://www.minicircuits.com/WebStore/dashboard.html?model=ZC4PD-E40653%2B>.





IEEE Journal of Electromagnetics, RF and Microwaves in Medicine and Biology (J-ERM)

Call for Papers for the Special Issue on “Wireless Non-contact Sensing of Life Activities for Biomedical Applications”

The IEEE Journal of Electromagnetics, RF and Microwaves in Medicine and Biology (J-ERM), sponsored by IEEE MTT-S, AP-S, and EMBS societies and Sensors Council, will publish a special Issue devoted to “Wireless Non-contact Sensing of Life Activities for Biomedical Applications”.

Short-range RF/microwave sensors are capable of remotely detecting physiological movements and tracking the locations of human subjects. They are attractive for non-contact biomedical applications from long-term outpatient care to instant diagnosis during events such as COVID-19 pandemic. They have also enabled several interactive human-machine interfaces, such as gesture recognition, presence/occupancy tracking and human counting. Over the past few years, a new class of human sensing systems has spawned that leverage Wi-Fi signals to perform human sensing. Meanwhile, advances in machine learning, parallelization and the speed of graphics processing units (GPUs) have brought deep neural networks (DNNs) to the forefront of research, offering significant performance gains in the classification of signals.

This special issue is designed as an expanded forum of the the 2021 International Microwave Symposium (IMS) full-day workshop “Modern radar for IoT/biomedical applications”. To broaden the scopes, submissions to this special issue do not need to be associated with the workshop presentations. All potential authors are invited to submit original research papers and review papers on this topic. If you are unsure whether your paper is suitable for this special issue, please write to the guest editors at jermIMS21@gmail.com.

Please note that:

1. Papers should be submitted through the journal’s web page <http://ieee-jerm.org> leading to ScholarOne Manuscript Central.
2. In the menu for “Manuscript Type”, please select “Wireless Non-contact Sensing of Life Activities for Biomedical Applications Special Issue”.
3. Manuscript is limited to 6 pages maximum without counting the first (Visual Summary/Take-Home Messages) page, citation pages, and bio-sketch pages. The first page should include a figure for Visual Summary and Take-Home messages in bullet-points.
4. The guideline and template for manuscript preparation can be found on the J-ERM webpage.

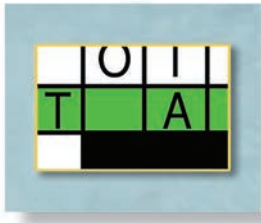
The due date for the paper submission is **September 30, 2021**. Peer review will start immediately once a paper is received. Accepted papers will appear in IEEE Xplore within a few days after acceptance. If you have any question, please contact guest editors at jermIMS21@gmail.com.

Guest Editors:

Dr. Changzhi Li, Texas Tech University, USA

Dr. Aly Fathy, University of Tennessee, USA

Dr. Jenshan Lin, University of Florida, USA



Enigmas, etc.

DC Power Consumption

■ Takashi Ohira

To provide a practical design example of the circuit topology discussed last month, we specify $V_{dc} = 100\text{ V}$, $1/\omega C_1 = 500\ \Omega$, and $R = 50\ \Omega$, as shown in Figure 1. Assuming a zero-voltage switching (ZVS) operation, find the dc power consumption P_{dc} . Which of the following is correct?

- a) 10 W b) 50 W c) 100 W d) 150 W

Solution to Last Month's "Enigmas, etc." Challenge

From the puzzle presented in the May 2021 issue, we remember that the current

$$i(t) = \frac{\pi}{2}(I_{dc} \sin \omega t - 2\omega C_1 V_{dc} \cos \omega t) \quad (1)$$

flows into the loop of L_2 , C_2 , and R connected in series. Across these elements, $i(t)$ induces the voltage

$$\begin{aligned} v_{LCR}(t) &= v_L(t) + v_C(t) + v_R(t) \\ &= L_2 \frac{d}{dt} i(t) + \frac{1}{C_2} \int i(t) dt + Ri(t) \\ &= V_{dc} + \frac{\pi}{2}(RI_{dc} + 2\omega C_1 X V_{dc}) \sin \omega t \\ &\quad + \frac{\pi}{2}(X I_{dc} - 2\omega C_1 R V_{dc}) \cos \omega t, \end{aligned} \quad (2)$$

Takashi Ohira (ohira@tut.jp) is with the Toyohashi University of Technology, Toyohashi, Aichi, 441-8580, Japan. He is a Life Fellow of IEEE.

Digital Object Identifier 10.1109/MMM.2021.3069622
Date of current version: 1 June 2021

Assuming a zero-voltage switching operation, find the dc power consumption P_{dc} .

where $X = \omega L_2 - 1/\omega C_2$. The integral constant is specified as V_{dc} because the dc power supply voltage fully applies to the capacitor C_2 .

Alternatively, the solution to last month's puzzle also reminds us of the shunt capacitor voltage

$$\begin{aligned} v(t) &= V_{dc} + \frac{\pi}{2} V_{dc} \sin \omega t \\ &\quad + \frac{1}{\pi \omega C_1} \left(\frac{\pi^2}{4} - 2 \right) I_{dc} \cos \omega t + \dots, \end{aligned} \quad (3)$$

where \dots represents higher-order Fourier harmonics. We now notice that (2) and (3) represent the same voltage (see the circuit diagram in Figure 1); hence, they must balance term by term.

The in-phase terms balance if we have

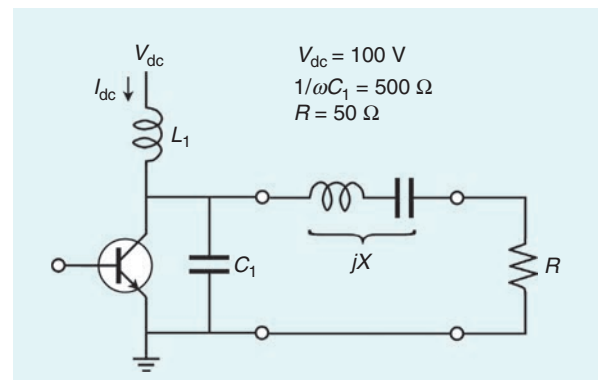


Figure 1. How much dc power ($V_{dc} I_{dc}$) is consumed? Note that the resonator reactance X is adjusted for the amplifier to perform the ZVS operation.



IEEE Topical Conference on Wireless Sensors and Sensor Networks



Paper Deadline
25 July 2021

<https://www.radiowirelessweek.org/>

Steering Committee

General Chair

Kevin Chuang, *MaxLinear*

General Co-Chair

Alexander Koelpin, *Hamburg University of Technology*

Technical Program Chair

Changzhi Li, *Texas Tech. University*

Finance Chair

Holger Maune, *Technical University of Darmstadt*

PAWR Co-Chairs

Václav Valenta, *European Space Agency*

Roberto Quaglia, *Cardiff University*

WiSNet Co-Chairs

Rahul Khanna, *Intel*

Paolo Mezzanotte, *University of Perugia*

SiRF General Chair

Saeed Zeinolabedinzadeh, *Arizona State University*

SHaRC Co-Chairs

Markus Gardill, *Julius-Maximilians-University Würzburg*

Maximilian C. Scardelletti, *NASA Glenn Research Center*

Executive Committee Chair

Rashaunda Henderson, *University of Texas Dallas*

Conference Management

Elsie Vega, *IEEE*

Deidre Artis, *IEEE*

Call For Papers

The 2022 IEEE Topical Conference on Wireless Sensors and Sensor Networks (WiSNet 2022) will be a part of 2022 IEEE Radio and Wireless Week (RWW 2022) which will be held during the week of 16 January 2022 in Las Vegas, NV, USA.

RWW 2022 will also feature:

- IEEE Radio and Wireless Symposium (RWS)
- 22nd Topical Meeting on Silicon Monolithic Integrated Circuits in RF Systems (SiRF)
- IEEE Topical Conference on RF/Microwave Power Amplifiers for Radio and Wireless Applications (PAWR)
- IEEE Space Hardware and Radio Conference (SHaRC)
- Special Sessions, Short Courses, and Design Competition

Each of these events will be organized separately, with their own call for papers found at <http://www.radiowirelessweek.org/>.

Wireless sensors and wireless sensor networks are crucial components for manufacturing, structural health, security monitoring, environmental monitoring, smart agriculture, transportation, commercial applications, localization, tracking systems and other important and emerging applications. WiSNet 2022 is intended to stimulate discussion and foster innovation on these components and applications.

Papers featuring innovative work are solicited in (but not limited to) the following areas:

- Wireless Sensors for Communication, Radar, Positioning and Imaging Applications
- Wireless Sensors for Localization and Tracking
- Wireless Integrated Sensors, Front-Ends and Building Blocks
- Wireless Sensors for Harsh Environments, Environmental, Health, Home and Commercial Applications
- Wireless Sensors Networks, Smart Sensor Systems, and Autonomous Networking
- RFID Sensors and Sensor Tags
- Sensor Networks for Sensor Network Topologies and Sensor Network Communication Architecture
- Coexistence, Synchronization and Scheduling in Hybrid and Social Networks
- Cryptography, Security, Privacy Issues in Ad-Hoc, Sensor and Mesh Networks
- Six-Port and Multi-Port Technology
- Internet of Things Hardware, Protocols and Applications
- Wireless Sensors Applications in Wearable Computing and Body Area Nets
- QoS Aware Design: Energy Optimization and Deployment Techniques Large, Dense and Dynamic Network Topologies

WiSNet 2022 Chair

Rahul Khanna, *Intel*

WiSNet 2022 Co-Chair

Paolo Mezzanotte, *University of Perugia*

Authors of papers presented at RWW 2022 will be invited to submit an expanded version to the **IEEE T-MTT Mini-Special Issue**.

Paper submission instructions can be found at <http://www.radiowirelessweek.org/>. Submissions should be formatted according to the submission review template available on the RWW website. Authors should indicate preference for oral or poster presentation. All submissions must be received by **25 July 2021**. All accepted papers will be published in a digest and included in the IEEE Xplore® Digital Library. Submissions will be evaluated based on novelty, significance of the work, technical content, interest to the audience, and quality of writing.

$$\frac{\pi}{2} V_{dc} = \frac{\pi}{2} (R I_{dc} + 2\omega C_1 X V_{dc}). \quad (4)$$

This equation is homogeneous with respect to V_{dc} and I_{dc} , which signifies that the dc current consumption increases linearly with the supplied voltage, even though the circuit contains a switch-mode transistor. Solving (4) for the dc voltage-to-current ratio, we obtain

$$\frac{V_{dc}}{I_{dc}} = \frac{R}{1 - 2\omega C_1 X}. \quad (5)$$

This condition should be held for the amplifier to perform the ZVS operation.

In the same way as the in-phase terms, the quadrature terms in (2) and (3) balance if we have

$$\frac{1}{\pi\omega C_1} \left(\frac{\pi^2}{4} - 2 \right) I_{dc} = \frac{\pi}{2} (X I_{dc} - 2\omega C_1 R V_{dc}). \quad (6)$$

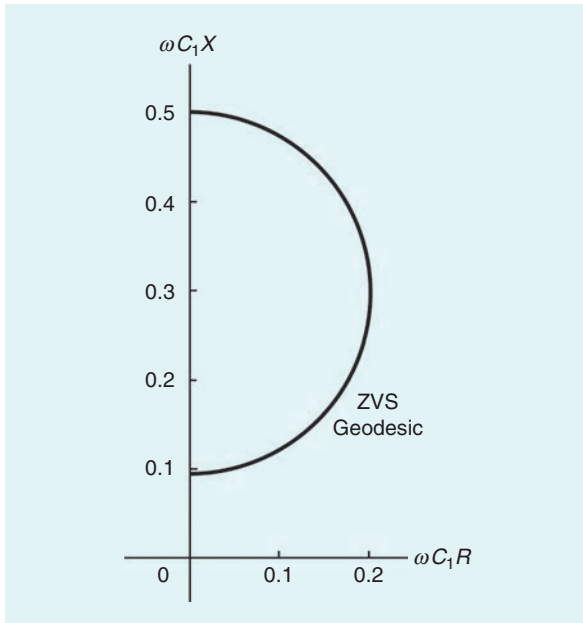


Figure 2. The load impedance locus for ZVS operation. The abscissa R and ordinate X are commonly normalized with $1/\omega C_1$. This specific semicircle is called the ZVS geodesic, and it will regularly appear in forthcoming puzzles in this “Enigmas, etc.” series.

Since the load resistance R is assumed to be always positive, the locus is truncated by half into a semicircle.

This condition should also be held simultaneously with condition (5). Conditions (5) and (6) are both homogeneous with respect to V_{dc} and I_{dc} , so we can eliminate them from the two conditions at once. As a result, we reach a triple-square-complete equation, that is,

$$(\omega C_1 R)^2 + \left(\omega C_1 X - \frac{1}{2} + \frac{2}{\pi^2} \right)^2 = \left(\frac{2}{\pi^2} \right)^2. \quad (7)$$

Let us project this equation onto the Cartesian R - X plane in question. Since R and X in (7) have the common multiplier ωC_1 , we can simplify the projection by employing the coordinate system $(\omega C_1 R, \omega C_1 X)$, as shown in Figure 2. As a result, (7) illustrates a circular locus centered at $(0, 1/2 - 2/\pi^2)$ with radius $2/\pi^2$. Since the load resistance R is assumed to be always positive, the locus is truncated by half into a semicircle.

We can choose any point (R, X) lying on this semicircle for the load of a ZVS amplifier. In summary, the correct answer to last month’s quiz is “d.” To explicitly locate the locus, we rewrite (7) as

$$\omega C_1 R = \sqrt{\left(\frac{1}{2} - \omega C_1 X \right) \left(\omega C_1 X - \frac{1}{2} + \frac{4}{\pi^2} \right)}, \quad (8)$$

which helps us illustrate that the semicircle is intercepted by the ordinate at $1/2$ and $1/2 - 4/\pi^2$.

Although this calculus may seem tough, it provides good practice on how to apply the harmonic-balance technique to RF power electronics. The result is demonstrated graphically, which is more persuasive than the use of equations.

The illustrated semicircular locus is geometrically the *shortest* route to link the two intercepts across the ordinate, which was pointed out by the French mathematician Henri Poincaré two centuries ago [1]. We will use this ZVS loading condition to design a practical power amplifier in next month’s puzzle.

Reference

- [1] T. Ohira, “A radio engineer’s voyage to double-century-old plane geometry,” *IEEE Microw. Mag.*, vol. 21, no. 11, pp. 60–67, Nov. 2020. doi: 10.1109/MMM.2020.3015136.





Conference Calendar

Editor's Note: Please check the website of each conference for any changes to paper or workshop deadlines or conference dates and modality (in person, virtual, or hybrid).

JULY 2021

2021 Fourth International Workshop on Mobile Terahertz Systems (IWMTS)
5–6 July 2021
(Virtual Conference)

AUGUST 2021

2021 IEEE 19th International Symposium on Antenna Technology and Applied Electromagnetics (ANTEM)
8–11 August 2021
Location: Winnipeg, Manitoba, Canada

2021 IEEE Radio-Frequency Integration Technology (RFIT)
25–27 August 2021
Location: Hualien, Taiwan

2021 46th International Conference on Infrared, Millimeter, and Terahertz Waves (IRMMW-THz)
29 August–3 September 2021
Location: Chengdu, China

Digital Object Identifier 10.1109/MMM.2021.3069623
Date of current version: 1 June 2021

OCTOBER 2021

2021 IEEE 30th Conference on Electrical Performance of Electronic Packaging and Systems (EPEPS)
17–20 October 2021
(Virtual Conference)

2021 15th International Conference on Advanced Technologies, Systems and Services in Telecommunications (TELSIKS)
20–22 October 2021
Location: Nis, Serbia

2021 SBMO/IEEE MTT-S International Microwave and Optoelectronics Conference (IMOC)
24–27 October 2021
(Virtual Conference)

NOVEMBER 2021

2021 IEEE International Conference on Microwaves, Antennas, Communications, and Electronic Systems (COMCAS)
1–3 November 2021
Location: Tel Aviv, Israel

2021 International Topical Meeting on Microwave Photonics (MWP)
15–17 November 2021
(Virtual Conference)

2021 IEEE MTT-S International Microwave Filter Workshop (IMFW)
17–19 November 2021
Location: Perugia, Italy

DECEMBER 2021

2021 IEEE BiCMOS and Compound Semiconductor Integrated Circuits and Technology Symposium (BCICTS)
5–8 December 2021
Location: Monterey, California, United States

2021 IEEE MTT-S International Microwave and RF Conference (IMARC)
9–11 December 2021
Location: Kanpur, India

JANUARY 2022

2022 IEEE Radio and Wireless Week (RWW)
16–19 January 2022
Location: Las Vegas, Nevada, United States

FEBRUARY 2022

2021 51st European Microwave Conference (EuMC), 2021 16th European Microwave Integrated Circuits Conference (EuMIC), and 2021 18th European Radar Conference (EuRAD)
14–15 February 2022
Location: London, United Kingdom





**2022 IEEE MTT-S
INTERNATIONAL
MICROWAVE
SYMPOSIUM**

**19-22 JUNE
COLORADO CONVENTION CENTER
Denver, Colorado**



IMS2022 is the centerpiece of Microwave Week 2022, which includes the RFIC Symposium (www.rfic-ieee.org) and the ARFTG Microwave Measurement Conference (www.arftg.org).

The Peaks of Microwaves

Join us as we explore the new Peaks of Microwaves including:

- Radar, Phased Arrays, OTA test: the triumvirate of modern microwave systems
- Microwaves for Tiny AI and IoT
- Hardware for Intelligent Mobility, Automotive, and IIoT applications
- Microwaves and satellites for Space 2.0
- 5G/6G Hardware: from components to system-on-chip and RF to THz
- Quantum RF Engineering
- Evolving RF/EM design strategies

Microwave Week provides a wide variety of technical and social activities for attendees and exhibitors.

New This Year: IMS2022 Systems Forum

- "The Connected Futures Summit," presenting current thinking on next generation wireless technologies at mmWave and THz frequencies, will include presentations, panels and a pavilion on the exhibition floor
- Focused sessions investigating the synergy between radar, phased arrays, and OTA test and applications
- Space 2.0 event highlighting advances in aerospace, the Internet-of-Space and the MTT CubeSat competition

Something for Everyone

- Competitions for best Advanced Practices Paper and Student Paper
- RF Bootcamp intended for students, engineers, and managers new to microwave engineering disciplines
- Workshops and application seminars from our exhibitors, explaining the technology behind their products
- Networking events for Amateur Radio (HAM) enthusiasts, Women in Microwaves (WiM), and Young Professionals
- Guest hospitality suite



Important Dates

17 September 2021 (Friday)

PROPOSAL SUBMISSION DEADLINE For workshops, technical lectures, focus and special sessions, panel and rump sessions. Preliminary workshop and technical lecture proposals due 16 July.

7 December 2021 (Tuesday)

PAPER SUBMISSION DEADLINE All submissions must be made electronically.

2 February 2022 (Wednesday)

PAPER DISPOSITION Authors will be notified by email.

9 March 2022 (Wednesday)

FINAL MANUSCRIPT SUBMISSION DEADLINE
Manuscript and copyright of accepted papers.

6 April 2022 (Wednesday)

SLIDE PRESENTATIONS DEADLINE FOR ALL AUTHORS AND PRESENTERS

19-22 June 2022

MICROWAVE WEEK IMS2022, RFIC 2022, ARFTG, and Exhibition





IMS2022 will feature technical sessions, interactive forums, plenary and panel sessions, workshops and technical lectures, application seminars, historical exhibits, and the world's largest RF and microwave industry exhibition.

With more than 9000 participants and 800 industrial exhibits of state-of-the-art microwave products, Microwave Week is the world's largest gathering of RF and microwave professionals.

NEW FOR 2022!

New! Systems Forum

The three-day Systems Forum will highlight the latest in telecommunications, radar and space applications.

New! Industrial Showcase

Papers with industrial authors can showcase their paper and answer questions about their company at the "Industrial Showcase" reception.

New! Industry-Supported Papers

Oral papers from industry-supported work may acknowledge industry sponsorship and/or booth number. Interactive-Forum Poster papers from industry-supported work may distribute approved coupons for prize at associated booth.

New! Industry Paper Contest Prize

Full-page ad in *IEEE Microwave Magazine* and *Microwave Journal*.

New! Paper Demonstrations

Authors of Oral and Interactive-Forum Poster papers may request time for live demonstrations in the Interactive Forum.

New! Interactive-Forum Poster Paper Previews

Interactive-Forum Poster papers and demonstrations will be previewed by an oral-session chair for greater visibility.

New! Virtual Content

See virtual previews and tutorials, participate in live events and attend virtual post-conference event with talks from prize-winning speakers.

New(ish)! Publication in MWCL

The 50 top-ranked papers, as determined by the Technical Paper Review Committee, will be invited to submit the paper to *IEEE Microwave and Wireless Components Letters*.



SPECIAL STUDENT PROGRAMS

IMS2022 encourages student participation! Visit the website for additional programs.

Student Design Competition:

All eligible students or student teams are invited to consider taking part in the Student Design Competitions (SDCs) during IMS2022. This is the premier IMS event where you can translate theory into real hardware and software designs.

Project Connect:

An exceptional group of undergraduate and first-year graduate students from underrepresented groups will be invited to IMS2022 on a travel grant provided by NSF and IEEE through a competitive application process.

PhD Student Initiative:

Available for all first- and second-year PhD students worldwide. The initiative provides sponsorship to attend IMS2022.



Technical Program Committee Members

Ronald Ginley, *General Chair*

Kate Remley/Dylan Williams, *TPC Chairs*

Osama Shana'a, *RFIC Conference General Chair*

Jeff Jargon, *ARFTG Conference General Chair*

Peter Aaen/Zoya Popovic, *Plenary Session Chairs*

Zoya Popovic/Michael Roberg/Scott Schafer, *Workshop and Technical Lecture Chairs*

Larry Dunleavy/Joanne Mistler/David Ricketts, *RF Boot Camp Chairs*

Jasmin Grosinger/Alan Brannon, *Panel Sessions Chairs*

Alan Brannon, *Focus/Special Sessions Chair*

Rob Horansky/Justus Brevic, *Interactive-Forum Chairs*

Gregor Lasser/Jan Verspecht/Taylor Barton, *Student Design Competition Chairs*

Elsie Vega, *Conference/Event Manager*



Technical Paper Submission

Authors are invited to submit technical papers describing original work and/or advanced practices on RF, microwave, mmWave, and THz theory and techniques. The deadline for submission is 7 December 2021.

Presentation Formats

1. Full-length (20 minute) oral papers report significant contributions, advancements, or applications.
2. Short (10 minute) oral papers report specific refinements or improvements in the state of the art.
3. Interactive-Forum Poster Papers provide a conversational setting where authors may also display hardware and perform demonstrations.

Paper Selection Criteria

There are four selection criteria: Originality, Quantitative Content, Clarity and Interest to MTT-S Membership.

Page Limit

For the initial submission deadline, the paper length should be 3 pages. An accepted paper may be 3 or 4 pages long.

Student Paper Competition

Full-time-student lead authors are encouraged to submit papers for the Student Paper Competition. First, second, and third prizes will be awarded based on content and presentation.

Industry and Advanced-Practice Paper Competitions

Submissions from industrial authors are automatically included in the Industry Competition. Advanced-Practice papers describe innovative techniques in practical aspects of design, processing, measurement or analysis that result in significant improvements in performance and/or time to production. Prizes will be awarded.

Submission Instructions

1. All submissions must be in English.
2. Authors should adhere to the format provided in the template, which can be downloaded from the conference website.
3. The initial submission should be in PDF format, and cannot exceed 4 MB in size.
4. Authors should upload their paper by midnight Hawaii time on 7 December 2021.

Details at www.ims2022.org



Paper Review

Papers are reviewed by IMS2022 Technical Program Subcommittees. A double-blind review process will be used to ensure anonymity for both authors and reviewers.

Notification

Authors will be notified of the decision by 2 February 2022 via email. For accepted papers, an electronic version of the final 3-4 page manuscript along with a copyright assignment to the IEEE must be submitted by 9 March 2022. The Symposium proceedings will be recorded on electronic media and archived in IEEE Xplore.

IEEE T-MTT Special Issue

Authors of all papers presented at IMS2022 can submit an expanded version of their papers to a special symposium issue of the IEEE Transactions on Microwave Theory and Techniques.

Clearances

It is the responsibility of the authors to acquire all required company and government clearances and IEEE copyright forms.

Health and Safety

Please refer to the conference website.



TECHNICAL AREAS:

Electromagnetic Field, Device and Circuit Techniques

- 1 Field analysis and guided waves** – Novel guiding and radiating structures, new physical phenomena in transmission lines and waveguides, and new analytical methods for solving guided-wave and radiation problems.
- 2 Numerical techniques & CAD algorithms** – Finite-difference, finite-element, integral equation, and hybrid methods for RF, microwave, and THz applications. Simulation, modeling, uncertainty quantification, and design optimization; circuit-, EM-, multi-physics-, and statistics-based, including surrogate modeling, space mapping, and model order reduction techniques.
- 3 Instrumentation and measurement techniques** – Theoretically supported and experimentally demonstrated linear and nonlinear measurement techniques for devices and materials, error correction, de-embedding, calibration, and novel instrumentation.
- 4 MHz-to-THz device modeling** – Active and passive, linear and nonlinear device and structure modeling (physical, empirical, and behavioral) including characterization, parameter extraction, and validation.
- 5 Nonlinear circuit and system analysis, simulation, and design** – Distortion, stability and qualitative dynamics analysis; circuits and systems (C&S) simulation techniques and applications; behavioral modeling of nonlinear C&S (excluding PAs); and nonlinear C&S design and implementations.
- 6 MHz-To-THz interaction of materials and tissues** – Electromagnetic field characterization and interaction at molecular, cellular, tissue and living systems levels; MRI and microwave imaging; medical applications; microwave-enhanced chemistry.

Passive Components and Packaging

- 7 Transmission-line structures** – Novel transmission-line structures and devices, transmission-line equivalent circuits, artificial transmission lines and metamaterial structures, transmission-line applications for devices and systems.
- 8 Passive circuit elements** – Couplers, dividers/combiners, hybrids, resonators, and lumped-element approaches.
- 9 Planar passive filters and multiplexers** – Planar passive filters and multiplexers including lumped elements, theoretical filter and multiplexer synthesis methods.
- 10 Non-planar passive filters and multiplexers** – Resonators, filters and multiplexers based on dielectric, waveguide, coaxial, or other non-planar structures.
- 11 Active, tunable, and integrated filters** – Integrated (on Si, LTCC, LCP, MCM-D, GaAs, etc.), active, and tunable filters.
- 12 Microwave acoustic, ferrite, ferroelectric, phase-change, and MEMS components** – Surface and bulk acoustic wave devices including FBAR devices, bulk and thin-film ferrite components, ferroelectric-based devices, and phase-change devices and components. RF microelectromechanical and micromachined components and subsystems.
- 13 Packaging, MCMs, and 3D manufacturing techniques** – Component and subsystem packaging, assembly methods, inkjet printing, multi-chip modules, wafer stacking, 3D interconnect, and integrated cooling. Novel processes related to 3D printing or additive manufacturing techniques.

Active Devices

- 14 Semiconductor devices and process characterization** – RF, microwave, mm-wave, and THz devices on III-V, silicon and other emerging technologies. MMIC and Si RFIC manufacturing, reliability, failure analysis, yield, and cost.
- 15 Low-noise amplifiers, variable-gain amplifiers and receivers** – LNAs, VGAs, detectors, receivers, integrated radiometers, cryogenic amplifiers and models, and characterization methods for low-noise integrated circuits and components.
- 16 Signal generation, modulators, frequency conversion, and signal shaping ICs** – CW and pulsed oscillators in silicon and III-V processes including VCOs, DROs, YTOs, PLOs, and frequency synthesizers, signal modulators, and frequency conversion ICs in silicon and III-V processes, such as IQ modulators, mixers, frequency multipliers/dividers, switches, and phase shifters.
- 17 Mixed-signal and wireline ICs** – High-speed mixed-signal components and subsystems for transmission; equalization and clock-data recovery techniques for electrical backplanes and electro-optical interfaces. High-speed mixed-signal components and subsystems, including ADC, DAC and DDS technologies.
- 18 High-power MHz, RF and microwave amplifiers** – Advances in discrete and IC power amplifier devices and design techniques based on III-V and LD-MOS devices, demonstrating improved power, efficiency, and linearity for HF, UHF, VHF, RF and microwave bands (< 26 GHz). Power-combining techniques for SSPA and vacuum electronics.
- 19 Compound semiconductor power amplifiers** – Advances in IC power amplifier devices, design techniques and power combining based on III-V and other compound semiconductor devices demonstrating improved power, efficiency, and linearity for millimeter-wave bands; vacuum electronics for millimeter-wave.
- 20 Silicon power amplifiers** – Advances in RFIC and digital power amplifier design and power combining techniques based on silicon CMOS and SiGe processes, demonstrating improved power, efficiency, and linearity for RF, millimeter-wave, and sub-THz bands.

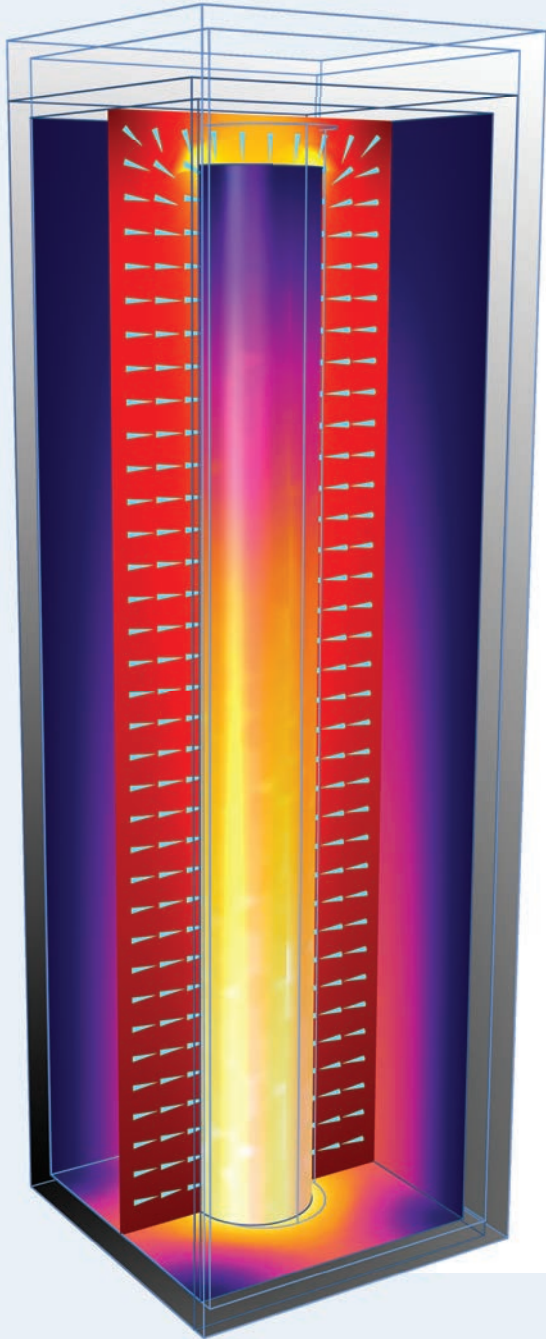
- 21 Linearization and transmitter techniques for power amplifiers** – Power amplifier design, characterization, and behavioral modeling; linearization and pre-distortion techniques; envelope-tracking, outphasing and Doherty transmitters for III-V and silicon technologies
- 22 Integrated transceivers, beamformers, imaging and phased-array chips and modules** – Design and characterization of complex III-V ICs, silicon ICs, heterogeneous systems, and related packaging in the RF to mm-wave including narrowband and wide-band designs. Innovative circuits and sub-systems for communications, radar, imaging, and sensing applications. Integrated on-chip antennas and on-package antennas.
- 23 Millimeter-wave and terahertz integrated circuits and systems** – Design and characterization of active components including LNAs, PAs, and frequency conversion ICs in silicon and III-V processes and/or packaging in the upper mm-wave and THz regimes; innovative THz circuits systems for communications, radar, imaging, and sensing applications. Demonstrations of on-chip antennas. Novel multi-feed antennas and antenna-electronics co-designs and co-integrations.
- 24 Microwave photonics and nanotechnology** – Integrated devices and 1D-2D material-based technology. Multidisciplinary field studying the interaction between microwaves, THz waves, and optical waves for the generation, processing, control, and distribution of microwave, mm-wave, and THz signals. Emerging RF applications of nanophotonics, nanoplasmonics, and nano-optomechanics; nanoscale metrology and imaging.
- 25 HF/VHF/UHF Technologies and Applications** – Advances in active and passive circuits, components, and systems that operate in the HF, VHF, and UHF frequency ranges.

Systems and Applications

- 26 Phased Arrays, MIMO and Beamformers** – Technology advances combining theory and hardware implementation in the areas of phased-array antennas, integrated beamformers, spatial power combining, retrodirective systems, built-in self-test techniques, broadband arrays, digital beamforming, and multi-beam systems. New beamforming, beam-tracking, and spatial notch algorithms, signal processing, and demonstrations.
- 27 Radar and Imaging Systems** – RF, millimeter-wave, and sub-THz radar and imaging systems, automotive radars, sensors for intelligent vehicular highway systems, UWB and broadband radar, remote sensing, radiometers, passive and active imaging systems, radar detection techniques, and related signal processing.
- 28 Wireless System Characterization and Architectures for 5G and Beyond** – RF, millimeter-wave, and sub-THz communication systems with hardware implementation for terrestrial, vehicular, satellite, and indoor applications, point-to-point links, backhaul and fronthaul applications, radio-over-fiber links, cognitive and software-defined radios, MIMO, massive MIMO, full-duplex technologies, simultaneous transmit and receive (STAR) systems, shared and novel spectrum use, waveform design, modulation schemes, and channel modeling.
- 29 Sensing and RFID Systems** – Short range wireless and RFID sensors, gas and fluidic sensors, passive and active tags from HF to millimeter-wave frequency, RFID systems including wearables and ultra-low-power.
- 30 Wireless Power Transmission** – Energy harvesting systems and applications, rectifiers, circuits, self-biased systems, combined data and power transfer systems
- 31 MHz-to-THz instrumentation for biological measurements and healthcare applications** – Devices, components, circuits and systems for biological measurements and characterizations; biomedical therapeutic and diagnostic applications; systems and instrumentation for biomedical applications; wireless sensors and systems, and implantable and wearable devices for health monitoring and telemedicine.
- 32 AI/ML for RF and mmWave** – AI/ML algorithms, implementations, and demonstrations for spectrum sensing, mobile edge networking, and MIMO and array beam operations and management; AI/ML algorithms for design and optimization of RF/mmWave components, circuits, and systems; AI/ML algorithms for in-situ sensing, diagnostics, control, reconfiguration, and optimization of MHz to THz communication and sensing circuits and systems.

Emerging Technologies

- 33 Innovative systems and applications** – Emerging technologies and novel system concepts for RF/microwave applications such as 6G, Internet of Things (IoT), Internet of Space (IoS), wearable computing/communication systems, machine-to-machine (M2M) communication, intelligent transportation, smart cities, smart environment, heterogeneous integration and 3D ICs, silicon photonics and plasmonics.
- 34 MHz-to-THz physical layer security** – Devices, circuits, and systems for secured communication and sensing from MHz to THz, addressing general security vulnerability due to electromagnetic emissions, hardware and software co-design for physical layer security, advanced devices and materials to enhance RF, mm-Wave, and THz physical layer security, trusted design, fabrication, packaging, and validation for RF, mm-Wave, and THz electronics.
- 35 Quantum devices, systems, and applications** – Cryogenic RF devices, circuits, systems and interfaces for quantum computing and sensing applications.



SIMULATION CASE STUDY

In 1 design, both electrothermal effects and structural deformation are at play.

Microwave transmitters rely on filters to maintain a desired frequency output, but thermal drift can affect their operation. In order to optimize the design of these components, engineers need to predict their performance under real-world conditions. Multiphysics modeling can be used to evaluate the electrothermal and structural effects of microwave filters — simultaneously.

LEARN MORE comsol.blog/microwave-filters



The COMSOL Multiphysics® software is used for simulating designs, devices, and processes in all fields of engineering, manufacturing, and scientific research.